Effects of variation in the visual environment on the feeding and catchability of Alaska fishes

Sean Khousuke Rohan

A dissertation

submitted in partial fulfillment of the

requirements for the degree of

Doctor of Philosophy

University of Washington

2021

Reading Committee:

Timothy E. Essington, Chair

Kerim Y. Aydin

David A. Beauchamp

Program Authorized to Offer Degree:

Aquatic and Fishery Sciences

University of Washington

Abstract

Effects of variation in the visual environment on the feeding and catchability of Alaska fishes

Sean Khosuke Rohan

Chair of the Supervisory Committee:
Professor Timothy E. Essington
School of Aquatic and Fishery Sciences

Aquatic animals use vision to perform tasks such as feeding, threat detection and avoidance, orientation, and social behavior. Thus, changes in light and water clarity can disrupt processes that affect the biological productivity of marine populations and alter visual interactions between fish and fishing gear. In the Bering Sea and Chukchi Sea, unprecedented warming due to climate change has enabled a poleward range expansion of historically subarctic fishes, which is likely to alter conditions for visual foraging and visual interactions between fish and fishing gear in fisheries independent surveys and commercial fisheries. In this dissertation, I examine the extent to which variation in light, depth, and water clarity influence visual foraging and catchability in the Bering Sea and Chukchi Sea. In Chapter 1, I develop a new generalized visual reaction distance model that predicts the reaction distance of fish to prey. In Chapter 2, I develop a novel method to monitor subsurface water clarity using bottom-trawl mounted archival tags equipped with a photodiode that measures irradiance. Using the method, I generate a time series of downwelling diffuse

attenuation coefficient and optical depth for the eastern Bering Sea, which I use to characterize spatial-temporal variation in light and water clarity from 2004 to 2018. In Chapter 3, I use a deterministic simulation model to evaluate the extent to which latitudinal variation in light regime affects the catchability of semi-pelagic and demersal fishes in the Bering Sea and Chukchi Sea. In Chapter 4, I characterize the extent to which visual foraging opportunity varies over space and time for a walleye-pollock-like predator visually searching for *Calanus* spp. copepods and juvenile walleye pollock during summer on the eastern Bering Sea continental shelf.

TABLE OF CONTENTS

List of Figures ix

List of Tables xi

Acknowledgements xii

Introduction 1

Chapter 1. Merging empirical and mechanistic approaches to modeling aquatic visual foraging using a generalizable visual reaction distance model 14

1.1 Abstract 14

1.2 Introduction 15

1.3 Materials and methods 19

1.3.1 Aksnes and Utne model of visual range 20

1.3.2 Generalized visual reaction distance model (GVRDM) 23

1.3.3 Parameterization for model evaluation 25

1.3.4 Evaluation of models 26

1.3.5 Model fitting and comparison 29

1.4 Results 30

1.4.1 Overall 30

1.4.2 Cases 31

1.5 Discussion 33

1.6 Conclusions 38

1.7 Acknowledgements 39

1.8 References 39

Chapter 2. Using bottom trawls to monitor subsurface water clarity in marine ecosystems 54

2.1 Abstract 54

2.2 Introduction 55

2.3 Regional setting 58

2.4 Methods 63

2.4.1 Data sources and processing 63

2.4.2 Satellite analysis 75

2.4.3 Regional and fine-scale analyses 75

2.4.4 Comparison with Bering10K model 80

2.5 Discussion 80

2.5.1 Overview 80

2.5.2 Patterns and trends 81

2.5.3 Implications for fisheries stock assessment and management 84

2.5.4 Limitations and uncertainties 86

2.5.5 Methodological improvements 87

2.5.6 Conclusions 88

2.6 Acknowledgements 88

2.7 References 89

Chapter 3. Light mediated changes in catchability due to poleward range expansion of fish stocks 115

3.1 Abstract 115

3.2 Introduction 116
3.3 Methods 121
3.3.1 Study area 121
3.3.2 Model framework 122
3.3.3 Scenarios 127
3.3.4 Code and software 128
3.4 Results 128
3.4.1 Standardized surveys 128
3.4.2 Bottom trawl fisheries 130
3.5 Discussion 131
3.5.1 Implications for fisheries stock assessment 132
3.5.2 Implications for fisheries 135
3.5.3 Other influences on catchability 135
3.5.4 Knowledge gaps and future research 136
3.5.5 Conclusions 139
3.6 Acknowledgements 139
3.7 References 139

Chapter 4. Water clarity, bathymetry, and light regime mediate visual foraging landscapes in the eastern Bering Sea 156

4.1 Abstract 156
4.2 Introduction 157
4.3 Methods 161
4.3.1 Generalized visual reaction distance model 162

4.3.2 Three-dimensional grids of diffuse attenuation coefficient, effective attenuation coefficient, and temperature 165
4.3.3 Downwelling irradiance 167
4.3.4 Analyzing spatial and diel variation in reaction distance 168
4.4 Results 169
4.4.1 Varation in diffuse attenuation coefficient and optical depth based on three-dimensional grids 169
4.4.2 Spatial, seasonal, and diel variation in reaction distance 170
4.5 Discussion 173
4.6 References 177
Synthesis 196
Appendix A: Chapter 1—Appendix 209
Appendix B: Chapter 2—Supplementary Material 256
Appendix C: Chapter 3—Supplementary Material 268
Appendix D: Chapter 4 (Supplementary Material) 287

LIST OF FIGURES

Figure 1.1. Conceptual diagram. 49
Figure 1.2. Dynamic scaling function. 49
Figure 1.3. Case #1—Reaction distances. 50
Figure 1.4. Case #2—Reaction distances. 51
Figure 1.5. Case #3—Reaction distances. 52
Figure 1.6. Composite predator-prey interaction term, T, and half-saturation constant, K_e.53
Figure 1.7. Case #4—Reaction distances. 53
Figure 2.1. Eastern Bering Sea bottom trawl survey area. 104
Figure 2.2. Archival tag assembly. 105
Figure 2.3. Surface-weighted archival tag $K_d(z_s, \lambda_{tag})$ versus OC-CCI $K_d(z_s, 490)$. 106
Figure 2.4. Depth versus optical depth. 106
Figure 2.5. Anomaly index correlations. 107
Figure 2.6. Maps of average optical depth $Z_{10\%}$, nepheloid layer index, mixed layer depth (MLD), $Z_{10\%}$-MLD. 108
Figure 2.7. Pearson correlation coefficients (r). 109
Figure 2.8. Cross-shelf profiles of optical and physical variables for rows S and P during 2011 and 2017. 110
Figure 2.9. Cross-shelf profiles of optical and physical water column structure for rows G and C during 2011 and 2017. 111
Figure 2.10. Change in $Z_{10\%}$, $Z_{1\%}$, and $\zeta(Z_{max}, \lambda_{tag})$ between 2004 and 2018. 112
Figure 2.11. Modeled (Bering10K-BESTNPZ) concentrations of chlorophyll-a (mg m^{-3}) and detrital carbon (mg m^{-3}) along rows C, G, P, and S during June–July of 2011 and 2017. 113
Figure 2.12. Modeled (Bering10K-BESTNPZ) depth-integrated chlorophyll-a (g m^{-2}) and detrital carbon (g m^{-2}) in the eastern Bering Sea during June–July 2011 and 2017. 114
Figure 3.1. Map of the study area, sea-ice coverage in April, day length by latitude, and summertime center-of-gravity distribution of groundfish species in the eastern Bering Sea. 151

Figure 3.2. Schematic of the simulation framework. 152
Figure 3.3.3. Gear efficiency (q_e) for the first bottom trawl haul of the day (i.e. early morning haul) on July 1. 153
Figure 3.3.4. Bottom trawl survey scenario catchability. 154
Figure 3.5. Daily mean gear efficiency (q_e; hourly gear efficiency averaged for each day). 155
Figure 3.6. Gear efficiency (q_e) at (A) midnight (00:00) and (B) noon (12:00) local time on August 1 at the 50% optical depth (average water clarity) quantile. 155
Figure 4.1. Map of study area. 190
Figure 4.2. Maps of the diffuse attenuation coefficient at 6-m off-bottom, optical depth 6-m off-bottom, and mixed layer depth. 190
Figure 4.3. Transect (cross-section) at 57°N on June 22, 2017 (solstice) at local noon and local midnight. 191
Figure 4.4. Transect (cross-section) at 62°N on June 22, 2017 (solstice) at local noon and local midnight. 192
Figure 4.5. Transect (cross-section) at 64.5°N on June 22, 2017 (solstice) at local noon and local midnight. 193
Figure 4.6. Transect (cross-section) along the 70-m isobath on June 22, 2017 (solstice) at local noon and local midnight. 194
Figure 4.7. Transect (cross-section) along the 70-m isobath on August 22, 2017 (solstice) at local noon and local midnight. 195

LIST OF TABLES

Table 1.1. Models used for case studies. 46
Table 1.2. Model terms and descriptions. 47
Table 1.3. Summary of model fits. 48
Table 2.1. Performance metrics and slope for the regression between archival tag $K_d(z_s, \lambda_{tag})$ and OC-CCI $K_d(z_s, 490)$. 103
Table 2.2. Estimated slopes (mean ± 2 standard errors) of linear mixed effects models between year (predictor) and $Z_{10\%}$, $Z_{1\%}$, and $\zeta(z_{max}, \lambda_{tag})$, where stations were included as a random effect. 103
Table 3.1. Herding proportions by species. 150
Table 4.1. Parameters in the generalized visual reaction distance model and environmental simulation. 188

ACKNOWLEDGEMENTS

I express my deepest gratitude to my advisor, Tim Essington, for his boundless enthusiasm and dedication to mentorship and teaching. It's been an absolute privilege to have Tim as an advisor. I'm extremely grateful for Tim's dedication to fostering a supportive and inclusive lab community, for his openness to new ideas and perspectives, and for being an extremely strong advocate for his students.

My research would not have been possible without the incredible support of my co-advisor, Dave Beauchamp. I'm extremely grateful to Dave for his mentorship, unwavering support, and continual encouragement to pursue bold and ambitious research goals.

The opportunity to go to graduate school and pursue this research would not have been possible without the support, encouragement, and enthusiasm of Kerim Aydin. I'm extremely grateful to Kerim for finding a way start me on my journey and serving on my committee for the past five years. I'm extremely thankful to Kerim for handling so many of the behind-the-scenes bureaucratic details so I could focus on my research with such little headache!

I'm incredibly grateful to John Horne for serving on my committee, for always taking the time to examine the details of my research and offering constructive feedback.

Thank you, LuAnne Thompson, for being an extremely responsive Graduate School Representative and for being an active and insightful participant in my exams. As you promised, I've come to learn that you ask really great questions!

I am extremely grateful to Stan Kotwicki for his incredible mentorship over the years, ardent support, enthusiasm for research, and steadfast dedication to ethical and principled leadership.

Science is a ‘team sport’ so I am thankful to have had the opportunity to work with a team of all-stars over the past five years. Thank you to all of my collaborators (Kerim Aydin, Lewis Barnett, Dave Beauchamp, Lyle Britt, Ned Cokelet, Tim Essington, Adam Hansen, Kelly Kearney, Stan Kotwicki, Ned Laman, Julie Nielsen, Susanne McDermott, Jen Schulien, Stephani Zador) for your contributions to the research in this dissertation and for teaching me so much! It’s been a delight to work with and learn from you!

To all of the members of the Essington and Beauchamp Labs, I’m thankful to have had your support and friendship over the years. It’s been inspirational to get to know so many amazing scientists who are also compassionate and caring members of the community. I can’t thank you all enough for your openness and trust, and for providing input and feedback on so many different things over the years.

Thank you to all of the members of Students Explore Aquatic Science and everyone in the School of Aquatic and Fishery Sciences who have taken on the challenge to be agents of change and continually strive to pursue a more equitable and inclusive future. Working with you all has been one of the most fulfilling experiences of my graduate school career and you have continually inspired me to strive to do better as a member of the scientific community.

Thank you to all of my friends in the SAFS Graduate Student community for your constant inspiration and support. From snowy peaks to dusty deserts and everywhere in between, your friendship and support have meant the world to me and I feel honored to know you all!

I’m grateful to my colleagues in NOAA/AFSC’s Resource Ecology and Ecosystem Modeling Program for encouraging me to pursue a graduate degree and providing support along the way. Thank you to all of my colleagues in the AFSC Groundfish Assessment Program who

have provided feedback and support, and carried some of the extra load while I have been completing my dissertation. I hope to be able to return the favor!

I'm grateful to my parents for their early support to pursue my interests and exposing me to the wonders of the natural world at an early age.

To my partner Caitlin, thank you for your patience and loving support. Thank you for standing by me on this journey. I love you so much and couldn't have done it without you!

INTRODUCTION

Marine animals rely on vision for feeding, threat detection, orientation, navigation, migration, and social behavior (Cronin et al., 2014; Douglas and Hawryshyn, 1990; Lythgoe, 1979). Consequently, changes in the visual environment affect the structure and function of marine ecosystems (Aksnes et al., 2004; Kaartvedt et al., 1996; Klevjer et al., 2016) and cause variation in the catchability of fish stocks (Glass and Wardle, 1989; Kotwicki et al., 2009; Ryer, 2008; Ryer and Olla, 2000), which can have implications for the assessment and management of marine fisheries. However, due to a lack of monitoring, there is little understanding of how much variation occurs in the visual environment of coastal marine ecosystems and to what extent variation affects the productivity, assessment, and management of marine animal populations.

To monitor the visual environment (light and water clarity) in a manner that characterizes the environmental experience of marine animal populations in coastal marine ecosystems, it is necessary to repeatedly sample across a broad spatial extent, at relatively high spatial resolution. Marine populations often have large ranges, and densities of marine animal populations vary over space and time due to seasonal migration, ontogeny, density-dependent habitat use, and shifting habitat mosaics. The visual environment varies due to stationary variation in the seasonal and diurnal light regime, and non-stationary variation in meteorological conditions and optically active constituents of the water column which regulate the transmission of light (Kirk, 2011). In coastal marine ecosystems, there is substantial mesoscale (1-100 km) and sub-mesoscale (< 1 km) variation in optically active constituents of the water column due to the mixing and layering of water masses of different origin with different physical, chemical, and biological properties (Babin et al., 2003; Morel and Prieur, 1977).

It is logistically challenging to monitor the visual environment of coastal marine ecosystems at a scale that is appropriate for characterizing the environmental experience of marine animal populations. Currently, ship-based sampling is the only feasible method of scale-appropriate sampling. Under clear-sky conditions, satellite-based remote sensing can be used as a basis to derive optical properties which characterize light transmission near the sea surface at high spatial resolution (Kirk, 2011; Naik et al., 2015, 2013). However, optical properties of a water column vary with depth (Capuzzo et al., 2015, 2013; Naik et al., 2013, 2010), so near-surface optical properties do not provide a reliable characterization of conditions experienced by deep-dwelling animals. Moorings can sample at high temporal resolution but have a small representative range. Autonomous underwater vehicles can obtain subsurface optical properties but have not been used prolifically, which is necessary for sustained monitoring. Finally, satellites, moorings, and autonomous underwater vehicles provide little or no information about the distribution, abundance, demography, diet, and behavior of marine fishes to accompany optical environment sampling. Such information is necessary to evaluate the ecological effects of variation in the visual environment on visual processes.

Despite a lack of monitoring of the visual environment, there is extensive knowledge of how changes in the visual environment can affect ecological processes. Changes in the subsurface light caused by variation atmospheric light and water clarity drive vertical migration in pelagic and semi-pelagic species (Beamish, 1966; Bozman et al., 2017; Kaartvedt et al., 2017, 1996; Roe, 1983). Because fishes rely on vision to school, the size and density of schools can change when visual conditions change (Glass et al., 1986). Although life stages of visual-orienting fishes may use light environments spanning at least nine orders of magnitude of variation in light (photon flux), the ability of a fish to perform visual tasks decreases from a maximum to zero over a 3-4

order of magnitude change in light (e.g. Vinyard and O'Brien 1976; Aksnes and Utne 1997; Utne 1997; Utne-Palm 1999; Vogel and Beauchamp 1999; Ryer and Olla 2000; Ryer et al. 2002; Hurst et al. 2007; Hansen et al. 2013; Cronin et al. 2014).

The effect of changes in light and water clarity on the strength of predator-prey interactions depends on the mode of feeding. Non-visual modes of feeding such as tactile feeding by gelatinous zooplankton become more efficient than visual feeding by fishes when vision is severely constrained (Eiane et al., 1999, 1997; Sørnes and Aksnes, 2004). Similarly, changes in turbidity affect far-field visual feeding by piscivores more than near-field visual feeding by planktivores (De Robertis et al., 2003; Giske et al., 1994). Under reduced water clarity, visual feeding fishes that are vulnerable to predation increase risk-taking behavior, potentially owing to a perceived decrease in predation risk (Gregory, 1994; McElroy et al., 2018). For predators which use multiple modes of foraging, the loss of visual foraging opportunity can lead to changes in foraging modes and prey types consumed (Gregory, 1994; Holbrook et al., 2013), altering the strength of predator-prey interactions within a food web. However, the effects of a change in the visual environment on predator-prey interactions depends on the ecological context in which changes occur.

Visual encounter distance models are a tool for understanding how light, water clarity, morphological traits of prey, and functional traits of predator vision systems influence the strength of visual predator-prey interactions (Beauchamp et al., 1999; Giske et al., 1994; Langbehn and Varpe, 2017; Lovvorn et al., 2001; Nilsson et al., 2014; Ruxton and Johnsen, 2016; Vinyard and O'Brien, 1976). However, mechanistic visual encounter distance models that are often used in marine ecology have a notable lack-of-fit to data from experiments conducted with real predators and prey (Meager et al., 2005; Utne-Palm, 2002), likely because assumptions of the model are violated in real predator-prey interactions. The lack-of-fit suggests theoretical models are likely to

generate inaccurate predictions of reaction distance and, therefore, inaccurate predictions for how changes in the visual environment will affect strength of trophic interactions or ecosystem structure. Despite the lack-of-fit, mechanistic visual encounter distance models have been widely used to make predictions about how variation in the visual environment affect the strength of trophic interactions, predation risk, and adaptive behaviors the mediate predation risk (e.g. Aksnes and Giske 1993; Giske et al. 1994; Fiksen and Giske 1995; Aksnes and Utne 1997; Eiane et al. 1997, 1999; Fiksen et al. 1998, 2002; De Robertis et al. 2000; Lovvorn et al. 2001; Maes et al. 2005; Lough and Kristiansen 2015; Varpe et al. 2015; Ruxton and Johnsen 2016; Langbehn and Varpe 2017). In part, this is possible because mechanistic models can be used for predator-prey systems where experimental observations of visual predator-prey interactions are not available. Thus, it would be beneficial to develop a mechanistic visual encounter distance model that fits experimental data well but can also be parameterized without observations of visual predator-prey interactions.

Changes in the visual environment can have implications for the assessment and management of fisheries. Catch rate data from fisheries and fisheries-independent stock assessment surveys are used as a basis to monitor changes in the abundance of fish stocks (Gunderson, 1993; Hilborn and Walters, 1992). Stochastic temporal variation in catchability increases the variance of stock assessment indices of abundance, while temporal trends in catchability cause indices of abundance to become biased over time (Wilberg et al., 2009). Because fishes use vision to detect and react to fishing gear and avoid habitat with unfavorable visual conditions, changes in light and water clarity affect catchability (Beamish, 1966; Godø, 1994; Hjellvik et al., 2002; Kotwicki et al., 2009).

Catch rate data from fisheries and fisheries-independent surveys are used as measures of relative abundance to track changes in the geographic distribution of marine populations (e.g. Pinsky et al. 2013). In the eastern Bering Sea, catch rate data have been used to track northward shifts of stocks from the southeastern Bering Sea to the shallower northeastern Bering Sea, due to climate change (Barbeaux, 2017; Barbeaux and Hollowed, 2018; Kotwicki and Lauth, 2013; Laman et al., 2018; Stevenson and Lauth, 2019; Thorson and Barnett, 2017). In the Gulf of Alaska, catch rate data were used to evaluate the depth distribution shift of marine populations in response to the 2015 warm-water anomaly in the eastern North Pacific ("The Blob"; Yang et al. 2019). However, changes in fish distribution and water clarity may expose animals to different visual conditions, which may affect catchability and the reliability of measures of species distribution.

In this dissertation, I develop a generalized visual reaction distance model that predicts reaction distances of aquatic predators to prey (Chapter 1). The model overcomes lack-of-fit issues of a widely used encounter distance model that are caused by a violation of model assumptions. In Chapter 2, I describe a new method to monitor subsurface water clarity using light sensors attached to bottom-trawl gear and use the method to chacterize variation in water clarity in the eastern Bering Sea during summers of 2004 to 2018. In Chapter 3, I use the water clarity data from Chapter 2, and a mechanistic model of gear efficiency (i.e., visual herding) and empirical models of vertical availability to evaluate the extent to which catchability of demersal and semipelagic fishes varies over space and time (daily and seasonally) on the continental shelves of the Bering Sea and Chukchi Sea. Finally, in Chapter 4, I use the generalized visual reaction distance model and water clarity information to examine the extent to which visual foraging opportunity varies for a walleye-pollock-like predator searching for zooplankton (*Calanus* spp.) and fish (15-cm juvenile walleye pollock) prey during summer on the eastern Bering Sea continental shelf.

REFERENCES

Aksnes, D. L., and J. Giske. 1993. A theoretical model of aquatic visual feeding. Ecological Modelling 67(2–4):233–250.

Aksnes, D. L., J. Nejstgaard, E. Sædberg, and T. Sørnes. 2004. Optical control of fish and zooplankton populations. Limnology and Oceanography 49(1):233–238.

Aksnes, D. L., and A. C. W. Utne. 1997. A revised model of visual range in fish. Sarsia 82:137–147.

Babin, M., A. Morel, V. Fournier-Sicre, F. Fell, and D. Stramski. 2003. Light scattering properties of marine particles in coastal and open ocean waters as related to the particle mass concentration. Limnology and Oceanography 48(2):843–859.

Barbeaux, S. J. 2017. Visualization of ontogenetic and interannual distributional shifts of groundfish from the Alaska Fisheries Science Center eastern Bering Sea bottom trawl survey, 1982-2015. United States Department of Commerce, NOAA Technical Memorandum NMFS-AFSC-348, 301 p.

Barbeaux, S. J., and A. B. Hollowed. 2018. Ontogeny matters: Climate variability and effects on fish distribution in the eastern Bering Sea. Fisheries Oceanography 27(1):1–15.

Beamish, F. W. H. 1966. Vertical migration by demersal fish in the Northwest Atlantic. Journal of the Fisheries Board of Canada 23(1):109–139.

Beauchamp, D. A., C. M. Baldwin, J. L. Vogel, and C. P. Gubala. 1999. Estimating diel, depth-specific foraging opportunities with a visual encounter rate model for pelagic piscivores. Canadian Journal of Fisheries and Aquatic Sciences 56(S1):128–139.

Bozman, A., J. Titelman, S. Kaartvedt, K. Eiane, and D. L. Aksnes. 2017. Jellyfish distribute vertically according to irradiance. Journal of Plankton Research 39(2):280–289.

Capuzzo, E., S. J. Painting, R. M. Forster, N. Greenwood, D. T. Stephens, and O. A. Mikkelsen. 2013. Variability in the sub-surface light climate at ecohydrodynamically distinct sites in the North Sea. Biogeochemistry 113(1–3):85–103.

Capuzzo, E., D. Stephens, T. Silva, J. Barry, and R. M. Forster. 2015. Decrease in water clarity of the southern and central North Sea during the 20th century. Global Change Biology 21(6):2206–2214.

Cronin, T. W., S. Johnsen, N. J. Marshall, and E. J. Warrant. 2014. Visual Ecology. Princeton University Press, Princeton, New Jersey.

Douglas, R. H., and C. W. Hawryshyn. 1990. Behavioral studies of fish vision: an analysis of visual capabilities. Pages 373–418 The Visual System of Fish.

Eiane, K., D. L. Aksnes, E. Bagøien, and S. Kaartvedt. 1999. Fish or jellies — a question of visibility? Limnology and Oceanography 44(5):1352–1357.

Eiane, K., D. L. Aksnes, and J. Giske. 1997. The significance of optical properties in competition among visual and tactile planktivores: a theoretical study. Ecological Modelling 98(2–3):123–136.

Fiksen, Ø., D. L. Aksnes, M. H. Flyum, and J. Giske. 2002. The influence of turbidity on growth and survival of fish larvae: a numerical analysis. Hydrobiologia 484:49–59.

Fiksen, O., and J. Giske. 1995. Vertical distribution and population dynamics of copepods by dynamic optimization. ICES Journal of Marine Science 52(3–4):483–503.

Fiksen, Ø., A. Utne, D. L. Aksnes, K. Eiane, J. V. Helvik, and S. Sundby. 1998. Modelling the influence of light, turbulence and ontogeny on ingestion rates in larval cod and herring. Fisheries Oceanography 7(3–4):355–363.

Giske, J., D. L. Aksnes, and Ø. Fiksen. 1994. Visual predators, environmental variables and zooplankton mortality risk. Vie Milieu 44(1):1–9.

Glass, C. W., and C. S. Wardle. 1989. Comparison of the reactions of fish to a trawl gear, at high and low light intensities. Fisheries Research 7(3):249–266.

Glass, C. W., C. S. Wardle, and W. Mojsiewicz. 1986. A light intensity threshold for schooling in the Atlantic mackerel, Scomber scombrus. Journal of Fish Biology 29(Supplement A):71–81.

Godø, O. R. 1994. Factors affecting the reliability of groundfish abundance estimates from bottom trawl surveys. Pages 166–199 in A. Fernö and S. Olsen, editors. Marine fish behavior in capture and abundance estimation. Fishing News Books, Oxford.

Gregory, R. S. 1994. The influence of ontogeny, perceived risk of predation, and visual ability on the foraging behavior of juvenile Chinook salmon. Pages 271–284 in K. L. Fresh and R. J. Feller, editors. Theory and Application in Fish Feeding Ecology. University of South Carolina Press, Columbia, South Carolina.

Gunderson, D. R. 1993. Surveys of Fisheries ResoucesJohn Wiley. New York.

Hansen, A. G., D. A. Beauchamp, and E. R. Schoen. 2013. Visual prey detection responses of piscivorous trout and salmon: Effects of light, turbidity, and prey size. Transactions of the American Fisheries Society 142(3):854–867.

Hilborn, R., and C. J. Walters. 1992. Quantitative fisheries stock assessment: choice, dynamics, & uncertainty. Chapman and Hall, New York.

Hjellvik, V., O. R. Godø, and D. Tjøstheim. 2002. Diurnal variation in bottom trawl survey catches: Does it pay to adjust? Canadian Journal of Fisheries and Aquatic Sciences 59(1):33–48.

Holbrook, B. V., T. R. Hrabik, D. K. Branstrator, and A. F. Mensinger. 2013. Foraging mechanisms of age-0 lake trout (*Salvelinus namaycush*). Journal of Great Lakes Research 39(1):128–137. Elsevier B.V.

Hurst, T. P., C. H. Ryer, J. M. Ramsey, and S. A. Haines. 2007. Divergent foraging strategies of three co-occurring north Pacific flatfishes. Marine Biology 151(3):1087–1098.

Kaartvedt, S., W. Melle, T. Knutsen, and H. R. Skjoldal. 1996. Vertical distribution of fish and krill beneath water of varying optical properties. Marine Ecology Progress Series 136(1–3):51–58.

Kaartvedt, S., A. Røstad, and D. L. Aksnes. 2017. Changing weather causes behavioral responses in the lower mesopelagic. Marine Ecology Progress Series 574:259–263.

Kirk, J. T. O. 2011. Light and photosynthesis in aquatic ecosystems, 3rd edition. Cambridge University Press, New York.

Klevjer, T. A., X. Irigoien, A. Røstad, E. Fraile-Nuez, V. M. Benítez-Barrios, and S. Kaartvedt. 2016. Large scale patterns in vertical distribution and behaviour of mesopelagic scattering layers. Scientific Reports 6(January):1–11. Nature Publishing Group.

Kotwicki, S., and R. R. Lauth. 2013. Detecting temporal trends and environmentally-driven changes in the spatial distribution of bottom fishes and crabs on the eastern Bering Sea shelf. Deep-Sea Research Part II: Topical Studies in Oceanography 94:231–243.

Kotwicki, S., A. De Robertis, P. von Szalay, and R. Towler. 2009. The effect of light intensity on the availability of walleye pollock (*Theragra chalcogramma*) to bottom trawl and acoustic surveys. Canadian Journal of Fisheries and Aquatic Sciences 66(6):983–994.

Laman, E. A., C. N. Rooper, K. Turner, S. Rooney, D. W. Cooper, and M. Zimmermann. 2018. Using species distribution models to describe essential fish habitat in Alaska. Canadian Journal of Fisheries and Aquatic Sciences 75(8):1230–1255.

Langbehn, T. J., and Ø. Varpe. 2017. Sea-ice loss boosts visual search: Fish foraging and changing pelagic interactions in polar oceans. Global Change Biology 23(12):5318–5330.

Lough, R. G., and T. Kristiansen. 2015. Potential growth of pelagic juvenile cod in relation to the 1978-2006 winter-spring zooplankton on the US continental shelf. ICES Journal of Marine Science 72(9):2549–2568.

Lovvorn, J. R., C. L. Baduini, and G. L. Hunt Jr. 2001. Modeling underwater visual and filter feeding by planktivorous shearwaters in unusual sea conditions. Ecology 82(8):2342–2356.

Lythgoe, J. . 1979. The Ecology of Vision. Clarendon Press, Oxford, United Kingdom.

Maes, J., K. E. Limburg, A. van de Putte, and F. Ollevier. 2005. A spatially explicit, individual-based model to assess the role of estuarine nurseries in the early life history of North Sea herring, Clupea harengus. Fisheries Oceanography 14(1):17–31.

McElroy, K. N., M. P. Beakes, and J. E. Merz. 2018. Hide and seek: Turbidity, cover, and ontogeny influence aggregation behavior in juvenile salmon. Ecosphere 9(4):1–15.

Meager, J. J., T. Solbakken, A. Utne-Palm, and T. Oen. 2005. Effects of turbidity on the reaction distance, search time, and foraging success of juvenile Atlantic cod (*Gadus morhua*). Canadian Journal of Fisheries and Aquatic Sciences 62(9):1978–1984.

Morel, A., and L. Prieur. 1977. Analysis of variations in ocean color. Limnology and Oceanography 22(4):709–722.

Naik, P., E. J. D'Sa, J. I. Goés, and H. R. Gomes. 2010. Assessment of particulate absorption properties in the southeastern Bering Sea from in-situ and remote sensing data. Journal of Applied Remote Sensing 4:43520–43561.

Naik, P., E. J. D'Sa, H. do R. Gomes, J. I. Goés, and C. B. Mouw. 2013. Light absorption properties of southeastern Bering Sea waters: Analysis, parameterization and implications for remote sensing. Remote Sensing of Environment 134:120–134. Elsevier Inc.

Naik, P., M. Wang, E. J. D'Sa, and C. W. Mordy. 2015. Bering Sea optical and biological properties from MODIS. Remote Sensing of Environment 163:240–252.

Nilsson, D. E., E. Warrant, and S. Johnsen. 2014. Computational visual ecology in the pelagic realm. Philosophical Transactions of the Royal Society B: Biological Sciences 369(1636).

Pinsky, M. L., B. Worm, M. J. Fogarty, J. L. Sarmiento, and S. A. Levin. 2013. Marine taxa track local climate velocities. Science 341:1239–1242.

De Robertis, A., J. S. Jaffe, and M. D. Ohman. 2000. Size-dependent predation risk and the timing of vertical migration in zooplankton. Limnology and Oceanography 45(8):1838–1844.

De Robertis, A., C. H. Ryer, A. Veloza, and R. D. Brodeur. 2003. Differential effects of turbidity on prey consumption of piscivorous and planktivorous fish. Canadian Journal of Fisheries and Aquatic Sciences 60(12):1517–1526.

Roe, H. S. J. 1983. Vertical distributions of euphausiids and fish in relation to light intensity in the Northeastern Atlantic. Marine Biology 77(3):287–298.

Ruxton, G. D., and S. Johnsen. 2016. The effect of aggregation on visibility in open water. Proceedings of the Royal Society B: Biological Sciences 283(20161463).

Ryer, C. H. 2008. A review of flatfish behavior relative to trawls. Fisheries Research 90:138–146.

Ryer, C. H., A. Lawton, R. J. Lopez, and B. L. Olla. 2002. A comparison of the functional ecology of visual vs. nonvisual foraging in two planktivorous marine fishes. Canadian Journal of Fisheries and Aquatic Sciences 59(8):1305–1314.

Ryer, C. H., and B. L. Olla. 2000. Avoidance of an approaching net by juvenile walleye pollock *Theragra chalcogramma* in the laboratory: the influence of light intensity. Fisheries Research 45:195–199.

Sørnes, T. A., and D. L. Aksnes. 2004. Predation efficiency in visual and tactile zooplanktivores. Limnology and Oceanography 49(1):69–75.

Stevenson, D. E., and R. R. Lauth. 2019. Bottom trawl surveys in the northern Bering Sea indicate recent shifts in the distribution of marine species. Polar Biology 42(2):407–421. Springer Berlin Heidelberg.

Thorson, J. T., and L. A. K. Barnett. 2017. Comparing estimates of abundance trends and distribution shifts using single- and multispecies models of fishes and biogenic habitat. ICES Journal of Marine Science 74(5):1311–1321.

Utne-Palm, A. 1999. The effect of prey mobility, prey contrast, turbidity and spectral composition on the reaction distance of *Gobiusculus flavescens* to its planktonic prey. Journal of Fish Biology 54(6):1244–1258.

Utne-Palm, A. 2002. Visual feeding of fish in a turbid environment: Physical and behavioural aspects. Marine and Freshwater Behaviour and Physiology 35(1–2):111–128.

Utne, A. 1997. The effect of turbidity and illumination on the reaction distance and search time of the marine planktivore Gobiusculus flavescens. Journal of Fish Biology 50(5):926–938.

Varpe, Ø., M. Daase, and T. Kristiansen. 2015. A fish-eye view on the new Arctic lightscape. ICES Journal of Marine Science 72(9):2532–2538.

Vinyard, G. L., and W. J. O'Brien. 1976. Effects of light and turbidity on the reactive distance of bluegill (*Lepomis macrochirus*). Journal of the Fisheries Research Board of Canada 33(12):2845–2849.

Vogel, J. L., and D. A. Beauchamp. 1999. Effects of light, prey size, and turbidity on reaction distances of lake trout (*Salvelinus namaycush*) to salmonid prey. Canadian Journal of Fisheries and Aquatic Sciences 56(7):1293–1297.

Wilberg, M. J., J. T. Thorson, B. C. Linton, and J. Berkson. 2009. Incorporating time-varying catchability into population dynamic stock assessment models. Reviews in Fisheries Science 18(1):7–24.

Yang, Q., E. D. Cokelet, P. J. Stabeno, L. Li, A. B. Hollowed, W. A. Palsson, N. A. Bond, and S. J. Barbeaux. 2019. How "The Blob" affected groundfish distributions in the Gulf of Alaska. Fisheries Oceanography 28(4):434–453.

Chapter 1. MERGING EMPIRICAL AND MECHANISTIC APPROACHES TO MODELING AQUATIC VISUAL FORAGING USING A GENERALIZABLE VISUAL REACTION DISTANCE MODEL[1]

1.1 ABSTRACT

Visual encounter distance models are important tools for predicting how light and water clarity mediate visual predator-prey interactions that affect the structure and function of aquatic ecosystems at multiple spatial, temporal, and organizational scales. The two main varieties of visual encounter distance models, mechanistic and empirical, are used for similar purposes but take fundamentally different approaches to model development and have different strengths and weaknesses in terms of predictive accuracy, physical and biological interpretability of parameters, ability to incorporate outside information, and utility for knowledge transfer. To overcome weaknesses of existing mechanistic and empirical models and bridge the gap between approaches, we developed a generalized visual reaction distance model that relaxes assumptions of a widely-used mechanistic model that are violated in real predator-prey interactions. We compared the performance of the generalized visual reaction distance model to a widely used mechanistic model and an empirical visual encounter distance model by fitting models to data from four predator-prey experiments. The generalized visual reaction distance model substantially outperformed the other models in all cases based on fit to reaction distance data and presents an attractive alternative

[1] This work is currently in review for publication. Co-authors: D.A. Beauchamp, T.E. Essington, A.G. Hansen

to prior models based on comparatively high predictive accuracy, use of interpretable parameters, and ability incorporate outside information—characteristics that facilitate knowledge transfer.

1.2 INTRODUCTION

Visual encounter distance models are an important tool for understanding how visual predator-prey interactions affect the structure and function of aquatic ecosystems. Visual encounter distance models link conditions in the visual environment (light and water clarity) to the distance at which predator-prey interactions are initiated (Aksnes and Giske, 1993; Aksnes and Utne, 1997; Mazur and Beauchamp, 2003; Vogel and Beauchamp, 1999; Wright and O'Brien, 1984). The models provide a basis for answering questions about how visual predator-prey interactions affect ecosystems across multiple spatial, temporal, and organizational (e.g. population, community, whole ecosystem) scales (DeRobertis, 2002; Giske et al., 1994; Hansen and Beauchamp, 2015; J Kitano et al., 2008; Maes et al., 2005).

We define three concepts that are important for understanding how visual predator-prey encounters are modeled in aquatic ecology: visual range, reaction distance, and encounter distance. Visual range is the distance at which an object (prey) is detectable to an animal (predator) based on visual sensory input exceeding the minimum threshold of detection for contrast, size, or motion of an animal's vision system. These thresholds are quantified using behavioral responses from conditioning experiments conducted with visual stimuli (e.g. Anthony, 1981), experiments that measure physiological (electrical) responses of the vision system response to stimuli of varying intensity (e.g. Horodysky et al., 2010; Naka and Rushton, 1966a; Semmelhack et al., 2014), histological and histological-physiological investigation of photoreceptor structure and function (e.g. Hairston, Jr. et al., 1982; Lythgoe, 1972; Warrant and Nilsson, 1998), and by fitting

mechanistic models of visual range to data from predator-prey visual foraging experiments (e.g. Aksnes and Utne, 1997; Meager et al., 2010). Reaction distance is the distance at which an animal exhibits a behavioral reaction towards a stimulus. In predator-prey interactions, reaction distance is the result of both detection and co-evolved dynamics of predator-prey interactions that determine whether a predator responds given detection of a stimulus. Reaction distances are quantified using predator-prey experiments or in situ observations of predator-prey interactions. We define encounter distance as the distance where a predator initiates a predator-prey interaction within the context of a model. Encounter distance can be synonymous with visual range or reaction distance, depending on how a visual encounter distance model is constructed. Some approaches for calculating visual range based on minimum detection criteria can combine information from physiological experiments, histological studies, and behavioral conditioning studies, but do not account for behavior.

Visual encounter distance models are a key component of coupled visual foraging models that predict prey encounter and consumption rates of predators as a function of light and water clarity, prey distribution and density, and predator distribution. There are two main varieties of visual encounter distance models used to characterize visual reactions of predators to prey, mechanistic and empirical (i.e. phenomenological). Mechanistic and empirical models take fundamentally different approaches to model development and parameterization. Mechanistic models characterize visual range as a proxy for encounter distance based on individual physical and biological components of predator-prey system. Mechanistic models are parameterized by statistically fitting models to reaction distance data from visual foraging experiments (e.g. Aksnes and Utne, 1997; Meager et al., 2010) or using morphological and functional traits of predators and prey (Giske et al., 1994; Lovvorn et al., 2001; Nilsson et al., 2014; Ruxton and Johnsen, 2016).

Mechanistic models have a tendency to produce unrealistically large estimates of reaction distance under conditions of low water clarity that are common in marine ecosystems. As such, mechanistic models often impose generic and un-validated constraints on visual range, such as setting a minimum contrast threshold to avoid unrealistically low signal detection thresholds for photoreceptors (e.g. Ruxton and Johnsen, 2016) or setting maximum encounter distance equal to one predator body length (e.g. Fiksen et al., 2002; Langbehn and Varpe, 2017; Varpe and Fiksen, 2010). Empirical models are developed by fitting generic functional forms (e.g. polynomial, sigmoidal, piecewise polynomial) to reaction distance data from visual foraging experiments, with the best-fitting model used to predict visual encounter distances (Hansen et al., 2013; Holbrook et al., 2013; Keyler et al., 2019).

Mechanistic and empirical encounter distance models have different strengths and weaknesses, owing to different assumptions about how to represent processes that regulate visual predator-prey interactions. By using specific functional representations of physical and biological processes, mechanistic models assume that functional representations accurately represent the physical process by which image-forming light propagates through water, and the physiological-behavioral process of vision and reaction (Aksnes and Giske, 1993; Aksnes and Utne, 1997). The strength of mechanistic models is that they use physically interpretable parameters, which allows them to incorporate information beyond what may be available for a single experiment, predator or prey; this is useful because it is infeasible to conduct experiments with every predator-prey system (Lythgoe, 1972). However, a weakness is that if assumptions of mechanistic models are not met, they have limited ability to fit empirical data and may produce biased estimates of parameters and encounter distances.

In contrast to mechanistic models, empirical models make few assumptions about how physical or physiological-behavioral processes should be functionally represented. Consequently, empirical models may be more flexible and thereby provide a better fit to the data. A weakness is that model terms do not always have a physical or biological interpretation outside the context of a specific predator-prey system, and parameters are not necessarily comparable among predators, prey, or experiments.

Despite the different approaches to model development and parameterization, mechanistic and empirical visual encounter distance models are used to address similar questions. For example, a mechanistic model showed how reduced water clarity caused by eutrophication can allow tactile-feeding jellyfish to gain a competitive advantage over visually-feeding fish larvae, reducing the productivity of marine fish stocks (Eiane et al., 1999), while an empirical model demonstrated how reduced water clarity can reduce predation risk and increase foraging opportunity and productivity of lake-dwelling planktivorous fishes (Hansen and Beauchamp, 2015). Similarly, a mechanistic model suggested how the loss of Arctic sea-ice due to climate change may increase light and enhance the productivity of visually foraging pelagic fish stocks (Langbehn and Varpe, 2017), while an empirical model showed how increases in light due to anthropogenic light pollution can increase visual predation mortality for planktivorous fishes (Mazur and Beauchamp, 2006).

Ideally, visual encounter distance models should have physically and biologically interpretable parameters and apply consistent representations of the physical process of visual image transfer and the physiological-behavioral process of vision and reaction, but do so under a broader range of assumptions to improve model fits. In this way, a more standardized approach can be used to estimate visual parameters from experimental data, thereby facilitating the transfer and generalization of knowledge (Bouchet et al., 2019; Yates et al., 2018). Moreover, models that

use explicit structural representations of physiological-behavioral and physical processes represent specific mechanistic hypotheses about how processes work. Thus, lack-of-fit can provide insight into why a hypothesis failed and guide refinement or generation of new hypotheses (Hilborn and Mangel, 1997).

It would be beneficial to develop a visual encounter distance model that mechanistically characterizes physical and biological relationships in the visual encounter process, fits visual reaction distance data well, can incorporate outside information, and facilitate knowledge transfer. To that end, we developed a generalized visual reaction distance model that bridges the gap between mechanistic and empirical modeling approaches by relaxing assumptions of the widely-used Aksnes and Utne (1997) mechanistic model of visual range that appear to be violated in real predator-prey interactions. Using data from four published experimental visual foraging studies, we then compare the performance of the generalized visual reaction distance model to the Aksnes and Utne model, and an empirical model. Studies were chosen to provide a representative set of predator-prey systems (planktivorous and piscivorous fish), sensory modes of foraging (visual and non-visual), environmental conditions (light and water clarity), and experimental configurations. Our primary aims were to evaluate whether assumptions of the Aksnes and Utne model were violated, compare the performance of the generalized visual reaction distance model to empirical models, and examine how different modeling approaches affect parameter estimates and the precision and accuracy of predicted reaction distances.

1.3 MATERIALS AND METHODS

We developed a generalized visual reaction distance model for aquatic predator-prey interactions by relaxing structural assumptions of the Aksnes and Utne model of visual range

(Aksnes and Utne, 1997). By applying the model to a series of cases from the literature, we then compared the performance of various formulations of the generalized visual reaction distance model to the Aksnes and Utne model, and an empirical visual encounter distance model (Table 1.1). Parameters associated with these models are defined in Table 1.2.

1.3.1 *Aksnes and Utne model of visual range*

The Aksnes and Utne model combines mechanistic relationships from physics and physiology, the law of contrast reduction and Naka-Rushton function (Supplementary Appendix A), to predict visual range, as a proxy for visual encounter distance, based on the visual environment, functional light sensitivity of predator vision systems, and morphological traits of prey (Table 1.1; Table 1.2). In the Aksnes and Utne model, the condition for visual detection is

$$(|C_0|\exp(-cr))\left(\frac{A_p}{r^2}\right)\left(\frac{E_{max}E_b}{K_e+E_b}\right) \geq \Delta S_e, \quad (1)$$

where $|C_0|$ is the inherent Weber contrast of a target (dimensionless), c is the beam attenuation coefficient of the medium (m^{-1}), r is viewing distance (m), A_p is the visible area of a target (m^2), E_{max} is the maximum irradiance processing level of an observer's vision system ($\mu E \cdot m^{-2} \cdot s^{-1}$), E_b is background irradiance in the environment ($\mu E \cdot m^{-2} \cdot s^{-1}$), K_e is the half-saturation level for processing of retinal irradiance ($\mu E \cdot m^{-2} \cdot s^{-1}$), and ΔS_e is the irradiance sensitivity threshold of the observer's vision system ($\mu E \cdot m^{-2} \cdot s^{-1}$). In the Aksnes and Utne model, a target (i.e. prey) is considered visible if the left side of Eqn. 1 is greater than or equal to ΔS_e. To solve for maximum visual range or reaction distance, ΔS_e can be combined into a composite saturation term, E' (dimensionless; $E' = E_{max}/\Delta S_e$,) which characterizes the visual capabilities of the observer, simplifying the model to

$$r^2\exp(cr) = |C_0|A_pE'\frac{E_b}{K_e+E_b}. \quad (2)$$

When used to predict visual encounter distance between a predator and prey, the Aksnes and Utne model makes five key assumptions that, when violated, result in a lack-of-fit to reaction distance data from visual foraging experiments: 1) predators detect prey visually; 2) predators view the object along a horizontal plane; 3) apparent contrast of an object decreases monotonically according to the law of contrast reduction; 4) reactions occur at the distance where apparent contrast of the object exceeds the minimum contrast threshold of the predator; and 5) the retinal-neural-behavioral response to changes in environmental light follows a Naka-Rushton function with $\alpha = 1$. There is evidence that real predator-prey interactions routinely violate the first four assumptions of the Aksnes and Utne model.

The first assumption of the Aksnes and Utne model can be violated because predators use senses other than vision to detect prey. When light levels fall below the minimum for visual detection of prey, reaction distances can approach an asymptote for some predator-prey systems (e.g. Hansen et al., 2013; Richmond et al., 2004). Filtering data a priori to ensure the model is only fit to visual reactions can prevent a violation of model assumptions, although the threshold light level between visual and non-visual reactions may not be obvious.

The second assumption that predators view prey along a horizontal plane is almost certainly violated in many real predator-prey interactions. In visual search, it is advantageous for predators to search for prey from below because downwelling light increases the luminance of the background, increasing the contrast of prey (e.g. Thetmeyer and Kils, 1995). To avoid issues of angular dependence and allow measurement of reaction distance at low light levels, some visual reaction distance experiments have constrained predator viewing angles by using shallow experimental arenas. Adding angular dependence to the Aksnes and Utne model would improve the flexibility of the model.

The third and fourth assumptions, regarding contrast reduction and contrast thresholds, can be violated in several ways, but reasons for a violation are inseparable based solely on predator behavior. As turbidity increases from clear-water conditions, fishes exhibit an increase or no change in reaction distance to prey at low levels of turbidity, followed by a decrease at higher levels of turbidity (Hansen et al., 2013; Mazur and Beauchamp, 2003; Utne-Palm, 2002; Vogel and Beauchamp, 1999). Hypotheses to explain a lack-of-fit to turbidity are that suspendoids increase the visual contrast of prey against the background by affecting color and brightness contrast (physical effects hypothesis; Utne-Palm, 2002), that feeding motivation of predators increases at specific levels of turbidity due to acclimation (feeding motivation hypothesis; Boehlert and Morgan, 1985; Utne-Palm, 2002), or that reactions depend on a predator recognizing an object as prey based on apparent size, shape, and movement (ideal stimulus hypothesis; (Hairston, Jr. et al., 1982; Semmelhack et al., 2014).

The third assumption may be violated because the law of contrast reduction may not apply to underwater visual foraging (Supplementary Appendix A). The law of contrast reduction was originally derived for the atmosphere, where objects are visible at long distances (Lee et al., 2015). A key assumption used to analytically derive the law of contrast reduction for the atmosphere is that targets can be treated as point sources. This is likely violated in many underwater visibility applications because underwater objects become visible at distances that are orders-of-magnitude shorter distances than in air (Lee et al., 2015).

The fourth assumption, that reactions occur at the point where the apparent contrast of prey exceeds the minimum detectable contrast threshold, can be violated because detection precedes recognition and reaction, and detection and recognition of prey does not guarantee a reaction. An object becomes detectable (i.e. is within visual range) when image-forming light radiating from

the object reaches an observer's photoreceptors and initiates a retinal-neural signaling response (phototransduction cascade) that exceeds some minimum threshold for detection (Dowling, 2012). Signals are processed in the retina and brain, leading to recognition and reaction (Semmelhack et al., 2014). However, detection and recognition does not necessarily lead to reaction because reactions are mediated by the physiological state of a predator (e.g. hunger, stress), learning, and co-evolved dynamics of predator attack and prey defense, factors that may be considered extensions of the ideal stimulus and feeding motivation hypotheses.

Moreover, an object moving through the visual field of a predator presents an attentive cue that can play a role in detection, recognition, and reaction. Consequently, visual predators may react to mobile prey at greater distances than stationary prey (Utne-Palm, 1999), which is not explicitly represented in the Aksnes and Utne model.

1.3.2 *Generalized visual reaction distance model (GVRDM)*

We developed various formulations of a generalized visual reaction distance model to relax structural assumptions of the Aksnes and Utne model that appear violated in real predator-prey interactions (Table 1.1) and define the parameters associated with these models (Table 1.2). Starting from the Aksnes and Utne model, we added a non-visual reaction distance component to the model to relax the first assumption, as

$$\begin{matrix} {r_V}^2 \exp(r_V c) = |C_0| A_p E' \dfrac{E_b}{K_e + E_b} & if\ E_b \geq q \\ r_{NV} = D & if\ E_b < q \end{matrix}, \tag{3}$$

where D is non-visual reaction distance (m), and q is the light intensity threshold (μmol·photons·m^{-2}·s^{-1}) below which non-visual reaction distance exceeds visual reaction distance.

We relaxed the second assumption of the Aksnes and Utne model by incorporating Duntley's angular contrast reduction equation (Duntley, 1952) into the model to allow non-horizontal viewing angles, as

$$\begin{matrix} {r_V}^2 \exp\left(r_V(c - k_d \cos\theta)\right) = |C_0| A_p E' \dfrac{E_b}{K_e + E_b} & if\ E_b \geq q \\ r_{NV} = D & if\ E_b < q \end{matrix} \quad (4)$$

where k_d is the downwelling diffuse attenuation coefficient (m^{-1}), and θ is the nadir viewing angle (up = 0°, down = 180°).

To address the violation of the law of contrast reduction in underwater visibility applications, we replaced the beam attenuation coefficient, c, with the effective attenuation coefficient, κ (m^{-1}), based on the contrast reduction equation from Lee et al.'s (2015) underwater visibility theory (Supplementary Appendix A).

Finally, we relaxed the third and fourth assumptions, that turbidity has a monotonic effect on reaction distance and reactions occur at a specific contrast threshold, by including a dynamic scaling function, $\omega(\cdot)$:

$$\begin{matrix} {r_V}^2 \exp\left(r_V(\kappa - k_d \cos\theta)\right) = \omega(\kappa) |C_0| A_p E' \dfrac{E_b}{K_e + E_b} & if\ E_b \geq q \\ r_{NV} = D & if\ E_b < q \end{matrix}. \quad (5)$$

The dynamic scaling function models the effect of turbidity (e.g. effective attenuation coefficient, κ) as a function of shape parameters β, δ, h:

$$\omega(\kappa) = \left(\beta + \frac{\delta^h \kappa^{h-1} \exp(-\delta\kappa)}{\Gamma(h)}\right). \quad (6)$$

The β parameter is dimensionless, but represents a turbidity-dependent change in contrast (i.e. convergence to a new inherent contrast as turbidity increases). The h and δ parameters are dimensionless and do not have a direct physical or biological interpretation outside of the context of the dynamic scaling function. Rather, the parameters give the dynamic scaling function the

flexibility to take functional forms that represent hypotheses concerning the lack-of-fit of the Aksnes and Utne model.

The model does not address specific violations of the fourth assumption. However, in Case #3 (subsection 1.2.4.3) we examine how prey movement, a factor in the ideal stimulus hypothesis, can be accounted for in the generalized visual reaction distance model.

The generalized visual reaction distance model does not provide a basis to test mechanistic hypotheses about the lack-of-fit of the Aksnes and Utne model; rather it provides a framework for testing whether structural assumptions of the Aksnes and Utne are violated in visual foraging experiments. For plausible values of the effective attenuation coefficient, κ, the Aksnes and Utne model is a special case of the generalized visual reaction distance model where $\theta = 90°$, $q = 0$, $\beta = 1$, $h \rightarrow 0$, $\delta \rightarrow 0$, and $\varepsilon = 0$ or $b_f \rightarrow 0$.

1.3.3 *Parameterization for model evaluation*

We used the generalized visual reaction distance model, Aksnes and Utne model, and an empirical broken-stick model for our cases (Tables 1.1–1.2; Supplementary Appendix B). We reparameterized the Aksnes and Utne model and generalized visual reaction distance model for our cases using an approach typically used to fit the Aksnes and Utne model to visual reaction distance data. Inherent contrast, $|C_0|$, and prey area, A_p, typically are not measured in behavioral reaction distance experiments due to the complexities of prey orientation, predator viewing angle, color and brightness of prey, spectral sensitivity of the predator's vision system, and spectral characteristics of the light field. Instead, $|C_0|$, A_p, and E' are typically combined into a composite predator-prey interaction term, T (m^2), which simplifies the Aksnes and Utne model to

$$r^2 \exp(cr) = T \frac{E_b}{K_e + E_b}, \tag{7}$$

and the visual component of the generalized visual reaction distance model to

$$r_V{}^2 \exp\left(r_V(\kappa - k_d \cos\theta)\right) = \omega(\kappa) T \frac{E_b}{K_e + E_b} \quad if\ E_b \geq q. \tag{8}$$

For our study, we treated model terms for the effective attenuation coefficient, κ, beam attenuation coefficient, c, and experimentally measured absorption coefficients as interchangeable values, although physically they characterize light transmission in different ways.

1.3.4 *Evaluation of models*

We evaluated the performance of the generalized visual reaction distance model relative to the Aksnes and Utne model and an empirical encounter distance model. Specifically, we evaluated whether assumptions of the Aksnes and Utne model were violated in real predator-prey interactions, whether the generalized visual reaction distance model performs as well as empirical models, and which version of the dynamic scaling function (with or without β) had the best performance in the generalized visual reaction distance model. We reviewed 32 visual foraging studies (65 predator-prey combinations among experiments) that involved manipulation of the visual environment and measurements of reaction distance (Table B2) and screened studies for inclusion in model evaluation based on suitability criteria (Table B1). Based on the screening criteria, we selected cases from four visual foraging studies for model evaluation based on our goal to include a representative set of predators (planktivores and piscivores), prey (fish and zooplankton; individuals and aggregations), and sensory modes of prey detection (visual and non-visual). Information about studies we reviewed and details of experimental designs from cases are

described in Supplementary Appendix B. Specific objectives and models used for each case are described below.

1.3.4.1 Case #1—Piscivore reacting to fish prey

We evaluated model performance for a piscivore system that may involve a non-visual reaction to prey at low light levels. We fit models to data from an experiment where yearling Chinook salmon *Oncorhynchus tshawytscha* reacted to juvenile rainbow trout *O. mykiss* under varying levels of light and turbidity (Hansen et al., 2013; Supplementary Appendix B). In the experiments, Chinook salmon reaction distances approached an asymptote at ~50 cm at low light levels, potentially owing to a response to non-visual stimulus or an unexplained artifact of the experimental design. Because there was evidence of non-visual reaction, we used versions of the Aksnes and Utne model and generalized visual reaction distance model that included a non-visual reaction distance component (AUM.2, GVRDM.1, GVRDM.2; Table 1.1). We also fit a version of the best-fit empirical model (broken stick model [BSM]) from the original study to the data (Supplementary Appendix C). Attack angles were not measured during the study so we assumed the nadir viewing angle was horizontal (θ = 90°). Under this assumption, the diffuse attenuation coefficient, k_d, is irrelevant because $k_d \cos(90°)$ always equals zero.

1.3.4.2 Case #2—Planktivore reacting to group of ten zooplankton prey

We evaluated whether the dynamics governing detection of prey aggregations were the same as for detection of individual prey and estimated model parameters for Case #3. Thus, for Case #2, we fit models to data from an experiment where two-spotted goby *Gobius flavescens*

reacted to aggregations of ten *Calanus finmarchicus*, a transparent calanoid copepod. Copepod aggregations were retained in 10 cm × 3 cm vials under varying levels of light and turbidity (Utne, 1997). No non-visual reactions were reported (i.e. no asymptote at low light levels) so we used formulations of the Aksnes and Utne model and generalized visual reaction distance model without a non-visual reaction (AUM.1, GVRDM.3, GVRDM.4). Attack angles were not reported so we assumed $\theta = 90°$.

Because the Aksnes and Utne model uses beam attenuation, c, rather than effective attenuation coefficient, κ, we also evaluated whether this difference affected model performance (Aksnes and Utne, 1997; Supplementary Appendix F: *Attenuation*).

1.3.4.3 Case #3—Planktivore reacting to single zooplankton

Case #3—We evaluated model performance for a planktivore reacting to individual prey, to assess if models could be used to simultaneously characterize the relative visibility of multiple prey types from the perspective of a predator and determine if the generalized visual reaction distance model and Aksnes and Utne model predicted similar visibility relationships among prey. We fit models to data from an experiment where two-spotted goby reacted to individual copepod (*C. finmarchicus/C. helgolandicus*) prey across a range of turbidities but only one light level, 20 $\mu E \cdot m^{-2} \cdot s^{-1}$ (Utne-Palm, 1999; Supplementary Appendix B). Treatments used mobile transparent, immobile transparent, or mobile red-colored prey. No non-visual reactions were reported so we used models formulations without a non-visual reaction (AUM.1, GVRDM.3, GVRDM.4). Attack angles were not reported, so we assumed $\theta = 90°$. We included a different T parameter for each prey type (T_{TM} –transparent-mobile, T_{TI}–transparent immobile, T_{RM}–red-mobile). Because

experimental light levels were constant, we could not estimate K_e using only Case #3 data. Instead, we parameterized models using the maximum likelihood estimates of K_e from Case #2.

1.3.4.4 Case #4—Planktivore reacting to single zooplankton, with angular dependence

We evaluated whether information about nadir viewing angle improved model fit to reaction distance data. To do so, we fit models to data from a planktivore experiment where stone moroko *Pseudoraspbora parva* reacted to *Daphnia pulex* under varying levels of light and turbidity (Asaeda et al., 2002; Supplementary Appendix B). The study was the only one we are aware of where both nadir viewing angles and reaction distances were reported. No non-visual reactions were reported so we used versions models without a non-visual component (AUM.1, GVRDM.3, and GVRDM.4; Table 1.1). To evaluate whether nadir viewing angle improved model fit, we compared models with nadir viewing angle to models where nadir viewing angle equaled 90° (Supplementary Appendix F: *Angular dependence*).

1.3.5 *Model fitting and comparison*

For each case (subsections 2.3.4.1–2.3.4.4), variance in reaction distance increased as reaction distance increased, so we fit models assuming reaction distances had log-normally distributed error. We estimated separate variances for visual, σ_V, and non-visual, σ_{NV}, components of models because they involve different predator sensory processes that would presumably have different residual error structures. Additional details about model fitting are provided in Supplementary Appendix B.

We used bias-corrected Akaike's Information Criterion (AIC_c) for model comparison and evaluated model fit based on visual inspection of Q-Q plots and residual plots.

1.4 RESULTS

1.4.1 *Overall*

The generalized visual reaction distance model substantially outperformed the Aksnes and Utne model in all cases, based on AIC_c, indicating assumptions of the Aksnes and Utne model were violated in all predator-prey interactions (Table 1.3). Turbidity did not have a monotonic effect on reaction distance for any of the cases, shown by the dynamic scaling functions (Fig. 1.2). The Aksnes and Utne model had a lack-of-fit to turbidity, as shown by model fits across ranges of effective attenuation coefficient, κ (Figs. 1.3A, 1.4A, 1.5A), and patterns in model residuals in relation to κ (Supplementary Figs. D1–D4). The generalized visual reaction distance model had comparable or better fit than the Aksnes and Utne model across gradients of light (Figs. 1.3B, 1.4B).

The generalized visual reaction distance model tended to estimate that predators were less dark-adapted (higher K_e) and could process more light or had higher contrast sensitivity (higher T) than predicted by the Aksnes and Utne model (Fig. 1.6). The higher half-saturation level for retinal irradiance processing, K_e, predicted by the generalized visual reaction distance model for Cases #2–4 indicates that more light was necessary to stimulate a physiological-behavioral response to light. Higher values of the composite predator-prey interaction term, T, indicate a higher maximum retinal radiance processing capability, E_{max}, or lower threshold for the predator's vision system to detect changes in irradiance between the target and the background, ΔS_e. The latter is analogous to contrast sensitivity (Supplementary Appendix A).

Turbidity-induced changes in prey contrast were not evident. For all cases, versions of the generalized visual reaction distance model without a β parameter outperformed versions with a β parameter (Table 1.3). Additionally, for Cases #2–4, versions of the model with a β parameter had wider confidence intervals for parameters than models without β, indicating that inclusion of β inflated uncertainty in estimates of other parameters (Supplementary Figs E2–E4). Thus, we focused on versions of the model without β.

Across gradients of light and turbidity, reaction distances predicted by the generalized visual reaction distance model differed from the Aksnes and Utne model, as shown by fitted reaction distance surfaces for Cases #1–3 (Figs 1.3C, 1.4C, 1.5B). This is important because visual encounter distance models are often used to predict encounter distances well outside the range of experimental observations.

1.4.2 *Cases*

For Case #1, the generalized visual reaction distance model outperformed the broken-stick model based on AIC_c, indicating that it can perform at least as well as empirical models (Table 1.3). Despite the better fit of the generalized visual reaction distance model, predictions were generally similar between the generalized visual reaction distance model and broken stick model within the range of experimental conditions (Fig. 1.3A–B). However, beyond the range of experimental conditions, differences in predicted reaction distances between the models were considerable (Fig. 1.3C).

For Case #2, fitting models to adjusted beam attenuation, c, instead of the effective attenuation coefficient, κ, improved the fit of the Aksnes and Utne model and worsened the fit of the generalized visual reaction distance model (Supplementary Table E1). Still, the generalized

visual reaction distance model outperformed the Aksnes and Utne model based on AIC_c. For the Aksnes and Utne model, K_e and T parameter estimates were ~2.1 and ~1.6 times higher than for the model with κ, respectively. For the generalized visual reaction distance model, K_e did not change, but T was ~10.6 times higher than for models with κ. Higher T indicates higher light processing capability or higher contrast sensitivity, while higher K_e indicate lower dark adaptation. Because light-intensity responses vary over orders-of-magnitude, small variations in K_e and T for the Aksnes and Utne model and K_e for the generalized visual reaction distance model would not substantially affect the predictive performance of models.

Processes regulating visual reactions of two-spotted goby to aggregations of ten copepods (Case #2) may have differed from those regulating reactions to individual copepods (Case #3). This was indicated by qualitative differences in the contour shapes between reaction distance surfaces for ten copepods (Fig. 1.4C) versus single copepods (Fig. 1.5B) and differences in dynamic scaling function parameters (Fig. 1.2; Supplementary Figs E2–E3). This difference may be an artifact of the experimental approach, the different levels at which data were aggregated for the cases, or because mechanisms that regulate visual reactions are functionally different between aggregations and individuals.

For Case #3, the generalized visual reaction distance model and Aksnes and Utne model both predicted that red mobile copepods (RM) were the most visible, followed by transparent mobile (TM), then transparent immobile (TI) copepods, as shown by fitted reaction distances (Fig. 1.5) and the rank-order of T parameters for different prey ($T_{RM} > T_{TM} > T_{TI}$; Supplementary Fig. E3). The Aksnes and Utne model and generalized visual reaction distance model estimated nearly identical relative visibility relationships among prey, as T_{RM}:T_{TM}:T_{TI} was approximately 1.00:0.66:0.33 for both models. For the highest turbidity treatment (highest κ), predator reactions

to transparent immobile prey were based on a single observation, whereas all other observations were the mean of multiple reactions (Utne-Palm, 1999). This likely explains the single large outlier residual for transparent immobile prey for the generalized visual reaction distance model (Supplementary Fig. E6).

In Case #4, the only case where viewing angles were observed, reaction distance was affected by nadir viewing angle, θ. The fit of the generalized visual reaction distance model was better using observed θ instead of $\theta = 90°$, as indicated by the lower AIC_c (Supplementary Table F3). Viewing angle had a larger effect on reaction distance at higher turbidity (higher κ) when compared to low turbidity (Fig. 1.7). The Aksnes and Utne model and generalized visual reaction distance model had similar trends in residual error across the range of θ, but the magnitude of residuals was much lower for the generalized visual reaction distance model (Supplementary Fig. D7). Based on residuals of the generalized visual reaction distance model for $\theta > 100°$, the assumed angular relationship of the generalized visual reaction distance model may have been violated in Case #4 (Supplementary Fig. E7). However, other factors may have affected the fit, such as: the experiment design, our digitization of plots with high point densities, our conversion of body lengths to meters, or our conversion of NTU to κ.

1.5 Discussion

Overall, the generalized visual reaction distance model provides a balance between model fit and characterization of physical and biological relationships that is advantageous for modelling predator-prey interactions. The generalized visual reaction distance model fit better in all cases and is an attractive alternative to the Aksnes and Utne model and empirical models. The generalized visual reaction distance model is continuous and uses physically and biologically

interpretable parameters. This allows the model to accommodate new information and extend to novel circumstances. Unlike the Aksnes and Utne model, the generalized visual reaction distance model is not entirely based on measureable physical and biological properties because the dynamic scaling function does not represent a specific mechanism. Instead, the generalized visual reaction distance model provides a heuristic representation of multiple hypotheses (physical effects hypothesis, feeding motivation hypothesis, ideal stimulus hypothesis).

The generalized visual reaction distance model overcomes an important assumption of the Aksnes and Utne model: that visual range (and encounter distance) decreases monotonically with turbidity. This assumption is violated in real predator-prey interactions (see review by Utne-Palm [2002]), and causes the Aksnes and Utne model to predict unreasonably high reaction distances at the low attenuation values that are common in marine ecosystems. As a solution, some studies have imposed a reaction distance constraint on the Aksnes and Utne model, such as setting the maximum reaction distance equal to one predator body length (e.g. Fiksen et al., 2002; Langbehn and Varpe, 2017; Varpe and Fiksen, 2010). Although the maximum reaction distance for some predator-prey interactions may approximately equal one predator body length (Richmond et al., 2004; Schwalbe and Webb, 2015; Utne, 1997), this cannot be considered a norm. Many predators react to prey at distances far-exceeding one predator body length (Asaeda et al., 2002; Blaxter, 1966; Hansen et al., 2013; Holbrook et al., 2013; Mazur and Beauchamp, 2003; Schmidt and O'Brien, 1982; Vinyard and O'Brien, 1976). The dynamic scaling function of the generalized visual reaction distance model imposes an empirically-derived constraint on reaction distance, obviating the need to impose arbitrary constraints. Further, if the generalized visual reaction distance model can fit reaction distance data as well as empirical visual encounter distance models, it may alleviate the need to use experimental designs that carefully stagger turbidity treatments to

identify critical thresholds for turbidity-dependent reaction distance, a primary design consideration for some visual reaction distance experiments.

Comparing the relative visibility of multiple prey types in Case #3 illustrates an advantage of using visual encounter distance models to characterize visibility. Traditionally, differences in apparent size and contrast of prey have often been inferred from human measurements of prey, and thus, may be prone to measurement error and biases of human perception. By contrast, we used the generalized visual reaction distance model to estimate the relative visibility of multiple prey types, from the perspective of a predator, using a single model that had a much better fit to the data than the Aksnes and Utne model, but the same relative visibility relationship among prey as in the Aksnes and Utne model. As such, the generalized visual reaction distance model can be used to validate human-derived measures that characterize relative visibility and, due to the use of physically and biologically interpretable terms, improves our knowledge transfer about the relative visibility of prey to other systems. This is important because the core question for many visual foraging studies is how prey visibility (size and contrast) interacts with the visual environment (light and water clarity) to affect predator-prey linkages and ecosystem structure (e.g. Hansen and Beauchamp, 2014; Lovvorn et al., 2001; Rosland and Giske, 1994).

The generalized visual reaction distance model can accommodate information about the visual encounter process that is not explicitly included in the physical and biological terms. In Case #3, for example, mobile and immobile transparent copepods would not have differences in C_0 or A_p, so the difference between T_{MT} and T_{TI} is a movement effect that was not explicitly represented in the model. The ratio T_{TM}/T_{TI} (1.5) can be interpreted as the proportional increase in visibility due to movement (50%), although it is not clear how T_{TM} and T_{TI} are functionally related. The model structure could be extended to accommodate known or hypothesized relationships. For

example, reaction distances can increase as a function of predator size (Mazur and Beauchamp, 2003; Schmidt and O'Brien, 1982) due to ontogenetic changes in visual acuity, spectral sensitivity, light sensitivity, or higher probability of capture success that increases the profitability of longer distance attacks (Breck and Gitter, 1983; Britt et al., 2001; Hairston, Jr. et al., 1982). Depending on what mechanism drives size-dependent variation in reaction distance, the parameters K_e, ΔS_e, E', E_{max}, or T could be modeled as a function of predator size, as suggested by Aksnes and Giske (1993).

In Case #1, the asymptotic reaction distance of adolescent Chinook salmon to juvenile rainbow trout at low light levels may have resulted from a scale-dependent artifact of the experimental design or a behaviorally-mediated change in visual prey detection, rather than a result of different responses to visual and non-visual stimuli. Regardless, other studies have shown that predators forage non-visually when light is limiting (e.g. Ryer et al., 2002), and that non-visual reactions occur at distances greater than zero (Richmond et al., 2004). Unfortunately, we were unable to fit the generalized visual reaction distance model to data from other studies where non-visual reactions may have occurred because they did not have adequate sample sizes or include a sufficient range of variation in light levels.

Much of the data we used were not independent and we did not account for pseudoreplication in our primary analyses. Doing so would have underestimated the variability of individual reactions to prey (i.e. low σ_V, σ_{NV}, and σ). Further, the digitized data did not allow identification of unique predators or treatments for Cases #2–4. For Case #1, we could identify individual experimental trials in the original exeprimetnal data. To evaluate whether pseudoreplication affected our conclusions, we fit models to the mean reaction distances of trials

for Case #1. Taking this approach, the generalized visual reaction distance model still outperformed the other models (Supplementary Appendix F: *Pseudoreplication*).

Our approach to model-fitting does not provide direct insight into the visual range of the predators because reaction distance is an indirect measure of visual range. Acknowledging the difference between visual range and reaction distance, Aksnes and Utne (1997) fit their model to data by first calculating the mean and standard deviation of reaction distance for each experimental light and turbidity treatment level, then fit their model to a visual range which they defined as the mean plus two standard deviations. While this approach may be reasonable, there is no inherent justification for such a definition of visual range. Multiple factors can drive variation in reaction distance, such as viewing angle, prey movement, prey orientation relative to the predator, spatial variation in the predator's visual acuity, feeding motivation of the predator, learning, social factors, and co-evolved attack-defense dynamics of a predator-prey system. Rather than accounting for differences between visual range and reaction distance *a priori*, we suggest a model with a well-behaved error structure could produce post hoc estimates of visual range that are conceptually similar to the visual range definition of Aksnes and Utne (1997).

Although the cases showed evidence that four assumptions of the Aksnes and Utne model were violated, there was reasonable support for the fifth assumption, that the light intensity-response for a predator reacting to prey is well-approximated by the Naka-Ruston function (Supplementary Appendix A). Other studies also support that the Naka-Ruston function affords a good fit to experimental visual reaction distance data along a gradient of light, albeit using different names, symbols, and quantities for functional representation. In Supplementary Appendix G, we demonstrate that over short distances and with low attenuation, empirical visual encounter distance

models with Naka-Rushton dynamics are asymptotically equivalent to the Aksnes and Utne model and generalized visual reaction distance model.

The experimental cases we examined used relatively narrow ranges of light and turbidity, limiting our ability to assess model performance across broader environmental gradients. Although the experiments spanned ranges generating the most dynamic visual responses, we suggest that future visual reaction distance experiments be conducted across wider ranges of light and turbidity to allow better assessment of model performance. Acoustic technologies such as dual-frequency identification sonar overcome limitations of video.

1.6 CONCLUSIONS

Visual encounter distance models provide valuable insights into how visual processes affect the structure and function of aquatic ecosystems. The generalized visual reaction distance appears to be an attractive alternative to empirical models of reaction distance because it provides a good fit to reaction distance data from predator-prey systems within a single framework. It improves upon the Aksnes and Utne model by providing a better fit to empirical data when assumptions of the Aksnes and Utne model are met, although it does not provide a means to test hypotheses concerning why assumptions are violated. We speculate that testing these hypotheses will require improvements to the model based on a deeper integration of dynamics involved in predator-prey interactions that arise from physics, physiology, and ethology.

1.7 ACKNOWLEDGEMENTS

We are grateful to Lyle Britt, Ellis Loew, Jeff Napp, Jennifer Schulien, and Andy Whitehouse for constructive comments on an earlier version of this manuscript. We thank Anne-Christine Utne-Palm for providing clarification about experimental methods. Any use of trade, firm, or product names is for descriptive purposes only and does not imply endorsement by the U.S. Government.

1.8 REFERENCES

Aksnes, D.L., Giske, J., 1993. A theoretical model of aquatic visual feeding. Ecol. Modell. 67, 233–250. https://doi.org/10.1016/0304-3800(93)90007-F

Aksnes, D.L., Utne, A.C.W., 1997. A revised model of visual range in fish. Sarsia 82, 137–147. https://doi.org/10.1080/00364827.1997.10413647

Anthony, P.D., 1981. Visual contrast thresholds in the cod *Gadus morhua* L. J. Fish Biol. 19, 87–103. https://doi.org/10.1111/j.1095-8649.1981.tb05814.x

Asaeda, T., Park, B.K., Manatunge, J., 2002. Characteristics of reaction field and the reactive distance of a planktivore, *Pseudorasbora parva* (Cyprinidae), in various environmental conditions. Hydrobiologia 489, 29–43. https://doi.org/10.1023/A:1023298823106

Blaxter, J.H.S., 1966. The effect of light intensity on the feeding ecology of herring, in: Bainbridge, R., Evans, G.C., Rackham, O. (Eds.), Light as an Ecological Factor: A Symposium of the British Ecological Society Cambridge 30th March-1 April 1965. John Wiley & Sons Inc, New York, pp. 393–409.

Boehlert, G.W., Morgan, J.B., 1985. Turbidity enhances feeding abilities of larval Pacific herring, Clupea harengus pallasi. Hydrobiologia 123, 161–170.

Bouchet, P.J., Peterson, A.T., Zurell, D., Dormann, C.F., Schoeman, D., Ross, R.E., Snelgrove, P., Sequeira, A.M.M., Whittingham, M.J., Wang, L., Rapacciuolo, G., Oppel, S., Mellin, C., Lauria, V., Krishnakumar, P.K., Jones, A.R., Heinänen, S., Heikkinen, R.K., Gregr, E.J., Fielding, A.H., Caley, M.J., Barbosa, A.M., Bamford, A.J., Lozano-Montes, H., Parnell, S., Wenger, S., Yates, K.L., 2019. Better model transfers require knowledge of mechanisms. Trends Ecol. Evol. 34, 489–490. https://doi.org/10.1016/j.tree.2019.04.006

Breck, J.E., Gitter, M.J., 1983. Effect of fish size on the reactive distance of bluegill (*Lepomis macrochirus*) sunfish. Can. J. Fish. Aquat. Sci. 40, 162–167. https://doi.org/10.1139/f83-026

Britt, L.L., Loew, E.R., McFarland, W.N., 2001. Visual pigments in the early life stages of Pacific northwest marine fishes. J. Exp. Biol. 204, 2581–2587.

DeRobertis, A., 2002. Size-dependent visual predation risk and the timing of vertical migration: An optimization model. Limnol. Oceanogr. 47, 925–933.

Dowling, J.E., 2012. The retina: an approachable part of the brain, Revised Ed. ed. The Belknap Press of Harvard University Press, Cambridge, MA.

Duntley, S.Q., 1952. The visibility of submerged objects. Cambridge, Massachusetts.

Eiane, K., Aksnes, D.L., Bagøien, E., Kaartvedt, S., 1999. Fish or jellies — a question of visibility? Limnol. Oceanogr. 44, 1352–1357. https://doi.org/10.4319/lo.1999.44.5.1352

Fiksen, Ø., Aksnes, D.L., Flyum, M.H., Giske, J., 2002. The influence of turbidity on growth and survival of fish larvae: a numerical analysis. Hydrobiologia 484, 49–59. https://doi.org/10.1023/A:1021396719733

Giske, J., Aksnes, D.L., Fiksen, Ø., 1994. Visual predators, environmental variables and zooplankton mortality risk. Vie Milieu 44, 1–9.

Hairston, Jr., N.G., Li, K.T., Easter, Jr., S.S., 1982. Fish vision and the detection of planktonic prey. Science (80-.). 218, 1240–1242.

Hansen, A.G., Beauchamp, D.A., 2015. Latitudinal and photic effects on diel foraging and predation risk in freshwater pelagic ecosystems. J. Anim. Ecol. 84, 532–544. https://doi.org/10.1111/1365-2656.12295

Hansen, A.G., Beauchamp, D.A., 2014. Effects of prey abundance, distribution, visual contrast and morphology on selection by a pelagic piscivore. Freshw. Biol. 59, 2328–2341. https://doi.org/10.1111/fwb.12436

Hansen, A.G., Beauchamp, D.A., Schoen, E.R., 2013. Visual prey detection responses of piscivorous trout and salmon: Effects of light, turbidity, and prey size. Trans. Am. Fish. Soc. 142, 854–867. https://doi.org/10.1080/00028487.2013.785978

Hilborn, R., Mangel, M., 1997. The ecological detective: Confronting models with data. Princeton University Press.

Holbrook, B. V., Hrabik, T.R., Branstrator, D.K., Mensinger, A.F., 2013. Foraging mechanisms of age-0 lake trout (*Salvelinus namaycush*). J. Great Lakes Res. 39, 128–137. https://doi.org/10.1016/j.jglr.2012.12.008

Horodysky, A.Z., Brill, R.W., Warrant, E.J., Musick, J.A., Latour, R.J., 2010. Comparative visual function in four piscivorous fishes inhabiting Chesapeake Bay. J. Exp. Biol. 213, 1751–1761. https://doi.org/10.1242/jeb.038117

Keyler, T.D., Hrabik, T.R., Mensinger, A.F., Rogers, L.S., Gorman, O.T., 2019. Effect of light intensity and substrate type on siscowet lake trout (*Salvelinus namaycush siscowet*)

predation on deepwater sculpin (*Myoxocephalus thompsonii*). Hydrobiologia 840, 77–88. https://doi.org/10.1007/s10750-019-3944-5

Kitano, J., Bolnick, D.I., Beauchamp, D.A., Mazur, M.M., Mori, S., Nakano, S., Peichel, C.L., 2008. Reverse evolution of armour plates in the threespine stickleback. Curr. Biol. 18, 744–769.

Langbehn, T.J., Varpe, Ø., 2017. Sea-ice loss boosts visual search: Fish foraging and changing pelagic interactions in polar oceans. Glob. Chang. Biol. 23, 5318–5330. https://doi.org/10.1111/gcb.13797

Lee, Z., Shang, S., Hu, C., Du, K., Weidemann, A., Hou, W., Lin, J., Lin, G., 2015. Secchi disk depth: A new theory and mechanistic model for underwater visibility. Remote Sens. Environ. 169, 139–149. https://doi.org/10.1016/j.rse.2015.08.002

Lovvorn, J.R., Baduini, C.L., Hunt Jr., G.L., 2001. Modeling underwater visual and filter feeding by planktivorous shearwaters in unusual sea conditions. Ecology 82, 2342–2356.

Lythgoe, J.., 1972. The adaptation of visual pigments to the photic environment, in: Dartnell, H.J.A. (Ed.), The Handbook of Sensory Physiology VII/1. Springer, pp. 566–603.

Maes, J., Limburg, K.E., van de Putte, A., Ollevier, F., 2005. A spatially explicit, individual-based model to assess the role of estuarine nurseries in the early life history of North Sea herring, Clupea harengus. Fish. Oceanogr. 14, 17–31. https://doi.org/10.1111/j.1365-2419.2004.00300.x

Mazur, M.M., Beauchamp, D.A., 2006. Linking piscivory to spatial-temporal distributions of pelagic prey fishes with a visual foraging model. J. Fish Biol. 69, 151–175. https://doi.org/10.1111/j.1095-8649.2006.01075.x

Mazur, M.M., Beauchamp, D.A., 2003. A comparison of visual prey detection among species of piscivorous salmonids: Effects of light and low turbidities. Environ. Biol. Fishes 67, 397–405. https://doi.org/10.1023/A:1025807711512

Meager, J.J., Moberg, O., Strand, E., Utne-Palm, A., 2010. Effects of light intensity on visual prey detection by juvenile Atlantic cod (*Gadus morhua* L.). Mar. Freshw. Behav. Physiol. 43, 99–108. https://doi.org/http://dx.doi.org/10.1080/10236241003798910

Naka, K.I., Rushton, W.A.H., 1966. S-potentials from colour units in the retina of fish (Cyprinidae). J. Physiol. 185, 536–555.

Nilsson, D.E., Warrant, E., Johnsen, S., 2014. Computational visual ecology in the pelagic realm. Philos. Trans. R. Soc. B Biol. Sci. 369. https://doi.org/10.1098/rstb.2013.0038

Richmond, H.E., Hrabik, T.R., Mensinger, A.F., 2004. Light intensity, prey detection and foraging mechanisms of age 0 year yellow perch. J. Fish Biol. 65, 195–205. https://doi.org/10.1111/j.0022-1112.2004.00444.x

Rosland, R., Giske, J., 1994. A dynamic optimization model of the diel vertical-distribution of a pelagic planktivorous fish. Prog. Oceanogr. 34, 1–43. https://doi.org/10.1016/0079-6611(94)90025-6

Ruxton, G.D., Johnsen, S., 2016. The effect of aggregation on visibility in open water. Proc. R. Soc. B Biol. Sci. 283.

Ryer, C.H., Lawton, A., Lopez, R.J., Olla, B.L., 2002. A comparison of the functional ecology of visual vs. nonvisual foraging in two planktivorous marine fishes. Can. J. Fish. Aquat. Sci. 59, 1305–1314. https://doi.org/10.1139/f02-097

Schmidt, D., O'Brien, W.J., 1982. Planktivorous feeding ecology of Arctic grayling (*Thymallus arcticus*). Can. J. Fish. Aquat. Sci. 39, 475–482. https://doi.org/10.1155/2011/352451

Schwalbe, M.A.B., Webb, J.F., 2015. The effect of light intensity on prey detection behavior in two Lake Malawi cichlids, *Aulonocara stuartgranti* and *Tramitichromis* sp. J. Comp. Physiol. A Neuroethol. Sensory, Neural, Behav. Physiol. 201, 341–356. https://doi.org/10.1007/s00359-015-0982-y

Semmelhack, J.L., Donovan, J.C., Thiele, T.R., Kuehn, E., Francisco, S., Francisco, S., 2014. A dedicated visual pathway for prey detection in larval zebrafish. Elife 3, 1–19. https://doi.org/10.7554/eLife.04878

Thetmeyer, H., Kils, U., 1995. To see and not be seen: the visibility of predator and prey with respect to feeding behaviour. Mar. Ecol. Prog. Ser. 126, 1–8. https://doi.org/10.3354/meps126001

Utne-Palm, A., 2002. Visual feeding of fish in a turbid environment: Physical and behavioural aspects. Mar. Freshw. Behav. Physiol. 35, 111–128. https://doi.org/10.1080/10236240290025644

Utne-Palm, A., 1999. The effect of prey mobility, prey contrast, turbidity and spectral composition on the reaction distance of *Gobiusculus flavescens* to its planktonic prey. J. Fish Biol. 54, 1244–1258. https://doi.org/10.1111/j.1095-8649.1999.tb02052.x

Utne, A., 1997. The effect of turbidity and illumination on the reaction distance and search time of the marine planktivore *Gobiusculus flavescens*. J. Fish Biol. 50, 926–938. https://doi.org/10.1111/j.1095-8649.1997.tb01619.x

Varpe, Ø., Fiksen, Ø., 2010. Seasonal plankton-fish interactions: light regime, prey phenology, and herring foraging. Ecology 91, 311–318.

Vinyard, G.L., O'Brien, W.J., 1976. Effects of light and turbidity on the reactive distance of bluegill (*Lepomis macrochirus*). J. Fish. Res. Board Canada 33, 2845–2849.

Vogel, J.L., Beauchamp, D.A., 1999. Effects of light, prey size, and turbidity on reaction distances of lake trout (*Salvelinus namaycush*) to salmonid prey. Can. J. Fish. Aquat. Sci. 56, 1293–1297. https://doi.org/10.1139/cjfas-56-7-1293

Warrant, E.J., Nilsson, D., 1998. Absorption of White Light in Photoreceptors. Vision Res. 38, 195–207. https://doi.org/10.1016/S0042-6989(97)00151-X

Wright, D.I., O'Brien, W.J., 1984. The development and field test of a tactical model of the planktivorous feeding of white crappie (*Pomoxis annularis*). Ecol. Monogr. 54, 65–98.

Yates, K.L., Bouchet, P.J., Caley, M.J., Mengersen, K., Randin, C.F., Parnell, S., Fielding, A.H., Bamford, A.J., Ban, S., Barbosa, A.M., Dormann, C.F., Elith, J., Embling, C.B., Ervin, G.N., Fisher, R., Gould, S., Graf, R.F., Gregr, E.J., Halpin, P.N., Heikkinen, R.K., Heinänen, S., Jones, A.R., Krishnakumar, P.K., Lauria, V., Lozano-Montes, H., Mannocci, L., Mellin, C., Mesgaran, M.B., Moreno-Amat, E., Mormede, S., Novaczek, E., Oppel, S., Ortuño Crespo, G., Peterson, A.T., Rapacciuolo, G., Roberts, J.J., Ross, R.E., Scales, K.L., Schoeman, D., Snelgrove, P., Sundblad, G., Thuiller, W., Torres, L.G., Verbruggen, H., Wang, L., Wenger, S., Whittingham, M.J., Zharikov, Y., Zurell, D., Sequeira, A.M.M., 2018. Outstanding challenges in the transferability of ecological models. Trends Ecol. Evol. 33, 790–802. https://doi.org/10.1016/j.tree.2018.08.001

Table 1.1. Models used for case studies.

Abbrev.	Description	Model
AUM.1	Aksnes and Utne model	$r_V^2 \exp(c r_V) = T \frac{E_b}{K_e + E_b}$
AUM.2	Aksnes and Utne model with non-visual reaction	$r_V{}^2 \exp(c r_V) = T \frac{E_b}{K_e + E_b} \quad if\ E_b \geq q$ $r_{NV} = D \quad if\ E_b < q$
GVRDM.1	Generalized visual reaction distance model with non-visual reaction and β	$r_V{}^2 \exp(r_V(-k_d \cos\theta)) = \omega(\kappa) T_i \frac{E_b}{K_e + E_b} \quad if\ E_b \geq q$ $r_{NV} = D \quad if\ E_b < q$ $\omega(\kappa) = \beta + \frac{\delta^h \kappa^{h-1} \exp(-\delta\kappa)}{\Gamma(h)}$
GVRDM.2	Generalized visual reaction distance model with non-visual reaction, without β	$r_V{}^2 \exp(r_V(\kappa - k_d \cos\theta)) = \omega(\kappa) T \frac{E_b}{K_e + E_b} \quad if\ E_b \geq q$ $r_{NV} = D \quad if\ E_b < q$ $\omega(\kappa) = \frac{\delta^h \kappa^{h-1} \exp(-\delta\kappa)}{\Gamma(h)}$
GVRDM.3	Generalized visual reaction distance model and without non-visual reaction, with β	$r_V{}^2 \exp(r_V(\kappa - k_d \cos\theta)) = \omega(\kappa) T_i \frac{E_b}{K_e + E_b}$ $\omega(\kappa) = \beta + \frac{\delta^h \kappa^{h-1} \exp(-\delta\kappa)}{\Gamma(h)}$
GVRDM.4	Generalized visual reaction distance model without non-visual reaction or β	$r_V{}^2 \exp(r_V(\kappa - k_d \cos\theta)) = \omega(\kappa) T \frac{E_b}{K_e + E_b}$ $\omega(\kappa) = \frac{\delta^h \kappa^{h-1} \exp(-\delta\kappa)}{\Gamma(h)}$
BSM	Broken-stick model	$r = \begin{cases} (v + wE_b)p & if\ E_b > q_E \\ r_{max} p & if\ E_b \leq q_E \end{cases}$ $p = \begin{cases} 1 & if\ c \leq q_\kappa \\ e^{y(\kappa - q_\kappa)} & if\ c > q_\kappa \end{cases}$

Table 1.2. Model terms and descriptions.

Term	Units	Description
Aksnes and Utne model and generalized visual reaction distance model		
A_p	m^2	Visible area of prey
β	dimensionless	Dynamic scaling function intercept parameter
b_f	m^{-1}	Forward scattering coefficient (Appendix A)
c	m^{-1}	Beam attenuation coefficient
C_0	dimensionless	Inherent Weber contrast of prey
δ	dimensionless	Dynamic scaling function rate parameter
D	m	Non-visual reaction distance
E_b	$\mu E \cdot m^{-2} \cdot s^{-1}$	Background irradiance
E_{max}	$\mu E \cdot m^{-2} \cdot s^{-1}$	Maximum irradiance processing capability of the retina
E'	dimensionless	Composite saturation parameter ($E' = E_{max}\Delta S_e^{-1}$)
ε	dimensionless	Scaling factor for b_f (Appendix A)
h	dimensionless	Dynamic scaling function shape parameter
κ	m^{-1}	Effective attenuation coefficient $\kappa = c - \varepsilon b_f$ (Appendix A)
k_d	m^{-1}	Downwelling diffuse attenuation coefficient
K_e	$\mu E \cdot m^{-2} \cdot s^{-1}$	Half-saturation for irradiance processing
q	$\mu E \cdot m^{-2} \cdot s^{-1}$	Visual reaction threshold
r	m	Reaction distance
r_{NV}	m	Non-visual reaction distance
r_V	m	Visual reaction distance
σ_{NV}		Standard deviation of non-visual reaction distance
σ_V		Standard deviation of visual reaction distance
ΔS_e	$\mu E \cdot m^{-2} \cdot s^{-1}$	Sensitivity threshold of the vision system for detecting changes in irradiance
T	m^2	Composite predator-prey interaction term ($T = \lvert C_0 \rvert A_p E'$)
θ	°	Nadir viewing angle (up = 0°, down = 180°)
Broken-stick model		
c	m^{-1}	Beam attenuation coefficient
E_b	$\mu E \cdot m^{-2} \cdot s^{-1}$	Background irradiance
κ	m^{-1}	Effective attenuation coefficient $\kappa = c - \varepsilon b_f$
p	dimensionless	Turbidity scaling parameter
q_κ	m^{-1}	Minimum turbidity threshold for κ
q_E	$\mu E \cdot m^{-2} \cdot s^{-1}$	Saturation intensity threshold for E_b
r_{max}	m	Maximum reaction distance
σ		Standard deviation of reaction distance
v	m	Light function intercept
w	$m^3 \cdot s \cdot \mu E^{-1}$	Light function slope
y	m	Turbidity function slope

Table 1.3. Summary of model fits.

Summary of model fits showing the model, number of parameters, sample size (n), and AICc differences between the model and best model (ΔAICc). For each case, the model with the lowest AICc is shown in bold.

Model	Par. (#)	n	ΔAIC_c
Case #1 – Chinook salmon (predator), rainbow trout (prey)			
AUM.2	6	629	155.0
GVRDM.1	9	629	1.6
GVRDM.2	**8**	**629**	**0.0**
BSM	7	629	17.1
Case #2 – Two-spotted goby (predator), group of ten *Calanus* (prey)			
AUM.1	3	214	64.1
GVRDM.3	6	214	1.4
GVRDM.4	**5**	**214**	**0.0**
Case #3 – Two-spotted goby (predator), single *Calanus* (prey)			
AUM.1	6	24	32.1
GVRDM.3	9	24	2.9
GVRDM.4	**8**	**24**	**0.0**
Case #4 – Stone moroko (predator), *Daphnia pulex* (prey)			
AUM.1	3	177	233.4
GVRDM.3	6	177	1.0
GVRDM.4	**5**	**177**	**0.0**

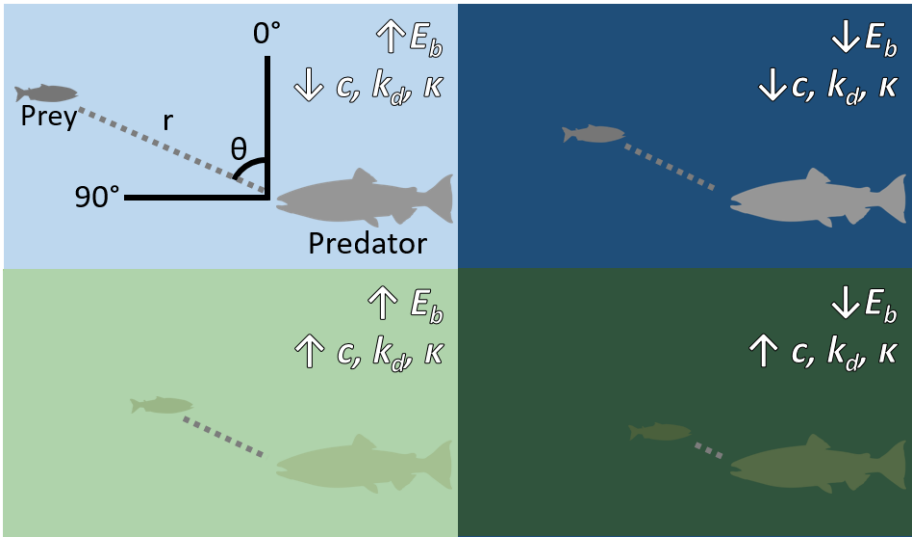

Figure 1.1. Conceptual diagram.

Conceptual diagram of reaction distance of a predator to prey under conditions of light (i.e., background irradiance, E_b) and water clarity (beam attenuation (c), diffuse downwelling attenuation coefficient (k_d), and effective attenuation coefficient (κ)), where r = reaction distance and θ = nadir viewing angle. Clockwise from the top left: high light/high water clarity, low light/high water clarity, high light/low water clarity, low light/low water clarity.

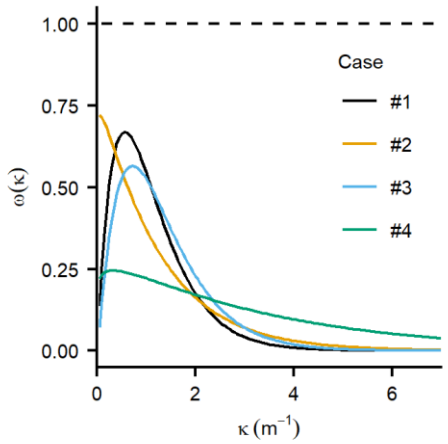

Figure 1.2. Dynamic scaling function.

Dynamic scaling function, ω(κ), for the best-fit version of the generalized visual reaction distance model for each Case. None of the dynamic scaling functions include an intercept term for the dynamic scaling function (β parameter). Horizontal dashed line denotes asymptotic expectation under the Aksnes and Utne model.

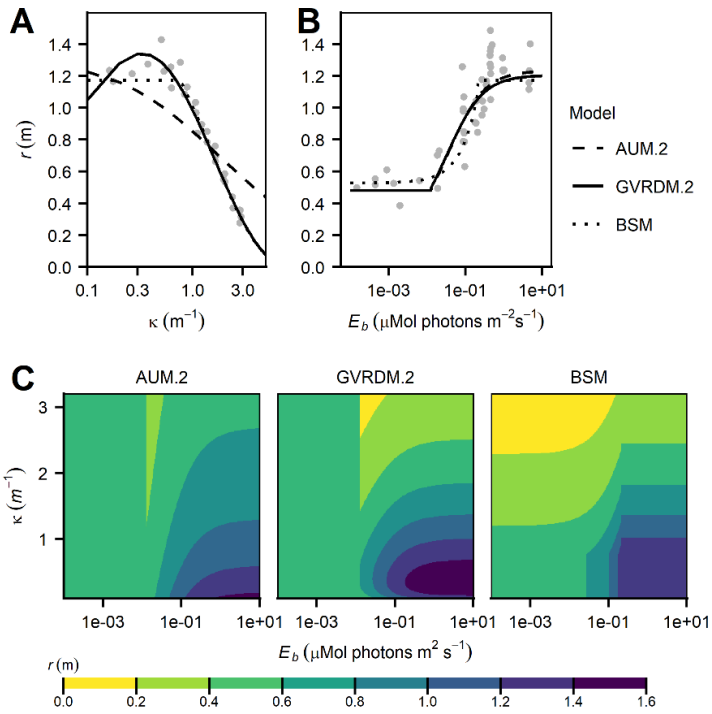

Figure 1.3. Case #1—Reaction distances.

Reaction distances of yearling Chinook salmon reacting to juvenile rainbow trout along gradients of effective attenuation coefficient, κ, and light, E_b, for the Aksnes and Utne model with a non-visual reaction (AUM.2), generalized visual reaction distance model with a non-visual reaction, without β (GVRDM.2), and empirical broken stick model (BSM). Panels: (a) fitted and observed reaction distance along a gradient of κ under constant $E_b \approx 0.75$ µMol photons $m^{-2}s^{-1}$, where points denote means for individual experimental trials; (b) fitted and observed reaction distances along a gradient of E_b under constant $\kappa = 0.1408$; (c) fitted reaction distance surfaces.

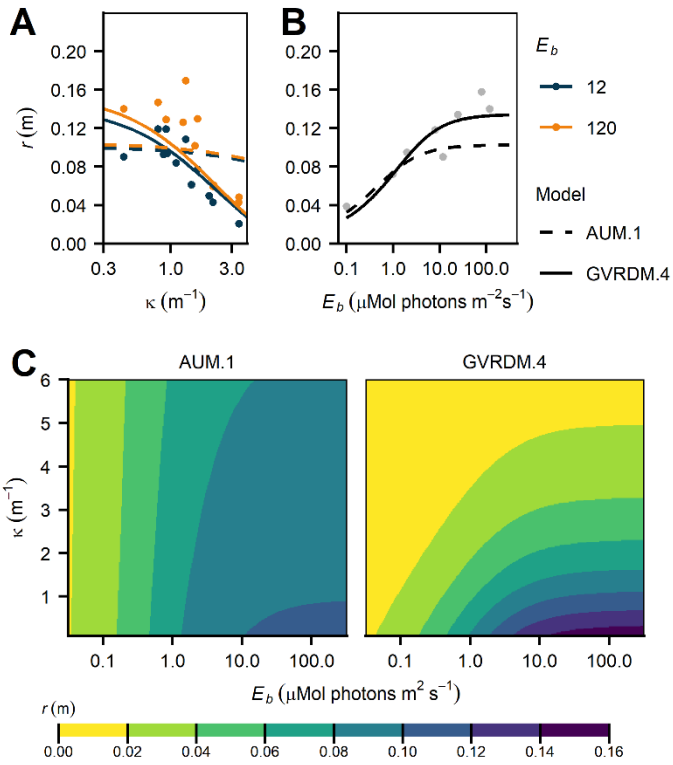

Figure 1.4. Case #2—Reaction distances.

Reaction distances for two-spotted goby reacting to ten *Calanus finmarchicus* along a gradient of effective attenuation coefficient, κ, and light, E_b, for the Aksnes and Utne model (AUM.1) and generalized visual reaction distance model without a non-visual reaction or β (GVRDM.4). Panels: (A) fitted and observed reaction distance along a gradient of κ at two levels of E_b (12 and 120 µMol·photons·m-2·s-1); (B) fitted (lines) and observed (points) reaction distances along a gradient of E_b under constant κ = 0.43 m-1, where points denote mean reaction distances for treatment levels; (C) fitted reaction distance surfaces.

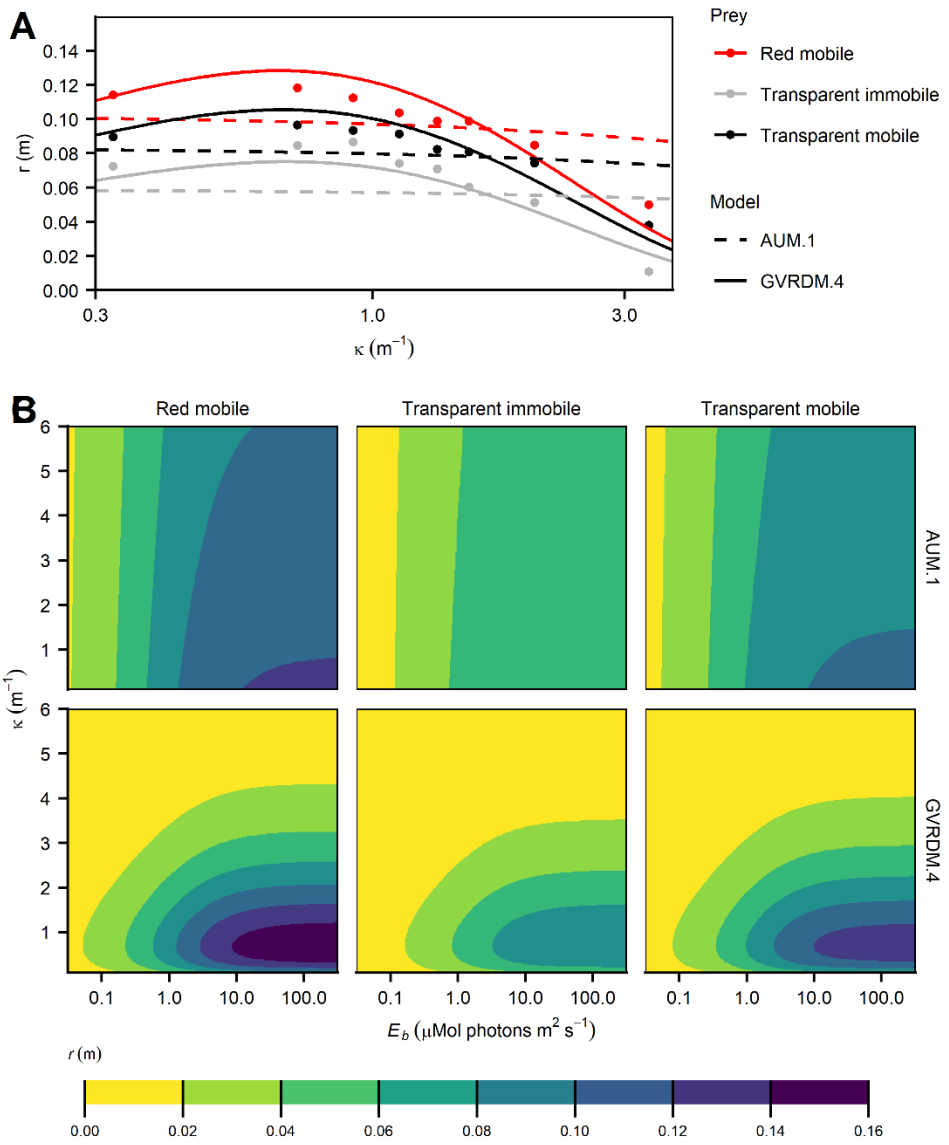

Figure 1.5. Case #3—Reaction distances.

Reaction distances for two-spotted goby reacting to single copepods along gradients of light, E_b, and the effective attenuation coefficient, κ, for the Aksnes and Utne model (AUM.1) and the generalized visual reaction distance model without a non-visual reaction or β (GVRDM.4). Panels: (a) fitted (lines) and observed (points) reaction distances along a gradient of κ under constant E_b = 20 μMol·photons·m^{-2}·s^{-1}; (b) fitted reaction distance surfaces.

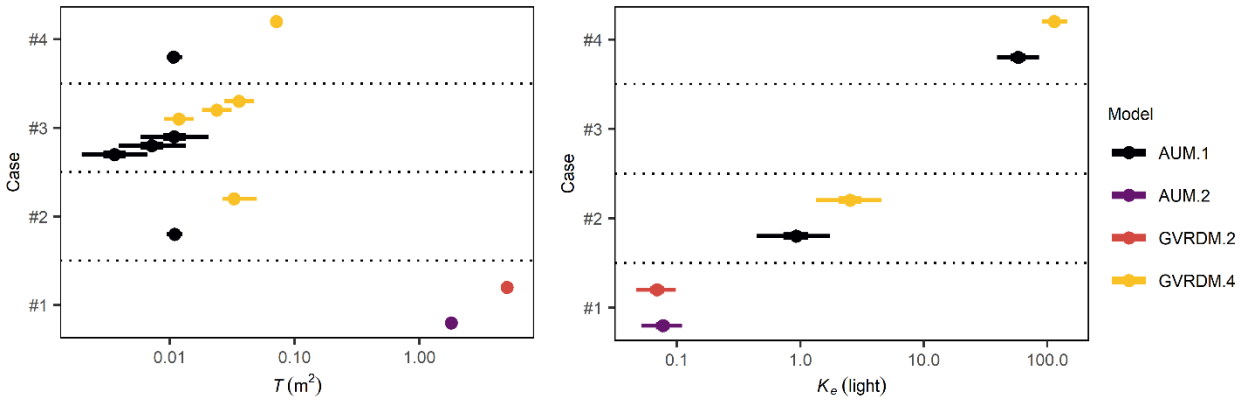

Figure 1.6. Composite predator-prey interaction term, T, and half-saturation constant, K_e.

Parameter estimates, by case, for forms of the Aksnes and Utne model and generalized visual reaction distance model. For Case #3, T parameter estimates are shown for each prey type. K_e is in quantum units (μMol·photons·m^{-2}·s^{-1}) for Cases #1–3 and photometric units (lux) for Case #4.

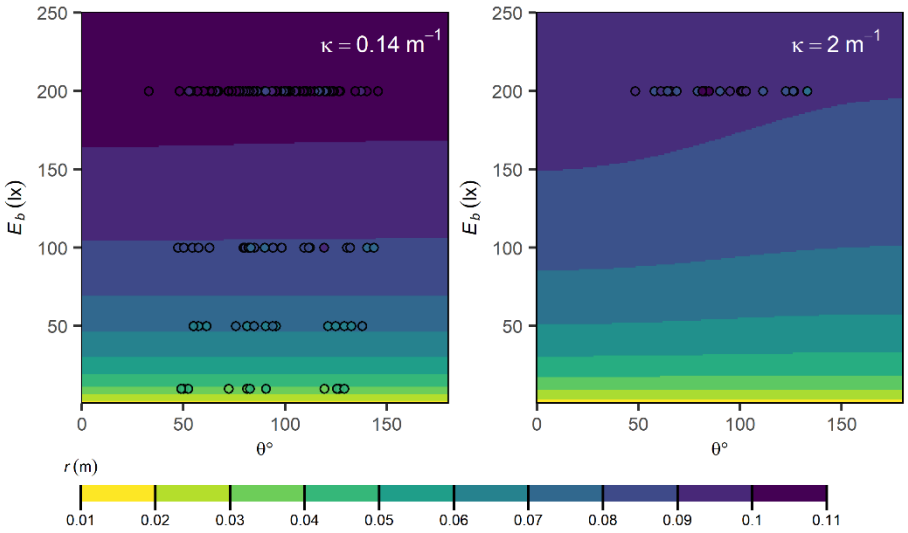

Figure 1.7. Case #4—Reaction distances.

Reaction distances for stone moroko reacting to *Daphnia pulex*, as a function of light, E_b, and nadir viewing angle, θ, and two levels of the effective attenuation coefficient: $\kappa = 0.14$ m^{-1}(left) and $\kappa = 2$ m^{-1} (right). Colored surfaces show the fit of the generalized visual reaction distance model without a non-visual reaction or β (GVRDM.4). Color-coded points denote observed reaction distances.

Chapter 2. USING BOTTOM TRAWLS TO MONITOR SUBSURFACE WATER CLARITY IN MARINE ECOSYSTEMS[2]

2.1 ABSTRACT

Biophysical processes that affect subsurface water clarity play a key role in ecosystem function. However, subsurface water clarity is poorly monitored in marine ecosystems because doing so requires in-situ sampling that is logistically difficult to conduct and sustain. Novel solutions are thus needed to improve monitoring of subsurface water clarity. To that end, we developed a sampling method and data processing algorithm that enable the use of bottom trawl fishing gear as a platform for conducting subsurface water clarity monitoring using trawl-mounted irradiance sensors without disruption to fishing operations. The algorithm applies quality control checks to irradiance measurements and calculates the downwelling diffuse attenuation coefficient, K_d, and optical depth, ζ– apparent optical properties (AOPs) that characterize the rate of decrease in downwelling irradiance and relative irradiance transmission to depth, respectively. We applied our algorithm to irradiance measurements, obtained using bottom-trawl-mounted archival tags equipped with a photodiode collected during NOAA's Alaska Fisheries Science Center annual summer bottom trawl surveys of the eastern Bering Sea continental shelf from 2004 to 2018. We validated our AOPs by quantitatively comparing surface-weighted K_d from tags to the multi-sensor K_d(490) product from the Ocean Colour Climate Change Initiative project (OC-CCI) and

[2] This work has been published:
Rohan, S.K., Kotwicki, S, Kearney, K.A., Schulien, J.A., Laman, E.A., Cokelet, E.D., Beauchamp, D.A., Britt, L.L., Aydin, K.Y., Zador, S.G. (2021) Using bottom trawls to monitor subsurface water clarity in marine ecosystems. Progress in Oceanography 194: 102554. https://doi.org/10.1016/j.pocean.2021.102554

qualitatively evaluating whether tag K_d was consistent with patterns of subsurface chlorophyll-a concentrations predicted by a coupled regional physical-biological model (Bering10K-BESTNPZ). We additionally examined patterns and trends in water clarity in the eastern Bering Sea. Key findings are: 1) water clarity decreased significantly from 2004 to 2018; 2) a recurrent, pycnocline-associated, maximum in K_d occurred over much of the northwestern shelf, putatively due to a subsurface chlorophyll maximum; and 3) a turbid bottom layer (nepheloid layer) was present over a large portion of the eastern Bering Sea shelf. Our study demonstrates that bottom trawls can provide a useful platform for monitoring water clarity, especially when trawling is conducted as part of a systematic stock assessment survey.

2.2 INTRODUCTION

Water clarity regulates heat transfer and mediates rates of primary production that set the baseline for total ecosystem production and food chain efficiency (Dickman et al., 2008; Kirk, 2011; Opdal et al., 2019). Water clarity also affects visual processes, so changes in water clarity can shift the balance of competition among animals with different visual capabilities, sensory modes of foraging, and vulnerability to visual predation (Aksnes et al., 2004; Eiane et al., 1997). Consequently, changes in water clarity can provide useful insights into ecosystem change.

Near-surface water clarity has changed over multiple decades in many marine regions, providing information on how changes in water clarity are associated with changes in the structure and function of marine ecosystems (Aksnes, 2007; Aksnes and Ohman, 2009; Capuzzo et al., 2015; Haraldsson et al., 2012). These insights result from systematic monitoring of near-surface water clarity conducted since the invention of the Secchi disk in 1865 (Pitarch, 2020). In recent decades, satellite-based remote sensing has vastly improved the capacity to monitor near-surface water

clarity under clear-sky conditions, at a global extent, with increasingly fine spatial and temporal resolution. By combining data sets from multiple sampling methods (*e.g.*, Secchi disk, Forel-Ule color comparator, satellite based passive remote sensing), many marine systems have time-series that inform how near-surface water clarity has changed over multiple decades, affecting ecological processes across multiple spatial, temporal, and organizational scales (Aksnes and Ohman, 2009; Capuzzo et al., 2015; Dupont and Aksnes, 2013; Sandén and Håkansson, 1996; Tolvanen et al., 2013; Wernand et al., 2013; Boyce et al., 2014).

In contrast to extensive near-surface monitoring, subsurface water clarity remains poorly characterized due to the logistical difficulties of sampling. Despite near global coverage, passive satellite-based remote sensing only characterizes near-surface water clarity down to first optical depth (*i.e.*, depth of 10% downwelling diffuse irradiance). Subsurface monitoring requires in situ sampling from crewed vessels, fixed moorings, or mobile samplers such as Biogeochemical-Argo floats and autonomous underwater vehicles (Bittig et al., 2019; Brown et al., 2004; Mitchell et al., 2018). While autonomous mobile samplers have continually improved (Hemsley et al., 2015; Mitchell et al., 2018), they have not achieved ubiquitous coverage due to cost, relatively slow speed, currents, and potential for interference with vessel traffic.

Despite generally limited monitoring, it is clear that changes in subsurface water clarity are indicative of ecosystem change. Subsurface algal blooms generate subsurface chlorophyll maximum layers that contribute substantially to total productivity in many marine systems (Cullen, 2015). Changes in the timing or intensity of subsurface blooms would therefore be expected to alter subsurface water clarity. In addition, currents drive the resuspension of seafloor sediments (organic and inorganic), producing nepheloid layers that may play an important role in nutrient cycling, benthic suspension and filter feeding, and animal distribution and behavior (Jumars et al.,

2015; McCave, 2019; Riisgård and Larsen, 2015). Subsurface chlorophyll maximum layers and nepheloid layers occur too deep to be monitored using passive satellite-based remote sensing (Barbieux et al., 2019; Hostetler et al., 2018; Schulien et al., 2017).

One option to improve subsurface monitoring is to deploy optical sampling equipment on existing platforms that are not explicitly designed to collect optical data. For example, attenuation coefficients derived from irradiance measurements collected using light-sensitive archival tags attached to pinnipeds and large pelagic fishes are used to make reasonably accurate predictions of chlorophyll-a concentration in the mixed layer (Jaud et al., 2012; O'Toole et al., 2017, 2014) and at fine-scale vertical resolution within the water column (Bayle et al., 2015; Nowak, 2019; Teo et al., 2009). However, unconventional sampling platforms can make it challenging to obtain measurements that are accurate, precise, reproducible and comparable to conventional data.

Given their regular frequency of sampling, standardized approach to data collection, and often large spatial coverage, fisheries-independent bottom trawl surveys are an appealing platform for water clarity monitoring. Already, physical ocean data collected during bottom trawl surveys have been used to characterize ocean circulation patterns and the fine-scale thermohaline structure of the water column (Cokelet, 2016). These data have also been used as covariates in species distribution models that have improved understanding of habitat requirements of marine fauna (Laman et al., 2018, 2014; Rooper et al., 2019). The addition of water clarity information will likely improve understanding of species-environment relationships because the intensity and spectrum of environmental light affect the sensory capabilities of aquatic animals (Britt et al., 2001; Caves et al., 2017; Lythgoe, 1972; Schweikert et al., 2018). Further, combining water clarity monitoring with biogeochemical sampling would facilitate the development of bio-optical models

that may be used to estimate the composition of optically active constituents of the water column (*e.g.*, chlorophyll-a, chromophoric dissolved organic matter [CDOM]).

In this study, we derived apparent optical properties (AOPs), the downwelling diffuse attenuation coefficient (K_d) and optical depth (ζ), from bottom-trawl-mounted light-sensitive archival tags to evaluate the utility of bottom trawl surveys as a platform for monitoring surface and subsurface water clarity. Our study region was the eastern Bering Sea, a subarctic semi-enclosed sea with an expansive shelf where summer bottom trawl surveys have been conducted annually since 1982 and water column light data have been collected annually since 2004. To validate trawl-derived AOPs, we 1) quantitatively evaluate if near-surface tag-based attenuation coefficients are consistent with attenuation coefficients derived from satellite-based measurements of ocean color, and 2) qualitatively evaluate whether the patterns in AOPs are consistent with predictions from a coupled physical-biological model of primary production. We describe patterns of variation in AOPs in the eastern Bering Sea during summer 2004–2018 and synthesize our findings with the current understanding of physical and biological processes that drive variation in water clarity in the eastern Bering Sea. Finally, we provide recommendations for how sampling during bottom trawl surveys can be extended to improve monitoring of water clarity.

2.3 REGIONAL SETTING

The eastern Bering Sea is a highly productive subarctic coastal ecosystem that supports several of the world's largest commercial fisheries along with large populations of marine mammals and seabirds. The broad continental shelf of the eastern Bering Sea slopes gently from the Alaska mainland to the continental shelf break at ~180 m (Fig. 2.1). Factors that influence water clarity in the eastern Bering Sea are: surface and subsurface phytoplankton, chromophoric dissolved organic matter (CDOM) and sediment originating from rivers, and resuspension of

seafloor sediment driven by currents, winds, and tides (*i.e.*, nepheloid layers). The relative importance of these factors varies over space and time due to physical and biogeochemical processes.

During summer, the eastern Bering Sea continental shelf is generally divided into three biophysical domains: the inner domain (0–50 m bottom depth), middle domain (50–100 m), and outer domain (100–180 m) (Coachman, 1986). The inner and middle domains are divided by an inner front that occurs roughly along the 50 m isobath. The middle and outer shelf domains are divided by a front that occurs roughly along the 100 m isobath. The domains have differences in biological processes, physical processes, and water column structure. The inner domain has relatively low salinity and features a fully-mixed or weakly stratified water column maintained by wind and tidal mixing (Coachman, 1986; Kachel et al., 2002; Ladd and Stabeno, 2012). North of Nunivak Island (~62°N), the inner front is located inshore of the 50 m isobath due to weaker tidal mixing and alongshore northward advection of freshwater input from rivers (Danielson et al., 2011; Ladd and Stabeno, 2012; Mordy et al., 2017). South of ~57°N, the inner domain can extend offshore to depths of ~70 m (Cokelet, 2016). The middle domain features a stratified two-layer water column with a sharp pycnocline. The density structure over the middle domain is maintained by wind mixing of the surface layer and tidal mixing of the bottom layer (Coachman, 1986; Stabeno et al., 2012a). The outer domain is characterized by a wind-mixed surface layer and a tidally mixed bottom layer with a gradual density transition between the two domains. Summertime geostrophic current velocities are slow, averaging 0–2 cm s^{-1} over most of the eastern Bering Sea shelf, with a net northward transport through Bering Strait (Cokelet, 2016). Stronger flow is observed along the 50 m and 100 m isobaths, which accounts for 50% of transport through Bering Strait (Stabeno et al., 2016).

The extent of seasonal sea-ice and timing of sea-ice melt sets up the summer thermohaline structure of the eastern Bering Sea. Interannual variation in wind velocity, air temperature, and water temperature drive variation in winter sea-ice extent (Stabeno et al., 2017). Since the 1970s, at maximum, seasonal sea ice has extended to the Alaska Peninsula (most recently in 2012), while at its minimum in 2018, the ice edge was north of St. Matthew Island (Stabeno and Bell, 2019). As sea-ice melts in the spring–summer, it cools and freshens the water column and causes the formation of a cold pool (bottom temperature <2° C) over the middle and outer shelf. Thus, the cold pool is considered a remnant of winter sea ice. When ice melts in early spring, strong winds mix the water column and stratification is delayed until the water column begins to warm (Ladd and Stabeno, 2012). When sea-ice melts later, the abatement of winter storms leads to weaker wind-mixing, allowing meltwater to form a low salinity surface layer that contributes to stratification (Cokelet, 2016; Ladd and Stabeno, 2012; Stabeno et al., 2012a). Further north where sea-ice persists longer, freshening from ice melt and temperature contribute to stratification (Ladd and Stabeno, 2012).

The timing of sea-ice melt affects the spring phytoplankton bloom timing in the mixed layer. When sea-ice persists until mid-March, a spring bloom of ice-associated phytoplankton occurs at the surface as the sea-ice thins and melts (Hunt et al., 2011; Sigler et al., 2014). When ice melts earlier than mid-March, the spring bloom is delayed and concurrent with the onset of thermal stratification. The spring bloom produces a surface chlorophyll maximum and causes rapid depletion of nutrients in the mixed layer (Mordy et al., 2012). During summer, primary production is nutrient-limited in the mixed layer because strong stratification inhibits vertical infusion of nutrients from the nutrient-rich bottom layer of the middle and outer domain. However, energetic

storms can deepen the mixed layer and replenish nutrients to produce a phytoplankton bloom that peaks 1–2 weeks after the storm (Sambrotto et al., 1986; Stabeno et al., 2010).

Spatiotemporal variation in nutrient cycling and replenishment causes variation in primary production dynamics across the eastern Bering Sea. In the bottom layer over the northern middle and outer domain, nitrate concentrations are relatively high, and are sufficient to sustain production throughout the summer if enough light penetrates into the pycnocline (Stabeno et al., 2019). This production leads to the formation of a pycnocline-associated subsurface chlorophyll maximum layer that can persist through summer (Stabeno et al., 2012a, 2012b). Summer observations of the subsurface layer are sporadic because there is no regular in-situ monitoring. However, coupled bio-physical models predict the spatiotemporal dynamics of the layer (Kearney et al., 2020). Towards the inner domain, nitrate concentrations decrease due to limited onshore advection of bottom water. As such, primary production in the inner domain is mainly the result of regenerative production (*i.e.*, production supported by the reuptake of excreted ammonia; Mordy et al., 2017).

Numerous rivers discharge from the Alaska mainland into the eastern Bering Sea, supplying freshwater rich with CDOM and suspended sediment. These optically unique water sources affect water clarity over the eastern Bering Sea shelf (Naik et al., 2013). From October–May, strong winds and weak cross-shelf density gradients allow advection of fluvial water sources over the middle and outer shelf (Danielson et al., 2011). During spring and summer, river discharge is predominantly advected northward alongshore of mainland Alaska by the Alaska Coastal Current; minimal offshore advection occurs due to a strong cross-shelf density gradient and weak offshore wind (Danielson et al., 2011).

There is a bottom-associated nepheloid layer over parts of the eastern Bering Sea shelf, although variation in the nepheloid layer and processes that cause its formation are poorly

characterized due to a lack of monitoring (Feely et al., 1981; Kawana, 1975; McManus and Smyth, 1970). Generally, nepheloid layers are caused by resuspension of seafloor sediment by currents generated by wind, tides, geostrophic circulation, internal waves, benthic storms, and eddies (McCave, 2019). The structure of a nepheloid layer depends on current velocities, sediment composition, settling rates of particulates, and the density structure of the water column.

Although changes in the subsurface environment have been poorly characterized, changes in light transmission dynamics through the upper water column are both a cause and consequence of ecosystem changes in the eastern Bering Sea. Near-surface waters of the eastern Bering Sea became bluer from 1935 to 1998, which suggests changes in the ecosystem caused a decrease in near-surface chlorophyll concentrations (Wernand et al., 2013). In recent warm years with low sea-ice extent (2014–2016), findings suggest chlorophyll and net primary production have increased relative to recent cold years (2007–2011) (Lomas et al., 2020). Since 1997, large-scale blooms of the coccolithophore *Emiliania huxleyi* have become common in the fall (August–September) despite being absent from the stratigraphic sediment record in preceding decades (Harada et al., 2012; Iida et al., 2012; Ladd et al., 2018). This change is thought to be the result of a climate-mediated shift in the thermohaline structure of the water column and nutrient that favors the growth of *E. huxleyi* and may affect zooplankton grazing (Olson and Strom, 2002) and foraging efficiency for visually foraging predators (Lovvorn et al., 2001). Finally, it has been suggested that reduction of seasonal sea-ice due to climate change will increase the productivity of pelagic fish stocks in the eastern Bering Sea by enhancing visual foraging opportunity (Langbehn and Varpe, 2017).

2.4 METHODS

2.4.1 *Data sources and processing*

2.4.1.1 Bottom trawl irradiance data

Irradiance, temperature, and salinity data were collected during annual summer (early June–early August) bottom trawl surveys of the eastern Bering Sea continental shelf conducted by the Resource Assessment and Conservation Engineering Division of NOAA's Alaska Fisheries Science Center. Each year, the bottom trawl survey sampled the same 376 survey stations arranged on a regularly-spaced 20×20 nmi (37×37 km) grid, with 'corner stations' in some areas (Fig. 2.1). Sampling was generally conducted near the center of survey grid cells at approximately the same bottom depth every year. Bottom depths sampled by the survey ranged from ~20 m along the Alaska mainland to ~180 m along the continental shelf break. Two vessels were used to conduct surveys each year, with each vessel sampling approximately half of the stations. Surveys progressed from interior Bristol Bay in the southeast to the outer continental shelf in the northwest. Bottom trawl sampling started no earlier than 30 minutes after sunrise and ended no later than 30 minutes before sunset (Stauffer, 2004).

Bottom trawl surveys collected environmental data using sensors (described below) attached to the outside of the top panel of the bottom trawl gear (83-112 Eastern trawl). The sensors were positioned 0.5–2.0 m aft of the headrope of the trawl gear. When deployed in fishing configuration, the headrope of the bottom trawl gear was ~2.5 m above the seafloor. Thus, sensors collected data from the sea surface to ~2.5 m above the seafloor during each trawl deployment (downcast) and retrieval (upcast). Tows were conducted at a target vessel speed of 2.8–3.2 knots (1.44–1.65 m s^{-1}) for 30 minutes, typically resulting in upcasts and downcasts ~1.5 nmi (2.8 km)

apart. Vessels were underway during trawl deployment and retrieval, so upcasts and downcasts were oblique profiles of the water column.

From 2004 to 2018, irradiance measurements were collected using archival tags equipped with a blue-filtered photodiode (Wildlife Computers TDR-Mk9). Photodiodes are rugged, energy efficient, have a relatively stable response, and are simple to calibrate, but are less sensitive than specialized detectors (Mobley, 1994). Archival tags were used because they are relatively inexpensive, have a low-profile that minimizes drag on trawl gear, and can withstand rough treatment during deployment. Archival tags were affixed to a triangular, white polyurethane base plate assembly with shackles at the forward corners (Fig. 2.2). During bottom trawl survey hauls, archival tag assemblies were shackled to the trawl gear with the photoelectric cell facing upward to approximate downwelling irradiance. Shading of the archival tag was not a concern because the trawl gear was >50 m behind vessels during casts and vessel wake was negligible. From 2006 to 2018, a deck-mounted archival tag was deployed in an unobstructed location atop of the wheelhouse of each survey vessel, providing surface irradiance measurements. Trawl-mounted archival tags sampled at a rate of 1 Hz, while deck-mounted archival tags sampled at 0.1 Hz. Depths for archival tag irradiance measurements were obtained from a Seabird SBE-39 temperature depth recorder with an internal clock synchronized to the archival tag internal clock to increase measurement precision and mitigate bias in archival tag depth measurements (Rohan et al., 2020).

The archival tags used an onboard conversion to record irradiance measurements in relative units that had a maximum integer range of 25–225, corresponding with intensities from 10×10^{-12} W cm^{-2} to 5×10^{-2} W cm^{-2}. A blue filter on the photoelectric cell causes the archival tag to have a peak spectral sensitivity at 465 nm, with a 50% response bandwidth of 420–470 nm (Vacquié-

Garcia et al., 2017). The tags have some sensitivity extending to shorter (ultraviolet A) and longer wavelengths (green–red), as detailed by Rohan et al. (2020). Herein, we symbolically represent the spectral band of the tag as λ_{tag}.

Archival tag measurements are not direct analogues of measurements from conventional radiant energy detectors because they are not designed to measure radiant energy with a specific geometry (*e.g.* radiance, planar irradiance, diffuse irradiance). Measurements from TDR-Mk10[3] archival tags are irradiances that geometrically fall between radiance and planar irradiance. The peak response of the sensor occurs when the main axis of the incident radiance field is perpendicular to the plane of the sensor (*i.e.* 90° zenith angle) and decreases at lower incident angles (Vacquié-Garcia et al., 2017). Yet at low angles, the drop-off in the response is more extreme than for a cosine corrected planar irradiance detector (Vacquié-Garcia et al., 2017). Despite their unconventional geometry, archival tag irradiance measurements can be used to derive attenuation coefficients that closely approximate the downwelling planar attenuation coefficient from conventional detectors (Nowak, 2019). Further, archival tag irradiance measurements have been used to calculate vertical attenuation coefficients that allow reasonably accurate predictions of chlorophyll-a concentrations in marine systems (Bayle et al., 2015; Jaud et al., 2012; O'Toole et al., 2017, 2014; Teo et al., 2009). Thus, archival tags can be used to indirectly characterize bio-optical properties.

2.4.1.2 Irradiance data processing

[3] Light sensor components on TDR-Mk10 archival tags are identical to components on TDR-Mk9 archival tags (Hamamatsu S2387 photodiode, blue spectral bandpass filter, epoxy casing with a refractive index of 1.56).

We developed an algorithm to quality control bottom trawl irradiance data and calculate two apparent optical properties (AOPs): optical depth, $\zeta(z, \lambda)$, and the downwelling diffuse attenuation coefficient, $K_d(z, \lambda)$ m^{-1}. Optical depth, $\zeta(z, \lambda)$, is a dimensionless ratio that characterizes the proportion of downwelling irradiance of wavelength λ just beneath the sea surface that reaches depth z (m). The downwelling diffuse attenuation coefficient, $K_d(z, \lambda)$ m^{-1}, characterizes the rate of decrease of the natural logarithm of the downwelling irradiance of wavelength λ at depth z.

Initial phases of the design, application, and evaluation of the algorithm are described in Rohan et al. (2020), who found the algorithm generated reproducible and precise values of $\zeta(z, \lambda_{tag})$ and $K_d(z, \lambda_{tag})$ in the eastern Bering Sea. Here, we build on this research by additionally evaluating whether $\zeta(z, \lambda_{tag})$ and $K_d(z, \lambda_{tag})$ are consistent with optical properties obtained using established sampling and data processing methods and applying these optical metrics to evaluate changes in water clarity in the eastern Bering Sea. Below, we summarize the design of the algorithm and underlying rationale.

The algorithm first converts archival tag irradiance measurements units to radiometric units based on a blue-spectrum conversion equation reported by the tag manufacturer:

$$y = 10^{(x-250)/20}, \quad (1)$$

where y is irradiance in W cm^{-2}, and x is the integer measurement recorded by the tag. Under constant irradiance, archival tag measurements vary by two integer units (absolute precision) and, for a given irradiance level, individual tags differ by approximately two integer units (Kotwicki et al., 2009; Vacquié-Garcia et al., 2017). Nevertheless, $\zeta(Z, \lambda_{tag})$ and $K_d(Z, \lambda_{tag})$ are calculated using relative changes in irradiance so the absolute range of individual tags is irrelevant so long as tags

have a proportionally equal response to changes in downwelling planar irradiance and values are within the absolute sensitivity range of the tags.

Next, the algorithm calculates the geometric mean irradiance for 2-m depth bins for every cast. The depth interval for binning (2-m) and use of a geometric mean were chosen based on trial-and-error to minimize near-surface fluctuations that were likely caused by wave-induced refraction and potentially unstable orientation of the archival tag near the surface.

Filters are often used to distinguish signal from noise in irradiance measurement cast data (*e.g.* Smith and Baker, 1984) but conventional filter methods (*e.g.* Kalman filter) were unsuitable for bottom trawl survey irradiance profiles because they retained data from casts where irradiance measurements fluctuated abruptly due to probable sampling artifacts (e.g. successive order-of-magnitude increases and decreases in irradiance). The abrupt shifts may have occurred due to obstruction of the tag or a change in the orientation of the tag. To address this issue, the algorithm uses a stepwise point removal filter to remove shallower irradiances that are lower (darker) than irradiances deeper in the water column, based on the expectation that irradiance should decrease as depth increases. For example, the stepwise filter omits $E_d(1, \lambda_{tag})$ if $E_d(1, \lambda_{tag}) < E_d(3, \lambda_{tag})$. The stepwise filter removes points until the following condition is satisfied:

$$E_d(z_1, \lambda_{tag}) \geq E_d(z_2, \lambda_{tag}) \geq \cdots \geq E_d(z_{max}, \lambda_{tag}) ,$$

where $E_d(z_i, \lambda_{tag})$ are downwelling irradiance values ordered by depth. Casts where data are missing or omitted from three consecutive depth bins are flagged and excluded from subsequent processing.

The archival tag photodiode should be facing upward in order to calculate AOPs that approximate those based on diffuse downwelling irradiance. Thus, the algorithm employs quality

control checks to detect and exclude casts with improper orientation (Rohan et al. [2020]; Supplementary Material: *Detecting archival tag orientation errors*).

Irradiance measurements from the 1-m depth bin are missing or excluded during quality control checks for some casts, which prevents subsequent calculation of $\zeta(z, \lambda_{tag})$. Therefore, the algorithm uses a linear extrapolation to estimate irradiance for the 1-m depth bin when missing. The extrapolation method explains 96% of the variation in log-transformed irradiance for the 1-m depth bin (Rohan et al., 2020).

The algorithm is used to calculate optical depth $\zeta(z, \lambda_{tag})$, and the diffuse irradiance attenuation coefficient, $K_d(z, \lambda_{tag})$, from casts that pass quality control checks. From the Beer-Lambert equation, downwelling irradiance at depth z, $E_d(z, \lambda)$, is approximately related to downwelling irradiance just below the surface, $E_d(0^-, \lambda)$, as:

$$E_d(z,\lambda) = E_d(0^-,\lambda)e^{-K_d(0^-\to z,\lambda)z}\,, \tag{2}$$

where $K_d(0^-\to z, \lambda)$ (m^{-1}) is the downwelling diffuse attenuation coefficient between just below the sea surface and depth Z (Gordon, 1989). Optical depth, $\zeta(z,\lambda)$, is the product of depth and $K_d(0^-\to z, \lambda)$:

$$\zeta(z,\lambda) = K_d(0^-\to z,\lambda)z = \ln\big(E_d(0^-,\lambda)\big) - \ln\big(E_d(z,\lambda)\big)\,. \tag{3}$$

Larger values of $\zeta(z,\lambda)$ correspond with darker conditions.

Because $E_d(1)$ is the shallowest value for each cast, the algorithm calculates $\zeta(z, \lambda_{tag})$ as:

$$\zeta\big(z,\lambda_{tag}\big) = \ln\Big(E_d\big(1,\lambda_{tag}\big)\Big) - \ln\Big(E_d\big(z,\lambda_{tag}\big)\Big)\,. \tag{4}$$

Through an infinitesimally thin slice of water at depth z, the downwelling diffuse attenuation coefficient, $K_d(z, \lambda)$, is defined as:

$$K_d(z,\lambda) = -\frac{1}{E_d(z,\lambda)}\frac{dE_d(z,\lambda)}{dz}\,. \tag{5}$$

In natural waters, $K_d(z, \lambda)$ varies with depth due to variation in optically active constituents (e.g. chlorophyll-a, CDOM). Because in-situ radiometric measurements alone do not provide a basis to analytically calculate $K_d(z, \lambda)$, a numerical approximation is typically used to estimate $K_d(z, \lambda)$. Our approach to numerical approximation of $K_d(z, \lambda_{tag})$ is described in the Supplementary Material (*Numerical approximation of $K_d(z, \lambda_{tag})$*) and Rohan et al. (2020).

We used $\zeta(z, \lambda_{tag})$ to estimate the following proxies of near-surface water clarity: the depths where irradiance was reduced to 10% ($Z_{10\%}$) and 1% ($Z_{1\%}$) of irradiance for the 1-m depth bin. We calculated $Z_{1\%}$ and $Z_{10\%}$, by linearly interpolating $\zeta(z, \lambda_{tag})$ between the depth bins that were immediately above and below the target optical depths. To allow for a qualitative evaluation of the extent of the bottom nepheloid layer, we also used $K_d(z, \lambda_{tag})$ to calculate a nepheloid layer index (NLI), which we define as:

$$NLI = 100 * \left(\frac{K_d(z_{bot}, \lambda_{tag}) - \overline{K_d(z, \lambda_{tag})}}{\overline{K_d(z, \lambda_{tag})}} \right) \quad (6)$$

where $K_d(z_{bot}, \lambda_{tag})$ is the mean $K_d(z, \lambda_{tag})$ for the bottom five meters of a cast and $\overline{K_d(z, \lambda_{tag})}$ is the mean for the entire cast.

2.4.1.3 CTD data processing

From 2008 to 2017, temperature, salinity, and depth data were collected using a CTD (Falmouth Scientific Instruments NXIC CTD or Teledyne RD Instruments Citadel CTD-NV). CTDs sampled at a rate of 15 Hz. CTD data from each cast were binned to 1-m resolution and used to derive profiles of temperature (°C), salinity (PSS-78), and density anomaly, σ_t (kg m^{-3}) (Cokelet, 2016). For each profile, we calculated mixed layer depth (MLD) as the shallowest depth where the

density anomaly first exceeded the average value from the upper 5 m by 0.1 kg m^{-3} and bottom layer depth (BLD) as the deepest depth where the density anomaly first exceeded the average value from the bottom 5 m by 0.1 kg m^{-3} (Cokelet, 2016; Danielson et al., 2011). If the density anomaly did not exceed the threshold, we did not calculate a bottom layer depth, and considered the mixed layer depth to be equal to the bottom depth. We also calculated the density difference between the mixed layer and bottom layer, $\Delta\sigma_{t,}$ which we defined as the difference between σ_t average for the upper 5 m of the water column and the density at either 30 m below the mixed layer depth, or the deepest measurement in the water column (Cokelet, 2016).

3.2 Analysis

3.2.1 Satellite validation

We evaluated whether $K_d(z, \lambda_{tag})$ were reliable (accurate and precise) by comparing data from $K_d(z, \lambda_{tag})$ profiles to the European Space Agency's (ESA) Ocean Colour Climate Change Initiative (OC-CCI Version 5.0) daily, 4-km resolution downwelling diffuse attenuation coefficients at 490 nm, $K_d(z_s, 490)$ where z_s is the near-surface portion of the water column that is 'visible' to the satellite. OC-CCI $K_d(z_s, 490)$ is a multi-sensor satellite data product (NASA, NOAA, ESA, Copernicus) that is derived from inherent optical properties calculated using the Quasi-Analytical Algorithm (Lee et al., 2002; Lee et al., 2005). For our evaluation, we found all same-day spatial match-ups between OC-CCI $K_d(z_s, 490)$ and the final $K_d(z, \lambda_{tag})$ profiles. We first excluded upcast profiles to avoid pseudoreplication in our evaluation. We also excluded downcasts where $E_d(1, \lambda_{tag})$ was estimated by the algorithm. We followed Zaneveld et al. (2005) to calculate surface-weighted values of $K_d(z_s, \lambda_{tag})$ from the remaining $K_d(z, \lambda_{tag})$ profiles.

To evaluate the reliability of the tag-based data products, we fit a linear regression model between $\log_{10}$-transformed $K_d(z_s, \lambda_{tag})$ (predictor) and $\log_{10}$-transformed satellite $K_d(z_s, 490)$ (response), then used the model to calculate four performance metrics : the coefficient of determination (r^2), root mean square log error (RMSLE),

$$\mathrm{RMSLE} = N^{-1} \sum_{i=1}^{N} \sqrt{\left(\ln K_d(\widehat{z_s, 490})_i - \ln K_d(z_s, 490)_i\right)^2}, \tag{7}$$

mean relative error (MRE),

$$\mathrm{MRE} = \frac{100}{N} \sum_{i=1}^{N} \frac{\left|K_d(\widehat{z_s, 490})_i - K_d(z_s, 490)_i\right|}{K_d(z_s, 490)_i}, \tag{8}$$

and mean absolute error (MAE),

$$\mathrm{MAE} = 10^{\left(N^{-1} \sum_{i=1}^{N} \left|\log_{10} K_d(\widehat{z_s, 490})_i - \log_{10} K_d(z_s, 490)_i\right|\right)}. \tag{9}$$

We consider RMSLE, MRE, and MAE to be more informative than r^2 because they are less sensitive to outliers and the dynamic range of samples in the data set (Seegers et al., 2018).

We used relative error from the regression to evaluate whether there were detectable biases caused by obtaining measurements across a broad range of solar zenith angles (30°–90°). Solar zenith angle can cause 5–30% variation in K_d near the surface depending on wavelength and optical properties of active constituents in the water column because measurements are influenced by the angular distribution of the radiance field (Baker and Smith, 1979; Kirk, 2011).

3.2.2 Regional analysis

We conducted analyses at regional and fine spatial scales to evaluate whether regional patterns and trends were representative of finer-scale variability and vice versa, and to generate hypotheses about mechanisms responsible for variation in AOPs. For the regional analyses, we characterized region-wide patterns and trends in AOPs and associations between AOPs and physical covariates.

Because depth has often been used as a proxy for ambient irradiance in visual ecology, we evaluated whether depth was a reasonable predictor of subsurface irradiance in the eastern Bering Sea. To do so, we fit a generalized additive model (GAM) between maximum sampling depth for a cast, z_{max} (predictor), and near-bottom optical depth, $\zeta(z_{max})$ (response) and calculated the deviance explained by the model. We focused on bottom depth because it is most relevant to environmental conditions for highly abundant bottom-dwelling species in the eastern Bering Sea.

We tested for regional temporal trends in $\zeta(z_{max,}\lambda_{tag})$, $Z_{10\%}$, and $Z_{1\%}$ using linear-mixed effects models where $\zeta(z_{max,}\lambda_{tag})$, $Z_{10\%}$, and $Z_{1\%}$ were response variables, year was a continuous fixed effect, and survey station was a random effect. Because observations from a single haul are not independent samples, we weighted casts in the models by the number of casts from a station in a single year that passed quality control checks.

To evaluate if region-wide variation in the level of near-bottom radiation was explained by variation in near-surface water clarity and if water clarity was related to physical covariates (mixed layer depth, $\Delta\sigma_t$), we performed linear regressions on indices of $\zeta(z_{max,}\lambda_{tag})$, $Z_{10\%}$, $Z_{1\%,}$ mixed layer depth, and $\Delta\sigma_t$. The indices were calculated from the annual interpolated raster surfaces (Supplementary Material: *Spatial interpolation to generate rasters*) as:

$$I_t = N^{-1} \sum_{k=1}^{N} \frac{(\hat{y}_{it} - \hat{\mu}_i)}{\hat{s}_i}, \quad (4)$$

where N is the number of 5 km x 5 km pixels in the interpolated surface (17,765), I_t is the anomaly index for year t, $\hat{y}_{it}$ is the estimated value of $\zeta(z_{max}, \lambda_{tag})$, $Z_{10\%}$, or $Z_{1\%}$ for pixel i, $\hat{\mu}_i$ is the mean for the pixel, and $\hat{s}_i$ is the standard deviation for the pixel. This approach was used to calculate anomalies instead of directly using observations because data were missing from different combinations of stations each year. We then fit linear regression models between combinations of anomaly indices to evaluate whether shelf-wide variation in near-bottom irradiance was explained by variation in near-surface water clarity (*i.e.*, $Z_{10\%}$, $Z_{1\%}$), whether variation in near-surface water clarity and near-bottom irradiance were explained by variation in physical covariates (mixed layer depth, $\Delta\sigma_t$), and whether there was covariation between physical covariates.

3.2.3 Fine-scale analysis

For the fine-scale analysis, we characterized patterns and trends using interpolated 5 × 5 km resolution raster surfaces of environmental variables ($\zeta(z_{max}, \lambda_{tag})$, $Z_{10\%}$, $Z_{1\%}$, mixed layer depth, $\Delta\sigma_t$), interpolated transects of environmental variables (Rows C, G, P, S; Fig. 2.1), and vertical profiles from individual stations. We analyzed fine-scale areal patterns in $\zeta(z_{max}, \lambda_{tag})$, $Z_{10\%}$, $Z_{1\%}$, mixed layer depth, and the nepheloid layer index by calculating pixel-wise summary statistics from annual raster surfaces. To evaluate whether the density structure of the water column was related to fine-scale variation in irradiance and water clarity (indirectly through processes that affect optically active constituents), we conducted regressions between annual raster surfaces of $\zeta(z_{max}, \lambda_{tag})$, $Z_{10\%}$, $Z_{1\%}$, mixed layer depth, and $\Delta\sigma_t$. We analyzed fine-scale vertical patterns by visually

inspecting cross-sections of $K_d(z, \lambda_{tag})$, mixed layer depth, $Z_{10\%}$ and $Z_{1\%}$ that were interpolated along survey rows.

To test for fine-scale temporal trends, we conducted pixel-wise linear regressions on annual rasters of $\zeta(z_{max}, \lambda_{tag})$, $Z_{10\%}$, $Z_{1\%}$, using year as a predictor. In an effort to identify potential causes of change, we then examined vertical profiles of $K_d(z, \lambda_{tag})$ from areas where the slope of the relationship was significantly different from zero at the $p < 0.05$ level, based on a *t*-test.

3.2.4 Comparison with Bering10K ROMS model

We compared AOP patterns to predicted patterns of chlorophyll and detritus from a coupled bio-physical regional ocean model (Bering10K-BESTNPZ) in order to qualitatively validate our AOPs and evaluate whether patterns of $K_d(z, \lambda_{tag})$ were associated with predicted patterns of chlorophyll and detritus. Our regional ocean model uses the Regional Ocean Modeling System (ROMS), a free-surface, primitive equation hydrographic model (Haidvogel et al., 2008; Shchepetkin and McWilliams, 2005). The Bering Sea implementation, referred to as the Bering10K domain, spans the Bering Sea and northern Gulf of Alaska with 10-km horizontal resolution and 30 terrain-following depth levels. The physical model is coupled to the Bering Ecosystem Study nutrient-phytoplankton-zooplankton (BESTNPZ) biogeochemical model, which simulates lower trophic level dynamics spanning the pelagic, benthic, and ice environments (Gibson and Spitz, 2011; Kearney et al., 2020).

In this analysis, we use output from the hindcast simulation of the Bering10K-BESTNPZ model. The hindcast simulation covers the period of 1970 to the present, using surface and lateral boundary forcing from the Climate Forecast System Reanalysis (CFSR) (Saha et al., 2010; 1995–March 2011) and the Climate Forecast System Operational Analysis (CFSv2-OA) (April 2011–

present). Further details of this model configuration, as well as analysis of the simulation's biophysical skill, can be found in Kearney et al. (2020). For this study, we examine simulated chlorophyll-a across the two phytoplankton size classes (large and small), as well as the concentration of detrital matter in the water column, to elucidate possible mechanisms influencing the observed patterns in $K_d(z, \lambda_{tag})$.

3. RESULTS

2.4.2 *Satellite analysis*

Performance metrics from the regression between $K_d(z_s, \lambda_{tag})$ and OC-CCI $K_d(z_s, 490)$ demonstrate that our data collection method and algorithm provide a reliable measure of near-surface K_d based on the strong positive correlation and 23.3% mean relative error (Fig. 2.3A; Table 2.1). There were no clear spatial patterns in prediction error, based on a visual inspection of relative error (Fig. 2.3B). Contrary to expectation, we did not detect a systematic bias in measurements due to solar zenith angles (32°–90°), based on residuals from the linear regression model (Fig. S7).

2.4.3 *Regional and fine-scale analyses*

2.4.3.1 Regional patterns and trends

At a regional scale, depth was not a reliable predictor of near-bottom downwelling irradiance, as the GAM between z_{max} and $\zeta(z_{max}, \lambda_{tag})$ explained only 53.0% of total deviance (Fig. 2.4). There was a positive relationship between z_{max} and $\zeta(z_{max}, \lambda_{tag})$ at depths <80 m. The relationship was relatively flat at depths ≥ 80 m, which suggests bottom depth was not a reliable predictor of irradiance at these depths. There was considerable interannual variation in $\zeta(z_{max}, \lambda_{tag})$ as shown by the range of $\zeta(z_{max}, \lambda_{tag})$ at individual stations during 2004–2018 (Fig. 2.4). Ranges of

$\zeta(z_{max}, \lambda_{tag})$ between 2004–2018 were 2.57–12.72 (median: 5.52), corresponding with 1.1–5.5 (median: 2.4) orders of magnitude of variation in near-bottom downwelling irradiance at individual stations (Fig. 2.4). From 2004 to 2018, 22.1% of stations (83/376) had variation in $\zeta(z_{max}, \lambda_{tag})$ corresponding with greater than three orders of magnitude of variation in near-bottom downelling irradiance (range of $\zeta(z_{max}, \lambda_{tag}) > 6.9$).

Lower near-surface water clarity was associated with a darker near-bottom environment as shown by the strong negative correlation between the $Z_{10\%}$ and $\zeta(z_{max}, \lambda_{tag})$ anomalies during 2004–2018 ($r_{[15]} = -0.79$; $p = 0.00042$; Fig. 2.5A). A deeper mixed layer was also associated with weaker stratification, as shown by the strong negative correlation between mixed layer depth and density difference anomalies during 2008–2017 ($r_{[10]} = -0.81$; $p = 0.0044$; Fig 2.5B). However, there was no evidence that variation in near-surface water clarity was linked to variation in the density structure of the water column, as density anomalies were not correlated with $Z_{10\%}$ anomalies ($r_{[10]} = 0.09$; $p = 0.80$; Fig. 5C) or near-bottom optical depth anomalies ($r_{[10]} = -0.32$; $p = 0.37$), and mixed layer depth anomalies were not correlated with $Z_{10\%}$ anomalies ($r_{[10]} = -0.10$; $p = 0.78$) or near-bottom optical depth anomalies ($r_{[10]} = 0.03$; $p = 0.94$).

Near-surface water clarity decreased and the near-bottom environment grew darker from 2004–2018, based on the effect of year in the linear mixed effects models (Table 2.2). On average, $\zeta(z_{max}, \lambda_{tag})$ increased by 0.035 ± 0.008 yr^{-1} (mean ± 2 std. err.), $Z_{10\%}$ decreased by 0.14 ± 0.03 m yr^{-1}, and $Z_{1\%}$ decreased by 0.21 ± 0.05 m yr^{-1}.

2.4.3.2 Fine-scale patterns and trends

The reason why depth alone was not a reliable predictor of near-bottom optical depth (Fig. 2.4) is illustrated by spatial patterns in near-bottom optical depth (Fig. 2.6A). Although $\zeta(z_{max}, \lambda_{tag})$

generally increased with depth, near-bottom conditions were darker inshore of the continental shelf break in the north and in the middle domain in the southeast, as shown by areas of high average $\zeta(z_{max}, \lambda_{tag})$ during 2004–2018 (Fig. 2.6A). Over the northwest middle and outer shelf, near-surface water clarity was high as shown by the 25–30 m deep $Z_{10\%}$ (Fig. 2.6B), but near-bottom conditions were dark, as shown by the high $\zeta(z_{max}, \lambda_{tag})$. In part, this can be explained by a near-bottom nepheloid layer in the northwest (Fig. 2.6C). However, the nepheloid layer alone did not explain the disconnect between $Z_{10\%}$ and $\zeta(z_{max}, \lambda_{tag})$ in the northwest, as will be shown later.

In the northern middle and outer domain, $Z_{10\%}$ was deeper than the mixed layer depth during 2008–2017 due to high near-surface water clarity and a shallow mixed layer (Figs. 2.6E). This is notable because the mixed layer of the eastern Bering Sea is nutrient-depleted after the spring bloom and onset of stratification, but nutrient concentrations below the mixed layer over the middle and outer domain are sufficient to sustain primary production during summer if there is sufficient light (Mordy et al., 2012; Stabeno et al., 2012a). By contrast, $Z_{10\%}$ was shallower than the mixed layer over the southern middle and outer domain (Figs. 2.6E). In the inner domain, $Z_{10\%}$ was shallower than the mixed layer of the typically fully mixed water column. The inner domain is nutrient-depleted after the spring bloom, however, so light is not expected to be the limiting factor for primary production (Kachel et al., 2002; Mordy et al., 2017).

Measures of near-surface water clarity, $Z_{10\%}$ and $Z_{1\%}$, were strongly correlated over most of the eastern Bering Sea shelf during 2004–2018 (Fig. 2.7A). However, over the northern middle and outer domains, $Z_{10\%}$ and $Z_{1\%}$ were weakly correlated or uncorrelated and $Z_{10\%}$ and $\zeta(z_{max}, \lambda_{tag})$ were uncorrelated, indicating that near-surface water clarity was not the primary driver of variation in subsurface light (Fig. 2.7B). Further south and in the inner domain, $Z_{10\%}$ was strongly correlated

with $\zeta(z_{max}, \lambda_{tag})$, indicating that variation in near-surface water clarity was closely linked to variation in light transmission through the full water column (Fig. 2.7B).

In the north (>~58° N), bottom and midwater light attenuating layers played an important role in regulating light transmission to the seafloor. This is shown by profiles of $K_d(z, \lambda_{tag})$ along rows P and S during 2011 (Figs. 2.8A,E) and 2017 (Figs. 2.8B,F). The thickness of the pycnocline decreased towards the inner domain as bottom depth decreased. In the northern middle and outer domain, mixed layer depth was often shallower than $Z_{10\%}$ and there was a recurrent mid-water peak in $K_d(z, \lambda_{tag})$ associated with the pycnocline or bottom of the mixed layer. Mid-water peaks in $K_d(z, \lambda_{tag})$ were likely caused by a subsurface chlorophyll maximum. In the bottom layer of the outer and middle domain, $K_d(z, \lambda_{tag})$was elevated in a 15–50 m thick bottom-associated nepheloid layer. Together, midwater and bottom layers caused dark near-bottom conditions in the middle and outer domain of the northwest (Fig. 2.6A) despite low $K_d(z, \lambda_{tag})$ in the mixed layer.

Vertical profiles of $K_d(z, \lambda_{tag})$ were more variable in the south, as shown by profiles along rows C and G during 2011 and 2017 (Figs. 2.9A, B, E, F). Over the middle domain, the vertical structure in $K_d(z, \lambda_{tag})$ was characterized by fine-scale (≤ 20 nmi) variability during many years, and near-surface water clarity played an important role in regulating light transmission, as shown by the row G cross-section during 2011 (Fig. 2.9A). Unlike in the north, there was no consistent bottom-associated nepheloid layer over the middle and outer domain in the south. Patches of elevated near-bottom $K_d(z, \lambda_{tag})$ values occurred sporadically, such as along row C at ~165.0 °W in 2011 (Fig. 2.9E) and at ~166.5 °W and 164.0 °W in 2017 (Fig. 2.9F). Due to variations in near-surface water clarity and mixed layer depth, the position of $Z_{10\%}$ relative to mixed layer depth was highly variable in the south, as shown by $Z_{10\%}$ being shallower than the mixed layer over the middle domain of row G during 2011 and much deeper during 2017 (Fig. 2.9A–B). Over the southern

middle domain, there was often a sharp pycnocline between the mixed layer and bottom layer and, in contrast to the north, there was no regular peak in $K_d(z, \lambda_{tag})$ associated with the pycnocline—midwater peaks in $K_d(z, \lambda_{tag})$ only occurred sporadically. However, a sharp pycnocline was not always present in the south, potentially because the pycnocline was still forming in early summer (e.g. Fig. 2.9G).

Trends in $\zeta(z_{max}, \lambda_{tag})$, $Z_{10\%}$, and $Z_{1\%}$ were patchy at fine-spatial scales and, in some areas, were the opposite of the regional trends of increasing $\zeta(z_{max}, \lambda_{tag})$ and decreasing $Z_{10\%}$, and $Z_{1\%}$ during 2004–2018 (Figs. 2.10A–C). Decreasing $Z_{10\%}$ was most prominent along the 50 m isobath north of 57 °N, in the interior of Bristol Bay, and inshore of the 50 m isobath south of Nunivak Island (Fig. 2.10A). Decreasing $Z_{1\%}$ occurred over the middle shelf and outer shelf in areas centered at ~58 °N and along the 50 m isobaths in Bristol Bay. Increases in $\zeta(z_{max}, \lambda_{tag})$ occurred in the same areas as the decreases in $Z_{1\%}$, while a significant decrease in $\zeta(z_{max}, \lambda_{tag})$ occurred over the northern outer shelf at ~ 61 °N (Fig. 2.10C).

In areas where there were significant changes in $\zeta(z_{max}, \lambda_{tag})$, $Z_{10\%}$, and $Z_{1\%}$, cumulative moving averages of $K_d(z, \lambda_{tag})$ at representative stations provide insight into how changes in the vertical structure of $K_d(z, \lambda_{tag})$ drove temporal trends. In the area around station K-03 (58° 18’ N, 166° 33’ W), a general increase in $K_d(z, \lambda_{tag})$ throughout the water column (Fig. 2.10D) led to the decrease in $Z_{10\%}$ and $Z_{1\%}$ and an increase in $\zeta(z_{max}, \lambda_{tag})$, although the trend was not monotonic (Figs. 10A–C). In the area around station I-25 (57° 40’ N, 172° 48’ W), an increase in $K_d(z, \lambda_{tag})$ near the surface and bottom (Fig. 2.10D) led to a decrease in $Z_{10\%}$ and $Z_{1\%}$ and an increase in $\zeta(z_{max}, \lambda_{tag})$ (Figs. 2.10A–C). Around Station S-30 (61° 00’ N, 176° 58’W), a decrease in $K_d(z, \lambda_{tag})$ at depths >40 m (Fig. 2.10D) led to a decrease in $\zeta(z_{max}, \lambda_{tag})$ (Figs. 2.10A–C).

2.4.4 *Comparison with Bering10K model*

The hypothesis that $K_d(z, \lambda_{tag})$ in the surface and mid-water was strongly influenced by variation in primary productivity is supported by predictions from the Bering10K-BESTNPZ model. Along rows C, G, P and S observed patterns in $K_d(z, \lambda_{tag})$ were qualitatively similar to modeled June–July chlorophyll-a for surface and mid-water depths (Figs. 2.8–2.9, 2.11). Throughout the eastern Bering Sea, model chlorophyll-a was higher during 2011 than 2017 (Figs 2.11, 2.12A–B), mainly due to effects of temperature on model dynamics. This pattern comports with observed differences in near-surface $K_d(z, \lambda_{tag})$ on the southern shelf between 2011 and 2017, as shown for rows C and G (Figs. 2.8–2.9). Further north, interannual variation in midwater $K_d(z, \lambda_{tag})$ was not clearly associated with modeled interannual variation chlorophyll-a (Figs. 2.8, 2.11). The model did not provide a mechanistic explanation for the bottom associated nepheloid layer, as chlorophyll-a and detritus were not elevated near the bottom over the middle and outer domain. The model predicted an onshore-offshore gradient in whole column detritus (Fig. 2.12C–D). Areal patterns of depth-integrated chlorophyll and detritus (Fig. 2.12) did not match the footprint of the bottom associated nepheloid layer (Fig. 2.6C).

2.5 DISCUSSION

2.5.1 *Overview*

We characterized variation in subsurface water clarity in the eastern Bering Sea shelf at an unprecedented spatial resolution and annual frequency using AOPs derived from bottom trawl irradiance measurements. Based on performance metrics for the regression between archival tag $K_d(z_s, \lambda_{tag})$ and satellite $K_d(z_s, 490)$, we conclude the sampling method and algorithm provided a

reliable characterization of in situ conditions. At a regional scale, we found the summertime near-bottom environment of the eastern Bering Sea grew darker and near-surface water clarity decreased from 2004 to 2018, as shown by the region-scale linear mixed effects models. Lower near-surface water clarity was associated with darker near-bottom conditions. At finer scales, however, local trends often differed from regional trends and changes in near-surface water clarity were not always associated with variation in irradiance deeper in the water column. These findings underscore that the eastern Bering Sea contains a complex mosaic of optical habitat and that subsurface dynamics play a key role in regulating optical conditions. Across the optical habitat mosaic, there are likely to be differences in primary productivity, trophic transfer efficiency, and community structure due to variation in light-dependent processes such as photosynthesis and visual foraging.

2.5.2 *Patterns and trends*

Over the northern middle and outer shelf, the recurrent peak in attenuation around the pycnocline was likely caused by a subsurface chlorophyll maximum, as predicted by the Bering10K-BESTNPZ model and frequently observed by in situ sampling (Stabeno et al., 2012b). Over the northern middle and outer shelf, high near-surface water clarity allows light to penetrate through the mixed layer and into the nutrient-rich waters below, where primary production can continue throughout the summer (Mordy et al., 2012; Stabeno et al., 2012a, 2012b). However, substances other than chlorophyll-a may also affect light transmission through the pycnocline, as concentrations of non-algal particulate and CDOM can be higher in subsurface layers than in the mixed layer (Naik et al., 2013).

Although patterns of $K_d(z, \lambda_{tag})$ generally matched spatial patterns of total chlorophyll predicted by the Bering10K-BESTNPZ model in the surface and midwater, they did not match modeled interannual variation in subsurface total chlorophyll in the north and the model did not provide a mechanistic explanation for the bottom-associated nepheloid layer. The mismatch between observed $K_d(z, \lambda_{tag})$ and modeled patterns of interannual variation in subsurface chlorophyll-a in the northern region may derive from the BESTNPZ model's inability to fully simulate the under-ice and ice-edge phytoplankton blooms and sinking dynamics that occur in this region (Kearney et al., 2020). The absence of a nepheloid layer may be due to the fact that the Bering10K-BESTNPZ model does not include sediment resuspension dynamics. It may also point to model deficiencies related to sinking, remineralization, and resuspension of organic matter in this region. Overall, dynamics of the Bering10K-BESTNPZ model are poorly constrained by in-situ observations due to a paucity of observations, especially with respect to spatial variation in the north. The tag-based AOP data set or future trawl-based AOP data may help to improve the Bering10K-BESTNPZ model by informing efforts to constrain or refine processes in the model.

We hypothesize that the bottom-associated nepheloid layer over the northern middle and outer shelf is maintained by tidally-driven resuspension of sediment. Nepheloid layers form when current velocities along the seafloor generate enough shear stress to resuspend substrate. The shear stress needed to resuspend sediment depends on the composition of the sediment. Flow velocities $\geq$7 cm s^{-1} generate enough shear stress to resuspend phytodetrital aggregates (Lampitt, 1985; McCave, 2019), 10–15 cm s^{-1} can resuspend loosely consolidated silt, and 25–30 cm s^{-1} can resuspend sand (Gardner, 1989). Mean geostrophic flow velocities are < 5 cm s^{-1} over most of the eastern Bering Sea shelf (Cokelet, 2016; Stabeno et al., 2016), insufficient to resuspend sediment. However, diurnal and semidiurnal tides in the eastern Bering Sea generate 10–30 cm s^{-1} currents

over much of the shelf and currents >70 cm s^{-1} can occur in some areas (Coachman, 1986; Stabeno et al., 2008). These current speeds would be sufficient to resuspend phytoplankton, detritus, and the predominantly mud and sand substrate of the eastern Bering Sea shelf, although tidal currents are weaker further north (Stabeno et al., 2012b). If it is caused by tidal currents, variation in the nepheloid layer would be caused by variation in accumulated phytoplankton and detritus in the bottom layer, tidal amplitude, composition of surface sediment, and rates of consumption by benthic consumers (Lampitt, 1985). Further research is needed to clarify what causes the nepheloid layer, what effect the nepheloid layer has on ecological processes near the seafloor, and why the nepheloid layer is most prominent in the north.

Contact between trawl gear and the seafloor generates sediment clouds, but is unlikely to explain the bottom-associated nepheloid layer for several reasons. First, review of hundreds of hours of underwater video footage of the 83-112 bottom-trawl gear in motion in the eastern Bering Sea shows the archival tag location (top panel, 0.5–1 m behind headrope, ~2.5 m off-bottom) is well outside of the mudcloud (L.L. Britt and S. Kotwicki, personal observation). Second, the nepheloid layer typically extends tens of meters off bottom, well beyond where a mud cloud would likely begin. Third, the grain size of seafloor sediment generally decreases from onshore-to-offshore on the eastern Bering Sea shelf (Richwine et al. 2018), which suggests mudclouds would be more prevalent in deeper areas. However, the nepheloid layer is absent or less pronounced in deep areas and patterns of sediment size (Richwine et al. 2018) do not align with the footprint of nepheloid layer. Thus, the nepheloid layer is unlikely to be an artifact of our sampling method.

2.5.3 *Implications for fisheries stock assessment and management*

The level of variation in near-bottom optical depth is likely sufficient to cause variation in the catchability (*i.e.*, capture efficiency) of bottom trawl fishing gear that is also used in abundance-biomass trawl surveys. At many survey stations, variation in $\zeta(z_{max,}\ \lambda_{tag})$ corresponded with multiple-order-of magnitude variation in downwelling irradiance that would be expected to cause variation in capture efficiency. A 3–4 order-of-magnitude decrease in background irradiance can cause a complete cessation of fish visual reactions to bottom trawl gear (Blaxter and Parrish, 1966, 1964; Cui et al., 1991; Glass and Wardle, 1989) and variation in downwelling irradiance during bottom trawl surveys affects catch rates of walleye pollock in the eastern Bering Sea (Kotwicki et al., 2018, 2009). Changes in catchability can be a concern for fisheries management because they affect the precision and accuracy of fisheries indices of abundance that are used for stock assessment (Wilberg et al., 2009). The relatively low cost of the archival tags and minimal disruption to bottom trawl survey operations suggests that archival tags could similarly be deployed on commercial fishing gear to improve understanding of how variation in light and water clarity affects catchability.

Similarly, variation in near-bottom optical depth may also affect demographic rates of fish populations by altering the strength of predator-prey interactions (Eiane et al., 1999). As with trawl efficiency, the ability of a fish to feed visually can cease entirely given a 2–4 order-of-magnitude change in background irradiance (*e.g.* Ryer et al., 2002; Utne, 1997). The effect of a change in water clarity on predator-prey interactions depends on the visual capabilities of the predator and prey, the relative visibility of prey, and foraging mode of predators (*e.g.* Eiane et al., 1999; Giske et al., 1994; Chapter 1). Reduced water clarity affects piscivory more than planktivory (De Robertis et al., 2003), and favors tactile feeding over visual feeding (Eiane et al., 1999).

Depth is often treated as a proxy for the ambient level of radiation in visual ecology studies and species distribution models (Caves et al., 2017; Kaartvedt et al., 2017, 1996; Schweikert et al., 2018) but it is not a reliable predictor of optical depth in the eastern Bering Sea. Studies in the eastern Bering Sea may benefit from using optical depth to characterize the level of ambient radiation, such as by using it as a predictor in species distribution models. Doing so may clarify how visual habitat requirements influence fish distribution and habitat availability in the eastern Bering Sea.

Changes in water clarity can indicate changes in the dynamics of primary production and thereby productivity of higher trophic levels. The trend of decreasing near-bottom optical depth over the northern middle-outer domain indicates there has been a decrease in optically active substances (*i.e.*, chlorophyll-a, CDOM, non-algal particulate) in the water column during the survey period. The trend is notable because it occurred in an area where primary productivity continues throughout the summer by virtue of high near-surface water clarity, high nutrient availability below the mixed layer, and a gradual pycnocline (Stabeno et al., 2012a). The reason for this change may be the decline in dissolved inorganic nitrate and phosphate in the bottom layer that occurred from summer 2005 to 2016 that would presumably affect primary production and chlorophyll in the pycnocline (Stabeno et al., 2019). The change from 2005–2016 was associated with a concomitant decrease in salinity, indicating nutrient variability was mediated by physical processes (Stabeno et al., 2019). Alternative explanations could be changes in the timing of productivity or shifts in the balance between primary production and consumption. Further research is needed to evaluate whether changes in optical depth were associated with changes in salinity productivity, which may be facilitated by developing empirical models that relate $K_d(z, \lambda_{tag})$ to chlorophyll-a concentrations (e.g. Bayle et al., 2015; O'Toole et al., 2014).

2.5.4 *Limitations and uncertainties*

Our sampling method and analyses have several limitations and uncertainties when it comes to characterizing changes in water clarity in the eastern Bering Sea. First, we treated year as the time step for our analyses, but surveys were sampled over two months every year, progressing from interior Bristol Bay to the northwest outer continental shelf. Because individual stations were sampled at approximately the same time each year, the optical properties provide an annual snapshot of the system. However, sampling within-year, between years, and among stations was conducted at different times relative to the non-stationary phenology of phytoplankton blooms, stratification, sea-ice retreat, and tides. Second, the archival tags do not collect spectral irradiance measurements so we could not derive spectrally-resolved AOPs. This is an important limitation because photopigments of autotrophs and animals are sensitive to specific colors of light, and the different substances that cause variation in the optical environment have spectral differences in absorption and scattering. Third, we could not verify what caused variation in AOPs because we did not conduct any sampling to determine how the composition of optically-active constituents of the water column changed over space and time. Instead, our inferences are based on previous work to elucidate how physical and biological processes affect water clarity in the eastern Bering Sea. Finally, the wide acceptance angle of the archival tag photodiode suggests archival tag measurements can approximate, but are not equal to diffuse irradiance because tags are not equipped with a cosine corrector. While we do not believe these issues meaningfully affected our results and interpretation, improving sampling methods or constraining analyses to particular subsets of the data can overcome some of these limitations and uncertainties. Moreover,

the patterns we identified may be useful for guiding focused process-oriented research using more sophisticated sampling methods and instrumentation.

2.5.5 *Methodological improvements*

Our sampling method could be modified to improve characterization of visual conditions for animals and identification of optically active constituents of the water column. We used archival tags equipped with photodiodes because they have a large range of absolute sensitivity and could withstand the rough operating conditions of bottom trawl surveys with little risk of equipment failure. This required a trade-off in terms of information quality and comparability with measurements from conventional sampling equipment. In the future, archival tags could be replaced with purpose-built optical sampling equipment if the equipment meets the operational requirements for bottom trawl surveys (*e.g.* ruggedized, low profile to minimize drag on the trawl). Bio-optical sampling equipment could be deployed alongside archival tags to develop models that characterize relationships between physical constituents of the water column and tag-derived AOPs in the eastern Bering Sea, as has been done using archival tags deployed on marine animals (Bayle et al., 2015; Jaud et al., 2012; O'Toole et al., 2014; Teo et al., 2009). Spectral radiometers could be deployed to derive spectrally specific AOPs or archival tags could be equipped with spectral filters that match wavelengths that are relevant to vision or other biological processes (*e.g.* Gal et al., 1999). All of these options represent cost-efficient solutions to improve in situ monitoring.

2.5.6 *Conclusions*

Monitoring subsurface water clarity in marine ecosystems remains an immense logistical challenge. While burgeoning technologies such as autonomous underwater vehicles, biogeochemical Argo floats, and satellite-based high spectral resolution LiDAR may eventually achieve broader coverage and improve subsurface monitoring, coverage gaps will persist in the near-term. In the meantime, researchers should continue to explore how existing sampling platforms can be used to fill coverage gaps. Our study provides one such method for monitoring subsurface water clarity.

2.6 ACKNOWLEDGEMENTS

We thank the survey participants who collected data for this study, including the masters and crews of FV *Alaska Knight*, FV *Aldebaran*, FV *Arcturus*, FV *Ocean Explorer*, and FV *Vesteraalen*. We thank Cal Mordy, Jens Nielsen, Steve Rubin, Jeff Napp, Morgan Arrington, Cheryl Barnes, Tim Essington, Helena McMonagle, and two anonymous reviewers for constructive feedback on an earlier version of this manuscript. Funding to support this research was provided by the NOAA Fisheries and the Environment (FATE) Program and the Joint Institute for the Study of the Atmosphere and Ocean (JISAO) under NOAA Cooperative Agreement NA15OAR4320063. This manuscript is contribution number EcoFOCI-0953 to NOAA PMEL-AFSC's Ecosystems and Fisheries-Oceanography Coordinated Investigations, contribution number 5143 to NOAA's Pacific Marine Environmental Laboratory, and contribution 2020-1101 to JISAO. Any use of trade, firm, or product names is for descriptive purposes only and does not imply endorsement by the U.S. Government. The scientific results and conclusions, as well as any views or opinions

expressed herein, are those of the author(s) and do not necessarily reflect those of NOAA or the Department of Commerce.

2.7 REFERENCES

Aksnes, D.L., 2007. Evidence for visual constraints in large marine fish stocks. Limnol. Oceanogr. 52, 198–203. https://doi.org/10.4319/lo.2007.52.1.0198

Aksnes, D.L., Nejstgaard, J., Sædberg, E., Sørnes, T., 2004. Optical control of fish and zooplankton populations. Limnol. Oceanogr. 49, 233–238. https://doi.org/10.4319/lo.2004.49.1.0233

Aksnes, D.L., Ohman, M.D., 2009. Multi-decadal shoaling of the euphotic zone in the southern sector of the California Current System. Limnol. Oceanogr. 54, 1272–1281. https://doi.org/10.4319/lo.2009.54.4.1272

Baker, K.S., Smith, R.C., 1979. Quasi-inherent characteristics of the diffuse attenuation coefficient for irradiance. Ocean Opt. IV 208, 60–63.

Barbieux, M., Uitz, J., Gentili, B., Pasqueron De Fommervault, O., Mignot, A., Poteau, A., Schmechtig, C., Taillandier, V., Leymarie, E., Penkerc'H, C., D'Ortenzio, F., Claustre, H., Bricaud, A., 2019. Bio-optical characterization of subsurface chlorophyll maxima in the Mediterranean Sea from a Biogeochemical-Argo float database. Biogeosciences 16, 1321–1342. https://doi.org/10.5194/bg-16-1321-2019

Bayle, S., Monestiez, P., Guinet, C., Nerini, D., 2015. Moving toward finer scales in oceanography: Predictive linear functional model of Chlorophyll *a* profile from light data. Prog. Oceanogr. 134, 221–231. https://doi.org/10.1016/j.pocean.2015.02.001

Bittig, H.C., Maurer, T.L., Plant, J.N., Wong, A.P., Schmechtig, C., Claustre, H., Trull, T.W.,

Bhaskar, T.V.S.U., Boss, E., Dall'Olmo, G., Organelli, E., Poteau, A., Johnson, K.S., Hanstein, C., Leymarie, E., Le Reste, S.L., Riser, S.C., Rupan, A.R., Taillandier, V., Thierry, V., Xing, X., 2019. A BGC-Argo guide: Planning, deployment, data handling and usage. Front. Mar. Sci. 6. https://doi.org/10.3389/fmars.2019.00502

Blaxter, J.H.S., Parrish, B.B., 1966. The reaction of marine fish to moving netting and other devices in tanks. Mar. Res. No. 1 1–15.

Blaxter, J.H.S., Parrish, B.B., 1964. The importance of vision in the reaction of fish to driftnets and trawls, in: Modern Fishing Gear of the World 2. Fishing News Books, London, pp. 529–536.

Boyce, D.G., Dowd, M., Lewis, M.R., Worm, B., 2014. Estimating global chlorophyll changes over the past century. Prog. Oceanogr. 122, 163–173. https://doi.org/10.1016/j.pocean.2014.01.004

Britt, L.L., Loew, E.R., McFarland, W.N., 2001. Visual pigments in the early life stages of Pacific Northwest marine fishes. J. Exp. Biol. 204, 2581–2587.

Brown, C.A., Huot, Y., Purcell, M.J., Cullen, J.J., Lewis, M.R., 2004. Mapping coastal optical and biogeochemical variability using an autonomous underwater vehicle and a new bio-optical inversion algorithm. Limnol. Oceanogr. Methods 2, 262–281. https://doi.org/10.4319/lom.2004.2.262

Capuzzo, E., Stephens, D., Silva, T., Barry, J., Forster, R.M., 2015. Decrease in water clarity of the southern and central North Sea during the 20th century. Glob. Chang. Biol. 21, 2206–2214. https://doi.org/10.1111/gcb.12854

Caves, E.M., Sutton, T.T., Johnsen, S., 2017. Visual acuity in ray-finned fishes correlates with eye size and habitat. J. Exp. Biol. 220, 1586–1596. https://doi.org/10.1242/jeb.151183

Coachman, L.K., 1986. Circulation, water masses, and fluxes on the southeastern Bering Sea shelf. Cont. Shelf Res. 5, 23–108. https://doi.org/10.1016/0278-4343(86)90011-7

Cokelet, E.D., 2016. 3-D water properties and geostrophic circulation on the eastern Bering Sea shelf. Deep Sea Res. Part II Top. Stud. Oceanogr. 134, 65–85. https://doi.org/http://dx.doi.org/10.1016/j.dsr2.2016.08.009

Cui, G., Wardle, C.S., Glass, C.W., Johnstone, A.D.F., Mojsiewicz, W.R., 1991. Light level thresholds for visual reaction of mackerel, *Scomber scombrus* L., to coloured monofilament nylon gillnet materials. Fish. Res. 10, 255–263. https://doi.org/10.1016/0165-7836(91)90079-U

Cullen, J.J., 2015. Subsurface chlorophyll maximum layers: Enduring enigma or mystery solved? Ann. Rev. Mar. Sci. 7, 207–239. https://doi.org/10.1146/annurev-marine-010213-135111

Danielson, S., Eisner, L., Weingartner, T., Aagaard, K., 2011. Thermal and haline variability over the central Bering Sea shelf: Seasonal and interannual perspectives. Cont. Shelf Res. 31, 539–554. https://doi.org/10.1016/j.csr.2010.12.010

De Robertis, A., Ryer, C.H., Veloza, A., Brodeur, R.D., 2003. Differential effects of turbidity on prey consumption of piscivorous and planktivorous fish. Can. J. Fish. Aquat. Sci. 60, 1517–1526. https://doi.org/10.1139/f03-123

Dickman, E.M., Newell, J.M., González, M.J., Vanni, M.J., 2008. Light, nutrients, and food-chain length constrain planktonic energy transfer efficiency across multiple trophic levels. Proc. Natl. Acad. Sci. U. S. A. 105, 18408–18412. https://doi.org/10.1073/pnas.0805566105

Dupont, N., Aksnes, D.L., 2013. Centennial changes in water clarity of the Baltic Sea and the North Sea. Estuar. Coast. Shelf Sci. 131, 282–289. https://doi.org/10.1016/j.ecss.2013.08.010

Eiane, K., Aksnes, D.L., Bagøien, E., Kaartvedt, S., 1999. Fish or jellies — a question of visibility?

Limnol. Oceanogr. 44, 1352–1357. https://doi.org/10.4319/lo.1999.44.5.1352

Eiane, K., Aksnes, D.L., Giske, J., 1997. The significance of optical properties in competition among visual and tactile planktivores: a theoretical study. Ecol. Modell. 98, 123–136.

Feely, R.A., Massoth, G.J., Paulson, A.J., Lamb, M.F., Martin, E.A., 1981. Distribution and elemental composition of suspended matter in Alaskan coastal waters. NOAA Tech. Memo. ERL-PMEL-2, 119.

Gal, G., Loew, E.R., Rudstam, L.G., Mohammadian, A.M., 1999. Light and diel vertical migration: spectral sensitivity and light avoidance by *Mysis relicta*. Can. J. Fish. Aquat. Sci. 56, 311–322. https://doi.org/2

Gardner, W.D., 1989. Periodic resuspension in Baltimore Canyon by focusing of internal waves. J. Geophys. Res. 94. https://doi.org/10.1029/jc094ic12p18185

Gibson, G.A., Spitz, Y.H., 2011. Impacts of biological parameterization, initial conditions, and environmental forcing on parameter sensitivity and uncertainty in a marine ecosystem model for the Bering Sea. J. Mar. Syst. 88, 214–231. https://doi.org/10.1016/j.jmarsys.2011.04.008

Giske, J., Aksnes, D.L., Fiksen, Ø., 1994. Visual predators, environmental variables and zooplankton mortality risk. Vie Milieu 44, 1–9.

Glass, C.W., Wardle, C.S., 1989. Comparison of the reactions of fish to a trawl gear, at high and low light intensities. Fish. Res. 7, 249–266. https://doi.org/10.1016/0165-7836(89)90059-3

Gordon, H.R., 1989. Can the Lambert-Beer law be applied to the diffuse attenuation coefficient of ocean water? Limnol. Oceanogr. 34, 1389–1409. https://doi.org/10.1097/00003246-200206000-00018

Haidvogel, D.B., Arango, H., Budgell, W.P., Cornuelle, B.D., Curchitser, E., Di Lorenzo, E., Fennel, K., Geyer, W.R., Hermann, A.J., Lanerolle, L., Levin, J., McWilliams, J.C., Miller,

A.J., Moore, A.M., Powell, T.M., Shchepetkin, A.F., Sherwood, C.R., Signell, R.P., Warner, J.C., Wilkin, J., 2008. Ocean forecasting in terrain-following coordinates: Formulation and skill assessment of the Regional Ocean Modeling System. J. Comput. Phys. 227, 3595–3624. https://doi.org/10.1016/j.jcp.2007.06.016

Harada, N., Sato, M., Oguri, K., Hagino, K., Okazaki, Y., Katsuki, K., Tsuji, Y., Shin, K.H., Tadai, O., Saitoh, S.I., Narita, H., Konno, S., Jordan, R.W., Shiraiwa, Y., Grebmeier, J., 2012. Enhancement of coccolithophorid blooms in the Bering Sea by recent environmental changes. Global Biogeochem. Cycles 26, 1–13. https://doi.org/10.1029/2011GB004177

Haraldsson, M., Tönnesson, K., Tiselius, P., Thingstad, T.F., Aksnes, D.L., 2012. Relationship between fish and jellyfish as a function of eutrophication and water clarity. Mar. Ecol. Prog. Ser. 471, 73–85. https://doi.org/10.3354/meps10036

Hemsley, V.S., Smyth, T.J., Martin, A.P., Frajka-Williams, E., Thompson, A.F., Damerell, G., Painter, S.C., 2015. Estimating oceanic primary production using vertical irradiance and chlorophyll profiles from ocean gliders in the North Atlantic. Environ. Sci. Technol. 49, 11612–11621. https://doi.org/10.1021/acs.est.5b00608

Hostetler, C.A., Behrenfeld, M.J., Hu, Y., Hair, J.W., Schulien, J.A., 2018. Spaceborne lidar in the study of marine systems. Ann. Rev. Mar. Sci. 10, 121–147. https://doi.org/10.1146/annurev-marine-121916-063335

Hunt, G.L., Coyle, K.O., Eisner, L., Farley, E. V, Heintz, R., Mueter, F., Napp, J.M., Overland, J.E., Ressler, P.H., Sale, S., Stabeno, P.J., 2011. Climate impacts on eastern Bering Sea food webs: A synthesis of new data and an assessment of the Oscillating Control Hypothesis. ICES J. Mar. Sci. 68, 1230–1243. https://doi.org/10.1093/icesjms/fsr036

Iida, T., Mizobata, K., Saitoh, S.I., 2012. Interannual variability of coccolithophore *Emiliania*

huxleyi blooms in response to changes in water column stability in the eastern Bering Sea. Cont. Shelf Res. 34, 7–17. https://doi.org/10.1016/j.csr.2011.11.007

Jaud, T., Cile Dragon, A.-C., Garcia, J.V., Guinet, C., 2012. Relationship between chlorophyll a concentration, light attenuation and diving depth of the southern elephant seal *Mirounga leonina*. PLoS One 7, e47444. https://doi.org/10.1371/journal.pone.0047444

Jumars, P.A., Dorgan, K.M., Lindsay, S.M., 2015. Diet of worms emended: an update of polychaete feeding guilds. Ann. Rev. Mar. Sci. 7, 497–520. https://doi.org/10.1146/annurev-marine-010814-020007

Kaartvedt, S., Melle, W., Knutsen, T., Skjoldal, H.R., 1996. Vertical distribution of fish and krill beneath water of varying optical properties. Mar. Ecol. Prog. Ser. 136, 51–58. https://doi.org/10.3354/meps136051

Kaartvedt, S., Røstad, A., Aksnes, D.L., 2017. Changing weather causes behavioral responses in the lower mesopelagic. Mar. Ecol. Prog. Ser. 574, 259–263. https://doi.org/10.3354/meps07467

Kachel, N.B., Hunt, G.L., Salo, S.A., Schumacher, J.D., Stabeno, P.J., Whitledge, T.E., 2002. Characteristics and variability of the inner front of the southeastern Bering Sea. Deep. Res. Part II Top. Stud. Oceanogr. 49, 5889–5909. https://doi.org/10.1016/S0967-0645(02)00324-7

Kawana, K., 1975. Turbidity distribution of the Bering Sea in the summer. Bull. Fac. Fish. Hokkaido Univ. 26, 73–86.

Kearney, K., Hermann, A., Cheng, W., Ortiz, I., Aydin, K., 2020. A coupled pelagic-benthic-sympagic biogeochemical model for the Bering Sea: documentation and validation of the BESTNPZ model (v2019.08.23) within a high-resolution regional ocean model. Geosci.

Model Dev. 13, 597–650. https://doi.org/10.5194/gmd-13-597-2020

Kirk, J.T.O., 2011. Light and photosynthesis in aquatic ecosystems, 3rd ed. Cambridge University Press, New York.

Kotwicki, S., De Robertis, A., von Szalay, P., Towler, R., 2009. The effect of light intensity on the availability of walleye pollock (*Theragra chalcogramma*) to bottom trawl and acoustic surveys. Can. J. Fish. Aquat. Sci. 66, 983–994. https://doi.org/10.1139/f09-055

Kotwicki, S., Ressler, P.H., Ianelli, J.N., Punt, A.E., Horne, J.K., 2018. Combining data from bottom trawl and acoustic surveys to estimate an index of abundance for semipelagic species. Can. J. Fish. Aquat. Sci. 75, 60–71.

Ladd, C., Eisner, L.B., Salo, S.A., Mordy, C.W., Iglesias-Rodriguez, M.D., 2018. Spatial and temporal variability of coccolithophore blooms in the eastern Bering Sea. J. Geophys. Res. Ocean. 123, 9119–9136. https://doi.org/10.1029/2018JC014302

Ladd, C., Stabeno, P.J., 2012. Stratification on the eastern Bering Sea shelf revisited. Deep Sea Res. Part II Top. Stud. Oceanogr. 65–70, 72–83. https://doi.org/10.1016/j.dsr2.2012.02.009

Laman, E.A., Kotwicki, S., Rooper, C.N., 2014. Correlating environmental and biogenic factors with abundance and distribution of Pacific ocean perch (*Sebastes alutus*) in the Aleutian Islands, Alaska. Fish. Bull. 113, 270–289. https://doi.org/10.7755/FB.113.3.4.The

Laman, E.A., Rooper, C.N., Turner, K., Rooney, S., Cooper, D.W., Zimmermann, M., 2018. Using species distribution models to describe essential fish habitat in Alaska. Can. J. Fish. Aquat. Sci. 75, 1230–1255. https://doi.org/10.1139/cjfas-2017-0181

Lampitt, R.S., 1985. Evidence for the seasonal deposition of detritus to the deep-sea floor and its subsequent resuspension. Deep Sea Res. Part A, Oceanogr. Res. Pap. 32, 885–897. https://doi.org/10.1016/0198-0149(85)90034-2

Langbehn, T.J., Varpe, Ø., 2017. Sea-ice loss boosts visual search: Fish foraging and changing pelagic interactions in polar oceans. Glob. Chang. Biol. 23, 5318–5330. https://doi.org/10.1111/gcb.13797

Lee, Z., Carder, K.L., Arnone, R.A., 2002. Deriving inherent optical properties from water color: a multiband quasi-analytical algorithm for optically deep waters. Appl. Opt. 41, 5755. https://doi.org/10.1364/ao.41.005755

Lee, Z.P., Du, K.P., Arnone, R., 2005. A model for the diffuse attenuation coefficient of downwelling irradiance. J. Geophys. Res. C Ocean. 110, 1–10. https://doi.org/10.1029/2004JC002275

Lomas, M., Eisner, L., Gann, J., Baer, S., Mordy, C., Stabeno, P., 2020. Time-series of direct primary production and phytoplankton biomass in the southeastern Bering Sea: Responses to cold and warm stanzas. Mar. Ecol. Prog. Ser. 642, 39–54. https://doi.org/10.3354/meps13317

Lovvorn, J.R., Baduini, C.L., Hunt Jr., G.L., 2001. Modeling underwater visual and filter feeding by planktivorous shearwaters in unusual sea conditions. Ecology 82, 2342–2356.

Lythgoe, J.., 1972. The adaptation of visual pigments to the photic environment, in: Dartnell, H.J.A. (Ed.), The Handbook of Sensory Physiology VII/1. Springer, pp. 566–603.

McCave, I.N., 2019. Nepheloid layers, 3rd ed, Encyclopedia of Ocean Sciences. Elsevier Ltd. https://doi.org/10.1016/B978-0-12-409548-9.11207-2

McManus, D.A., Smyth, C.S., 1970. Turbid bottom water on the continental shelf of the northern Bering Sea. J. Sediment. Petrol. 40, 869–873.

Mitchell, C., Gordon, H.R., Bowler, B., Drapeau, D., Balch, W.M., 2018. Optical inversions of the water column based on glider measurements. Opt. Express 26, 32824. https://doi.org/10.1364/oe.26.032824

Mobley, C.D., 1994. Light and water: Radiative transfer in natural waters. Academic Press.

Mordy, C.W., Cokelet, E.D., Ladd, C., Menzia, F.A., Proctor, P., Stabeno, P.J., Wisegarver, E., 2012. Net community production on the middle shelf of the eastern Bering Sea. Deep. Res. Part II Top. Stud. Oceanogr. 65–70, 110–125. https://doi.org/10.1016/j.dsr2.2012.02.012

Mordy, C.W., Devol, A., Eisner, L.B., Kachel, N., Ladd, C., Lomas, M.W., Proctor, P., Sambrotto, R.N., Shull, D.H., Stabeno, P.J., Wisegarver, E., 2017. Nutrient and phytoplankton dynamics on the inner shelf of the eastern Bering Sea. J. Geophys. Res. Ocean. 122, 2422–2440. https://doi.org/10.1002/2016JC012071

Naik, P., D'Sa, E.J., Gomes, H. do R., Goés, J.I., Mouw, C.B., 2013. Light absorption properties of southeastern Bering Sea waters: Analysis, parameterization and implications for remote sensing. Remote Sens. Environ. 134, 120–134. https://doi.org/10.1016/j.rse.2013.03.004

Nowak, B.V.R., 2019. In situ measurements by instrumented grey seals (*Halichoerus gryups*) reveal fine-scale oceanographic properties and environmental influences on movement patterns. Dalhouse University.

O'Toole, M., Guinet, C., Lea, M.A., Hindell, M.A., 2017. Marine predators and phytoplankton: How elephant seals use the recurrent Kerguelen plume. Mar. Ecol. Prog. Ser. 581, 215–227. https://doi.org/10.3354/meps12312

O'Toole, M.D., Lea, M.A., Guinet, C., Hindell, M.A., 2014. Estimating trans-seasonal variability in water column biomass for a highly migratory, deep diving predator. PLoS One 9. https://doi.org/10.1371/journal.pone.0113171

Olson, M.B., Strom, S.L., 2002. Phytoplankton growth, microzooplankton herbivory and community structure in the southeast Bering Sea: Insight into the formation and temporal persistence of an *Emiliania huxleyi* bloom. Deep. Res. Part II Top. Stud. Oceanogr. 49, 5969–

5990. https://doi.org/10.1016/S0967-0645(02)00329-6

Opdal, A.F., Lindemann, C., Aksnes, D.L., 2019. Centennial decline in North Sea water clarity causes strong delay in phytoplankton bloom timing 3946–3953. https://doi.org/10.1111/gcb.14810

Pitarch, J., 2020. A review of Secchi's contribution to marine optics and the foundation of Secchi disk science. Oceanography 33, 26–37. https://doi.org/10.5670/oceanog.2020.301

Richwine, K.A., Smith, K.R., McConnaughey, R.A., 2018. Surficial sediments of the eastern Bering Sea continental shelf: EBSSED-2 database documentation. United States Department of Commerce, NOAA Technical Memorandum NMFS-AFSC-377, 48 p. https://doi.org/10.25923/yygp-xs96

Riisgård, H.U., Larsen, P.S., 2015. Filter-feeding zoobenthos and hydrodynamics, in: Rossi, S. (Ed.), Marine Animal Forests. Springer International Publishing, pp. 1–25. https://doi.org/10.1007/978-3-319-17001-5

Rohan, S.K., Beauchamp, D.A., Essington, T.E., Hansen, A.G., *In review*. A generalized model of aquatic visual foraging.

Rohan, S.K., Kotwicki, S., Laman, E.A., Britt, L.L., Aydin, K., 2020. Deriving apparent optical properties from light measurements obtained using bottom-trawl-mounted archival tags. United States Department of Commerce, NOAA Technical Memorandum NMFS-AFSC-403, 91 p. https://doi.org/10.25923/42yn-1q79

Rooper, C.N., Hoff, G.R., Stevenson, D.E., Orr, J.W., Spies, I.B., 2019. Skate egg nursery habitat in the eastern Bering Sea: A predictive model. Mar. Ecol. Prog. Ser. 609, 163–178. https://doi.org/10.3354/meps12809

Ryer, C.H., Lawton, A., Lopez, R.J., Olla, B.L., 2002. A comparison of the functional ecology of visual vs. nonvisual foraging in two planktivorous marine fishes. Can. J. Fish. Aquat. Sci. 59, 1305–1314. https://doi.org/10.1139/f02-097

Saha, S., Moorthi, S., Pan, H.L., Wu, X., Wang, Jiande, Nadiga, S., Tripp, P., Kistler, R., Woollen, J., Behringer, D., Liu, H., Stokes, D., Grumbine, R., Gayno, G., Wang, Jun, Hou, Y.T., Chuang, H.Y., Juang, H.M.H., Sela, J., Iredell, M., Treadon, R., Kleist, D., Van Delst, P., Keyser, D., Derber, J., Ek, M., Meng, J., Wei, H., Yang, R., Lord, S., Van Den Dool, H., Kumar, A., Wang, W., Long, C., Chelliah, M., Xue, Y., Huang, B., Schemm, J.K., Ebisuzaki, W., Lin, R., Xie, P., Chen, M., Zhou, S., Higgins, W., Zou, C.Z., Liu, Q., Chen, Y., Han, Y., Cucurull, L., Reynolds, R.W., Rutledge, G., Goldberg, M., 2010. The NCEP climate forecast system reanalysis. Bull. Am. Meteorol. Soc. 91, 1015–1057. https://doi.org/10.1175/2010BAMS3001.1

Sambrotto, R.N., Niebauer, H.J., Goering, J.J., Iverson, R.L., 1986. Relationships among vertical mixing, nitrate uptake, and phytoplankton growth during the spring bloom in the southeast Bering Sea middle shelf. Cont. Shelf Res. 5, 161–198. https://doi.org/10.1016/0278-4343(86)90014-2

Sandén, P., Håkansson, B., 1996. Long-term trends in Secchi depth in the Baltic Sea. Limnol. Oceanogr. 41, 346–351. https://doi.org/10.1016/j.ecss.2012.02.015

Schulien, J.A., Behrenfeld, M.J., Hair, J.W., Hostetler, C.A., Twardowski, M.S., 2017. Vertically-resolved phytoplankton carbon and net primary production from a high spectral resolution lidar. Opt. Express 25, 13577. https://doi.org/10.1364/oe.25.013577

Schweikert, L.E., Caves, E.M., Solie, S.E., Sutton, T.T., Johnsen, S., 2018. Variation in rod spectral sensitivity of fishes is best predicted by habitat and depth. J. Fish Biol.

https://doi.org/10.1111/jfb.13859

Seegers, B.N., Stumpf, R.P., Schaeffer, B.A., Loftin, K.A., Werdell, P.J., 2018. Performance metrics for the assessment of satellite data products: an ocean color case study. Opt. Express 26, 7404. https://doi.org/10.1364/oe.26.007404

Shchepetkin, A.F., McWilliams, J.C., 2005. The regional oceanic modeling system (ROMS): A split-explicit, free-surface, topography-following-coordinate oceanic model. Ocean Model. 9, 347–404. https://doi.org/10.1016/j.ocemod.2004.08.002

Sigler, M.F., Stabeno, P.J., Eisner, L.B., Napp, J.M., Mueter, F.J., 2014. Spring and fall phytoplankton blooms in a productive subarctic ecosystem, the eastern Bering Sea, during 1995-2011. Deep. Res. Part II Top. Stud. Oceanogr. 109, 71–83. https://doi.org/10.1016/j.dsr2.2013.12.007

Smith, R.C., Baker, K.S., 1984. The analysis of ocean optical data, in: Blizard, M.A. (Ed.), SPIE, Ocean Optics VII. pp. 119–126. https://doi.org/10.1117/12.943295

Stabeno, P., Napp, J., Mordy, C., Whitledge, T., 2010. Factors influencing physical structure and lower trophic levels of the eastern Bering Sea shelf in 2005: Sea ice, tides and winds. Prog. Oceanogr. 85, 180–196. https://doi.org/10.1016/j.pocean.2010.02.010

Stabeno, P.J., Bell, S.W., 2019. Extreme conditions in the Bering Sea (2017–2018): record-breaking low sea-ice extent. Geophys. Res. Lett. 46, 8952–8959. https://doi.org/10.1029/2019GL083816

Stabeno, P.J., Bell, S.W., Bond, N.A., Kimmel, D.G., Mordy, C.W., Sullivan, M.E., 2019. Distributed Biological Observatory Region 1: Physics, chemistry and plankton in the northern Bering Sea. Deep. Res. Part II Top. Stud. Oceanogr. 162, 8–21. https://doi.org/10.1016/j.dsr2.2018.11.006

Stabeno, P.J., Danielson, S., Kachel, D., Kachel, N.B., Mordy, C.W., 2016. Currents and transport on the Eastern Bering Sea shelf: An integration of over 20 years of data. Deep Sea Res. Part II Top. Stud. Oceanogr. 134, 13–29. https://doi.org/10.1016/j.dsr2.2016.05.010

Stabeno, P.J., Duffy-Anderson, J.T., Eisner, L.B., Farley, E. V., Heintz, R.A., Mordy, C.W., 2017. Return of warm conditions in the southeastern Bering Sea: Physics to fluorescence. PLoS One 12, 1–16. https://doi.org/10.1371/journal.pone.0185464

Stabeno, P.J., Farley, E. V., Kachel, N.B., Moore, S., Mordy, C.W., Napp, J.M., Overland, J.E., Pinchuk, A.I., Sigler, M.F., 2012a. A comparison of the physics of the northern and southern shelves of the eastern Bering Sea and some implications for the ecosystem. Deep. Res. Part II Top. Stud. Oceanogr. 65–70, 14–30. https://doi.org/10.1016/j.dsr2.2012.02.019

Stabeno, P.J., Kachel, N., Mordy, C., Righi, D., Salo, S., 2008. An examination of the physical variability around the Pribilof Islands in 2004. Deep. Res. Part II Top. Stud. Oceanogr. 55, 1701–1716. https://doi.org/10.1016/j.dsr2.2008.03.006

Stabeno, P.J., Kachel, N.B., Moore, S.E., Napp, J.M., Sigler, M., Yamaguchi, A., Zerbini, A.N., 2012b. Comparison of warm and cold years on the southeastern Bering Sea shelf and some implications for the ecosystem. Deep. Res. Part II Top. Stud. Oceanogr. 65–70, 31–45. https://doi.org/10.1016/j.dsr2.2012.02.020

Stauffer, G., 2004. NOAA protocols for groundfish bottom-trawl surveys of the Nation's fishery resources. United States Department of Commerce, NOAA Technical Memorandum NMFS-F/SPO-65, 205 p.

Teo, S., Kudela, R., Rais, A., Perle, C., Costa, D., Block, B., 2009. Estimating chlorophyll profiles from electronic tags deployed on pelagic animals. Aquat. Biol. 5, 195–207. https://doi.org/10.3354/ab00152

Tolvanen, H., Suominen, T., Kalliola, R., 2013. Annual and long-term water transparency variations and the consequent seafloor illumination dynamics in the Baltic Sea archipelago coast of SW Finland. Boreal Environ. Res. 18, 446–458.

Utne, A., 1997. The effect of turbidity and illumination on the reaction distance and search time of the marine planktivore *Gobiusculus flavescens*. J. Fish Biol. 50, 926–938. https://doi.org/10.1111/j.1095-8649.1997.tb01619.x

Vacquié-Garcia, J., Mallefet, J., Bailleul, F., Picard, B., Guinet, C., 2017. Marine bioluminescence: measurement by a classical light sensor and related foraging behavior of a deep diving predator. Photochem. Photobiol. 93, 1312–1319. https://doi.org/10.1111/php.12776

Wernand, M.R., van der Woerd, H.J., Gieskes, W.W.C., 2013. Trends in ocean colour and chlorophyll concentration from 1889 to 2000, worldwide. PLoS One 8, e63766. https://doi.org/10.1371/journal.pone.0063766

Wilberg, M.J., Thorson, J.T., Linton, B.C., Berkson, J., 2009. Incorporating time-varying catchability into population dynamic stock assessment models. Rev. Fish. Sci. 18, 7–24. https://doi.org/10.1080/10641260903294647

Zaneveld, J.R. V., Barnard, A.H., Boss, E., 2005. Theoretical derivation of the depth average of remotely sensed optical parameters. Opt. Express 13, 9052–9061. https://doi.org/10.1364/opex.13.009052

Table 2.1. Performance metrics and slope for the regression between archival tag $K_d(z_s, \lambda_{tag})$ and OC-CCI $K_d(z_s, 490)$.

Performance metrics are the coefficient of determination (r^2), mean relative error (MRE), root mean square log error (RMSLE), and mean absolute error (MAE). Also shown are the fitted mean regression slopes and sample sizes (n).

Metric	Value
r^2	0.49
MRE (%)	23.3
RMSLE	0.227
MAE	1.254
Slope	0.72
n	351

Table 2.2. Estimated slopes (mean ± 2 standard errors) of linear mixed effects models between year (predictor) and $Z_{10\%}$, $Z_{1\%}$, and $\zeta(z_{max}, \lambda_{tag})$, where stations were included as a random effect.

Response	Slope (year^{-1})
$Z_{10\%}$	-0.14 ± 0.03
$Z_{1\%}$	-0.21 ± 0.05
$\zeta(z_{max}, \lambda_{tag})$	0.035 ± 0.008

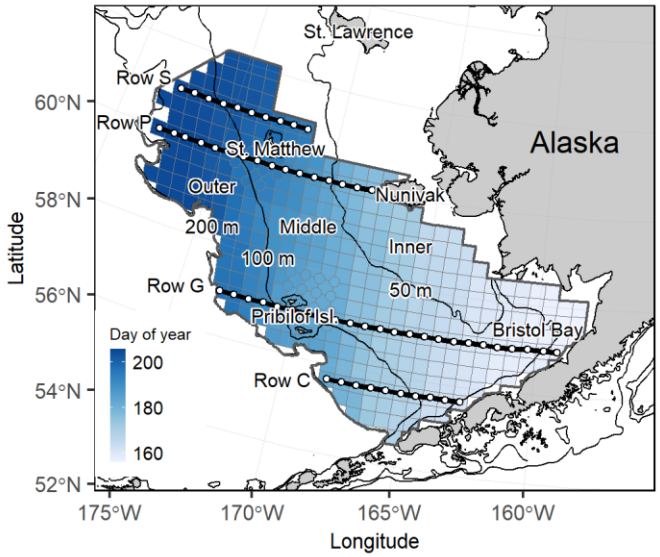

Figure 2.1. Eastern Bering Sea bottom trawl survey area.

Fill color showing the average sampling day of year during 2004–2018 for each of the 376 survey grid stations. Thick black lines and white points denote the location of shelf-wide cross-sections and stations highlighted in analyses of the vertical structure of the water column. Inner (0–50 m bottom depth), middle (50–100 m), and outer (100–180 m) domains are shown.

Figure 2.2. Archival tag assembly.

Archival tag affixed to polyurethane base plate assembly with shackles at the forward corners.

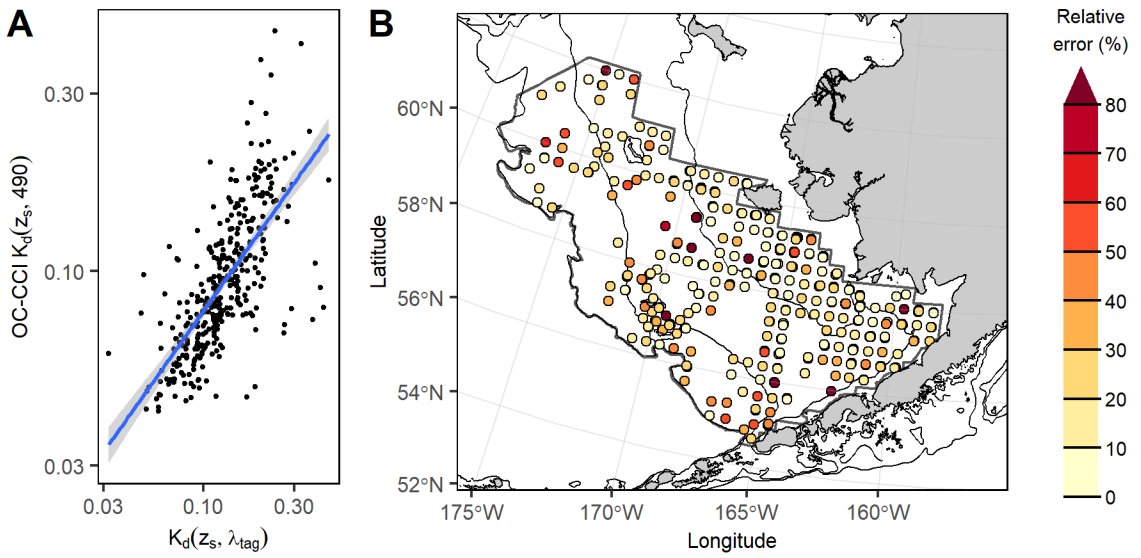

Figure 2.3. Surface-weighted archival tag $K_d(z_s, \lambda_{tag})$ versus OC-CCI $K_d(z_s, 490)$.

Panels show: (A) Linear regression model fit between log10-transformed $K_d(z_s, \lambda_{tag})$ and log-transformed OC-CCI $K_d(z_s, 490)$, shown by the solid blue line and shaded area (mean ± 2 standard errors); (B) Relative error (%) of regression fit over space, based on an absolute scale. See Table 1 for regression performance metrics.

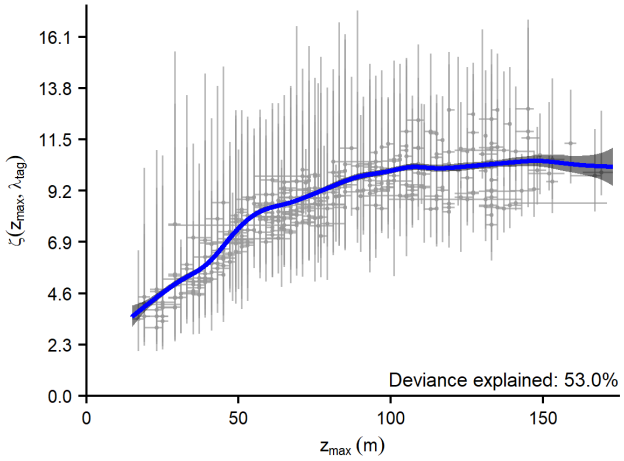

Figure 2.4. Depth versus optical depth.

Maximum profile depth (z_{max}, λ_{tag}) versus near-bottom optical depth $\zeta(z_{max},, \lambda_{tag})$ from 2004–2018. Points denote station median, vertical and horizontal bars denote the range. Generalized additive model fit shown by solid blue line and shaded area (mean ± 2 std. err.). GAM deviance explained: 53.0%.

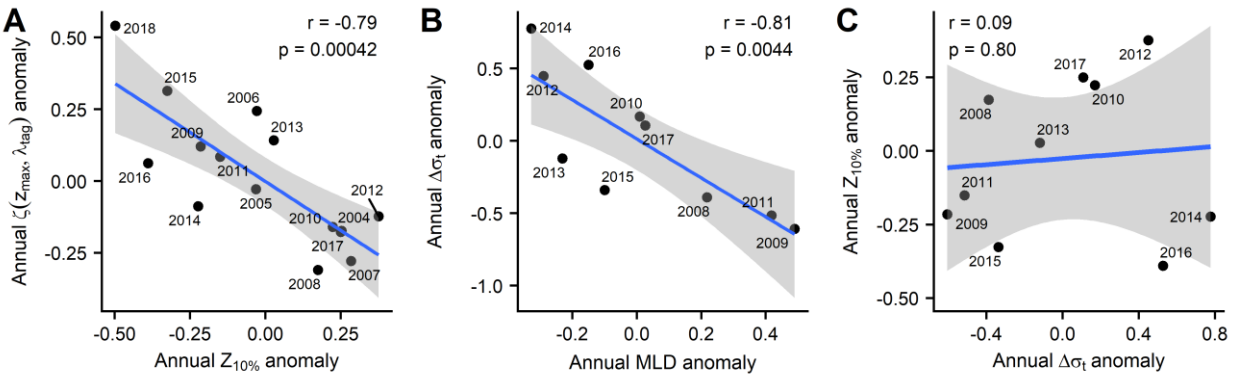

Figure 2.5. Anomaly index correlations.

Relationships between anomaly indices for (A) $Z_{10\%}$ versus $\zeta(z_{max}, \lambda_{tag})$ from 2004–2018, (B) mixed layer depth versus $\Delta\sigma_t$ from 2008–2017, (C) $\Delta\sigma_t$ versus $Z_{10\%}$ from 2008–2017. Solid blue line and shading denote the linear regression fitted-mean ± two standard errors. The Pearson correlation coefficient (r) and p-value are shown on each panel.

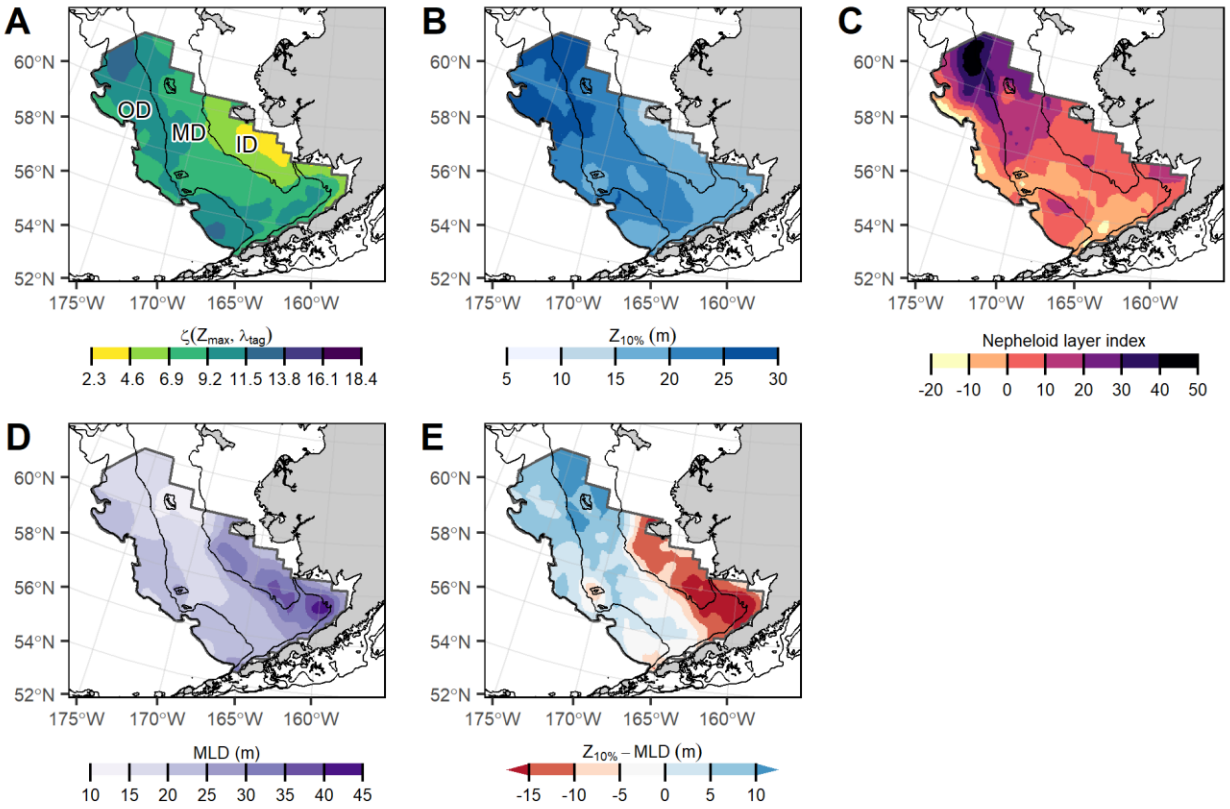

Figure 2.6. Maps of average optical depth $Z_{10\%}$, nepheloid layer index, mixed layer depth (MLD), $Z_{10\%}$-MLD.

Means of (A) near-bottom optical depth, $\zeta(z_{max}, \lambda_{tag})$, for 2004–2018, (B) depth of the 10% irradiance, $Z_{10\%}$, for 2004–2018, (C) nepheloid layer index (NLI) for 2004–2018, (D) mixed layer depth for 2008–2017, (E) depth of $Z_{10\%}$ minus mixed layer depth for 2008–2017. Text labels in panel A denote the Inner (ID), Middle (MD), and Outer (OD) domains.

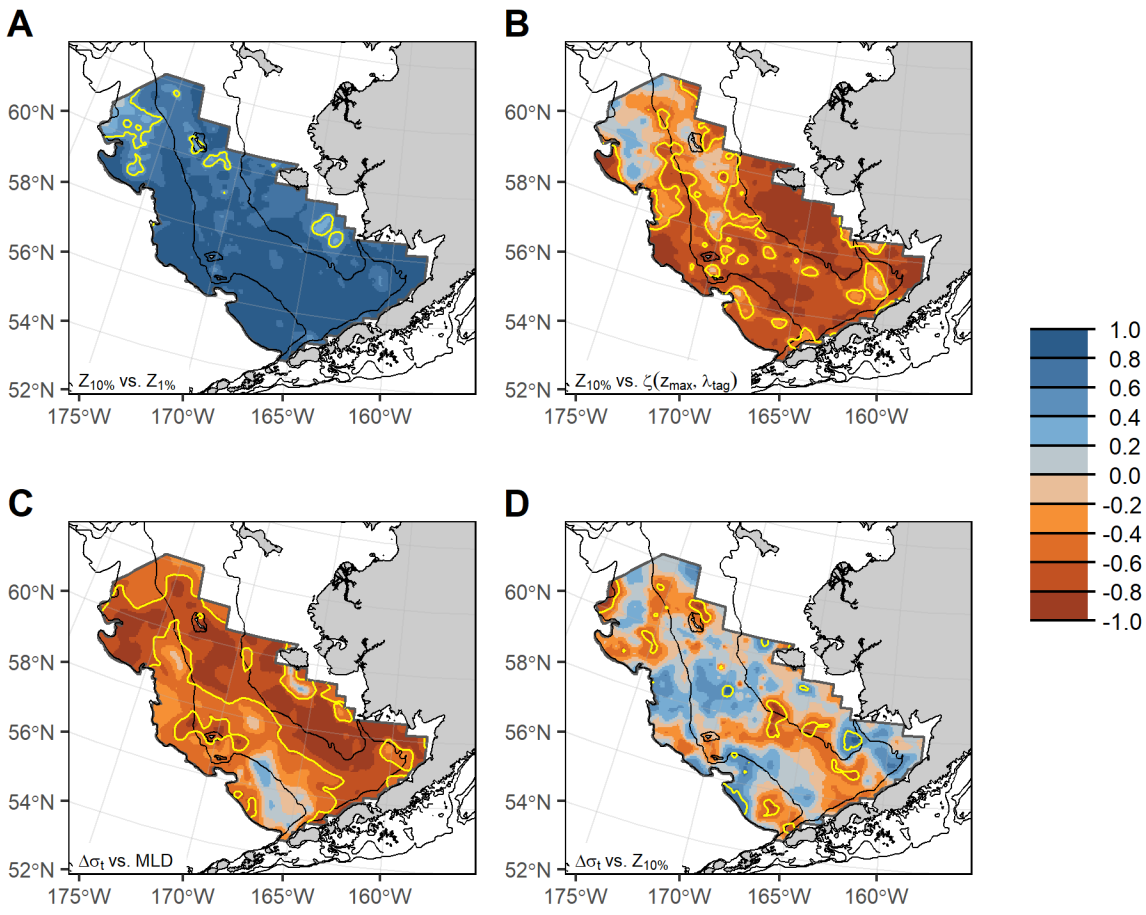

Figure 2.7. Pearson correlation coefficients (r).

Panels show: (A) $Z_{10\%}$ versus $Z_{1\%}$ for 2004–2018; (B) $Z_{10\%}$ versus $\zeta(z_{max}, \lambda_{tag})$ for 2004–2018; (C) $\Delta\sigma_t$ versus mixed-layer depth for 2007–2017; (D) $\Delta\sigma_t$ versus $Z_{10\%}$ for 2007–2017. Yellow contour lines denote the areas with a non-zero correlation at the $\alpha = 0.05$ significance level.

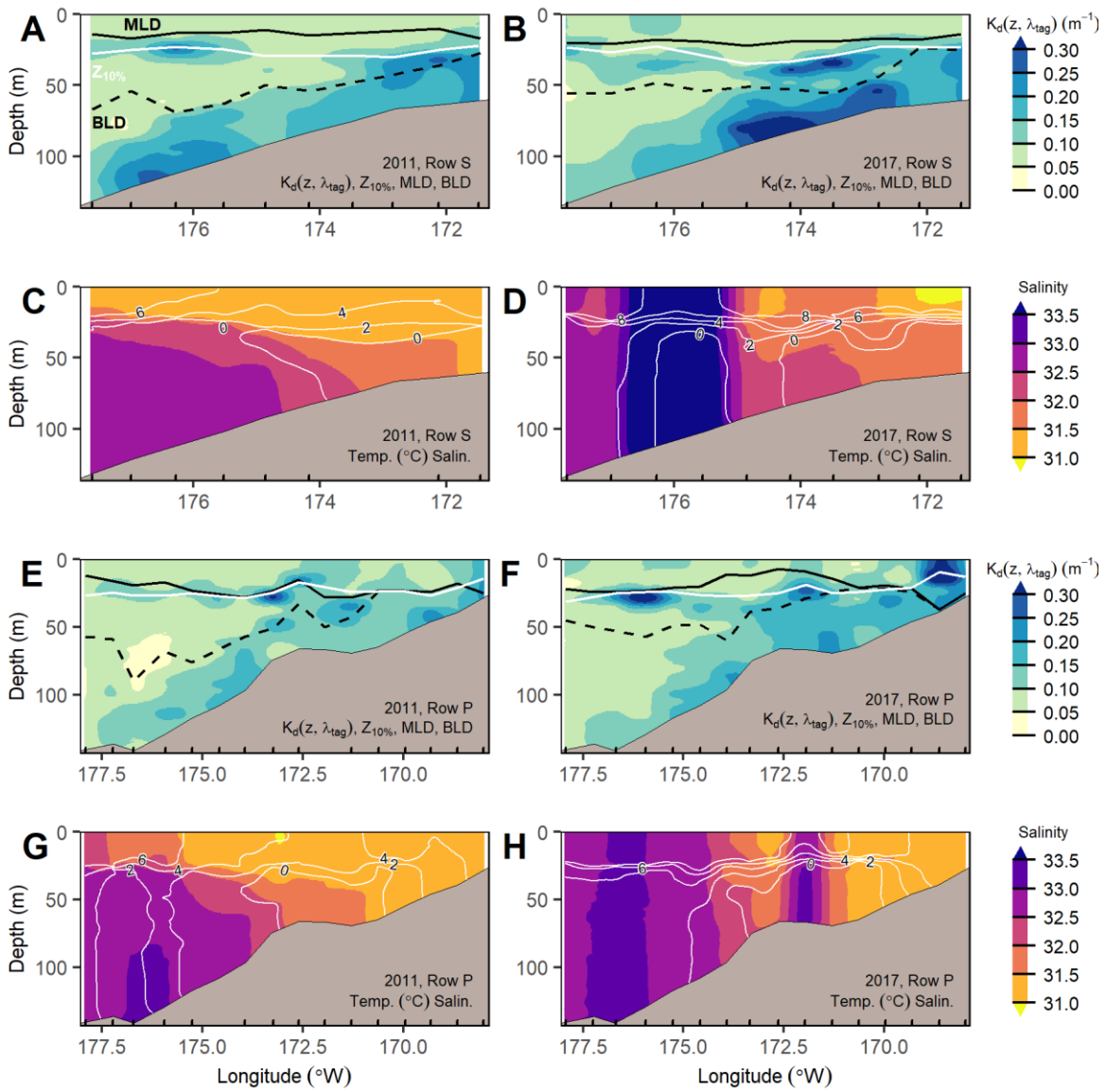

Figure 2.8. Cross-shelf profiles of optical and physical variables for rows S and P during 2011 and 2017.

Panels show: (A, B, E, F) the vertical attenuation coefficient (color), mixed layer depth (MLD; solid black line), bottom layer depth (BLD; dashed black line), $Z_{10\%}$ (solid white line); (C, D, G, H) salinity (color) and temperature (white lines). Ticks along the horizontal axis denote sample locations for optical and physical variables that were obtained using archival tags and CTDs, respectively. Row S was sampled from 7/18–7/21 in 2011 and 7/23–7/30 in 2017; row P was sampled from 7/3–7/23 in 2011 and 6/30–7/29 in 2017.

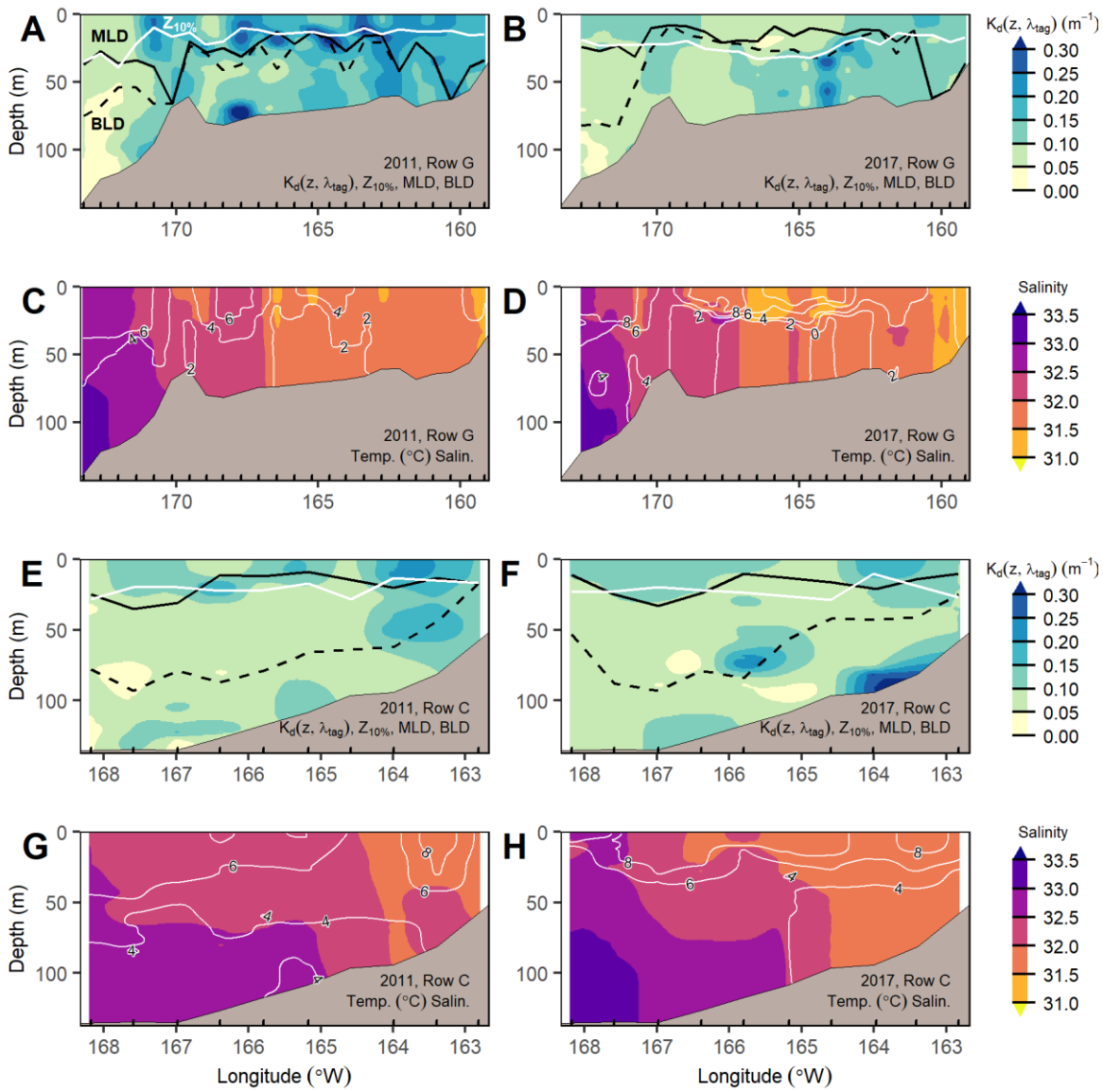

Figure 2.9. Cross-shelf profiles of optical and physical water column structure for rows G and C during 2011 and 2017.

Panels show: (A, B, E, F) the vertical attenuation coefficient (color), mixed layer depth (MLD; solid black line), bottom layer depth (BLD; dashed black line), $Z_{10\%}$ (solid white line); (C, D, G, H,) salinity (color) and temperature (white lines). Ticks along the horizontal axis denote sample locations for optical and physical variables that were obtained using archival tags and CTDs, respectively. Row C was sampled from 6/10–7/14 in 2011 and 6/10–7/1 in 2017; row G was sampled from 6/5–7/15 in 2011 and 6/4–7/18 in 2017.

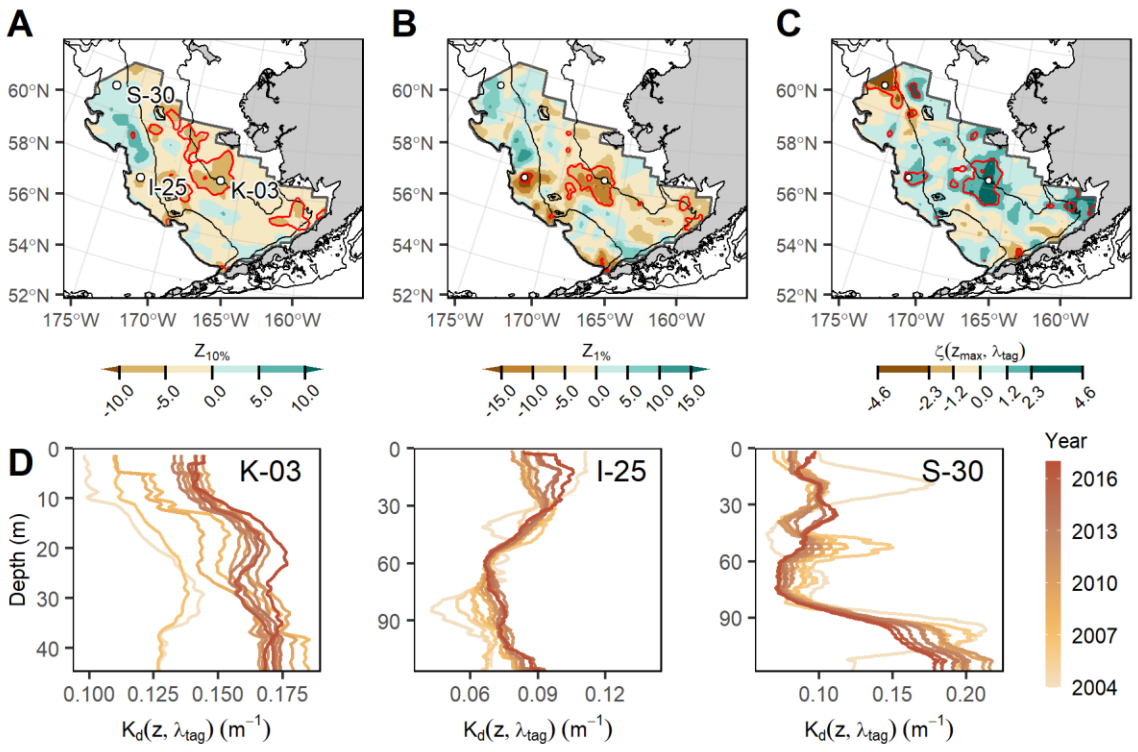

Figure 2.10. Change in $Z_{10\%}$, $Z_{1\%}$, and $\zeta(Z_{max}, \lambda_{tag})$ between 2004 and 2018.

Panels show change in (A) $Z_{10\%}$, (B) $Z_{1\%}$, (C) $\zeta(Z_{max}, \lambda_{tag})$ between 2004 and 2018 based on the mean of pixel-wise linear regression on annual raster surfaces. Red contours denote areas where the regression slope was non-zero at the $\alpha = 0.05$ level and points denote locations of stations for Panel D. Panel D shows the cumulative moving average of the vertical attenuation coefficient for stations K-03, I-25, and S-30 from 2004–2018, where line color denotes the year of the average.

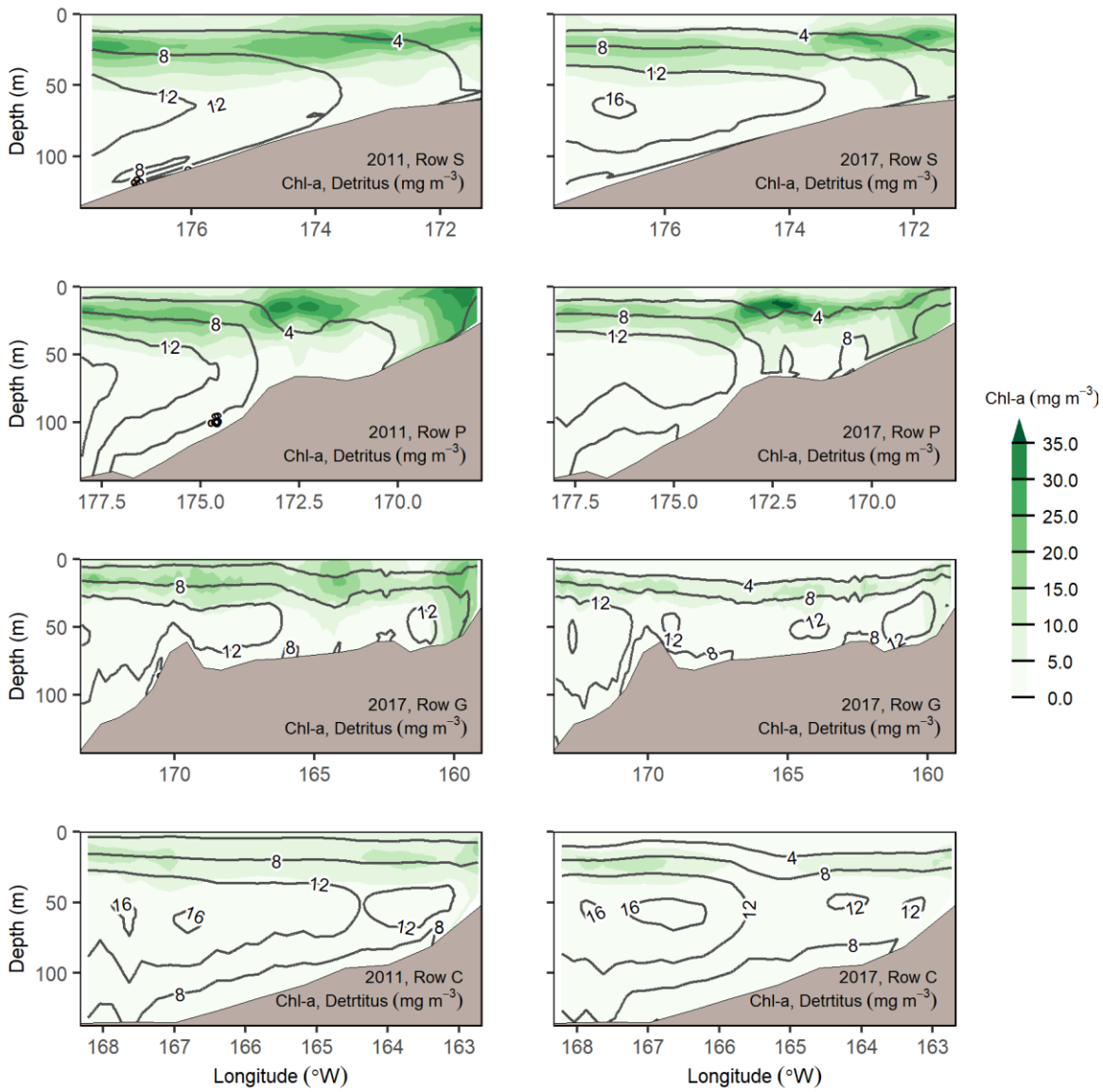

Figure 2.11. Modeled (Bering10K-BESTNPZ) concentrations of chlorophyll-a (mg m^{-3}) and detrital carbon (mg m^{-3}) along rows C, G, P, and S during June–July of 2011 and 2017.

Fill color shows chlorophyll-a, contour lines show detrital carbon. Bottom depth follows trawl survey bathymetry rather than model bathymetry.

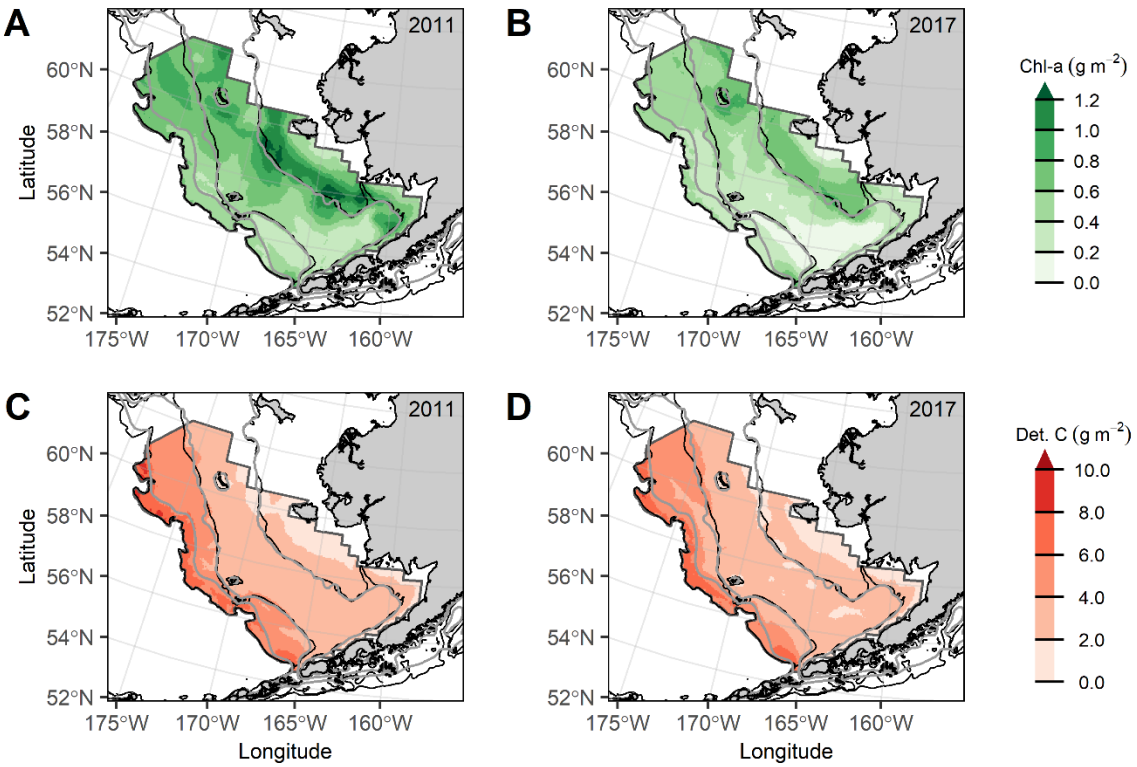

Figure 2.12. Modeled (Bering10K-BESTNPZ) depth-integrated chlorophyll-a (g m^{-2}) and detrital carbon (g m^{-2}) in the eastern Bering Sea during June–July 2011 and 2017.

Black bathymetric contour lines show presumed survey bathymetry, grey lines show bathymetry used in the Bering10K-BESTNPZ model.

Chapter 3. LIGHT MEDIATED CHANGES IN CATCHABILITY DUE TO POLEWARD RANGE EXPANSION OF FISH STOCKS[4]

3.1 ABSTRACT

In recent years, unprecedented warm conditions in the Pacific Arctic and subarctic have facilitated a rapid poleward range expansion of subarctic fish stocks in the Bering and Chukchi Seas, thereby changing the light environment where fisheries and fishery-independent surveys encounter the stocks. The range expansion is likely to affect the catchability of fisheries and fishery-independent surveys because fishing gears exploit visually mediated behaviors of fish in the capture process. However, there is little understanding of how the changing light environment will affect catchability of subarctic stocks relative to catchability their historical range. In this study, we sought to improve understanding of how poleward range expansion will affect catchability by simulating catchability of fishery-independent bottom trawl and acoustic surveys and bottom trawl fisheries in the Pacific Arctic and subarctic. We ask how catchability varies over space and time due to (1) variation in bottom trawl gear efficiency caused by spatial-temporal variation in visual herding of demersal fishes, and (2) variation in the availability of a vertically migrating semi-pelagic species, walleye pollock (*Gadus chalcogrammus*), to bottom trawl and acoustic surveys due to light-and-depth-dependent variation in vertical distribution. Our results show pronounced latitudinal and seasonal variability in catchability (e.g., high bottom trawl gear efficiency at high latitude during summer and low gear efficiency during winter), and that water clarity and regional

[4] This work will be resubmitted. Co-authors: S. Kotwicki, L.A.K. Barnett, T.E. Essington, D.A. Beauchamp, J.K. Nielsen, S.F. McDermott, L.L. Britt

bathymetry strongly influence catchability, including within-day gear efficiency of bottom trawl surveys. Our findings suggest that catch standardization may be warranted to mitigate potential biases in stock assessments as subarctic stocks expand poleward.

3.2 INTRODUCTION

Unprecedented warming and a loss of sea ice in the Arctic have facilitated a rapid northward range expansion of subarctic fish stocks (Fossheim et al., 2015; O'Leary et al., 2020; Orlov et al., 2019; Spies et al., 2020; Stevenson & Lauth, 2019). Fisheries for historically subarctic stocks are being prosecuted at latitudes well north of historical fishing grounds and stock assessment boundaries (e.g., Thompson & Thorson, 2019). These shifts require a spatial expansion of stock boundaries and stock assessment. However, given the spatial-temporal patterns in underlying environmental conditions that govern the catchability (i.e. the relationship between catch and true abundance) of fish, an expansion may need to account for non-stationary catchability to more accurately interpret fishery-independent survey and fishery data that are inputs to fisheries stock assessment (Link et al., 2011). Failure to detect and account for emergent bias and uncertainty in data sources may result in fisheries stock assessments becoming less reliable over time.

One way a poleward range expansion may contribute to bias and uncertainty in stock assessment is by changing the visual environment (light and water clarity) where fish are encountered by fisheries and fishery-independent surveys. Fishing gears exploit visual behaviors of fish in the capture process so changes in the visual environment can cause non-stationary variation in catchability (Glass & Wardle, 1989; Kotwicki et al., 2009, 2015, 2018; Ryer et al., 2010). Near the Arctic, there is extreme seasonal and latitudinal variation in day length, ranging from 24-hour daylight during summer to 24-hour night during winter. Thus, at Arctic latitudes,

visual interactions between fish and fishing gear are likely to differ from interaction at lower latitudes. This may be exacerbated by spatial variation in bathymetry and spatial-temporal variation in water clarity, including ongoing changes in water clarity that have been linked to climate-driven shifts in primary production in the subarctic and Arctic (Lewis et al., 2020; Lomas et al., 2020).

Vision mediates interactions between fish and fishing gear in many ways. Many fish species exhibit an ordered herding behavior in response to visual detection of trawl gear that entails swimming away from the gear in an effort to outrun it (e.g., Blaxter & Parrish, 1964; Glass & Wardle, 1989). To exploit this behavior, some commercial trawl gear designs aim to maximize herding. For example, commercial bottom trawls for flatfish often use long sweeps/bridles to herd fish into the path of a much smaller net. Other visual behaviors that influence the catch process include the innate use of visual cues to form schools that are targeted by fisheries (e.g., Glass et al., 1986) and light-mediated vertical migration that can affect the availability of fishes to different gears at different times (e.g., mid-water trawls and acoustics versus bottom trawls; Gauthier & Rose, 2005; Kotwicki et al., 2009).

From a stock assessment perspective, changes in the visual environment affect catchability, q, the parameter that relates an abundance index, I, to true abundance, N, as $I = qN$ (derived from fishery or fishery-independent survey data). Temporal trends in catchability can lead to bias fishery and fishery-independent abundance indices (Maunder & Punt, 2004; Wilberg et al., 2009). Also, some stock assessments that use abundance indices from fishery-independent surveys use fishery catch and effort data as a qualitative ‘check’ on survey inputs and assessment outcomes (e.g., Ianelli et al., 2019). Thus, changes in fishery catchability may cause historical relationships between fishery and fishery-independent survey data to change through time, thereby affecting the

reliability of the qualitative check. Overall, abundance indices the most important data source for fisheries stock assessment so it is critical that they accurately track changes in true population size over time.

To minimize visually mediated variation in catchability, many fishery-independent stock assessment surveys use sampling schemes that aim to minimize variation in the visual environment, such as sampling only during daylight hours (Stauffer, 2004). However, when sampling design does not adequately mitigate variation in the visual environment, post hoc catch standardization can sometimes account for light driven variation in catchability (e.g., Addison et al., 2003; Kotwicki et al., 2018). Understanding how interactions between the visual environment, fish distribution, and behavior affect catchability can help to guide efforts to account for catchability variation in fisheries stock assessment via sampling design or post hoc catch standardization.

The continental shelf of the Bering and Chukchi Seas, a region spanning territorial waters of the United States and Russia (Fig. 3.1A), has recently undergone substantial poleward range expansion of subarctic stocks. Historically, the presence of substantial seasonal sea ice during winter and spring has resulted in bottom temperatures < 2 °C across much of the continental shelf during summer and fall that has served as a barrier to northward migration of subarctic demersal fish stocks (Wyllie-Echeverria & Wooster, 1998). In 2018–2019, however, unprecedented low seasonal sea-ice extent (Fig. 3.1B) resulted in unusually warm bottom temperatures during summer, which facilitated a rapid northward range expansion of subarctic stocks. Recent United States bottom trawl surveys of the eastern Bering Sea (EBS) found northward range shifts of several subarctic stocks on the continental shelf of the EBS (Fig. 3.1C; Fig. S1) and an August 2019 Russian bottom trawl and acoustic survey reported an estimated biomass of 890,000 tons (t)

of walleye pollock (*Gadus chalcogrammus*) in a 229,200 km^2 area of the western Chukchi Sea, including high densities of large walleye pollock (≥ 40 cm) in the vicinity of Wrangell Island, Russia (Orlov et al., 2019; Vasilyev & Datsky, 2020). In 2020, a new Russian fishery for walleye pollock began in the western Chukchi Sea with a total allowable catch set at 68,000 t (Vasilyev & Datsky, 2020). Given that climate driven sea ice projections predict that sea ice duration will continue to decrease in the region through the middle of the 21st century—by up to 60 days in the Chukchi Sea (Wang et al., 2018)—recent range expansions may be a harbinger of future conditions.

The availability of walleye pollock to fishery-independent bottom trawl and acoustic surveys is influenced by light and bottom depth in the southeastern Bering Sea (SEBS). During the day, the vertical availability of walleye pollock to bottom trawl gear is higher when it is brighter near-bottom and availability to acoustic sampling is higher when it is darker because light influences patterns of vertical migration and distribution (Kotwicki et al., 2009, 2015, 2018). Walleye pollock availability to bottom trawl gear is higher in shallow areas and availability to acoustic gear is higher in deep areas (Kotwicki et al., 2009, 2015, 2018; Monnahan et al., *In review*). These factors suggest catchability will be influenced by changes in light and bathymetry where walleye pollock are encountered by fisheries-independent bottom trawl and acoustic surveys.

Visual herding appears to play a key role in the bottom trawl catchability of abundant flatfish stocks in the EBS (Table 3.1). Herding by bottom trawl bridles accounts for 25–49% of NOAA bottom trawl survey catch of EBS flatfishes (Table 3.1; Somerton et al., 2007; Somerton & Munro, 2001) and more in commercial flatfish trawl gears that have long bridles (Gibson et al., 2015; Ryer et al., 2010). Flatfish catch rates in bottom trawls are generally higher during daylight

hours and visual herding is considered to a key driver of the diel variation (Gibson et al., 2015; Ryer et al., 2010; Table 3.1). The proportion of bottom trawl catch attributed to herding varies by species and gear type (Godø, 1994; references in Table 3.1).

Considering the light-dependent catchability of subarctic fishes and fishing fleet composition in the Bering Sea, it is likely that poleward shifts in fish distribution and fishing effort would change fisheries catchability. Among the eight most abundant groundfish species in the EBS, six show evidence of light-dependent variation in catchability in bottom trawls, including all of the flatfishes (Table 3.1; Family: Pleuronectidae). Meanwhile, a substantial proportion of the groundfish fleet within the United States and Russian exclusive economic zones of the Bering Sea is comprised of catch-processor vessels that are capable of fishing 24 hours/day, travelling far from port, and spending >200 days per year at sea (Fissel et al., 2019). From 2014–2018 in the Bering Sea-Aleutian Islands region of the U.S. Exclusive Economic Zone, 57.6% of total groundfish landings were attributed to the catcher-processor fleet, including 93.7% of flatfish landings (Fissel et al., 2019). Combined, these factors suggest that fishing fleets in the region can to reallocate fishing effort to adapt to changes in fish distribution and that fishery catchability for abundant groundfish would change if fish and fisheries expand poleward into a new light regime. However, the effect that fishery distribution shift would have on catchability has not been examined.

In this study, we conduct simulations to evaluate how a northward range expansion of subarctic stocks is likely to affect the catchability of demersal and semi-pelagic fish in the Pacific Sector of the subarctic and Arctic. Specifically, we ask how catchability varies seasonally and spatially due to the influences of seasonal light regime, water clarity, and bathymetry on behavioral interactions between fish and bottom trawl and acoustic gears. Scenarios for the simulations focus on fishery-independent bottom trawl and acoustic surveys and bottom trawl fisheries. Behaviors

in the simulations are the visual herding behavior of demersal fish by bottom trawl gear that affects gear efficiency and the light-mediated vertical migration of a semi-pelagic fish (walleye pollock) that affects availability to bottom trawl and acoustic sampling. Simulated behaviors were intended to be characteristic of demersal flatfishes and walleye pollock (semi-pelagic) from our study region. We use insights from the simulations to suggest potential ways to account for latitudinal variation in catchability in fisheries stock assessment.

3.3 METHODS

3.3.1 *Study area*

Our study area is the continental shelves (10–200 m bottom depth) of the Bering and Chukchi Seas near Bering Strait (66°30′N 169°0′W), the ~82 km wide and <55 m deep ocean pass connecting the Pacific Ocean to the Arctic Ocean (Fig. 3.1A). The western Bering Sea (WBS) and southeastern Bering Sea (SEBS) are, on average, deeper than the northern Bering Sea (NBS) and Chukchi Sea. The region has extreme latitudinal and seasonal variation in day length (Fig 3.1D).

Seasonal sea ice has historically covered parts of the Bering Sea for around five months per year and the Chukchi Sea for 7–10 months per year (Wang et al., 2018). The maximum sea ice extent typically occurs in March–April (Stabeno & Bell, 2019). As solar heating increases and seasonal sea ice melts, the mixed layer warms and cold water remains in the bottom layer (Stabeno et al., 2012). In the EBS, the remnant ‘cold pool’ (bottom temperatures <2 °C) serves as a barrier to migration for subarctic species (Stabeno et al., 2019; Wyllie-Echeverria & Wooster, 1998). Anomalously warm ocean conditions and southerly winds resulted in extremely low sea-ice extent during 2018 and 2019 (Stabeno & Bell, 2019; Fig. 3.1B).

3.3.2 *Model framework*

We developed a framework of interconnected models to simulate spatial-temporal variation in catchability throughout the study area (Fig. 3.2) based on bottom depth, sea-ice extent data, and a statistical model of water clarity, combined with a model of surface light and three light-dependent catchability models. Components of the framework are described in subsections 2.2.1–2.2.4.

3.3.2.1 Bathymetry and sea-ice extent

We used the 1-km nominal grid Arctic Region Digital Elevation Model (ARDEM) version 2.0 for bottom depth for spatial-temporally explicit catchability simulations (Danielson et al., 2015). We limited simulations to the continental shelf (10–200 m). For sea-ice extent, we used 4 km resolution daily Multisensor Analyzed Sea Ice Extent – Northern Hemisphere (MASIE-NH), version 1 data for October 2018–September 2019 from the National Snow & Ice Data Center (NSIDC) (U.S. National Ice Center and National Snow and Ice Data Center).

3.3.2.2 Optical depth (water clarity) model

We simulated water clarity using optical depth models based on water clarity information derived from light data collected during NOAA bottom trawl surveys of the EBS and NBS continental shelves from summers (May–August) 2004–2019. Optical depth, $\zeta(z)$, is a dimensionless ratio that characterizes the relative transmission of light from just below the surface to depth z (in units of m). The light measurements used to calculate optical depth were collected using archival tags equipped with blue-filtered photodiodes that were mounted to the top panel of

the bottom trawl gear. An algorithm was used to quality check light data, filter signal from noise, and calculate optical depth (Rohan et al. 2020). Optical depth, $\zeta(z)$, is calculated based on the Beer-Lambert equation which characterizes the attenuation of light passing through water, as

$$E_d(z) = E_d(0^-)e^{-K_d z},$$

where $E_d(Z)$ is diffuse downwelling irradiance at depth z (μMol photons m^{-2} s^{-1}), $E_d(0^-)$ is diffuse downwelling irradiance just beneath the sea surface (μMol photons m^{-2} s^{-1}), and K_d is the diffuse attenuation coefficient (m^{-1}), the rate at which light decreases with depth. Optical depth is defined as

$$\zeta(z) = \ln\big(E_d(0^-)\big) - \ln\big(E_d(z)\big),$$

which is equivalent to

$$\zeta(z) = K_d z.$$

Higher values of optical depth correspond with darker conditions. Increments of 2.303 in optical depth correspond with an order-of-magnitude change in light.

We fitted statistical models between depth and optical depth and used the models as a basis to simulate bottom light under a representative range of variation in water clarity. The statistical models we fitted were quantile generalized additive models (QGAM) of the form:

$$\log(\zeta(z_{max})_i) \sim \alpha + s\big(z_{max,i}\big) + \varepsilon \quad \varepsilon \sim N(0, \sigma^2),$$

where $\zeta(z_{max})_i$ is optical depth for the maximum depth sampled, z_{max}, during cast i, α is the intercept, $s(z_{max},i)$ is a penalized cubic regression spline with a maximum of 10 knots, and ε is a normally distributed error. The log-transformation of $\zeta(z_{max})_i$ was to ensure a positive response. The QGAM models were fitted to the 25%, 50%, and 75% quantiles of optical depth using the R package *qgam* (Fasiolo et al., 2017). We used the fitted means of QGAM models to simulate bottom optical depth, $\zeta(z_{bot})$, on the continental shelf (Figs. S2–S3). By coincidence, the average ~2.3 difference in

optical depth between the 25% and 75% quantiles corresponds with an approximately an order-of-magnitude difference in light at a given depth.

3.3.2.3 Surface and bottom light

We simulated downwelling irradiance at the sea surface, $E_d(0^+)$, using a solar and lunar illuminance model (Janiczek & DeYoung, 1987) that we programmed in R. The Janiczek and DeYoung (1987) model requires specifying cloud cover conditions, which we selected to be 'sun or moon obscured by thin clouds' (i.e. sky condition = 2). The output of the Janiczek and DeYoung (1987) model is in units of lux, a photometric quantity. We converted to lux to quantum units ($\mu Mol \cdot photons \cdot m^{-2} \cdot s^{-1}$) following Thimijan and Heins (1983) because quantum units are more useful for characterizing animal vision and have been used in vision experiments involving Alaska groundfishes (e.g., Olla et al., 2000). We also converted quantum units to archival tag integer units using the conversion equation from Kotwicki et al. (2009) to model availability in a manner consistent with previous availability studies (Kotwicki et al., 2015, 2018). Code for the Janiczek and DeYoung (1987) model and conversion functions are included in the R package *trawllight* (Rohan, 2020; Rohan et al., 2020).

We modeled the transmission of downwelling irradiance through the sea surface as

$$E_d(0^-) = E_d(0^+)(1 - \alpha),$$

where α is albedo. We set α = 0.06 which is representative of broadband surface albedo during daylight hours under overcast skies (Payne, 1972). Bottom downwelling irradiance, $E_d(z_{bot})$, was calculated using the Beer-Lambert equation, as

$$E_d(z_{bot}) = E_d(0^-)e^{-\zeta(z_{bot})}.$$

3.3.2.4 Catchability

We define catchability for a sample or haul as

$$q = \frac{C}{EN}, \tag{1}$$

where q is catchability, C is a measure of observed abundance such as catch, E is effort (e.g., area swept by a bottom trawl in hectares), N is true abundance (Godø, 1994). Extending our definition, catchability is the product of vertical availability (q_v), areal availability (q_a), and gear efficiency (q_e):

$$q = q_v q_a q_e. \tag{2}$$

Vertical availability and areal availability are the proportion of the stock that overlaps vertically and areally (i.e., horizontally) with the extent sampled by the gear, respectively (Francis et al., 2003; Godø, 1994). Gear efficiency is the proportion of a stock within sampling range of the gear (e.g., volume swept by a trawl) that is caught by the gear. In our framework, we consider variation in the vertical distribution of walleye pollock to affect vertical availability (q_v) and visual herding of a demersal stock to affect gear efficiency (q_e).

In this study, catchability was modeled as a proportion of maximum catchability ($0 \leq q \leq 1$) that would occur under 'optimal' conditions. We did not include effort-dependent catchability or the selectivity of different fishing gears that typically varies as a function of fish size due to differences in swimming ability or gear construction (e.g., trawl mesh size [Williams et al., 2011]). We did not include any size structure in our simulations so we did not model size selectivity.

3.3.2.4.1 Bottom trawl herding model

We simulated the effect of visual herding on gear efficiency, q_e, based on a generic herding relationship that characterizes the proportion of fish exhibiting herding behavior in response to a simulated trawl as a function of light (Blaxter & Parrish, 1964, 1966). The function was

$$p = b + \frac{hE_d}{E_{50} + E_d}, \tag{3}$$

where p is the proportion of fish in the path of the gear that herd, b is the herding proportion in complete darkness, h is the visually herding proportion, E_d is downwelling irradiance (μMol·photons·m^{-2}·s^{-1}), and E_{50} is the half-saturation light level that denotes the light level at 50% of the maximum herding response (μMol·photons·m^{-2}·s^{-1}). In real herding, terms b and h depend on the species and gear. Rather than modeling herding for a specific species/gear combination, we represent gear efficiency for the dynamic range of variation in gear efficiency, as:

$$q_e = \frac{E_d}{E_{50} + E_d}. \tag{4}$$

We set the half-saturation light level (E_{50}) to 10^{-4} μMol photons $m^{-2}s^{-1}$ based on ranges from mesocosm visual herding and foraging experiments that have been conducted using EBS flatfishes (Table 3.1).

3.3.2.4.2 Bottom trawl and acoustic availability models

We simulated the effect of bottom depth and bottom light on the vertical availability of walleye pollock to bottom trawl, $q_{v,BT}$, and acoustic, $q_{v,A}$, sampling using beta regression models fitted to data from NOAA stock assessment surveys of the EBS. A description of the walleye pollock availability data and details of beta regression model fitting are provided in the Supplementary Materials (*Walleye pollock availability data and model fitting*).

3.3.3 *Scenarios*

We used the model to simulate catchability using scenarios designed to be representative of standardized fishery-independent surveys (Subsection 3.2.3.1) and scenarios designed to be broadly representative of bottom trawl fisheries (Subsection 3.2.3.2). All scenarios were limited to ice-free waters based on an understanding that subarctic fishes migrate to avoid sea ice (De Robertis & Cokelet, 2012) and because ice-covered seas are generally inaccessible to fishing. Ice cover was based on MASIE-NH data for October 2018–September 2019, a recent ice minimum period.

3.3.3.1 Standardized survey scenarios

We developed catchability scenarios intended to be representative of summer (May–September) bottom trawl surveys in the study region. NOAA bottom trawl surveys of the SEBS and NEBS operate from late May–late August. NOAA acoustic-trawl surveys for walleye pollock operate from June–August in the EBS. United States bottom trawl and acoustic surveys of the eastern Chukchi Sea were conducted during August–September 2012–2013 and Russian bottom trawl surveys of the western Chukchi Sea operate from August–September. Typically, NOAA bottom trawl surveys conduct 4–5 hauls per day and travel ~20 nmi between stations. Bottom trawl sampling is limited from 30 minutes after sunrise to 30 minutes before sunset (Stauffer, 2004). Scenarios focused on the first and second bottom trawl survey hauls of the day because the largest daily change in surface light conditions generally occurs between the first and second hauls. The first haul was 30 minutes after sunrise or 7:00 am Alaska Daylight Time (GMT-8), whichever was later. We used the 7:00 am start time constraint because the first haul typically starts from 6:30–

7:30 am Alaska Daylight Time if sunrise is very early. The second haul was 2.5 hours after the first haul. Scenarios were not spatially limited to survey sampling locations.

3.3.3.2 Bottom trawl fisheries scenarios

For bottom trawl fisheries scenarios, we examined gear efficiency at the 50% optical depth quantile throughout the year. We predicted hourly gear efficiency across latitudes (54°–74°N) at 50 m depth for 24 hour increments and calculated the mean catchability for each latitude and day. We also examined hourly spatial variation in catchability throughout the study area.

3.3.4 *Code and software*

We conducted the analysis using the R programming language (R Team, 2020) and code is available in an online GitHub repository (https://www.github.com/Sean-Rohan-NOAA/light-catchability).

3.4 RESULTS

3.4.1 *Standardized surveys*

Survey scenarios show that interactions between latitude (i.e., solar-lunar cycles), bottom depth, and water clarity (optical depth) strongly influence survey catchability. During the first bottom trawl haul of the day, gear efficiency (q_e) and bottom trawl vertical availability ($q_{v,BT}$) are higher in shallow areas (Fig. 3.3; Fig. S7A–B). Acoustic vertical availability ($q_{v,A}$) was negligibly higher in deeper areas during the first haul of the day (Fig. S7C–D). The model suggests variation in water clarity may cause substantial spatial variation in catchability by driving variation in

bottom light, as shown by differences in first haul (early morning) gear efficiency between 25% (Fig. 3.3A) and 75% (Fig. 3.3B) quantiles of optical depth on July 1 (assuming $E_{50} = 10^{-4}$ μMol photons m^{-2} s^{-1}). For the bottom trawl survey haul on July 1, bottom trawl availability of walleye pollock was up to 0.17 higher at the 25% quantile of optical depth than at the 75% quantile in deeper parts of the study area (Fig. S7A-B), while acoustic availability was only 0.02 lower (Fig. S7C-D).

NOAA bottom trawl surveys conduct multiple hauls per day and the results of our scenarios suggest there are notable differences in bottom trawl survey catchability between the first (early morning) and second (mid-morning) hauls because light levels are much higher for the second haul of the day. Gear efficiency and bottom trawl vertical availability are higher during the second haul of the day than the first haul (Fig. 3.4A–B). Acoustic availability is higher during the first haul of the day (Fig. S8). Deeper areas and lower water clarity are associated with larger differences in catchability between the first and second hauls in (Figs. 3.4A–B, S8).

The fishery-independent survey scenarios suggest there may be latitudinal variation in fishery-independent bottom trawl and acoustic survey catchability that changes seasonally, in large part due to sampling protocols. During mid-summer (June-July), for example, first haul gear efficiency and bottom trawl vertical availability are higher in the north (Figs. 3.4A–B), while acoustic vertical availability is higher in the south (Figs. S8). During mid-summer, the first haul of the day starts at 0700 AKDT across most of the area, rather than 30 minutes after sunrise. At 0700 AKDT during mid-summer, surface light is brighter towards the north due to the light regime (Fig. 3.1D). Consequently, gear efficiency and bottom trawl vertical availability are higher, and acoustic vertical availability is lower at high latitudes during mid-summer.

The light regime changes considerably from mid-summer to September, resulting in later haul start times and changes in the catchability differences between the first and second hauls of the day (Fig. 3.4A–B). At high latitudes, differences in gear efficiency between the first and second hauls are smallest during the summer solstice (June 20–22) and increase towards the spring and fall, as shown by gear efficiency at 75 m depth (Fig. 3.4A). At 54°N, differences are largest during the summer solstice and smallest during the fall. The same general pattern occurs in bottom trawl vertical availability of walleye pollock at 125 m (Fig. 3.4B), while the opposite pattern occurs for acoustic vertical availability (Fig. S8). Water clarity can have a greater effect on catchability than surface light, as shown by size of the differences between hauls one and two compared to differences in optical depth (Fig. 3.4B).

3.4.2 *Bottom trawl fisheries*

Bottom trawl fishery scenarios show that latitude and season have a large influence on gear efficiency. Averaged over a 24-hour day, daily mean gear efficiency is highest during mid-summer and lowest during winter, as shown by daily mean gear efficiency for 50 m depth at the 50% optical depth quantile (Fig. 3.5). Gear efficiency is highest in the north during mid-summer and lowest in the north during winter (Fig. 3.5). Across latitudes, daily mean gear efficiency was approximately equal in early March (March 13–15) and late September (September 27–29). The influence of latitude on gear efficiency is also evident when mapped over space and time. For example, at midnight local time on August 1 for the 50% optical depth quantile, gear efficiency south of 64°N is near zero but is much greater than zero across most of the Chukchi Sea (Fig. 3.6). By noon local time on August 1, gear efficiency is close to the maximum (one) throughout the study area (Fig. 3.6).

3.5 DISCUSSION

Our simulations indicate that latitude, bottom depth, and water clarity have a potentially strong influence on spatial-temporal patterns of catchability of subarctic fish stocks on the continental shelves of the Bering and Chukchi Seas. In survey scenarios, survey protocols contributed to non-stationary variation in catchability over space and time (season and within day). Survey gear efficiency and bottom trawl vertical availability were higher by the second haul of the day and acoustic vertical availability was lower, which reinforces earlier findings that variation in light drives within-day variation in the availability of walleye pollock to bottom trawl and acoustic surveys in the EBS (Kotwicki et al., 2009, 2013, 2015, 2018). However, there was much less variation in acoustic availability between hauls and optical depth quantiles than for the bottom-trawl availability of walleye pollock. In bottom trawl fishery scenarios, gear efficiency during mid-summer was higher in the north than the south, while the opposite was the case by mid-winter. The magnitude of variation in catchability across latitude and season suggests a poleward range shift of subarctic stocks may lead to bias and uncertainty in stock assessment due to a change in catchability over space and time.

Although we focused on the Pacific Sector of the subarctic and Arctic, the general patterns of latitudinal and seasonal variation in catchability may apply to many stocks, surveys, and management regions. Our simulations suggest that any fishery or survey that spans a reasonably large range of latitudes or seasons is prone to latitudinal and seasonal variation in catchability. Effects are likely to occur at high latitudes due to the extreme variation in day length, such as in the Barents Sea (68°–81° N) where climate-driven poleward shifts of boreal fish have occurred (Fossheim et al., 2015; Frainer et al., 2017).

Although numerous studies have found that season and light influence catchability (e.g., Arreguín-Sánchez, 1996; Kotwicki et al., 2009; Ryer et al., 2010), we are unaware of any studies that have mechanistically linked season and latitude to catchability across broad latitudinal and seasonal scales, either empirically or through simulation. We note, however, that empirical studies have found diel vertical migration patterns of Arctic-endemic species vary by season, latitude, and sea ice cover, presumably due to the influence light (e.g. Hobbs et al., 2018). Specifically, synchronized diel vertical migrations occur when there is diel variation in light and the extent of vertical migration depends on the magnitude of variation in light, which is a function of season, latitude, and sea ice thickness (e.g. Hobbs et al., 2018). Because vision mediates diel vertical migration and behaviors that affect catchability (including diel vertical migration), empirical evidence suggests that catchability at high latitude would follow latitudinal and seasonal patterns that are similar to patterns for diel vertical migration.

3.5.1 *Implications for fisheries stock assessment*

Our simulations suggest that the northward range expansion is increasing the vertical availability of walleye pollock to bottom trawl surveys relative to their historical range. Areas occupied by walleye pollock in the NBS and Chukchi Sea are much shallower than the SEBS and WBS (Fig. 3.1C, Fig. S1; Stevenson & Lauth, 2019), where our simulation predicts they will be more available to bottom trawl gear.

Conversely, acoustic-trawl surveys are likely to have a negative trend in catchability if surveys extend to higher latitude. On the SEBS shelf, standardized acoustic-trawl surveys for walleye pollock do not sample in shallow coastal areas (< 50 m) because walleye pollock are close to bottom during the day. The Chukchi Sea and NBS are relatively shallow south of 72° N, which

suggests walleye pollock are more likely to be close to the bottom during the day, in the bottom acoustic dead zone. However, factors other than bottom light and depth (e.g., temperature, current speed) also influence vertical distribution and availability of walleye pollock, as has been shown in the SEBS (Kotwicki et al., 2009, 2013, 2015, 2018). The role of life history stage in vertical distribution patterns may be a particular concern in the Chukchi Sea because Russian (TINRO) survey results suggest that walleye pollock in the Chukchi Sea are predominantly large (> 45 cm) fish (Vasilyev & Datsky, 2020) that tend to use near-bottom habitat during the day (Kotwicki et al., 2015).

It remains unclear if the poleward range expansion will cause a bias in fishery-independent bottom trawl survey catchability of demersal stocks. Our scenarios suggest that bottom trawl survey gear efficiency is non-stationary and that survey design influences catchability, although whether there is a bias depends on the spatial distribution of the stock, seasonal and daily timing of sampling, depth, and water clarity in addition to other life history and environmental characteristics. For example, across all latitudes, our scenarios show that gear efficiency for the first haul of the day at 75 m depth and 75% optical depth quantile is ~0.7 at some point from May–September (Fig. 3.4A). These results highlight the need to examine spatially varying catchability as a potential source of bias in model-based indices of abundance that are being used to account for range expansion of subarctic stocks, but tend to assume catchability is spatially stationary (e.g. Thompson and Thorson, 2019). Further investigation of survey timing is necessary to determine whether there is a likely to be a temporal bias in catchability.

Catch standardization or changes to survey sampling methods may be necessary to minimize temporal biases in indices of abundance that arise due to northward range expansion of subarctic stocks. Our simulations reinforce earlier findings that the current survey design has a

systematic bias where catchability is lower during the first haul of the day than subsequent hauls (Kotwicki et al., 2009), which likely increases uncertainty in abundance indices (i.e., increases abundance index variance). To reduce uncertainty, sampling could be limited to periods when surface solar irradiance is near its asymptotic daily maximum instead of using the 30-minute rule. Unfortunately, such a change would positively bias indices of abundance and would not account for other sources of variation in near-bottom light, such as seasonal light regime, water clarity, and meteorological conditions. As an alternative, in situ light measurements may be useful for standardizing catchability, as has been done for walleye pollock in the EBS (Kotwicki et al., 2009, 2013, 2015, 2018).

We developed the simulation framework for heuristic purposes and it should not be used for catch standardization without empirical validation of our assumptions. Even if our simulation framework provides a plausible representation for some species, it is not universally representative. Light can have a positive or negative effect on catchability depending on specific dynamics of behavioral interactions between a species and gear (Walsh & Hickey, 1993). For example, brighter conditions are associated with lower bottom trawl catchability of Pacific halibut, potentially due to net avoidance behavior (Ryer et al., 2010; Ryer & Barnett, 2006). We also did not consider body size, which can influence swimming speed and stamina, thereby affecting whether a fish outside of the trawl path of a net enters the mouth the trawl (e.g. Somerton & Munro, 2001). Finally, other environmental factors such as temperature may also affect catchability by influencing behavioral patterns or swimming speed of fishes (Ryer & Barnett, 2006). Considering the diversity of behaviors that can occur, catch standardization methods are likely to be most useful if developed for specific stocks and gears.

3.5.2 *Implications for fisheries*

Our scenarios suggest that changes in the spatial distribution of subarctic stocks and bottom trawl fisheries will influence catchability. Gear efficiency increased with latitude during summer, suggesting fisheries would be more efficient at higher latitude during summer. The large-scale commercial fisheries in the Bering Sea include participation from large catcher vessels and catcher-processors that are capable of fishing around-the-clock and traveling long distances to track changes in fish distribution. Therefore, it is plausible that greater efficiency at high latitude may cause a redistribution of fishing effort to higher latitude, although many factors other than gear efficiency and availability affect the distribution of fishing effort.

Spatial management closures play a key role in limiting the distribution of fishing effort in our study region. In the U.S. exclusive economic zone (EEZ), most of the NEBS is within the Northern Bering Sea Research Area that is closed to commercial bottom trawling. The Arctic Management Area north of Bering Strait (eastern Chukchi Sea and Beaufort Sea) is closed to commercial fishing. By contrast, in the Russian EEZ, commercial fishing is open in the northwestern Bering Sea and a walleye pollock quota was set for the western Chukchi Sea in 2020. In the near-term, latitudinal differences in management suggest that latitudinal shifts in the distribution of commercial fishing effort in the Pacific Sector of the Arctic may differ between the U.S. and Russia, regardless of poleward range expansion and patterns of variation in gear efficiency.

3.5.3 *Other influences on catchability*

Changes in light can also affect the size selectivity of fishing gear. As visual herding decreases at low light levels, walleye pollock inside the mouth of a trawl increasingly make contact

with gear and escape through the mesh (Olla et al., 2000; Ryer & Olla, 2000). Smaller walleye pollock more easily pass through the trawl mesh so light disproportionately affects catchability of small fish (Williams et al., 2011). Dark conditions are associated with lower gear efficiency and larger size composition in the catch (Williams et al., 2011, 2013). Our simulation framework can be adapted to examine light-dependent size selectivity although we did not do so here.

3.5.4 *Knowledge gaps and future research*

Future research into light-dependent herding behavior of Alaska groundfish species across a gradient of light levels would facilitate development of species-and-gear-specific visual herding models. The model we used to simulate visual herding was based on experiments conducted with subarctic fishes from the Atlantic Ocean (Blaxter & Parrish, 1964, 1966). Herding studies suggest similar dynamics would occur for species from our study region (Table 3.1), although it is unclear whether the assumptions in our simulation are accurate. In part, this is because herding studies with demersal stocks in our region have focused on day-night differences in catch rates rather than characterizing variation across gradients of light levels. Furthermore, there is little-to-no understanding of light sensitivity for many abundant stocks (Table 3.1). Research is necessary to evaluate whether our functional representation of visual herding is reasonable and to characterize the light sensitivity of abundant stocks. Both of these objectives can be addressed by conducting herding experiments that measure catch rates across gradients of light.

Water clarity likely causes greater variability in catchability than shown by our results so a better characterization of spatial-temporal variation in water clarity would likely improve the reliability of our simulations. Our water clarity simulations do not represent the full range of variation in water clarity that occurs in the study region because we focused on the 25%, 50%, and

75% quantiles of optical depth based on summer data from the EBS. Accurately and precisely predicting water clarity throughout the study area is extremely challenging because many physical and biological processes that contribute to variation in water clarity occur beneath the sea surface and are not visible to satellites. In the EBS, a subsurface chlorophyll maximum and a turbid bottom layer affect light transmission to the sea floor during summer (Rohan et al., 2021). Some processes that affect water clarity can be monitored using satellites, such as spring and fall phytoplankton blooms (e.g. Lewis et al., 2020) and, during summer, variation in bottom optical depth is strongly correlated with near-surface water clarity over parts of the EBS shelf (e.g., Rohan et al., 2021). In other areas and at other times, variation in near-surface water clarity may not be associated with variation in bottom optical depth because subsurface layers have a stronger influence on light transmission to the seafloor (e.g., Rohan et al., 2021). Accurately and precisely modeling light transmission requires empirical models based on in situ observations or physical-biological models that reliably predict water clarity. Still, our simulation likely affords a qualitatively reasonable approximation of light transmission dynamics in the study region. In the supplementary material (*Modeled light versus Pacific cod archival tag light*), we demonstrate decent agreement between simulated light levels and measurements from pop-up satellite archival tags deployed on Pacific cod from August 2019– February 2020. A possible cost-effective solution to monitor in-situ light and water clarity, along with effects on catchability, is to deploy low-cost photodiode light sensors on trawl gear (Kotwicki et al., 2009).

We developed walleye pollock bottom trawl and acoustic vertical availability models using data from the EBS (2005–2009) so predictive accuracy may vary across the broader study area. Vertical distribution and migration is an adaptive behavior that is influenced by factors other than light and depth, such as food availability, physiological state, predation risk, and thermal structure

of the water column (Sogard & Olla, 1996). Although light plays a major role in vertical migration, other ecological factors may be more important in some contexts. In the Gulf of Alaska, Adams et al. (2009) found adult walleye pollock distributions did not follow light clines in August but did in November, potentially due to seasonal variation in the vertical distribution and migration of prey. Regardless, we expect visual processes play an important role in walleye pollock catchability throughout our study area. Under low light, walleye pollock are less able to school, and detect and react to trawl gear (Olla et al., 2000; Williams et al., 2013). Regional catchability studies, similar to the work from the EBS (Kotwicki et al., 2009, 2013, 2015, 2018), could improve understanding of the mechanistic role light plays in walleye pollock catchability across the study area.

Better understanding of fine-scale migration patterns of fish stocks would facilitate development of species-specific catchability scenarios. Many abundant stocks in the EBS undertake seasonal migrations between spawning grounds and summer feeding areas (e.g., Cooper et al., 2013; Kotwicki et al., 2005; Rand et al., 2014), but fine-scale migration patterns are largely unknown (e.g., routes between spawning and feeding ground). Tagging and genetic studies have yielded some insight into patterns of migration and population structure of species such as Pacific cod (e.g., Rand et al., 2014; Spies et al., 2020) and ongoing satellite tagging research has shown promise for improving understanding of fine-scale patterns of migration. Initial results of a satellite tagging study suggest Pacific cod tagged in the NEBS can remain in summer feeding areas until the ice edge advances in winter or they migrate to spawning grounds along the continental shelf break in March–April (S.F. McDermott and J.K. Nielsen, unpublished data). Similar studies of the fine-scale migration patterns of other regional fishes have not been conducted.

3.5.5 *Conclusions*

Our findings suggest that the northward range expansion of subarctic fish stocks and stock assessment surveys towards the Arctic may lead to temporally biased measures of population status for subarctic stocks. The expansion of stocks into areas with differences in depth and water clarity would amplify the bias. Standardizing catches to account for light-dependent variation may reduce the bias, but doing so will require efforts to improve understanding of how light affects catchability for individual stocks and gear types.

3.6 ACKNOWLEDGEMENTS

We grateful to Cole Monnahan, Cecilia O'Leary, and Steve Rubin for constructive comments on drafts of this manuscript that substantially strengthened this manuscript. We thank Liz Dawson and Rebecca Haehn for assistance with Pacific cod archival tag data. Funding to support this work was provided by the NOAA National Marine Fisheries Service's Fisheries and the Environment (FATE) Program. Any use of trade, firm, or product names is for descriptive purposes only and does not imply endorsement by the U.S. Government. The scientific results and conclusions, as well as any views or opinions expressed herein, are those of the author(s) and do not necessarily reflect those of NOAA or the Department of Commerce.

3.7 REFERENCES

Adams, C. F., Foy, R. J., Kelley, J. J., & Coyle, K. O. (2009). Seasonal changes in the diel vertical migration of walleye pollock (*Theragra chalcogramma*) in the northern Gulf of Alaska. Environmental Biology of Fishes, 86(2), 297–305. https://doi.org/10.1007/s10641-009-9519-y

Addison, J. T., Lawler, A. R., & Nicholson, M. D. (2003). Adjusting for variable catchability of brown shrimps (*Crangon crangon*) in research surveys. Fisheries Research, 65(1–3), 285–294. https://doi.org/10.1016/j.fishres.2003.09.020

Arreguín-Sánchez, F. (1996). Catchability: a key parameter for fish stock assessment. Reviews in Fish Biology and Fisheries, 6, 221–242.

Blaxter, J. H. S., & Parrish, B. B. (1964). The importance of vision in the reaction of fish to driftnets and trawls. In Modern Fishing Gear of the World 2 (pp. 529–536). Fishing News Books.

Blaxter, J. H. S., & Parrish, B. B. (1966). The reaction of marine fish to moving netting and other devices in tanks. Marine Research No. 1, 1–15.

Cooper, D. W., Duffy-Anderson, J. T., Stockhausen, W. T., & Cheng, W. (2013). Modeled connectivity between northern rock sole (*Lepidopsetta polyxystra*) spawning and nursery areas in the eastern Bering Sea. Journal of Sea Research, 84, 2–12. https://doi.org/10.1016/j.seares.2012.07.001

Danielson, S., Dobbins, E., Jakobsson, M., Johnson, M., Weingartner, T., Williams, W., & Zarayskaya, Y. (2015). Sounding the northern seas. Eos, 96. https://doi.org/10.1029/2015EO040975

De Robertis, A., & Cokelet, E. D. (2012). Distribution of fish and macrozooplankton in ice-covered and open-water areas of the eastern Bering Sea. Deep-Sea Research Part II: Topical Studies in Oceanography, 65–70, 217–229. https://doi.org/10.1016/j.dsr2.2012.02.005

Fasiolo, M., Wood, S. N., Zaffran, M., Nedellec, R., & Goude, Y. (2017). Fast calibrated additive quantile regression. Journal of the American Statistical Association, 1–39. https://doi.org/10.1080/01621459.2020.1725521

Fissel, B., Dalton, M., Garber-Yonts, B., Haynie, A., Kasperski, S., Lee, J., Lew, D., Seung, C., Sparks, K., Symkowiak, M., & Wise, S. (2019). Economic status of the groundfish fisheries off Alaska, 2018. In Stock Assessment and Fishery Evaluation Report for the Groundfish Resources of the Bering Sea/Aleutian Islands Regions (pp. 1–297).

Fossheim, M., Primicerio, R., Johannesen, E., Ingvaldsen, R. B., Aschan, M. M., & Dolgov, A. V. (2015). Recent warming leads to a rapid borealization of fish communities in the Arctic. Nature Climate Change, 5(7), 673–677. https://doi.org/10.1038/nclimate2647

Frainer, A., Primicerio, R., Kortsch, S., Aune, M., Dolgov, A. V., Fossheim, M., & Aschan, M. M. (2017). Climate-driven changes in functional biogeography of Arctic marine fish communities. Proceedings of the National Academy of Sciences of the United States of America, 114(46), 12202–12207. https://doi.org/10.1073/pnas.1706080114

Francis, R. I. C. C., Hurst, R. J., & Renwick, J. A. (2003). Quantifying annual variation in catchability for commercial and research fishing. Fishery Bulletin, 101(2), 293–304.

Gautier, S., & Rose, G. A. (2005). Diel vertical migration and shoaling heterogeneity in Atlantic redfish: effects on acoustic and bottom-trawl surveys. ICES Journal of Marine Science, 62, 75–85. https://doi.org/10.1016/j.icesjms.2004.10.001

Gibson, R. N., Stoner, A. W., & Ryer, C. H. (2015). The behaviour of flatfishes. In R. N. Gibson, R. D. M. Nash, A. J. Geffen, & H. W. van der Veer (Eds.), Flatfishes: Biology and Exploitation (Second Edi, pp. 314–345). John Wiley & Sons Ltd.

Glass, C. W., & Wardle, C. S. (1989). Comparison of the reactions of fish to a trawl gear, at high and low light intensities. Fisheries Research, 7(3), 249–266. https://doi.org/10.1016/0165-7836(89)90059-3

Glass, C. W., Wardle, C. S., & Mojsiewicz, W. (1986). A light intensity threshold for schooling in the Atlantic mackerel, Scomber scombrus. Journal of Fish Biology, 29(Supplement A), 71–81.

Godø, O. R. (1994). Factors affecting the reliability of groundfish abundance estimates from bottom trawl surveys. In A. Fernö & S. Olsen (Eds.), Marine fish behavior in capture and abundance estimation (pp. 166–199). Fishing News Books.

Hobbs, L., Cottier, F. R., Last, K. S., & Berge, J. (2018). Pan-Arctic diel vertical migration during the polar night. Marine Ecology Progress Series, 605, 61–72. https://doi.org/doi.org/10.3354/meps12753

Hurst, T. P. (2007). Thermal effects on behavior of juvenile walleye pollock (*Theragra chalcogramma*): implications for energetics and food web models. Canadian Journal of Fisheries and Aquatic Sciences, 64(3), 449–457. https://doi.org/10.1139/f07-025

Ianelli, J., Fissel, B., Holsman, K., Honkalehto, T., Kotwicki, S., Monnahan, C., Siddon, E., Stienessen, S., & Thorson, J. (2019). Assessment of the walleye pollock stock in the eastern Bering Sea. In Stock Assessment and Fishery Evaluation Report for the Groundfish Resources of the Bering Sea/Aleutian Islands Regions (pp. 1–169).

Janiczek, P. M., & DeYoung, J. A. (1987). Computer programs for sun and moon illuminance with contingent tables and diagrams. United States Naval Observatory Circular No. 171.

Kotwicki, S., Buckley, T. W., Honkalehto, T., & Walters, G. (2005). Variation in the distribution of walleye pollock (*Theragra chalcogramma*) with temperature and implications for seasonal migration. Fishery Bulletin, 103(4), 574–587.

Kotwicki, S., De Robertis, A., Ianelli, J. N., Punt, A. E., & Horne, J. K. (2013). Combining bottom trawl and acoustic data to model acoustic dead zone correction and bottom trawl efficiency parameters for semipelagic species. Canadian Journal of Fisheries and Aquatic Sciences, 70(2), 208–219. https://doi.org/10.1139/cjfas-2012-0321

Kotwicki, S., De Robertis, A., von Szalay, P., & Towler, R. (2009). The effect of light intensity on the availability of walleye pollock (*Theragra chalcogramma*) to bottom trawl and acoustic surveys. Canadian Journal of Fisheries and Aquatic Sciences, 66(6), 983–994. https://doi.org/10.1139/f09-055

Kotwicki, S., Horne, J. K., Punt, A. E., & Ianelli, J. N. (2015). Factors affecting the availability of walleye pollock to acoustic and bottom trawl survey gear. ICES Journal of Marine Science, 72(5), 1425–1439. https://doi.org/10.1093/icesjms/fsv011

Kotwicki, S., Ressler, P. H., Ianelli, J. N., Punt, A. E., & Horne, J. K. (2018). Combining data from bottom trawl and acoustic surveys to estimate an index of abundance for semipelagic species. Canadian Journal of Fisheries and Aquatic Sciences, 75, 60–71.

Lewis, K. L., van Dijken, G., & Arrigo, K. R. (2020). Changes in phytoplankton concentration, not sea ice, now drive increased Arctic Ocean primary production. Science, 369, 198–202.

Link, J. S., Nye, J. A., & Hare, J. A. (2011). Guidelines for incorporating fish distribution shifts into a fisheries management context. Fish and Fisheries, 12(4), 461–469. https://doi.org/10.1111/j.1467-2979.2010.00398.x

Lomas, M., Eisner, L., Gann, J., Baer, S., Mordy, C., & Stabeno, P. (2020). Time-series of direct primary production and phytoplankton biomass in the southeastern Bering Sea: Responses to cold and warm stanzas. Marine Ecology Progress Series, 642(2004), 39–54. https://doi.org/10.3354/meps13317

Maunder, M. N., & Punt, A. E. (2004). Standardizing catch and effort data: A review of recent approaches. Fisheries Research, 70(2-3 SPEC. ISS.), 141–159. https://doi.org/10.1016/j.fishres.2004.08.002

Monnahan, C.C., Thorson, J.T., Kotwicki, S., Lauffenburger, N., Ianelli, J.N., Punt, A.E. (*In review*). Incorporating vertical distribution in index standardization accounts for spatialtemporal availaiblity to acoustic and bottom trawl gear for semi-pelagic species.

O'Leary, C. A., Thorson, J. T., Ianelli, J. N., & Kotwicki, S. (2020). Adapting to climate-driven distribution shifts using model-based indices and age composition from multiple surveys in the walleye pollock (*Gadus chalcogrammus*) stock assessment. Fisheries Oceanography, July, 1–17. https://doi.org/10.1111/fog.12494

Olla, B. L., Davis, M. W., & Rose, D. C. (2000). Differences in orientation and swimming of walleye pollock *Theragra chalcogramma* in a trawl net under light and dark conditions: concordance between field and laboratory observations. Fisheries Research, 44, 261–266.

Olla, B. L., Davis, M. W., & Schreck, C. B. (1997). Effects of simulated trawling on sablefish and walleye pollock: the role of light intensity, net velocity and towing duration. Journal of Fish Biology, 50, 1181–1194.

Orlov, A. M., Benzik, A. N., Vedishcheva, E. V., Gafitsky, S. V., Gorbatenko, K. M., Goryanina, S. V., Zubarevich, V. L., Kodryan, K. V., Nosov, M. A., Orlova, S. Y., Pedchenko, A. P., Rybakov, M. O., Sokolov, A. M., Somov, A. A., Subbotin, S. N., Taptygin, M. Y., Firsov,

Y. L., Khleborodov, A. S., & Chikilev, V. G. (2019). Fisheries research in the Chukchi Sea at the RV Professor Levanidov in August 2019: some preliminary results. Trudy VNIRO, 178, 206–220. https://doi.org/10.36038/2307-3497-2019-178-206-220

Payne, R. E. (1972). Albedo of the sea surface. Journal of the Atmospheric Sciences, 29(5), 959–970. https://doi.org/10.1175/1520-0469(1972)029<0959:AOTSS>2.0.CO;2

R Core Development Team. (2020). R: A language and environment for statistical computing. R Foundation for Statistical Computing. https://www.r-project.org/

Rand, K. M., Munro, P., Neidetcher, S. K., & Nichol, D. G. (2014). Observations of seasonal movement from a single tag release group of Pacific cod in the eastern Bering Sea. Marine and Coastal Fisheries, 6(1), 287–296. https://doi.org/10.1080/19425120.2014.976680

Rohan, S. K., Kotwicki, S., Kearney, K. A., Schulien, J. A., Laman, E. A., Cokelet, E. D., Beauchamp, D. A., Britt, L. L., Aydin, K. Y., & Zador, S. G. (2021). Using bottom trawls to monitor subsurface water clarity in marine ecosystems. Progress in Oceanography 194: 102554.

Rohan, S. K., Kotwicki, S., Laman, E. A., Britt, L. L., & Aydin, K. (2020). Deriving apparent optical properties from light measurements obtained using bottom-trawl-mounted archival tags [United States Department of Commerce, NOAA Technical Memorandum NMFS-AFSC-403, 91 p].

Ryer, C. H., & Barnett, L. A. K. (2006). Influence of illumination and temperature upon flatfish reactivity and herding behavior: Potential implications for trawl capture efficiency. Fisheries Research, 81(2–3), 242–250. https://doi.org/10.1016/j.fishres.2006.07.001

Ryer, C. H., Lawton, A., Lopez, R. J., & Olla, B. L. (2002). A comparison of the functional ecology of visual vs. nonvisual foraging in two planktivorous marine fishes. Canadian Journal of Fisheries and Aquatic Sciences, 59(8), 1305–1314. https://doi.org/10.1139/f02-097

Ryer, C. H., & Olla, B. L. (1999). Light-induced changes in the prey consumption and behavior of two juvenile planktivorous fish. Marine Ecology Progress Series, 181, 41–51. https://doi.org/10.3354/meps181041

Ryer, C. H., & Olla, B. L. (2000). Avoidance of an approaching net by juvenile walleye pollock *Theragra chalcogramma* in the laboratory: the influence of light intensity. Fisheries Research, 45, 195–199.

Ryer, C. H., Rose, C. S., & Iseri, P. J. (2010). Flatfish herding behavior in response to trawl sweeps: A comparison of diel responses to conventional sweeps and elevated sweeps. Fishery Bulletin, 108(2), 145–154.

Sigler, M. F., Stabeno, P. J., Eisner, L. B., Napp, J. M., & Mueter, F. J. (2014). Spring and fall phytoplankton blooms in a productive subarctic ecosystem, the eastern Bering Sea, during 1995-2011. Deep-Sea Research Part II: Topical Studies in Oceanography, 109, 71–83. https://doi.org/10.1016/j.dsr2.2013.12.007

Sogard, S. M., & Olla, B. L. (1996). Food deprivation affects vertical distribution and activity of a marine fish in a thermal gradient: potential energy-conserving mechanisms. Marine Ecology Progress Series, 133, 43–55. https://doi.org/10.3354/meps133043

Somerton, D. A. (2004). Do Pacific cod (*Gadus macrocephalus*) and walleye pollock (*Theregra chalcogramma*) lack a herding response to the doors, bridles, and mudclouds of survey trawls? ICES Journal of Marine Science, 61(7), 1186–1189. https://doi.org/10.1016/j.icesjms.2004.06.003

Somerton, D. A., & Munro, P. (2001). Bridle efficiency of a survey trawl for flatfish. Fishery Bulletin, 99(4), 641–652.

Somerton, D. A., Munro, P. T., & Weinberg, K. L. (2007). Whole-gear efficiency of a benthic survey trawl for flatfish. Fishery Bulletin, 105(2), 278–291. https://doi.org/10.1016/0144-2449(94)90158-9

Spies, I., Gruenthal, K. M., Drinan, D. P., Hollowed, A. B., Stevenson, D. E., Tarpey, C. M., & Hauser, L. (2020). Genetic evidence of a northward range expansion in the eastern Bering Sea stock of Pacific cod. Evolutionary Applications, 13(2), 362–375. https://doi.org/10.1111/eva.12874

Stabeno, P. J., & Bell, S. W. (2019). Extreme conditions in the Bering Sea (2017–2018): record-breaking low sea-ice extent. Geophysical Research Letters, 46(15), 8952–8959. https://doi.org/10.1029/2019GL083816

Stabeno, P. J., Bell, S. W., Bond, N. A., Kimmel, D. G., Mordy, C. W., & Sullivan, M. E. (2019). Distributed Biological Observatory Region 1: Physics, chemistry and plankton in the northern Bering Sea. Deep-Sea Research Part II: Topical Studies in Oceanography, 162, 8–21. https://doi.org/10.1016/j.dsr2.2018.11.006

Stabeno, P. J., Farley, E. V., Kachel, N. B., Moore, S., Mordy, C. W., Napp, J. M., Overland, J. E., Pinchuk, A. I., & Sigler, M. F. (2012). A comparison of the physics of the northern and southern shelves of the eastern Bering Sea and some implications for the ecosystem. Deep-Sea Research Part II: Topical Studies in Oceanography, 65–70, 14–30. https://doi.org/10.1016/j.dsr2.2012.02.019

Stabeno, P. J., Mordy, C. W., & Sigler, M. F. (2020). Seasonal patterns of near-bottom chlorophyll fluorescence in the eastern Chukchi Sea: 2010–2019. Deep Sea Research Part II: Topical Studies in Oceanography, 104842. https://doi.org/10.1016/j.dsr2.2020.104842

Stauffer, G. (2004). NOAA protocols for groundfish bottom-trawl surveys of the Nation's fishery resources. United States Department of Commerce, NOAA Technical Memorandum NMFS-F/SPO-65, 205 p.

Stevenson, D. E., & Lauth, R. R. (2019). Bottom trawl surveys in the northern Bering Sea indicate recent shifts in the distribution of marine species. Polar Biology, 42(2), 407–421. https://doi.org/10.1007/s00300-018-2431-1

Thimijan, R. W., & Heins, R. D. (1983). Photometric, radiometric, and quantum light units of measure: A review or procedures for interconversion. HortScience, 18(6), 818–820.

Thompson, G. G., & Thorson, J. T. (2019). Asessment of the Pacific cod stock in the eastern Bering Sea. In Stock Assessment and Fishery Evaluation Report for the Groundfish Resources of the Bering Sea and Aleutian Islands Regions (pp. 1–271). https://archive.afsc.noaa.gov/refm/docs/2019/EBSpcod.pdf

U.S. National Ice Center and National Snow and Ice Data Center. (2010). Compiled by F. Fetterer, M. Savoie, S. Helfrich, and P. Clemente-Colón. Multisensor Analyzed Sea Ice Extent - Northern Hemisphere (MASIE-NH), Version 1. NSIDC: National Snow and Ice Data Center. https://doi.org/10.7265/N5GT5K3K

Vasilyev, D. A., & Datsky, A. V. (2020). Pollock (*Theragra chalcogramma*) Chukchi Sea Zone. In МАТЕРИАЛЫ, ОБОСНОВЫВАЮЩИЕ ВНЕСЕНИЕ ИЗМЕНЕНИЙ в РАНЕЕ УТВЕРжДЁННыЙ ОБЩИЙ ДОПУСТИМЫЙ улов в РАЙОНЕ ДОБЫЧИ (ВЫЛОВА) ВОДНЫХ БИОЛОГИЧЕСКИХ РЕСУРСОВ во ВНУТРЕННИХ МОРСКИХ ВОДАХ

Российской ФЕДЕРАЦИИ, В ТЕРРИТОРИАЛЬНОМ МОРЕ РОССИЙСКОЙ ФЕДЕРАЦИИ, НА КОНТИНЕНТАЛЬНО (pp. 18–24). VNIRO.

Walsh, S. J., & Hickey, W. M. (1993). Behavioural reactions of demersal fish to bottom trawls at various light conditions. ICES Marine Science Symposia, 196, 68–76.

Wang, M., Yang, Q., Overland, J. E., & Stabeno, P. (2018). Sea-ice cover timing in the Pacific Arctic: The present and projections to mid-century by selected CMIP5 models. Deep-Sea Research Part II: Topical Studies in Oceanography, 152(December 2017), 22–34. https://doi.org/10.1016/j.dsr2.2017.11.017

Wilberg, M. J., Thorson, J. T., Linton, B. C., & Berkson, J. (2009). Incorporating time-varying catchability into population dynamic stock assessment models. Reviews in Fisheries Science, 18(1), 7–24. https://doi.org/10.1080/10641260903294647

Williams, K., Punt, A. E., Wilson, C. D., & Horne, J. K. (2011). Length-selective retention of walleye pollock, *Theragra chalcogramma*, by midwater trawls. ICES Journal of Marine Science, 68(1), 119–129. https://doi.org/10.1093/icesjms/fsq155

Williams, K., Wilson, C. D., & Horne, J. K. (2013). Walleye pollock (*Theragra chalcogramma*) behavior in midwater trawls. Fisheries Research, 143, 109–118. https://doi.org/10.1016/j.fishres.2013.01.016

Wyllie-Echeverria, T., & Wooster, W. S. (1998). Year-to-year variations in Bering Sea ice cover and some consequences for fish distributions. Fisheries Oceanography, 7(2), 159–170. https://doi.org/10.1046/j.1365-2419.1998.00058.x

Table 3.1. Herding proportions by species.

Proportion of daytime catch attributed to herding by bridles of NOAA bottom trawl surveys (h) and likely ranges of the half-saturation light level for visual herding (E_{50}) for the eight most abundant groundfish species in the eastern Bering Sea and Pacific halibut. Based on studies of visual herding behavior, day-night variation in catch rates, and visual foraging. Dashes (-) denote no known published information.

			E_{50} (µMol photons m^{-2} s^{-1})		
Species	***h***	**Higher catch**	**Herding behavior**	**Catch**	**Foraging**
Alaska plaice	-	Day[c, ‡]	-	10^{-6}–10^{-4} [c, ‡]	-
Alaska skate	-	-	-	-	-
arrowtooth flounder	0.25[k,†]	Day[c, ‡]	-	10^{-6}–10^{-4} [c, ‡]	-
flathead sole	0.37[a,*] 0.32[k,†]	Day[c, ‡]	-	10^{-6}–10^{-4} [c, ‡]	-
northern rock sole	0.49[a,*]	Day[c,‡]	-	10^{-6}–10^{-4} [c, ‡]	10^{-6}–10^{-4} [h]
Pacific cod	0[b,*,†]	-	-	-	-
Pacific halibut	-	Night[c, ‡]	-	10^{-6}–10^{-4} [c, ‡]	10^{-6}–10^{-4} [h]
walleye pollock	0[b,*,†]	-	10^{-5}–10^{-3} [d,e,f,g]	-	10^{-6}–10^{-4} [i,j]
yellowfin sole	0.40[a,*]	Day[c,‡]	-	10^{-6}–10^{-4} [c, ‡]	-
flatfish spp.	-	-	10^{-6}–10^{-4} [c, ‡]	-	-

References: a- (Somerton & Munro, 2001), b-(Somerton, 2004) c- (Ryer et al., 2010), d-(Olla et al., 1997), e-(Williams et al., 2013), f- (Ryer & Olla, 2000), g-(Olla et al., 2000), h-(Hurst, 2007), i-(Ryer & Olla, 1999), j-(Ryer et al., 2002), k-(Somerton et al., 2007). Gears: *- NOAA/AFSC 83-112 eastern otter bottom trawl, †- NOAA/AFSC Poly Nor'easter bottom trawl; ‡- commercial and experimental flatfish bottom trawls; §- NOAA/AFSC Aleutian wing midwater trawl.

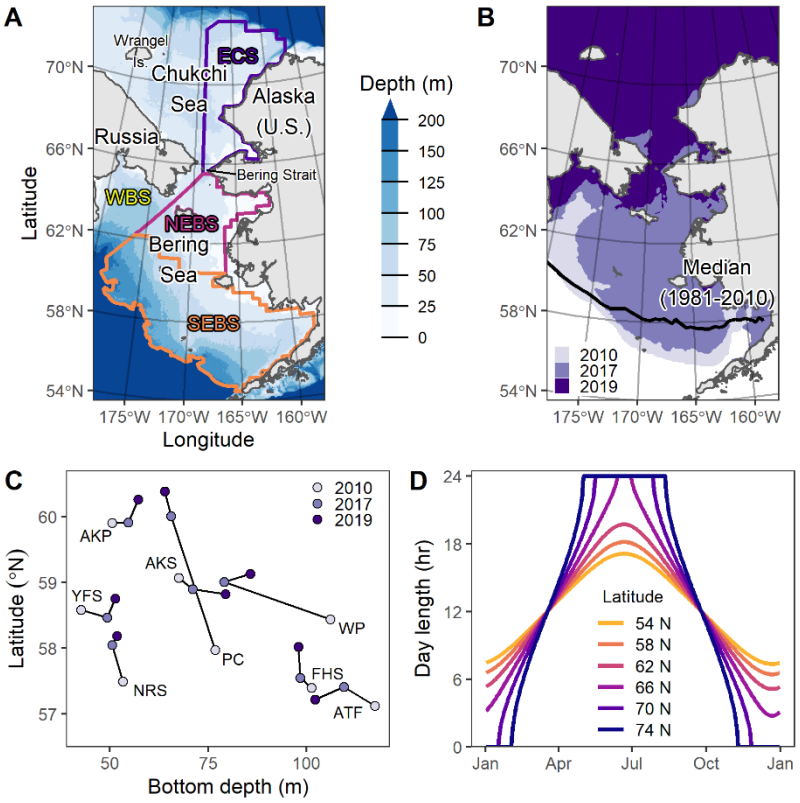

Figure 3.1. Map of the study area, sea-ice coverage in April, day length by latitude, and summertime center-of-gravity distribution of groundfish species in the eastern Bering Sea.

Panels: (A) Bathymetry for the Bering and Chukchi seas with denoting the western Bering Sea (WBS; Russia) and NOAA (U.S.) survey areas for the southeastern Bering Sea (SEBS), northeastern Bering Sea (NEBS), and eastern Chukchi Sea (ECS); (B) sea-ice extent on April 1 showing historical median (1981–1981) and recent years with NOAA summer bottom trawl surveys of the SEBS and NEBS (2010, 2017, 2019); (C) mean center of gravity distributions of bottom trawl survey catch-per-unit-effort for abundant groundfish species from NOAA Alaska Fisheries Science Center bottom trawl surveys of the SEBS and NEBS during 2010, 2017, and 2019 (AKP = Alaska plaice, AKS = Alaska skate, ATF = arrowtooth flounder, FHS = flathead sole, NRS = northern rock sole, PC = Pacific cod, WP = walleye pollock, YFS = yellowfin sole); (D) day of year (horizontal axis) versus day length (vertical axis) as a function of latitude.

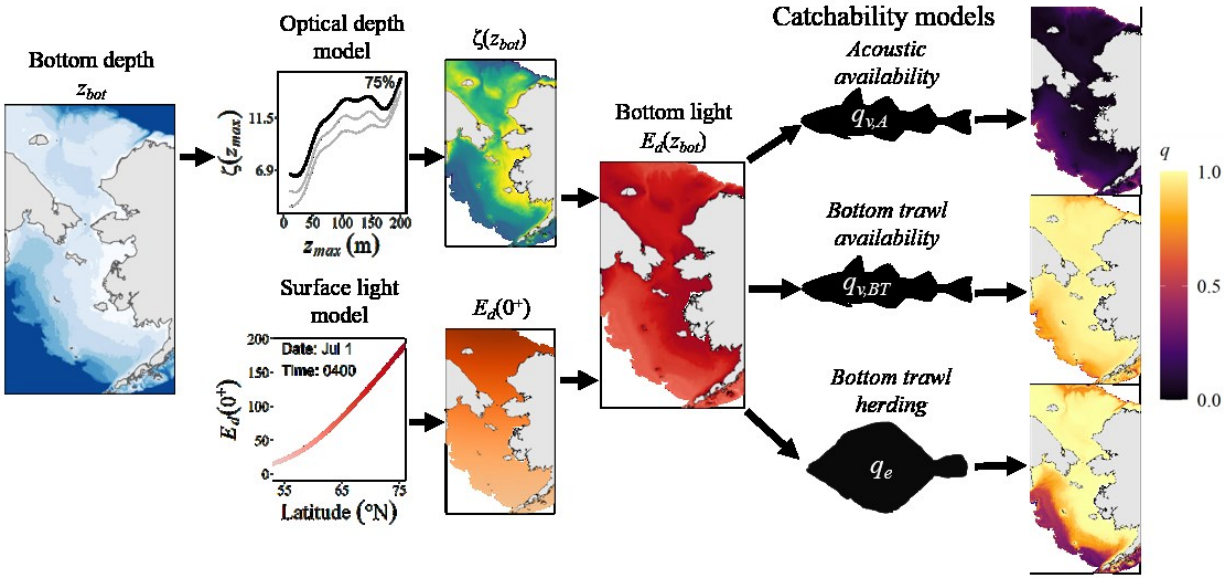

Figure 3.2. Schematic of the simulation framework.

Shows predicted catchability on July 1 at 0400 with for a bottom optical depth quantile of 50% and a demersal stock with a half-saturation light level, E_{50} = 1e^{-4} µMol photons m^{-2} s^{-1}. Symbols: z_{bot}–bottom depth (m), $E_d(0+)$–downwelling irradiance at the sea surface, $\zeta(z_{bot})$–bottom optical depth, $E_d(z_{bot})$–downwelling irradiance on-bottom, $q_{v,A}$–walleye pollock vertical availability to acoustic sampling, $q_{v,BT}$–walleye pollock vertical availability to bottom trawl sampling, q_e–gear efficiency.

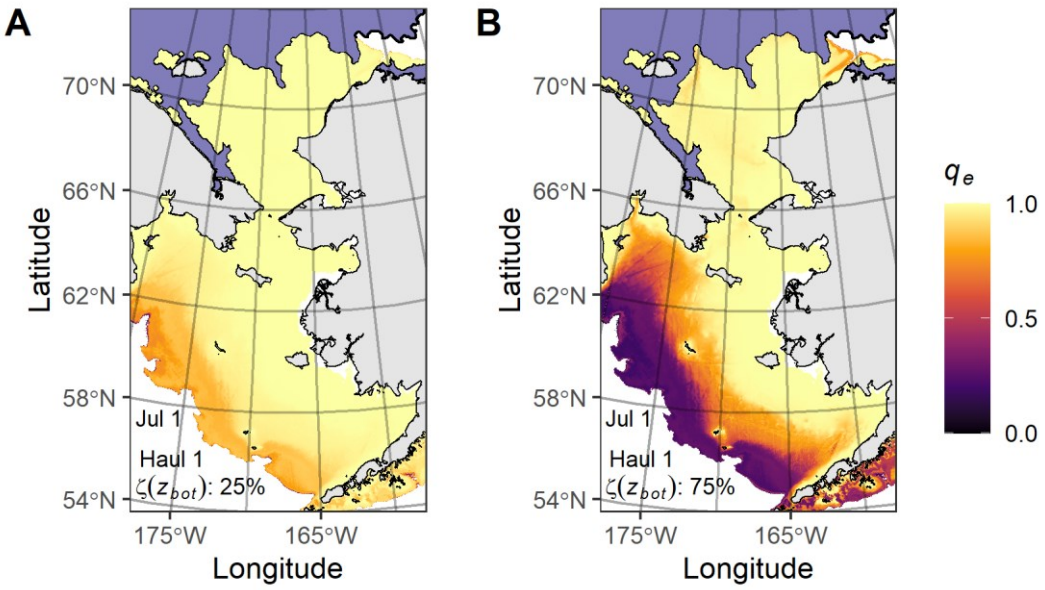

Figure 3.3.3. Gear efficiency (q_e) for the first bottom trawl haul of the day (i.e. early morning haul) on July 1.

Panels show quantiles of optical depth (i.e. water clarity): (A) 25% optical depth quantile (higher water clarity); (B) 75% optical depth quantile (lower water clarity). Gradient fill shows gear efficiency, light purple shading denotes MASIE-NH sea ice extent on July 1, 2019.

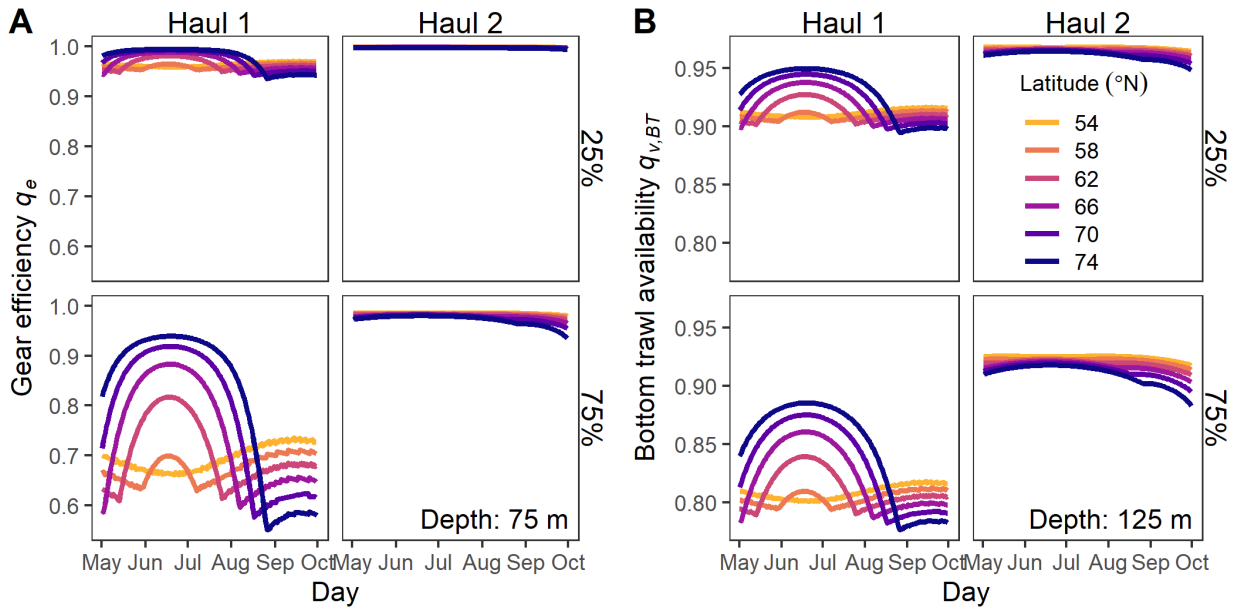

Figure 3.3.4. Bottom trawl survey scenario catchability.

Panels show: (A) gear efficiency for flatfish (q_e) at 75 m bottom depth, and (B) bottom trawl vertical availability of walleye pollock ($q_{v,BT}$) at 125 m bottom depth. Horizontal axes show day of year, vertical axes show q_e and $q_{v,BT}$, respectively. Panel columns show the first and second hauls of the day (i.e. early morning and mid-morning hauls). Panel rows show the 25% (higher water clarity) and 75% (lower water clarity) quantiles of optical depth. Line colors denote latitude.

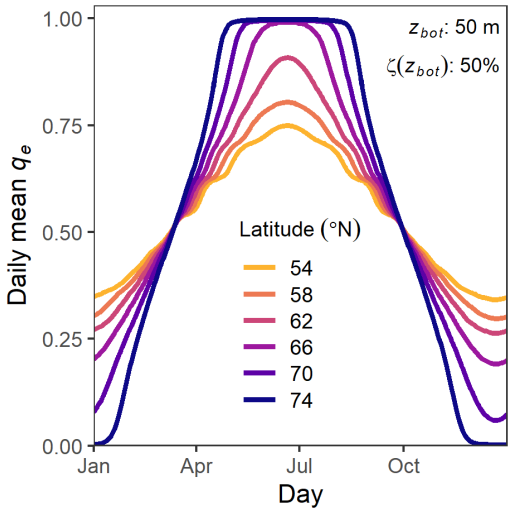

Figure 3.5. Daily mean gear efficiency (q_e; hourly gear efficiency averaged for each day). Predictions by latitude at 50 m depth and 50% optical depth (average water clarity) quantile. Axes show day of year (horizontal) and daily mean q_e (vertical), colors denote latitude.

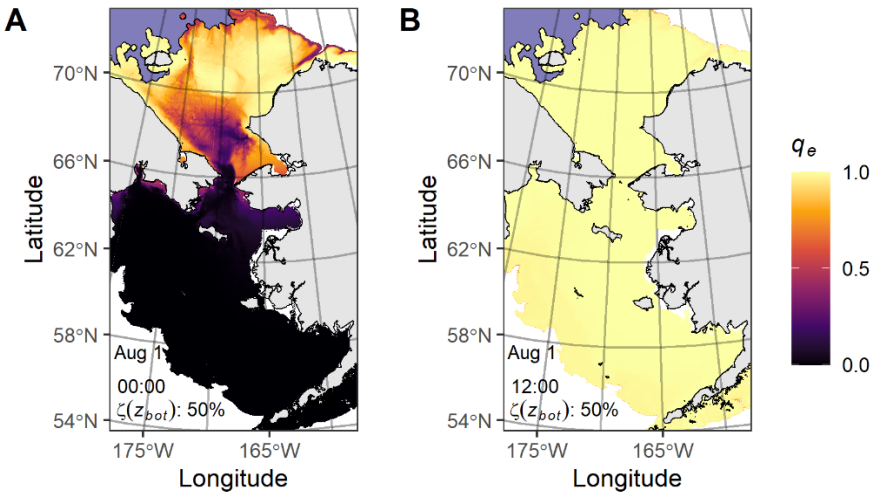

Figure 3.6. Gear efficiency (q_e) at (A) midnight (00:00) and (B) noon (12:00) local time on August 1 at the 50% optical depth (average water clarity) quantile.
Fill colow shows gear efficiency, light purple shading denotes MASIE-NH sea ice extent on August 1, 2019.

Chapter 4. WATER CLARITY, BATHYMETRY, AND LIGHT REGIME MEDIATE VISUAL FORAGING LANDSCAPES IN THE EASTERN BERING SEA

4.1 ABSTRACT

In recent years, a climate-driven loss of seasonal sea ice facilitated a poleward range expansion of commercially and ecological important fish species in the eastern Bering Sea. Due to long day lengths at high latitude during summer, differing seafloor depths, and water clarity, this distribution shift likely has altered fish visual foraging conditions compared to their historic range. Changes in visual foraging conditions may influence responses of biological communities to climate change, including the productivity of visual foraging predators and their prey. To improve understanding of how visual foraging opportunity varies spatially across the eastern Bering Sea, we used a mechanistic model of visual reaction distance and high spatial resolution water clarity data to evaluate the extent to which the light regime, bottom depth, and water clarity contribute to spatial variation in visual foraging opportunity. We parameterized the model for a walleye-pollock-like-predator feeding on 15-cm juvenile (age-1) conspecifics and *Calanus* spp. copepods. Walleye pollock are the most abundant fish species in the eastern Bering Sea, have recently had a poleward range expansion in the eastern Bering Sea, and have recruitment dynamics that appear to be influenced by top-down effects of cannibalism and bottom-up effects of copepod availability. Our findings suggest that, during summer of 2010 and 2017, there was no absolute refuge from visual predation on the eastern Bering Sea continental shelf during daytime. However, spatial variation in water clarity and light regime drive spatial variation in visual foraging opportunity. Due to distance-dependent effects of water clarity on visual reaction distance, areas that were

optimal for visual feeding on walleye pollock prey were often not optimal for visual feeding on copepods. At night during the summer solstice, there was a spatio-temporal predation refuge at low latitude but no refuge at high latitude. We conclude that changes in fish distribution have the potential to affect productivity of fish populations in the eastern Bering Sea by altering the strength of visual predator prey interactions, but that these effects are likely to vary among trophic levels.

4.2 INTRODUCTION

Many aquatic predators rely on vision to locate prey. As such, light, water clarity, and depth mediate the strength of predator-prey interactions in aquatic ecosystems. Over space and time, variation in light and water clarity create heterogeneity in visual foraging opportunity and predation risk, which can affect the biological productivity of visually foraging species and their prey (Langbehn et al., 2019; Maes et al., 2005; Mazur and Beauchamp, 2006). Changes in the visual environment can drive top-down changes in community structure (Aksnes, 2007; Haraldsson et al., 2012; Kitano et al., 2008; Sørnes and Aksnes, 2006). In some contexts, light regime (seasonal and diel), water clarity, and water column depth can affect predator consumption rates and productivity more than prey densities (Aksnes et al., 2004; Hansen and Beauchamp, 2015; Sørnes and Aksnes, 2006; Turesson and Brönmark, 2007). Therefore, understanding how light, water clarity, and depth influence spatial patterns of visual foraging opportunity and predation risk over space and time can provide insight into the mechanisms that drive spatial variation in the productivity of predator and prey populations and control community structure.

Variation in the visual environment contribute to spatial-temporal variation in community structure (Aksnes, 2007; Kitano et al., 2008; Sørnes and Aksnes, 2006). In the pelagic realm of aquatic systems, light, water clarity, and depth are the main factors that influence the visual

environment and regulate visual predation and the extent of predation refugia because there are few structural features that provide a refuge (Giske et al., 1994; Johnsen, 2014). Depth, light, and water clarity determine the extent to which pelagic species can regulate predation risk through vertical migration (e.g. diel vertical migration). The extent of visual predation refugia influences dynamics of predator-prey interactions and, therefore, community structure (Persson and Eklov, 1995; Sih, 1987).

Variation in water clarity contributes to variation in visual foraging opportunity and habitat-specific productivity in coastal marine ecosystems (Lovvorn et al., 2001; Maes et al., 2005; Sørnes and Aksnes, 2006). However, it is challenging to characterize variation in visual foraging opportunity in coastal marine ecosystems at mesoscales (1–100 km) that are representative of mobile and widely distributed marine species. Satellites may provide high spatial and temporal resolution monitoring of near-surface apparent optical properties, but many features that affect light transmission and water clarity occur in subsurface layers that are out of range of satellites, such as subsurface chlorophyll maxima (Cullen, 2015; Stabeno et al., 2020), and turbid nepheloid layers (McCave, 2019). As such, efforts to characterize spatial variation in visual foraging in marine ecosystems have typically focused on relatively small areas (Bhandiwad and Johnsen, 2011; Lovvorn et al., 2001), such as across an estuary or oceanographic transect, or treated sparse (e.g., single year and single transect) water clarity information as a proxy for conditions over a much larger extent (e.g., multiple years, basin-scale; Huse and Fiksen, 2010; Langbehn and Varpe, 2017; Maes et al., 2005). Due to the paucity of subsurface measurements, little attention has been paid to how mesoscale and sub-mesoscale spatial variation in water clarity affects visual foraging opportunity.

Rohan et al. (2020, 2021) developed a method to characterize subsurface water clarity (downwelling diffuse attenuation coefficient) using irradiance measurements collected with time-depth-recording archival tags equipped with a photodiode attached to bottom-trawl fishing gear. The method was used to characterize spatial variation in water clarity on the southeastern Bering Sea continental shelf from 2004 to 2018 using data collected during annual summer bottom trawl surveys across standardized stations arranged on a regularly-spaced grid (37.04 × 37.04 km cells; Rohan et al., 2020, 2021). Considerable mesoscale variation in water clarity in the eastern Bering Sea was observed, and depth was not a reliable predictor of bottom light due to spatial variation in water clarity. Light transmission to depth was strongly influenced by light attenuating layers around the pycnocline (presumably a subsurface chlorophyll maximum associated with a subsurface phytoplankton bloom) and in a bottom associated nepheloid layer (Rohan et al., 2021). Elevated near-bottom turbidity had been documented on the eastern Bering Sea continental shelf (Feely et al., 1981; Kawana, 1975; McManus and Smyth, 1970); however, the spatial footprint and recurrence of the benthic nepheloid layer had not previously been documented. This spatial variation in water clarity will likely contribute to spatial variation in visual foraging opportunity in the eastern Bering Sea.

Latitudinal variation in seasonal and diel light regime may also play an important role in structuring visual foraging opportunity in the eastern Bering Sea. The eastern Bering Sea is a high latitude system and spans a large latitudinal range (~54°N–66°N). During the middle of summer (i.e., summer solstice), days are 24 hours long at 66°N and 16 hours long at 54°N. This latitudinal gradient affects the extent of predation refugia and strength of visual predator-prey interactions (Hansen and Beauchamp, 2015; Langbehn and Varpe, 2017). In addition, the continental shelf in

the northeastern Bering Sea is generally shallower than the continental shelf further south. Therefore, visual foraging conditions are likely very different in the north than south.

Walleye pollock (*Gadus chalcogrammus*) is the most abundant fish species in the eastern Bering Sea and supports the world's largest single species fishery. In recent years (2018–2019), walleye pollock have undergone poleward range expansion into the northern Bering Sea and Chukchi Sea (Eisner et al., 2020b; Orlov et al., 2019). Walleye pollock are semi-pelagic zooplanktivores that ontogenetically shift to a more a piscivorous diet (Buckley et al., 2016; Dwyer et al., 1987), but exhibit some piscivory from age-0 onward (Moss et al. 2009). Cannibalism is the largest source of predation mortality for walleye pollock in the eastern Bering Sea (Holsman et al., 2019, 2016). The degree of spatial overlap between adult and age-1 juvenile walleye pollock appears to exert top-down influence on recruitment of walleye pollock to age-3 (Mueter et al., 2006). The availability of large copepod (i.e., *Calanus* spp*., Neocalanus* spp., *Metridia pacifica*) prey to age-0 walleye pollock also appears to influence recruitment to age-3 (Mueter et al., 2006).

Walleye pollock are visual predators so variation in light and water clarity affect their ability to feed (De Robertis et al., 2003; Ryer and Olla, 1999; Ryer et al., 2002). Due to variation in light regime, depth, and water clarity, visual foraging opportunity for walleye pollock and the extent of predation refugia for walleye pollock and their prey are likely to vary across the eastern Bering. Changes in walleye pollock distribution are likely to influence opportunities for visual foraging which, in turn, may affect the strength of visual predator-prey interactions that regulate growth and mortality of walleye pollock.

In this paper, we use a mechanistic visual foraging model and in situ water clarity data to characterize spatial variation in the pelagic visual foraging environment of the eastern Bering Sea continental shelf during summers of 2010 and 2017. Specifically, we examine how the extent of

predation refugia varies due to temporal (diel and seasonal) and latitudinal variation in light, and spatial variation in turbidity and bathymetry by characterizing reaction distance and search volume of walleye pollock searching for fish (juvenile walleye pollock) and zooplankton prey. We hypothesize that (1) the northern Bering Sea will offer less refuge from visual predation than further south because of relatively shallow depths and longer day length; (2) piscivore visual reaction distance and search volume will increase with latitude at a higher rate than zooplanktivore reaction distance due to asymmetric effects of light on reaction distance; (3) the dark conditions in the northwestern portion of the southeastern Bering Sea associated with the bottom nepheloid layer and subsurface chlorophyll maximum provides a refuge from visual predation; (4) high turbidity in coastal areas provides a refuge from visual predation.

4.3 METHODS

We characterized spatial and temporal patterns of visual foraging opportunity in the eastern Bering Sea during summer (June-August) using a model of visual reaction distance coupled with a three-dimensional light and water clarity simulation to predict reaction distances of pelagic visual predators to fish and zooplankton prey. The reaction distance model was parameterized based on the visual capabilities of walleye pollock, behavioral reaction distances of pelagic fishes to prey from visual foraging experiments, and morphological traits of prey. For the environmental simulation, we modeled light using a global irradiance model and downwelling diffuse attenuation coefficients obtained from the eastern Bering Sea during summers (June-August) of 2010 and 2017. Below we describe the reaction distance model and approach to parameterization, environmental data and interpolation, simulation of surface irradiance using a solar and lunar illuminance model, and approach to simulating reaction distance in the three-dimensional grid.

4.3.1 *Generalized visual reaction distance model*

We predicted reaction distances of predators to prey using the generalized visual reaction distance model, a mechanistic model that predicts reaction distance of predators to prey as a function of prey morphology (body area and inherent contrast), functional traits of the predator's vision system, light, and water clarity (Rohan et al., *Chapter 1*).

The generalized visual reaction distance model can be used to predict visual and non-visual reactions to prey. Although walleye pollock can feed non-visually at low light levels, we used a functional form of the generalized visual reaction distance model that only predicts visual reaction distance, because there is no information about the non-visual reaction distances of walleye pollock to prey. Terms in the generalized visual reaction distance model are shown in Table 1, and the functional form of the model is

$$r^2 \exp\big(r(\kappa - K_d \cos\theta)\big) = \omega(\kappa)|C_0|A_p E' \frac{E_b}{E_{50} + E_b}, \quad (1)$$

where r is visual reaction distance (in meters), κ is the effective attenuation coefficient (m^{-1}), K_d is the diffuse attenuation coefficient of downwelling irradiance (m^{-1}), θ is nadir viewing angle between the predator and prey (°), $\omega(\cdot)$ is the dynamic scaling function, C_0 is the inherent contrast of prey (non-dimensional), A_p is the area of the prey (m^2), E' is a composite term that represents maximum retinal radiance capacity and minimum sensitivity threshold for detection of prey, E_b is background irradiance (μMol photons m^{-2} s^{-1}), and E_{50} is the half-saturation constant that characterizes the light level at half of the maximum response (μMol photons m^{-2} s^{-1}). The dynamic scaling function, $\omega(\cdot)$, is

$$\omega(\kappa) = \left(\frac{\delta^h \kappa^{h-1} \exp(-\delta\kappa)}{\Gamma(h)}\right), \quad (2)$$

where h and δ parameters are terms that give the dynamic scaling function flexibility to account for lack of fit (unitless) to experimental reaction distance data. An explanation for the lack-of-fit to data are beyond the scope of this manuscript, but Chapter 1 provides a description of potential mechanisms.

Visual reaction distance experiments have not been conducted with walleye pollock, so we could not parameterize the generalized visual reaction distance model by fitting it to data for walleye pollock. Instead, we fit the model to data from reaction distance experiments conducted with Chinook salmon reacting to juvenile rainbow trout prey (~50 mm; Hansen et al. 2013) and reparameterized the model for walleye pollock based on visible prey traits and understanding of the functional capabilities of the walleye pollock vision system. Notably, Chinook salmon and walleye pollock are often found in the same habitat in the eastern Bering Sea. It is necessary to make structural modifications to the generalized visual reaction distance model to fit it to experimental data because prey contrast and prey area visible to a predator and reaction angle typically are not measured in reaction distance experiments. We fit the model to Chinook salmon reaction distance data (Chapter 1) by estimating $|C_0|$, A_p and E' as a composite parameter, $\tau = |C_0|A_pE$':

$$r^2 \exp(r\kappa) = \omega(\kappa)\tau \frac{E_b}{E_{50} + E_b}. \quad (3)$$

We reparameterized the model for walleye pollock by setting the half-saturation term, E_{50}, to 1e-3 μMol photons m^{-2} s^{-1}, which we consider representative of a walleye-pollock-like predator based on plausible half-saturation parameters from light-dependent consumption rate experiments conducted using juvenile walleye pollock (Ryer et al., 2002; Ryer and Olla, 1999). Next, we

calculated E' from the Chinook salmon data by dividing τ by the product of the lateral area of ~50 mm juvenile salmonids that we calculated from digital photos using ImageJ and an inherent contrast of 0.5 (i.e., $E'=\tau/(|C_0|A_p)$). We calculated the lateral area of a 15-cm fork length juvenile walleye pollock from digital photos and assumed an inherent contrast of 0.5 for juvenile walleye pollock. We used an inherent contrast for both because it is a representative value for a cryptically-colored small-bodied fish (Ruxton & Johnsen, 2016; Langbehn et al. 2019). For copepod prey, we used the reported lateral area of a 3.5-mm body length adult *Calanus finmarchicus*, an Atlantic-endemic species that is similar in size and color to *C. glacialis* (Frost, 1974; Szabo & Gardner, 1982) that are key prey for walleye pollock in the eastern Bering Sea (Moss et al., 2009). Notably, our approach to parameterizing reaction distances of walleye pollock to copepods yielded a maximum reaction distance that is similar to the maximum mean reaction distances of several planktivorous fishes to similar-sized copepod, cladoceran, and branchiopod zooplankton prey in visual reaction distance experiments (e.g. Link & Edsall 1996, Utne 1997, Holbrook et al. 2013, Schwalbe & Webb 2015). Using our parameterization, the generalized visual reaction distance model predictst he maximum reaction distances of walleye pollock to *Calanus* spp. copepods and 15-cm juvenile walleye pollock are 11.6 cm (Fig. S1A) and 2.96 m (Figs. S1B), respectively. The model also predicts that turbidity has an asymmetric effect on reaction distance for copepods and juvenile walleye pollock because of non-linearities as shown by variation in the ratio between reaction distances to juvenile walleye pollock and copepods across gradients of light and turbidity (Figure S1C).

4.3.2 *Three-dimensional grids of diffuse attenuation coefficient, effective attenuation coefficient, and temperature*

We generated three-dimensional grids of temperature, T (°C), and downwelling diffuse attenuation coefficient, $K_d(Z)$ (m^{-1}), on the eastern Bering Sea continental shelf by interpolating data from NOAA bottom-trawl surveys of the eastern Bering Sea and northern Bering Sea during summers (June–August) of 2010 and 2017. Bottom-trawl survey stations are arranged on a regularly-spaced 37.04 km × 37.04 km grid, and the survey sampled at 520 stations in 2010 and 518 stations in 2017. During the surveys, vertical profiles of temperature and irradiance were collected at every survey station using trawl-mounted CTD units (1-m vertical resolution) and archival tags equipped with a light-sensitive photodiode. Profiles of downwelling diffuse attenuation coefficients were derived from irradiance measurements (2-m depth resolution) and quality control checks were applied to ensure data quality. CTD profiles were post-processed and quality control checks were applied as described by (Cokelet, 2016). Figure S2 shows stations with CTD and diffuse attenuation data from 2010 and 2017.

We interpolated temperature and the downwelling diffuse attenuation coefficient on a three dimensional grid with 10 km × 10 km horizontal and 2 m vertical resolution. We generated the grids using ordinary kriging interpolation, a method that provides a reasonable fit to three-dimensional physical ocean data (e.g. Chehata et al., 2007; Sahlin et al., 2014). Although computationally efficient algorithms for three-dimensional kriging exist in proprietary software packages (Gribov and Krivoruchko, 2020), we sought to use transparent, reproducible, and open source methods to generate interpolated grids. Therefore, we conducted ordinary kriging using the R package ‘gstat’ (Pebsma, 2004).

Our approach to ordinary kriging was based on the three-dimensional kriging method recommended by Deutsch (2002). First, we normal-score transformed T and $K_d(Z)$ data to better

match optimal conditions of multivariate normality. Then we multiplied the vertical coordinate (depth) by a vertical expansion factor to account for strong vertical anisotropy in oceanographic data that occurs because physical measurements change must faster vertically than horizontally (Chehata et al., 2007; Sahlin et al., 2014). We fit a variogram model to an experimental variogram (semi-variances calculated at 50 equally spaced lag distances). The variogram model was a first-order Bessel function of the second kind with a nugget effect, which we used because preliminary exploration suggests it fit the experimental variogram better than other commonly used variogram models (circle, exponential, Gaussian, linear, Matérn, spherical). We estimated vertical expansion factors using a non-linear numerical optimization method (golden-section search) to find the expansion factor that minimized the root mean square prediction error (RMSPE) from five-fold cross validation. Following common practice for cross-validating three-dimensional borehole and oceanographic data, casts were randomly assigned to cross-validation folds (i.e., all measurements from a single cast were assigned to the same fold) rather than the two-dimensional convention of conducting cross-validation on individual points (Deutsch, 2002; Sahlin et al., 2014). We constrained the golden section search for vertical expansion factors to the range 10,000–200,000 based on preliminary estimates of RMSPE for temperature and diffuse attenuation coefficient data sets. We used a target precision of 1-m for the golden section search.

We generated three-dimensional grids of T and $K_d(Z)$ using the Bessel variogram model and vertical expansion factors from numerical optimization. For computational efficiency, we restricted search neighborhoods for ordinary kriging interpolation to the 500 points closest to a prediction location. Finally, we back-transformed predictions from the normal scale to the raw scale using linear interpolation between ranked normal scores and without extrapolation beyond the range of the data (Deutsch and Journel, 1997). We checked for spatial (area and depth) biases

in prediction errors through visual inspection of error plots. The magnitude of prediction errors was higher at shallow depths than deeper in the water column, especially at typical clines depths for T and $K_d(z)$ (Figs. S3-S4). However, prediction errors were unbiased at depths < 175 m and only slightly biased at depths ≥ 175 m, that are along the boundaries of the region and where observations are a small fraction of the total eastern Bering Sea continental shelf (Figs. S3-S4).

The effective attenuation coefficient is a term in the generalized visual reaction distance model but we did not have in situ measurements of the effective attenuation coefficient. Therefore, we assumed that the effective attenuation coefficient was 2.7 times the diffuse attenuation coefficient based on the mean ratio between the diffuse attenuation coefficient and beam attenuation coefficient for the wavelength of maximum transmission in clear natural waters (Duntley, 1967). We verified the veracity of this assumption based on the ratio between the diffuse attenuation coefficient and beam attenuation coefficient in the violet to green spectrum (412–555 nm) from optical profiles collected at bottom depths ≤ 200 that are available from the world-wide ocean optics database (Smart, 2000) (Table S1; Fig. S5).

4.3.3 *Downwelling irradiance*

We simulated underwater downwelling irradiance at the sea surface using the three dimensional diffuse attenuation coefficient grids coupled with a mechanistic global irradiance model that estimates solar and lunar illuminance at the surface of the earth, $E_d(0^+)$ (Janiczek and DeYoung, 1987). The model requires specifying atmospheric conditions (i.e. cloud cover) as an input, which we set to 'sun and moon obscured by thin clouds (sky condition = 2)' because the eastern Bering Sea is relatively cloudy during summer (Naik et al., 2015). The output of the Janiczek and DeYoung model is illuminance in units of lux, a photometric quantity, which we converted to quantum irradiance using the conversion of Thimijan and Heins (1983).

We simulated irradiance transmission through the sea surface using an albedo of 0.06, which is a representative value in the shortwave visible spectrum under overcast skies (Payne, 1972). We estimated irradiance at depth by numerically integrating the diffuse attenuation coefficient based on the Beer-Lambert equation as,

$$E_d(z) = (1 - 0.06)E_d(0^+)e^{-\int_1^z 2K_d(i)di} \quad (4)$$

where $E_d(z)$ is downwelling irradiance at depth z, and i is the 2-m depth bin centered at depth i. We calculated irradiance for grid cells at hourly time steps from June 1-August 31. Model predictions of sea surface irradiance produced unbiased estimates of irradiance measurements collected during summer bottom-trawl surveys of the eastern Bering Sea using shipboard light-sensitive archival tags and discrepancies between predictions and shipboard measurements were generally within an order-of-magnitude (Fig. S6). Validation efforts using light-sensitive pop-up archival tags attached to bottom-dwelling fishes suggest that our approach to modeling near-bottom downwelling irradiance using diffuse downwelling attenuation coefficients from bottom-trawl survey data and the Janiczek and DeYoung model yield accurate predictions of near-bottom irradiance (Chapter 4 Appendix).

4.3.4 *Analyzing spatial and diel variation in reaction distance*

We sought to: (1) characterize spatial variation in light and turbidity; (2) examine the extent to which spatial variation in light and turbidity potentially affects visual foraging opportunity for a walleye-pollock-like predator feeding visually on *Calanus* spp. copepods and juvenile walleye pollock; (3) characterize how areas with elevated turbidity affect visual predator-prey interactions (coastal areas and bottom-nepheloid layer); (4) assess how spatial variation in light, turbidity, and

temperature are likely to affect the capacity for predators and prey to mediate visual foraging opportunity, predation risk, and temperature-dependent metabolic rates through vertical migration.

We examined representative latitudinal and cross-shelf transects of downwelling diffuse attenuation coefficient, temperature, and predicted reaction distance. We selected transects that spatially overlap with areas that have been a focus of sustained oceanographic monitoring: the 70-m isobath, 57°N in-line with the NOAA's Pacific Marine Environmental Laboratory's (PMEL) M2 mooring, 62° in-line with PMEL's M8 mooring, and at 64.5°N in the vicinity of Distributed Biological Observatory #2 (Fig. 4.1).

4.4 RESULTS

4.4.1 *Varation in diffuse attenuation coefficient and optical depth based on three-dimensional grids*

There was considerable spatial variation in water clarity, which contributes to spatial variation in the transmission of light to deeper in the water column (Figs. 4.2A–B). Near-bottom water clarity was lower in the northern Bering Sea than the southeastern Bering Sea, as shown by patterns of the downwelling diffuse attenuation coefficient 6-m above bottom (Fig. 4.2A). Near-bottom water clarity was also lower in shallow areas along the coast of the Alaska mainland, as shown by the cross-shelf gradient in the downwelling diffuse attenuation coefficient, especially north of Nunivak Island and in Norton Sound (Fig. 4.2A). Near-bottom water clarity was generally highest along the continental shelf break. Optical depth was generally higher in deeper areas, as expected, although the area west of 170°W between ~58°N and 62°N was darker than in areas of similar depth further south. The darker area is the result of a subsurface light attenuating layer that

is presumably associated with deep chlorophyll maximum around the pycnocline and a bottom-associated nepheloid layer of unknown origin (Chapter 2; Rohan et al., 2021).

4.4.2 *Spatial, seasonal, and diel variation in reaction distance*

Along the 57°N transect on the solstice, diel variation in surface light causes considerable diel variation in reaction distance to juvenile walleye pollock and copepods (Fig. 4.3A-F). West of 162°W and east of 170°W on the solstice, visual foraging was minimally constrained by reaction distance as shown by $r_{wp} > 2.8$ m throughout the water column and r_{cope} between 10.0 cm and 11.0 cm throughout the water column (Fig. 4.3A, E). In the outer domain west of 170°W, near surface reaction distances to copepods near the surface were similar to the near surface reaction distance in the middle domain but near-bottom reaction distances were shorter (r_{cope}: 8.8–9.6 cm) due to lower near-bottom turbidity. West of 159°W in the shallow inner domain (thermally unstratified area), reaction distance to copepods were near the maximum r_{cope} (11.4–11.6 cm) throughout the water (Fig. 4.3C). In the inner domain, r_{wp} was shorter than in the middle and outer domain (2.30–2.70 m) with reaction distance generally decreasing towards the coast (Fig. 4.4E). Reaction distances at midnight were much lower than reaction distances at noon (Figs. 4.3D,F). At midnight on the solstice in the middle and outer domain west of 162°W, near-surface r_{wp} was 1.8–1.9 m, near-bottom r_{wp} <0.1 m, near-surface r_{cope} was 5.0–6.5 cm and near-bottom $r_{cope} < 0.2$ cm. At midnight on the solstic in the inner domain east of 159°W, near-surface r_{wp} was ~1.6 m and near-bottom r_{wp} was 0.2–0.6 m, while near-surface r_{cope} was 6.0–7.0 cm and near-bottom r_{cope} was 0.5–2.0 cm. At midnight, reaction distances decreased with depth.

Along the 62°N transect on the solstice, diel variation in light drives diel variation in reaction distance to 15-cm juvenile walleye pollock and *Calanus* spp. copepods deep in the bottom

layer over stratified waters of the continental shelf (Figs. 4.4C-F). At noon on the solstice in the inner domain east of 168°W, reaction distances to juvenile walleye pollock and copepods decrease closer to shore because of higher turbidity; near-surface r_{wp} decreases from 2.6 to 1.5 m, near-bottom r_{wp} decreases from 2.0–1.1 m, and r_{cope} decreases from 11.4 cm to 9.0 cm. However, reaction distances are near maximum in the mixed layer except in the turbid inner domain east of ~168°W at bottom depths ≤ 25 m (where the mixed layer extends to the bottom; Figs 4.4D-F). At noon on the solstice in the stratified middle domain west of 169°W, reaction distances to 15-cm juvenile walleye pollock in the mixed layer were 90–99% of maximum (2.80–2.95 m) and declined near-bottom (in the bottom nepheloid layer) to 74–81% of maximum reaction distance (2.20–2.40 m). In the same area, reaction distances to copepods were 83–95% of maximum reaction distances (9.6–11.0) cm near the surface and 90–99% of the maximum in the nepheloid layer (11.0–11.4 cm). At midnight on the solstice along the 62°N transect, reaction distances near the surface were effectively the same as during the day but were lower deeper in the water column. In the inner domain east of 168°W on the solstice at midnight, near-bottom r_{wp} was 0.20–0.60 m (7–20% of maximum) and r_{cope} is 0.6–4.0 cm (5–35% of maximum).

In contrast, there was little diel variation in reaction distance to juvenile walleye pollock and copepods along the 64.5°N transect on the solstice due to the effects of long day length and shallow bottom depth (Fig. 4.5C-F). As with areas to the south, r_{wp} (Fig. 4.5C) and r_{cope} (Fig. 4.5E) were lower closer to the coast than offshore due to higher turbidity along the coast (Fig. 4.5B). East of 166°W at bottom depths < 25 m, near-surface and near-bottom r_{wp} were ~2.00 m and ~1.40–1.50 m, respectively, and did not differ between noon and midnight (Fig. 4.5C–D). West of 168°W at bottom depths > 30 m, near-surface r_{wp} was 2.30–2.70 m at noon and midnight, while near-bottom r_{wp} changed from 2.40–2.80 m at noon to 1.80–2.30 m at midnight (Fig. 4.5C–D).

East of 166°W on the solstice, near-surface r_{cope} was ~10.8 cm at noon and midnight, while near-bottom r_{cope} changed from 9.0–10.0 cm at noon to 7.0–9.0 cm at midnight (Fig. 4.5E–F). West of 168°W, near-surface r_{cope} was near the maximum (11.4–11.6 cm) at noon and midnight, while near-bottom r_{cope} changed from 11.3–11.4 cm at noon to 7.5–9.5 cm at midnight (Fig. 4.5E–F).

The diel latitudinal gradient described for transects above was also evident along north-south gradients. Here, I examined vertical profiles of reaction distance at midnight along the 70-m isobath (Figs. 4.6D,F). At noon, near-surface r_{wp} was 2.80–2.96 and r_{cope} is 9.9–10.8 cm for the entire transect. At midnight on the solstice, near-surface r_{wp} (2.10–2.30 m) and r_{cope} (6.0–8.0 cm) were shorter at the south end of the 70-m isobath (57°–58°N) but reaction distances did not change between noon and midnight in the north. At the top of the bottom layer in the south, r_{wp} varied from 2.80–2.90 m at noon to 0.90–1.10 m at midnight while r_{cope} showed even greater diel variation, from 10.8–11.0 cm at noon to 1.5–2.0 cm at midnight. At the northerly sections of the 70-m isobath, reaction distances at the top of the bottom layer were relatively unaffected by diel variation (r_{wp} changed from 2.80–2.90 m at noon to 2.70–2.80 m at midnight; r_{cope} changed from 10.3–11.0 cm at noon to 9.0–10.7 cm at midnight). In the bottom nepheloid layer reaction distances to walleye pollock were 71–81% of maximum (2.10–2.40 m) while reaction distances to copepods were 91–98% of maximum (10.5–11.3 cm; Figs. 4.6C,E).

The above diel patterns of reactive distance changed markedly in later summer (Fig. 4.7D–F). Although midday reaction distances did not change between June 22 and August 22, shorter days reduced the duration of the midday foraging period with the fewest constraints on visual foraging (Supplementary Video 1–3). At high latitudes (e.g., 62°N), lower light levels at midnight in August reduced reaction distances in the mixed layer and upper portion of the bottom layer across latitudes (Supplementary Video 1–3). Although extremely low reaction distances extend

throughout the water column earlier in the evening at low latitudes (~21:00 at 57°N in August) compared to high latitudes (~23:00 at 62°N in August), visual constraints near the seafloor started earlier in the evening at high latitudes due to the nepheloid layer (Supplementary Video 3).

4.5 Discussion

Spatial patterns of water clarity and latitudinal variation in light strongly influence spatial patterns of visual foraging opportunity and the extent of visual predation refugia during summer in the eastern Bering Sea. Our results suggest there is little refuge from visual predation by a walleye-pollock-like predator in the pelagic habitat on the eastern Bering Sea continental shelf, at least at midday during summer. At night, the extent of predation refugia varies seasonally and by latitude, being much larger to the south than in the north. Seasonal variation in light regime plays an important role in regulating the extent of nocturnal predation refugia. Variation in water clarity contributed to spatial variation in visual foraging opportunity that differed between *Calanus* spp. and 15-cm juvenile walleye pollock prey.

Our results challenge a common assumption that inhabiting deep water reduces visual predation risk during the day. Although pelagic predators may be able to reduce predation risk by following isolumes as the sun rises and sets, visual reaction distances were well above zero during midday, indicating that the daytime pelagic environment of the eastern Bering Sea offers less refuge from visual predation by a walleye-pollock-like predator during summer than might have been assumed. Similarly, copepods are also afforded little predation refuge at depth. Midday reaction distances to copepods were higher in the bottom layer than in the surface layer in many areas (e.g. along most of the 70-m isobath north of 59°N) because light did not limit visual detection of prey and turbidity was at a level that maximized reaction distance in the generalized

visual reaction distance model. Although this may seem counterintuitive under classic visibility theory (focused on absolute visual range; Aksnes & Utne [1997]), behavioral visual foraging experiments have shown that reaction distances and consumption rates of some zooplanktivorous fishes are higher at intermediate levels of water clarity than under clear-water conditions (Utne-Palm, 2002). This dynamic is included in the generalized visual reaction distance model, which substantially outperforms models based on classic visibility theory when fitted to data from piscivore and planktivore visual reaction distance experiments (Chapter 1).

Despite the lack of a daytime predation refuge, spatial variation in turbidity contributes to asymmetric patterns of variation in reaction distance for a walleye-pollock-like predator reacting to *Calanus* spp. and 15-cm juvenile walleye pollock in the eastern Bering Sea. For example, in the bottom-associated nepheloid layer on the middle and outer continental shelf, reaction distance to *Calanus* spp. was ~10.5–11.6 cm at noon on the solstice, which is 0–10% less than the maximum reaction distance of 11.6 cm. Meanwhile, reaction distances to juvenile walleye pollock were ~2.10–2.40 m, (~19–29% less than the maximum reaction distance of 2.96 m; Fig. 1S). The volume of water searched by a cruising visual predator (i.e., search volume) changes according to the predator's field of view, which scales as the square of reaction distance if a predator's swimming speed is constant (search volume = swimming speed × πr^2 or search volume = swimming speed × $0.5\pi r^2$). Thus, the search volume for *Calanus* spp. in the nepheloid layer at noon on the solstice is approximately 83–100% of the maximum search volume and search volume for 15-cm juvenile walleye pollock is 50–66% of the maximum search volume. Further south (e.g., 57° N), in areas without a nepheloid layer, near-bottom reaction distances of walleye pollock to *Calanus* spp. was 10.5–11.0 cm in the middle domain and 8.8–9.6 cm in the outer domain which corresponds with 83–91% and 58–69% of maximum search volume, respectively. These areas had reaction distances

to juvenile walleye pollock of 2.90–2.96, corresponding with 96–100% of maximum search volume. All else being equal, this suggests the bottom nepheloid layer may lower daytime predation risk for individual 15-cm juvenile walleye pollock and increase opportunities to forage on *Calanus* spp. (Duffy-Anderson et al., 2016; Eisner et al., 2020a).

It is likely that vertical migration behaviors of walleye pollock will vary with latitude due to variation in visual foraging conditions. In pelagic species, vertical migration is an adaptive behavior that varies due to trade-offs between predation risk and growth potential (DeRobertis, 2002; Gjelland et al., 2009; Hays, 2003; Langbehn et al., 2019). These trade-offs are mediated by light and, at high latitudes, the amplitude and timing of diel vertical migration (e.g., little synchronized diel vertical migration during 24-hour daylight or darkness) (Benoit et al., 2010; Darnis et al., 2017; Hobbs et al., 2018). Previous studies have examined the extent to which diel vertical migration of walleye pollock is influenced by time of day, season, bottom light, ontogeny, physical structure (temperature and salinity), chlorophyll concentrations, currents, bottom depth, prey densities, predator densities, and trade-offs between foraging opportunity and predation risk (Adams et al., 2009; Bailey, 1989; Duffy-Anderson et al., 2003; Kotwicki et al., 2015, 2009; Parker-Stetter et al., 2015; Schabetsberger et al., 2000; Smart et al., 2013; Swartzman et al., 2002). However, research has not been conducted to characterize how diel vertical migration of walleye pollock varies with latitude.

Due to gaps in knowledge about the predator-prey systems and apparent optical properties, we made simplifying assumptions in order to characterize spatial variation in effective attenuation coefficient and reaction distance. These assumptions are related to the angular structure and spectrum of the radiance field, prey morphology, and predator vision system. In our model, we assumed that predators were viewing prey along a horizontal plane, which may not be a realistic

representation of walleye pollock predator-prey interactions because it is generally advantageous for predators and prey to avoid horizontal viewing angles. Generally, prey viewed from below have higher contrast and prey viewed from above have low contrast (Johnsen et al., 2014; Thetmeyer and Kils, 1995). This angle-dependent contrast is represented by the angular terms in the generalized visual reaction distance model (Eqn. 1). However, there is no information on the distribution of viewing angles between walleye pollock and their prey. We also did not conside ontogenetic shifts in shifts in spectral sensitivity and acuity that may affect reaction distance. Based on minimum separable angle between cone photoreceptors, walleye pollock visual acuity improves ontogenetically, but reaches an asymptote by the time the fish reaches ~30 cm fork length (Zhang and Arimoto, 1993). The retinae of preflexion walleye pollock larvae is entirely composed of single cone photoreceptors with peak absorbance (λ_{max}) at 520±3.11 nm (Britt et al., 2001). Later life stages of walleye pollock from Puget Sound, Washington, USA have retinal pigments with peak absorbances in the blue-green to green (λ_{max} = 498 nm), green (506 nm), and ultraviolet-A (360 nm) (Beatty, 1969). These ontogenetic. Predator body size may also affect reaction distance, as larger predators may be more successful at capturing prey over longer distances.

The above assumptions highlight future research needed to improve knowledge of light-and-turbidity-dependent reaction distances for the predator-prey system, in situ validation of the relationship between diffuse attenuation coefficient and effective attenuation coefficient, fine-scale patterns of viewing angles between predators and prey, and spectral sensitivity of adult walleye pollock may improve understanding of spatial variation in visual foraging opportunity. Combining monitoring of prey densities with water clarity monitoring would allow the generalized visual reaction distance model to be used to estimate encounter and consumption rates which could

then be combined with a temperature-dependent bioenergetics model to estimate habitat specific growth rates.

Our findings reinforce the hypothesis that spatial and temporal variation in environmental conditions that include bottom depth, light, and water clarity lead to differences in visual foraging opportunity and predation risk. Effects of variation in water clarity are largely a result of short-term (sub-yearly) variation physical and biological properties, whereas periodic variation in light and bottom depth change over longer periods that scarcely change at human time scales.

4.6 REFERENCES

Adams CF, Foy RJ, Kelley JJ, Coyle KO (2009) Seasonal changes in the diel vertical migration of walleye pollock (*Theragra chalcogramma*) in the northern Gulf of Alaska. Environ Biol Fishes 86:297–305.

Aksnes DL (2007) Evidence for visual constraints in large marine fish stocks. Limnol Oceanogr 52:198–203.

Aksnes DL, Nejstgaard J, Sædberg E, Sørnes T (2004) Optical control of fish and zooplankton populations. Limnol Oceanogr 49:233–238.

Aksnes DL, Utne ACW (1997) A revised model of visual range in fish. Sarsia 82:137–147.

Bailey KM (1989) Interaction between the vertical distribution of juvenile walleye pollock *Theragra chalcogramma* in the eastern Bering Sea, and cannibalism. Mar Ecol Prog Ser 53:205–213.

Beatty DD (1969) Visual pigments of the burbot, *Lota lota*, and seasonal changes in their relative proportions. Vision Res 9:1173–1183.

Benoit D, Simard Y, Gagné J, Geoffroy M, Fortier L (2010) From polar night to midnight sun: Photoperiod, seal predation, and the diel vertical migrations of polar cod (*Boreogadus saida*) under landfast ice in the Arctic Ocean. Polar Biol 33:1505–1520.

Bhandiwad A, Johnsen S (2011) The effects of salinity and temperature on the transparency of the grass shrimp *Palaemonetes pugio*. J Exp Biol 214:709–716.

Britt LL, Loew ER, McFarland WN (2001) Visual pigments in the early life stages of Pacific northwest marine fishes. J Exp Biol 204:2581–2587.

Buckley TW, Livingston PA (1994) A bioenergetics model of walleye pollock (*Theragra chalcogramma*) in the Eastern Bering Sea: Structure and documentation. NOAA Tech Memo NMFS-AFSC-:55.

Buckley TW, Ortiz I, Kotwicki S, Aydin K (2016) Summer diet composition of walleye pollock and predator–prey relationships with copepods and euphausiids in the eastern Bering Sea, 1987–2011. Deep Sea Res Part II Top Stud Oceanogr 134:302–311.

Chehata M, Jasinski D, Monteith MC, Samuels WB (2007) Mapping three-dimensional water-quality data in the Chesapeake Bay using geostatistics. J Am Water Resour Assoc 43:813–828.

Ciannelli L, Brodeur RD, Buckley TW (1998) Development and application of a bioenergetics model for juvenile walleye pollock. J Fish Biol 52:879–898.

Cokelet ED (2016) 3-D water properties and geostrophic circulation on the eastern Bering Sea shelf. Deep Sea Res Part II Top Stud Oceanogr 134:65–85.

Cullen JJ (2015) Subsurface chlorophyll maximum layers: Enduring enigma or mystery solved? Ann Rev Mar Sci 7:207–239.

Danielson S, Eisner L, Weingartner T, Aagaard K (2011) Thermal and haline variability over the central Bering Sea shelf: Seasonal and interannual perspectives. Cont Shelf Res 31:539–554.

Darnis G, Hobbs L, Geoffroy M, Grenvald JC, Renaud PE, Berge J, Cottier F, Kristiansen S, Daase M, Søreide JE, Wold A, Morata N, Gabrielsen T (2017) From polar night to midnight sun: Diel vertical migration, metabolism and biogeochemical role of zooplankton in a high Arctic fjord. Limnol Oceanogr 62:1586–1605.

DeRobertis A (2002) Size-dependent visual predation risk and the timing of vertical migration: An optimization model. Limnol Oceanogr 47:925–933.

De Robertis A, Ryer CH, Veloza A, Brodeur RD (2003) Differential effects of turbidity on prey consumption of piscivorous and planktivorous fish. Can J Fish Aquat Sci 60: 1517–1526.

Deutsch C V. (2002) Geostatistical Reservoir Modeling. Oxford University Press, New York, NY.

Deutsch C V., Journel AG (1997) GSLIB: Geostatistical Software Library and User's Guide, Second edi. Oxford University Press, New York.

Duffy-Anderson JT, Barbeaux SJ, Farley E, Heintz R, Horne JK, Parker-Stetter SL, Petrik C, Siddon EC, Smart TI (2016) The critical first year of life of walleye pollock (*Gadus chalcogrammus*) in the eastern Bering Sea: Implications for recruitment and future research. Deep Res Part II Top Stud Oceanogr 134:283–301.

Duffy-Anderson JT, Ciannelli L, Honkalehto T, Bailey KM, Sogard SM, Springer AM, Buckley T (2003) Distribution of age-1 and age-2 walleye pollock in the North Pacific: sources of variation, implications for higher trophic levels and climate change. 26th Annu Larval Fish Conf:381–394.

Duntley SQ (1967) Visibility in the oceans. Opt Spectra Fourth Qua:64–69.

Dwyer DA, Bailey KM, Livingston PA (1987) Feeding habits and daily ration of walleye pollock (*Theragra chalcogramma*) in the Eastern Bering Sea, with special reference to cannibalism. Can J Fish Aquat Sci 44:1972–1984.

Eisner LB, Yasumiishi EM, Andrews AG, O'Leary CA (2020a) Large copepods as leading indicators of walleye pollock recruitment in the southeastern Bering Sea: Sample-Based and spatio-temporal model (VAST) results. Fish Res 232:105720.

Eisner LB, Zuenko YI, Basyuk EO, Britt LL, Duffy-Anderson JT, Kotwicki S, Ladd C, Cheng W (2020b) Environmental impacts on walleye pollock (*Gadus chalcogrammus*) distribution across the Bering Sea shelf. Deep Sea Res Part II Top Stud Oceanogr:104881.

Feely RA, Massoth GJ, Paulson AJ, Lamb MF, Martin EA (1981) Distribution and elemental composition of suspended matter in Alaskan coastal waters. NOAA Tech Memo ERL-PMEL-2:119.

Frost BW (1974) *Calanus marshallae*, a new species of calanoid copepod closely allied to sibling species *Calanus finmarchicus* and *Calanus glacialis*. Mar Biol 26:77–99.

Giske J, Aksnes DL, Fiksen Ø (1994) Visual predators, environmental variables and zooplankton mortality risk. Vie Milieu 44:1–9.

Gjelland KØ, Bøhn T, Horne JK, Jensvoll I, Knudsen FR, Amundsen PA (2009) Planktivore vertical migration and shoaling under a subarctic light regime. Can J Fish Aquat Sci 66:525–539.

Gribov A, Krivoruchko K (2020) Empirical Bayesian kriging implementation and usage. Sci Total Environ 722:137290.

Hansen AG, Beauchamp DA (2015) Latitudinal and photic effects on diel foraging and predation risk in freshwater pelagic ecosystems. J Anim Ecol 84:532–544.

Haraldsson M, Tönnesson K, Tiselius P, Thingstad TF, Aksnes DL (2012) Relationship between fish and jellyfish as a function of eutrophication and water clarity. Mar Ecol Prog Ser 471:73–85.

Hays GC (2003) A review of the adaptive significance and ecosystem consequences of zooplankton diel vertical migrations. Hydrobiologia 503:163–170.

Hobbs L, Cottier FR, Last KS, Berge J (2018) Pan-Arctic diel vertical migration during the polar night. Mar Ecol Prog Ser 605:61–72.

Holbrook B V., Hrabik TR, Branstrator DK, Mensinger AF (2013) Foraging mechanisms of age-0 lake trout (*Salvelinus namaycush*). J Great Lakes Res 39:128–137.

Holsman KK, Aydin K (2015) Comparative methods for evaluating climate change impacts on the foraging ecology of Alaskan groundfish. Mar Ecol Prog Ser 521:217–235.

Holsman KK, Ianelli J, Aydin K, Punt AE, Moffitt EA (2016) A comparison of fisheries biological reference points estimated from temperature-specific multi-species and single-species climate-enhanced stock assessment models. Deep Res Part II Top Stud Oceanogr 134:360–378.

Holsman KK, Ianelli JN, Aydin K, Spies I (2019) Multi-species supplement: 2019 Climate-enhanced multi-species Stock Assessment for walleye pollock, Pacific cod, and arrowtooth flounder in the Eastern Bering Sea. NPFMC Stock Assess Fish Eval Rep Groundf Resour Bering Sea/Aleutian Islands Reg:1–43.

Hurst TP (2007) Thermal effects on behavior of juvenile walleye pollock (*Theragra chalcogramma*): implications for energetics and food web models. Can J Fish Aquat Sci 64:449–457.

Huse G, Fiksen Ø (2010) Modelling encounter rates and distribution of mobile predators and prey. Prog Oceanogr 84:93–104.

Janiczek PM, DeYoung JA (1987) Computer programs for sun and moon illuminance with contingent tables and diagrams. United States Naval Observatory Circular No. 171. Washington, D.C.

Johnsen S (2014) Hide and seek in the open sea : Pelagic camouflage and visual countermeasures. Ann Rev Mar Sci 6:369–392.

Johnsen S, Gassmann E, Reynolds RA, Stramski D, Mobley C (2014) The asymmetry of the underwater horizontal light field and its implications for mirror-based camouflage in silvery pelagic fish. Limnol Oceanogr 59:1839–1852.

Kawana K (1975) Turbidity distribution of the Bering Sea in the summer. Bull Fac Fish Hokkaido Univ 26:73–86.

Kitano J, Bolnick DI, Beauchamp DA, Mazur MM, Mori S, Nakano T, Peichel CL (2008) Reverse evolution of armor plates in the threespine stickleback. Curr Biol 18:769–774.

Kotwicki S, Horne JK, Punt AE, Ianelli JN (2015) Factors affecting the availability of walleye pollock to acoustic and bottom trawl survey gear. ICES J Mar Sci 72:1425–1439.

Kotwicki S, De Robertis A, von Szalay P, Towler R (2009) The effect of light intensity on the availability of walleye pollock (*Theragra chalcogramma*) to bottom trawl and acoustic surveys. Can J Fish Aquat Sci 66:983–994.

Langbehn TJ, Aksnes DL, Kaartvedt S, Fiksen Ø, Jørgensen C (2019) Light comfort zone in a mesopelagic fish emerges from adaptive behaviour along a latitudinal gradient. Mar Ecol Prog Ser 623:161–174.

Langbehn TJ, Varpe Ø (2017) Sea-ice loss boosts visual search: Fish foraging and changing pelagic interactions in polar oceans. Glob Chang Biol 23:5318–5330.

Link J, Edsall TA (1996) The effect of light on lake herring (*Coregonus artedi*) reactive volume. Hydrobiologia 332:131–140.

Lovvorn JR, Baduini CL, Hunt Jr. GL (2001) Modeling underwater visual and filter feeding by planktivorous shearwaters in unusual sea conditions. Ecology 82:2342–2356.

Maes J, Limburg KE, van de Putte A, Ollevier F (2005) A spatially explicit, individual-based model to assess the role of estuarine nurseries in the early life history of North Sea herring, Clupea harengus. Fish Oceanogr 14:17–31.

Mazur MM, Beauchamp DA (2006) Linking piscivory to spatial-temporal distributions of pelagic prey fishes with a visual foraging model. J Fish Biol 69:151–175.

McCave IN (2019) Nepheloid layers, 3rd ed. Elsevier Ltd.

McManus DA, Smyth CS (1970) Turbid bottom water on the continental shelf of the northern Bering Sea. J Sediment Petrol 40:869–873.

Mordy CW, Devol A, Eisner LB, Kachel N, Ladd C, Lomas MW, Proctor P, Sambrotto RN, Shull DH, Stabeno PJ, Wisegarver E (2017) Nutrient and phytoplankton dynamics on the inner shelf of the eastern Bering Sea. J Geophys Res Ocean 122:2422–2440.

Moss JH, Farley E V., Feldmann AM, Ianelli JN (2009) Spatial distribution, energetic status, and food habits of eastern Bering Sea age-0 walleye pollock. Trans Am Fish Soc 138:497–505.

Mueter FJ, Ladd C, Palmer MC, Norcross BL (2006) Bottom-up and top-down controls of walleye pollock (*Theragra chalcogramma*) on the Eastern Bering Sea shelf. Prog Oceanogr 68:152–183.

Naik P, D'Sa EJ, Gomes H do R, Goés JI, Mouw CB (2013) Light absorption properties of southeastern Bering Sea waters: Analysis, parameterization and implications for remote sensing. Remote Sens Environ 134:120–134.

Naik P, Wang M, D'Sa EJ, Mordy CW (2015) Bering Sea optical and biological properties from MODIS. Remote Sens Environ 163:240–252.

Orlov AM, Benzik AN, Vedishcheva EV, Gafitsky SV, Gorbatenko KM, Goryanina SV, Zubarevich VL, Kodryan KV, Nosov MA, Orlova SY, Pedchenko AP, Rybakov MO, Sokolov AM, Somov AA, Subbotin SN, Taptygin MY, Firsov YL, Khleborodov AS, Chikilev VG (2019) Fisheries research in the Chukchi Sea at the RV «Professor Levanidov» in August 2019: some preliminary results. Tr VNIRO 178:206–220.

Parker-Stetter SL, Horne JK, Urmy SS, Heintz RA, Eisner LB, Farley E V. (2015) Vertical distribution of age-0 walleye pollock during late summer: Environment or ontogeny? Mar Coast Fish 7:349–369.

Payne RE (1972) Albedo of the sea surface. J Atmos Sci 29:959–970.

Pebsma EJ (2004) Multivariable geostatistics in S: The gstat package. Comput Geosci 30:683–691.

Pedersen J (2001) Hydroacoustic measurement of swimming speed of North Sea saithe in the field. J Fish Biol:1073–1085.

Persson L, Eklov P (1995) Prey refuges affecting interactions between piscivorous perch and juvenile perch and roach. Ecology 76:70–81.

Rohan SK, Kotwicki S, Kearney KA, Schulien JA, Laman EA, Cokelet ED, Beauchamp DA, Britt LL, Aydin KY, Zador SG (2021) Using bottom trawls to monitor subsurface water clarity in marine ecosystems. Prog Oceanogr. 194: 102254.

Rohan SK, Kotwicki S, Laman EA, Britt LL, Aydin K (2020) Deriving apparent optical properties from light measurements obtained using bottom-trawl-mounted archival tags. United States Department of Commerce, NOAA Technical Memorandum NMFS-AFSC-403, 91 p

Ryer CH, Lawton A, Lopez RJ, Olla BL (2002) A comparison of the functional ecology of visual vs. nonvisual foraging in two planktivorous marine fishes. Can J Fish Aquat Sci 59:1305–1314.

Ryer CH, Olla BL (1998) Effect of light on juvenile walleye pollock shoaling and their interaction with predators. Mar Ecol Prog Ser 167:215–226.

Ryer CH, Olla BL (1999) Light-induced changes in the prey consumption and behavior of two juvenile planktivorous fish. Mar Ecol Prog Ser 181:41–51.

Sahlin J, Mostafavi MA, Forest A, Babin M (2014) Assessment of 3D spatial interpolation methods for study of the marine pelagic environment. Mar Geod 37:238–266.

Schabetsberger R, Brodeur RD, Ciannelli L, Napp JM, Swartzman GL (2000) Diel vertical migration and interaction of zooplankton and juvenile walleye pollock (*Theragra chalcogramma*) at a frontal region near the Pribilof Islands, Bering Sea. ICES J Mar Sci 57:1283–1295.

Schwalbe MAB, Webb JF (2015) The effect of light intensity on prey detection behavior in two Lake Malawi cichlids, *Aulonocara stuartgranti* and *Tramitichromis* sp. J Comp Physiol A Neuroethol Sensory, Neural, Behav Physiol 201:341–356.

Sih A (1987) Prey refuges and predator-prey stability. Theor Popul Biol 31:1–12.

Smart J (2000) World-wide ocean optics database (WOOD). Oceanography 13:70–74.

Smart TI, Siddon EC, Duffy-Anderson JT (2013) Vertical distributions of the early life stages of walleye pollock (*Theragra chalcogramma*) in the Southeastern Bering Sea. Deep Res Part II Top Stud Oceanogr 94:201–210.

Sørnes TA, Aksnes DL (2006) Concurrent temporal patterns in light absorbance and fish abundance. Mar Ecol Prog Ser 325:181–186.

Stabeno PJ, Bell SW, Bond NA, Kimmel DG, Mordy CW, Sullivan ME (2019) Distributed Biological Observatory Region 1: Physics, chemistry and plankton in the northern Bering Sea. Deep Res Part II Top Stud Oceanogr 162:8–21.

Stabeno PJ, Farley E V., Kachel NB, Moore S, Mordy CW, Napp JM, Overland JE, Pinchuk AI, Sigler MF (2012) A comparison of the physics of the northern and southern shelves of the eastern Bering Sea and some implications for the ecosystem. Deep Res Part II Top Stud Oceanogr 65–70:14–30.

Stabeno PJ, Mordy CW, Sigler MF (2020) Seasonal patterns of near-bottom chlorophyll fluorescence in the eastern Chukchi Sea: 2010–2019. Deep Sea Res Part II Top Stud Oceanogr:104842.

Stevenson DE, Lauth RR (2019) Bottom trawl surveys in the northern Bering Sea indicate recent shifts in the distribution of marine species. Polar Biol 42:407–421.

Swartzman G, Napp J, Brodeur R, Winter A, Ciannelli L (2002) Spatial patterns of pollock and zooplankton distribution in the Pribilof Islands, Alaska nursery area and their relationship to pollock recruitment. ICES J Mar Sci 59:1167–1186.

Szabo I, Gardner GA (Grant A (1982) British Columbia pelagic marine copepoda : an identification manual and annotated bibliography. Szabo I (ed) Ottawa : Dept. of Fisheries and Oceans, Ottawa.

Thetmeyer H, Kils U (1995) To see and not be seen: the visibility of predator and prey with respect to feeding behaviour. Mar Ecol Prog Ser 126:1–8.

Thimijan RW, Heins RD (1983) Photometric, radiometric, and quantum light units of measure: A review or procedures for interconversion. HortScience 18:818–820.

Turesson H, Brönmark C (2007) Predator-prey encounter rates in freshwater piscivores: Effects of prey density and water transparency. Oecologia 153:281–290.

Utne-Palm A (2002) Visual feeding of fish in a turbid environment: Physical and behavioural aspects. Mar Freshw Behav Physiol 35:111–128.

Utne A (1997) The effect of turbidity and illumination on the reaction distance and search time of the marine planktivore Gobiusculus flavescens. J Fish Biol 50:926–938.

Ware DM (1978) Bioenergetics of pelagic fish: Theoretical changes in swimming speed and ration with body size. J Fish Res Board Canada 35:220–228.

Zhang X, Arimoto T (1993) Visual physiology of walleye pollock (*Theragra chalcogramma*) in relation to capture by trawl nets. ICES J Mar Sci 196:113–116.

Table 4.1. Parameters in the generalized visual reaction distance model and environmental simulation.

Term	Description	Value	Source
α	Sea surface albedo	0.06	(Payne, 1972)
$A_{p,cope}$	Area of copepod (m^2)	3e-6	Varpe and Fiksen (2010); Utne-Palm (1999)
$A_{p,rt}$	Area of 50-mm fork length juvenile rainbow trout (m^2)	4.25e-4	This study
$A_{p,wp}$	Area of 15-cm fork length walleye pollock (m^2)	0.003	This study
$C_{0,cope}$	Inherent Weber contrast of copepod (dimensionless)	0.3	Utne-Palm (1999)
$C_{0,wp}$	Inherent Weber contrast of walleye pollock (dimensionless)	0.5	Ruxton and Johnsen (2016); Langbehn et al. (2019)
$C_{0,rt}$	Inherent Weber contrast of juvenile rainbow trout	0.5	-
δ	Dynamic scaling function term (dimensionless)	0.539	Chapter 1
E'	Composite saturation parameter (dimensionless)	$E'=E_{max}/S_e=\tau_{rt}/(\lvert C_{0,rt}\rvert A_{p,rt})$ = 29,585.93	This study
E_{50}	Half-saturation term (µMol photons m^{-2} s^{-1})	1e-3	Light-dependent consumption rates from (Ryer and Olla (1999); Ryer et al. (2002)
E_b	Background irradiance (µMol photons m^{-2} s^{-1})	-	-
$E_d(0^+)$	Downwelling irradiance at the sea-surface (µMol photons m^{-2} s^{-1})	-	Janiczek and DeYoung (1987)
$E_d(z)$	Downwelling irradiance at depth z (µMol photons m^{-2} s^{-1})	-	-
E_{max}	Maximum irradiance processing capability of the retina ($\mu E \cdot m^{-2} \cdot s^{-1}$)	$E'=E_{max}/S_e$	Subsumed by E', not estimated independently.
h	Dynamic scaling function term (dimensionless)	2.052	Chapter 1
$\kappa(z)$	Effective attenuation coefficient at depth z (m^{-1})	$\kappa(z)= 2.7K_d(z)$	Duntley (1967)
$K_d(z)$	Downwelling diffuse attenuation coefficient (m^{-1}) at depth z	-	-
r_{cope}	Reaction distance of walleye pollock to *Calanus* copepod (m)	r_{cope}	This study

Term	Description	Value	Source
r_{wp}	Reaction distance of walleye pollock to 15-cm juvenile walleye pollock (m)	-	This study
S_e	Sensitivity threshold of the vision system for detecting changes in irradiance ($\mu E \cdot m^{-2} \cdot s^{-1}$)	$E' = E_{max}/S_e$	Subsumed by E', not estimated independently.
T	Temperature (°C)	-	-
τ_{rt}	Composite predator-prey interaction term for Chinook salmon reacting to 50 mm rainbow trout (m^2)	$\tau_{rt} = \lvert C_{0,rt} \rvert A_{p,rt} E' = 5.038$	Chapter 1
V_{prey}	Time-integrated search volume (m^3)	-	-
z	Depth (m)	-	-

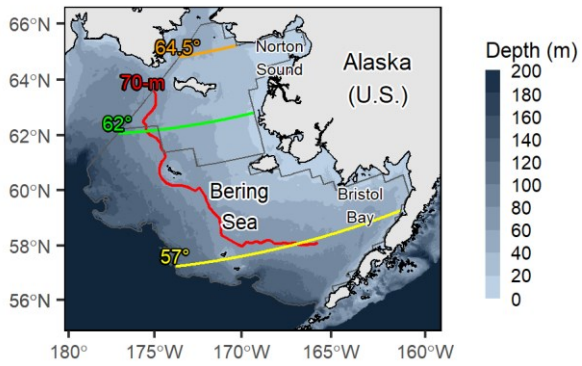

Figure 4.1. Map of study area.

Fill color shows bottom depth, NOAA Alaska Fishery Science Center's northeastern and eastern Bering Sea continental shelf survey areas and transect lines (57°, 60°, 62°, 64.5°, 70-m) used to show environmental conditions and model output.

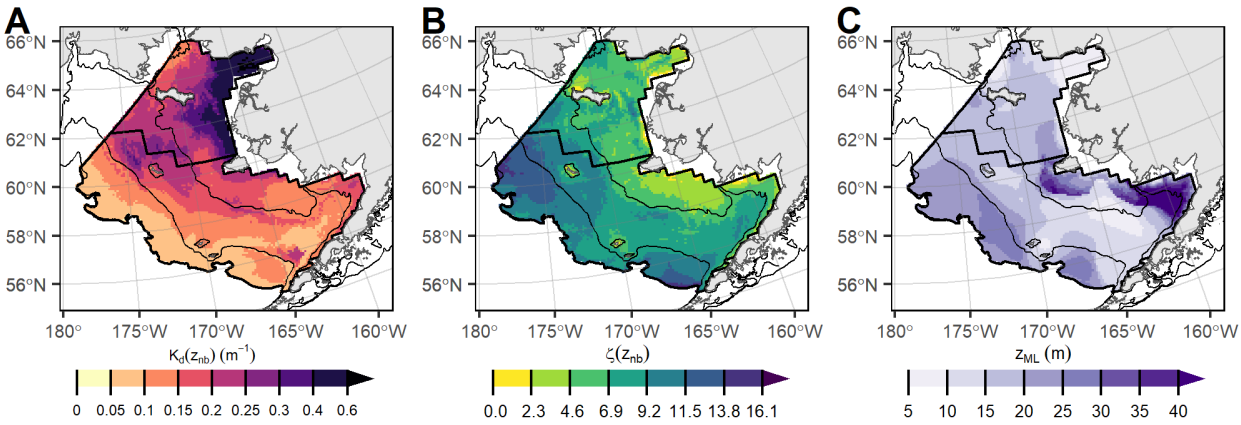

Figure 4.2. Maps of the diffuse attenuation coefficient at 6-m off-bottom, optical depth 6-m off-bottom, and mixed layer depth.

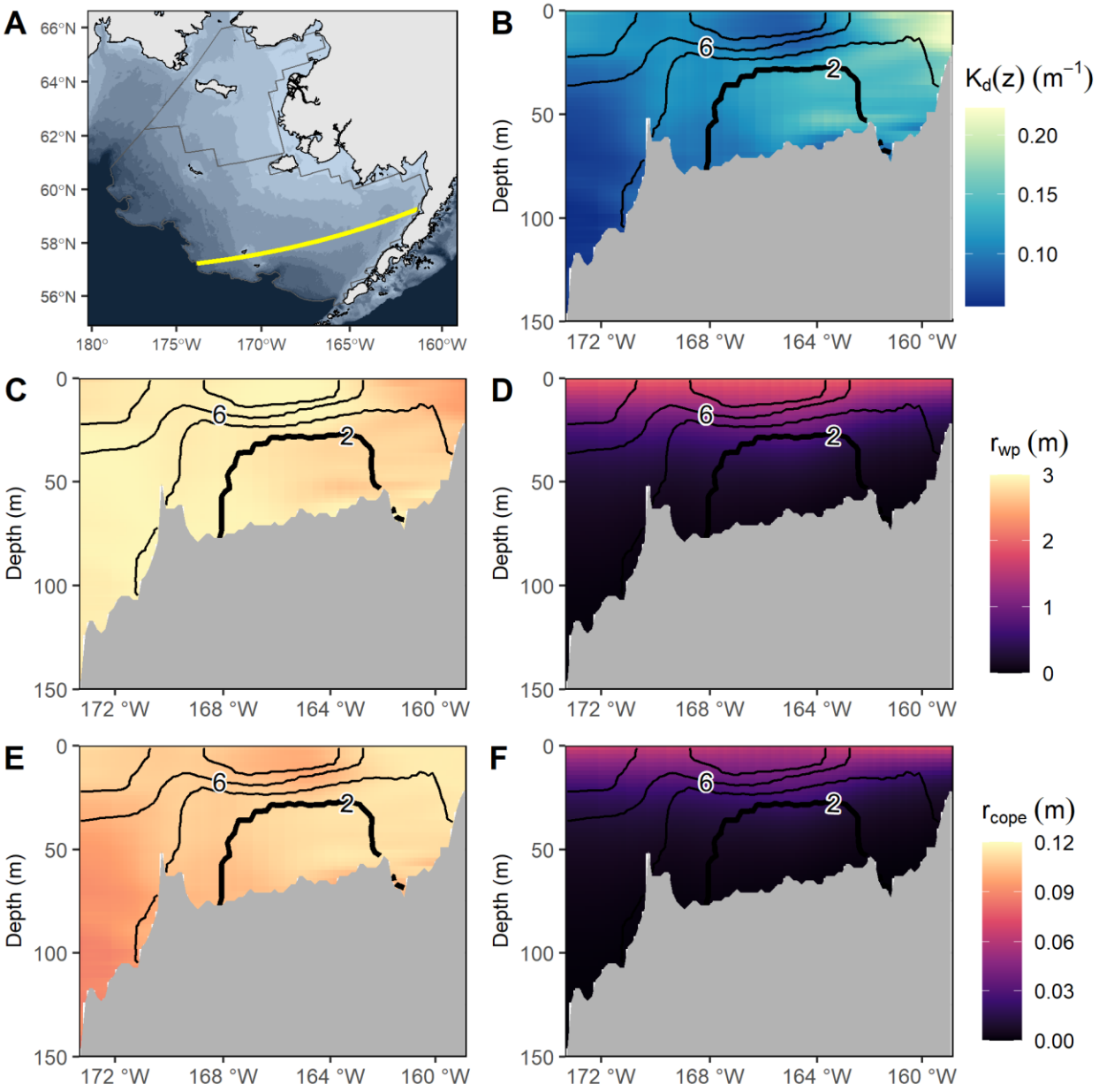

Figure 4.3. Transect (cross-section) at 57°N on June 22, 2017 (solstice) at local noon and local midnight.

Vertical structure diffuse attenuation coefficient, temperature, and predicted reaction distances of walleye pollock reacting to 15-cm walleye pollock and *Calanus* at local noon and local midnight on June 22, 2017 (solstice). Panels show (A) location of the transect; (B) diffuse attenuation coefficient; (C) reaction distance to 15-cm walleye pollock, r_{wp}, at noon; (D) r_{wp} at local midnight; (E) reaction distance to *Calanus*, r_{cope}, at noon; (F) r_{cope} at midnight. Contour lines on panels B–F denote temperature (°C); thick contour denotes the 2° C isotherm (i.e., cold pool).

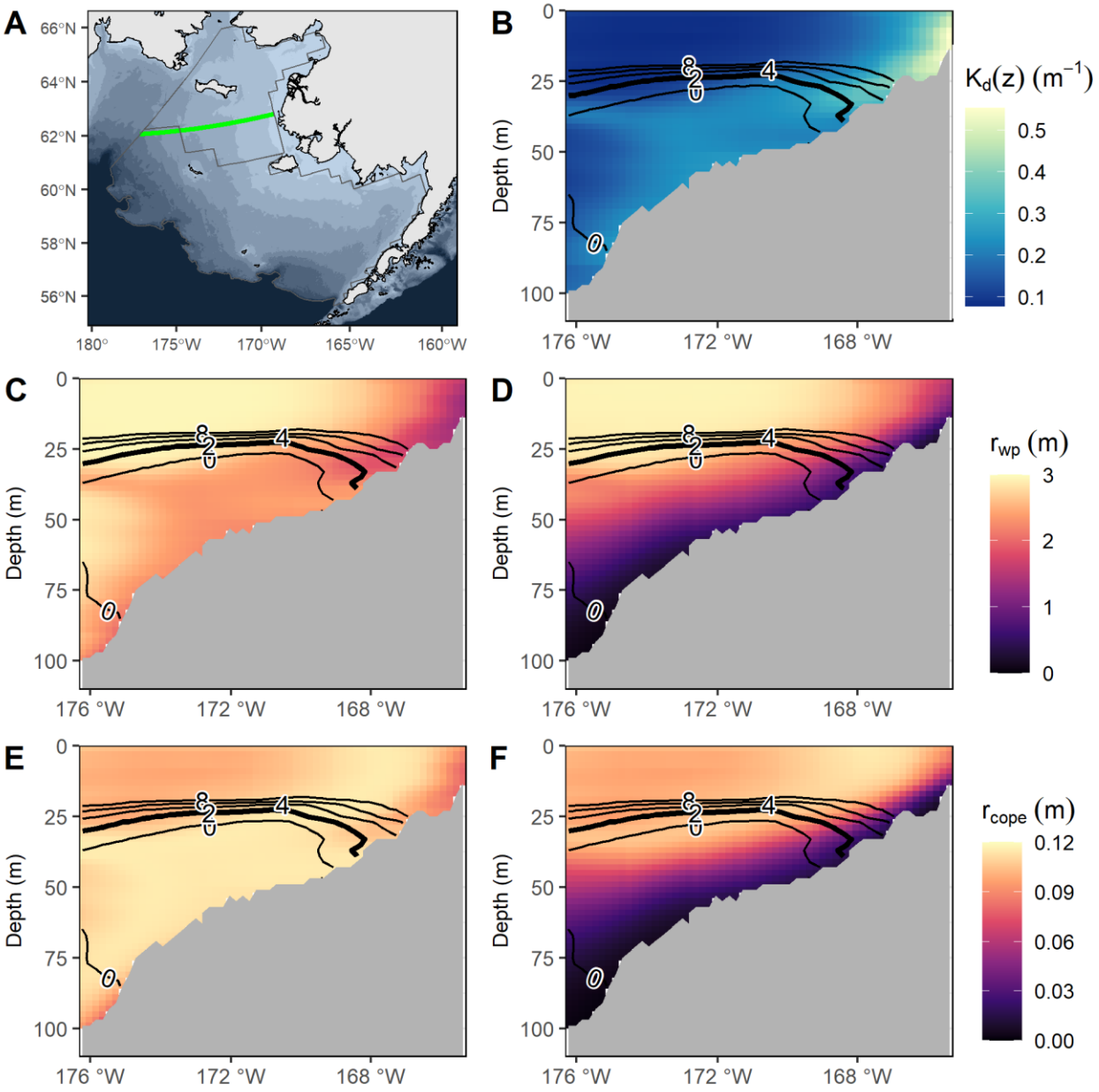

Figure 4.4. Transect (cross-section) at 62°N on June 22, 2017 (solstice) at local noon and local midnight.

Vertical structure diffuse attenuation coefficient, temperature, and predicted reaction distances of walleye pollock reacting to 15-cm walleye pollock and *Calanus* at local noon and local midnight on June 22, 2017 (solstice). Panels show (A) position of the 62°N transect; (B) diffuse attenuation coefficient; (C) reaction distance to 15-cm walleye pollock, r_{wp}, at noon; (D) r_{wp} at local midnight; (E) reaction distance to *Calanus*, r_{cope}, at noon. Contour lines on panels B–F denote temperature (°C); thick contour denotes the 2° C isotherm (i.e., cold pool).

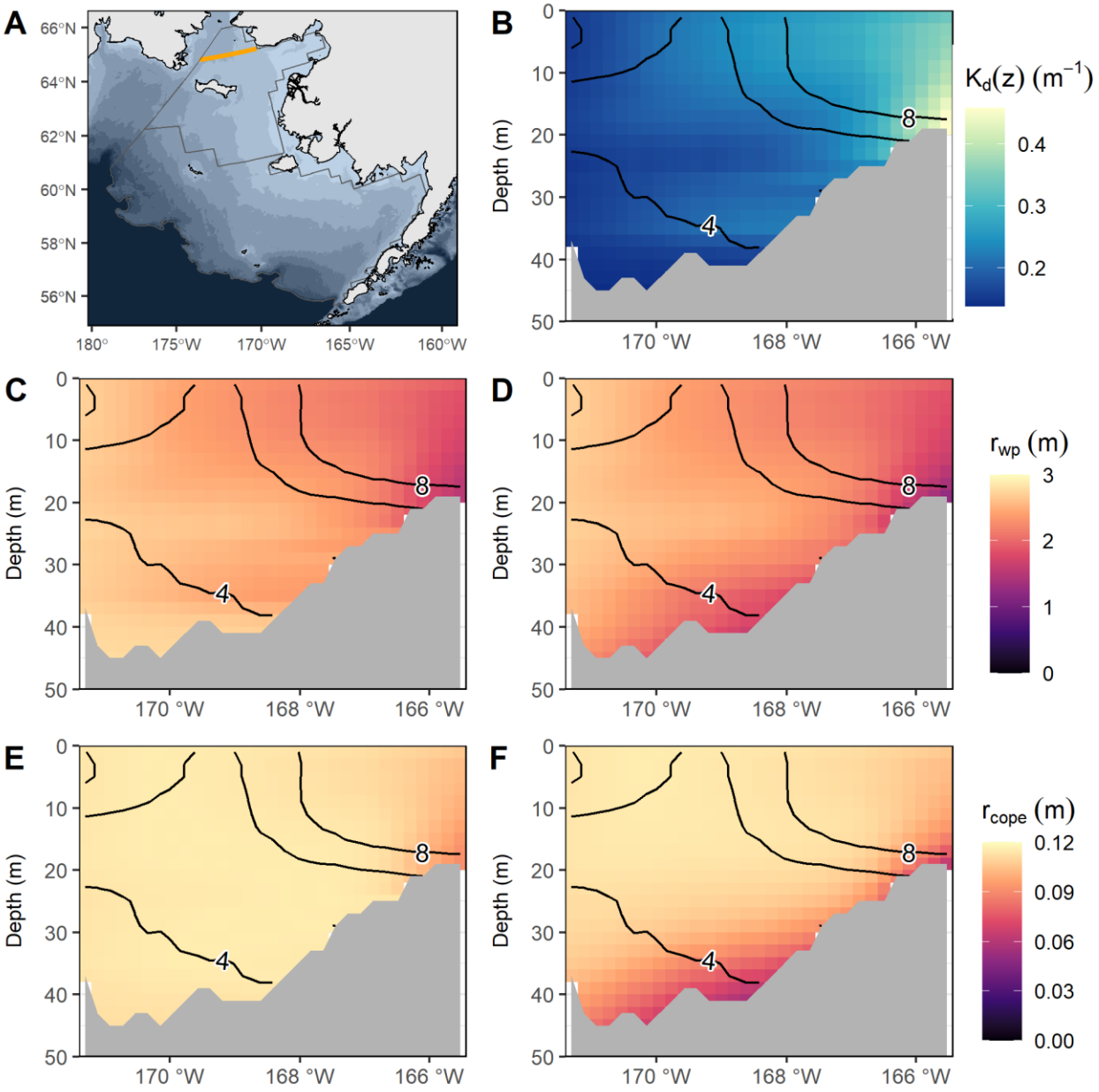

Figure 4.5. Transect (cross-section) at 64.5°N on June 22, 2017 (solstice) at local noon and local midnight.

Vertical structure diffuse attenuation coefficient, temperature, and predicted reaction distances of walleye pollock reacting to 15-cm walleye pollock and *Calanus* at local noon and local midnight on June 22, 2017 (solstice). Panels show (A) position of the 62°N transect; (B) diffuse attenuation coefficient; (C) reaction distance to 15-cm walleye pollock, r_{wp}, at noon; (D) r_{wp} at local midnight; (E) reaction distance to *Calanus*, r_{cope}, at noon. Contour lines on panels B–F denote temperature (°C); thick contour denotes the 2° C isotherm (i.e., cold pool).

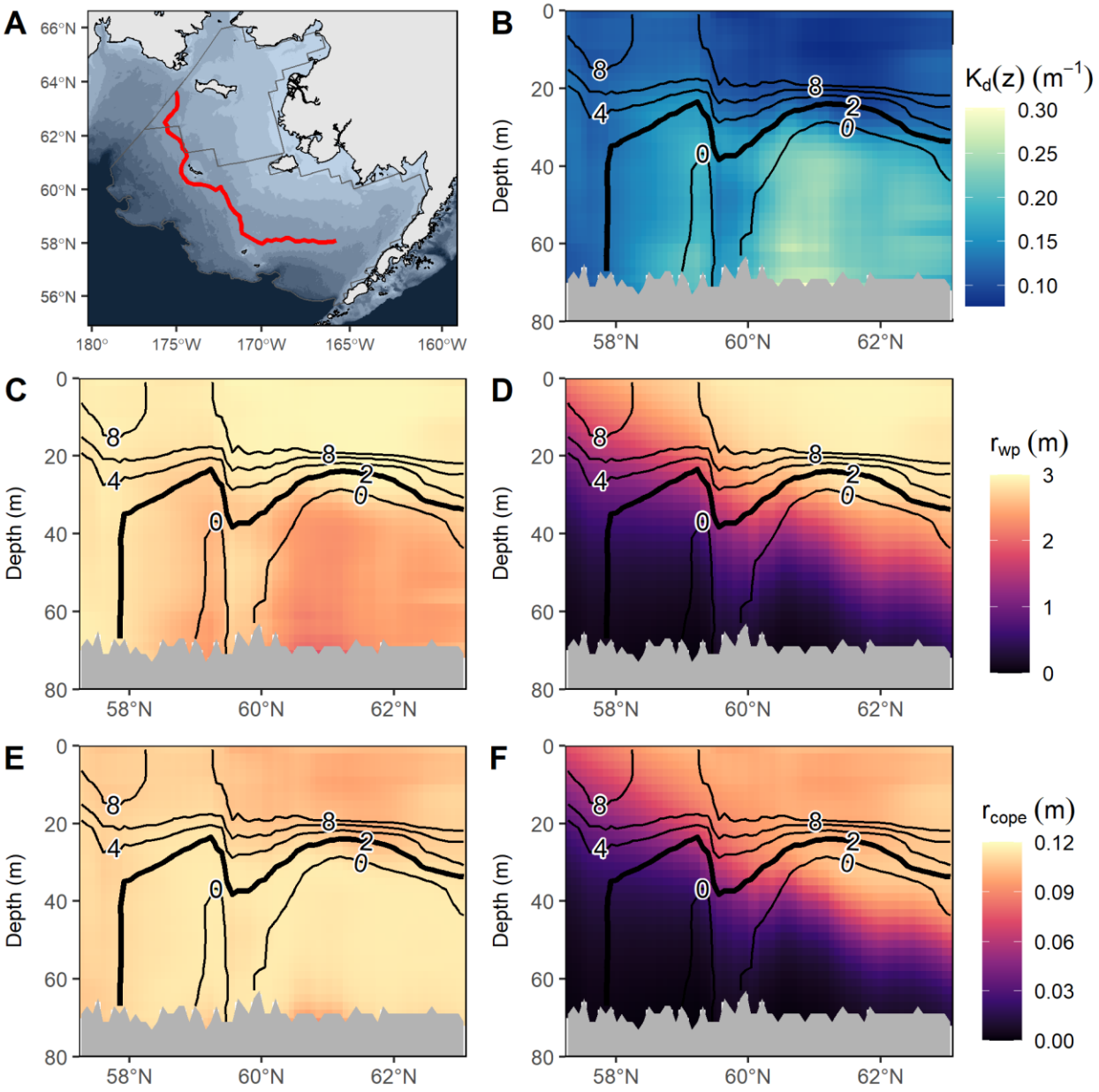

Figure 4.6. Transect (cross-section) along the 70-m isobath on June 22, 2017 (solstice) at local noon and local midnight.

Vertical structure diffuse attenuation coefficient, temperature, and predicted reaction distances of walleye pollock reacting to 15-cm walleye pollock and *Calanus* at local noon and local midnight on June 22, 2017 (solstice). Panels show: (A) location of the 70-m isobaths; (B) diffuse attenuation coefficient; (C) reaction distance to 15-cm walleye pollock, r_{wp}, at noon; (D) r_{wp} at local midnight; (E) reaction distance to *Calanus*, r_{cope}, at noon; (F) r_{cope} at midnight. Contour lines on panels B–F denote temperature (°C); thick contour denotes the 2° C isotherm (i.e., cold pool).

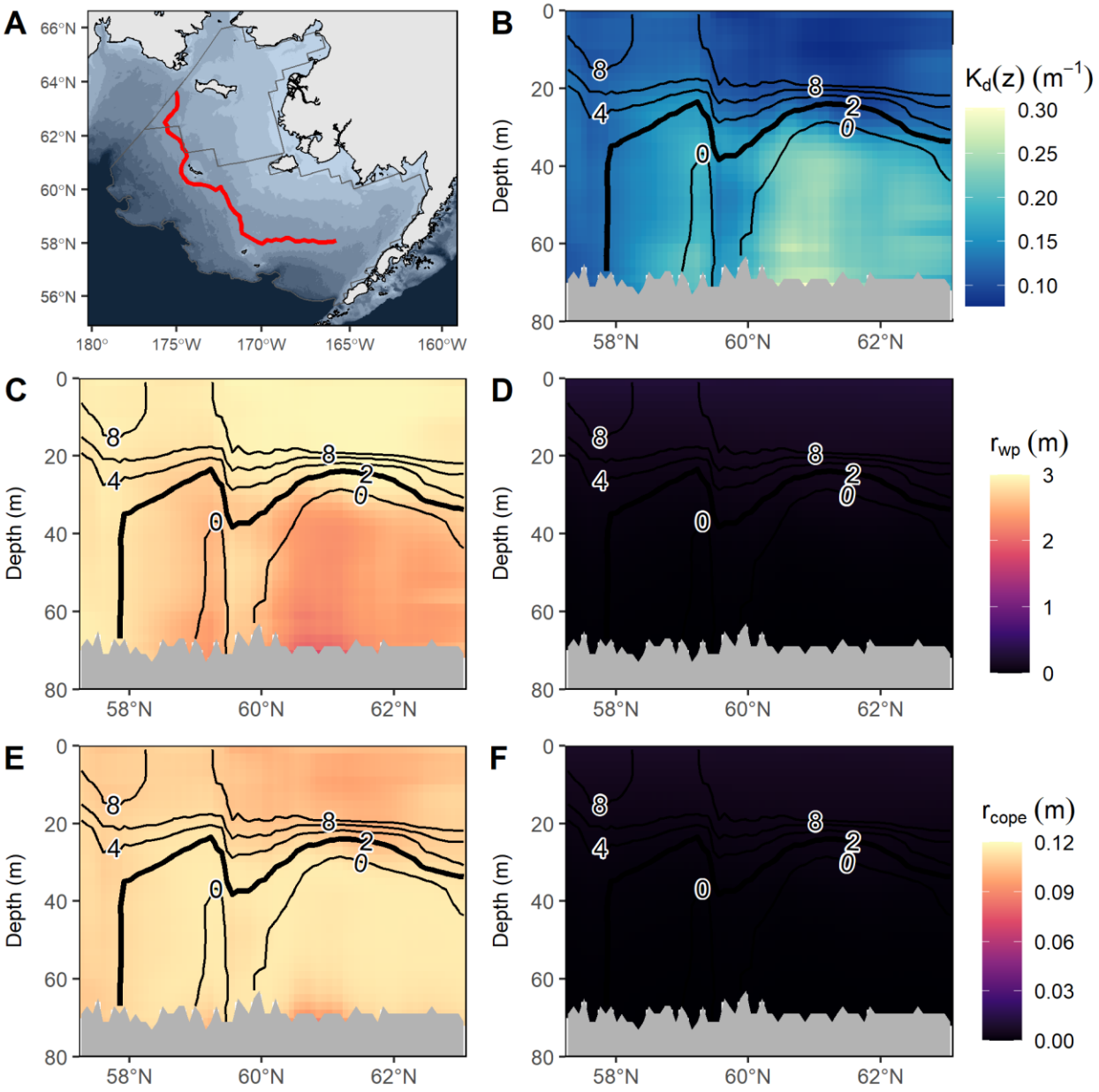

Figure 4.7. Transect (cross-section) along the 70-m isobath on August 22, 2017 (solstice) at local noon and local midnight.

Vertical structure diffuse attenuation coefficient, temperature, and predicted reaction distances of walleye pollock reacting to 15-cm walleye pollock and *Calanus* at local noon and local midnight on June 22, 2017 (solstice). Panels show: (A) location of the 70-m isobaths; (B) diffuse attenuation coefficient; (C) predicted reaction distance to 15-cm walleye pollock, r_{wp}, at noon; (D) r_{wp} at local midnight; (E) predicted reaction distance to *Calanus*, r_{cope}, at noon; (F) r_{cope} at midnight. Contour lines on panels B–F denote temperature (°C); thick contour denotes the 2° C isotherm (i.e., cold pool).

SYNTHESIS

This dissertation examines the role of light and water clarity in regulating visual predator-prey interactions, structuring habitat, and contributing to variation in fisheries catch rates and fisheries-independent surveys that monitor marine fish populations in the Bering Sea and Chukchi Sea. Since 2017, the Bering and Chukchi Seas have seen changes in marine fish distributions, and ecosystem structure due to climate-mediated changes in ocean conditions (Huntington et al., 2020; Stevenson and Lauth, 2019). Findings highlight the importance of light as an ecological factor that influences visually mediated behaviors (e.g., migration, visual foraging, interactions with fishing gears) that show pronounced variation across latitudinal gradients in light regime and spatial gradients in water clarity. If distributions of marine fish communities continue to change in the region, the visual environment will likely play a major role in determining ecosystem responses because of extreme latitudinal and seasonal variation in light. Changes in the visual environment may be exacerbated by climate driven changes in water clarity due to shifting patterns of primary (Brown and Arrigo, 2012; Lewis et al., 2020) and secondary (Grebmeier et al., 2018) production, along with increasing precipitation (e.g., Newman et al., 2021) that has the potential to contribute to coastal darkening (Aksnes et al., 2009; Opdal et al., 2019) through increased run-off of chromophoric dissolved organic matter and sediment into the Bering and Chukchi Seas. Overall, this work suggests that changes in visual processes due to climate-mediated changes in fish distribution should remain a focus of research in the Bering Sea and Chukchi Sea and other high latitude systems where climate change is driving changes in fish distributions.

One approach to filling knowledge gaps is to develop models that facilitate the transfer of information among systems (Bouchet et al., 2019; Yates et al., 2018), and conduct research in a

manner that facilitates the transfer and generalization of information. To this end, in Chapter 1, I developed the generalized visual reaction distance model to facilitate modeling visual foraging in aquatic predator-prey systems. The generalized visual reaction distance model provides a better fit to experimental data than a widely used visual range model while still retaining structural features that facilitate transfer of information about visual predator-prey interactions among predator-prey systems and provides a basis to incorporate outside information. Although the model provides a means for transferring information among predator-prey systems, a review of the visual reaction distance literature in Chapter 1 highlights how many visual foraging studies have been conducted in a manner that provides information that is only useful for characterizing dynamics of a single predator-prey system, and often only within the range of conditions present in the experiment. To facilitate information transfer, future visual reaction distance studies should place an emphasis on conducting experiments that yield data which can be transferred among predator-prey systems, such as by reporting physically interpretable measures of attenuation (as opposed to nephelometric turbidity units).

Although Chapter 2 provides a potential leap forward in water clarity monitoring, it highlights persistent challenges in monitoring subsurface water clarity measurements at scales that are representative of the environmental experience of widely distributed and highly mobile marine animals. The logistical challenge of monitoring makes it unlikely that empirical observations alone will adequately fill coverage gaps in the foreseeable future. Coupled physical-biological ecosystem models may provide a more useful means of linking variation in water clarity to variation in catchability and visual foraging than in situ monitoring if they can accurately reproduce subsurface features that are important for visual processes (e.g. bottom nepheloid layer; Chapter 2).

Regardless, novel approaches to monitoring water clarity will continue to be necessary to identify model deficiencies and provide an empirical benchmark of ecosystem change.

The utility of archival tag apparent optical properties would improve if they can be linked to biological and physical quantities of interest, such as chlorophyll, using theoretical models and empirical relationships (Bayle et al., 2015). The utility of measurements may also improve through better characterization of the spectral sensitivity and angular response of archival tags to light, and technological improvements to make archival tag measurements more similar to conventional radiance detectors that measure light with a specific geometry (e.g., by adding a cosine diffuser).

Monitoring long-term changes in subsurface water clarity can provide insight into changes in ecosystem structure and function but it remains difficult to sustain monitoring at spatial and temporal scales necessary to detect and accurately characterize changes. Changes in subsurface water clarity may be expected to occur gradually and over decades to centuries, similar to changes in surface water clarity (Aksnes et al., 2009; Aksnes and Ohman, 2009; Boyce and Worm, 2015; Dupont and Aksnes, 2013; Edmondson, 1994; Sørnes and Aksnes, 2006; Wernand et al., 2013). The slow rates of changes and logistical barriers to sampling make it impossible to sustain monitoring using specialized equipment and dedicated sampling platforms. Due to the rapid and accelerating rates of change around the world due to climate change and often static or decreasing budgets for monitoring, it is unlikely these logistical challenges will fade in the near future. As such, increasing attention should be paid to leveraging existing sampling platforms for monitoring and emphasizing the use of cost-effective technologies that can be deployed from multiple sampling platforms and have a low barrier-to-entry for sustained monitoring. Historical monitoring suggests that effective technologies for monitoring may need to be technologically simple, affordable, and easy to use to fill coverage gaps. For example, since the late 19th century,

understanding of changes in surface water clarity and primary productivity have come from the Secchi Disk and Forel-Ule color comparator which are rudimentary but have been extremely successful because they are easy to obtain and use (Pitarch, 2020; Wernand et al., 2013). Although there is a higher technological barrier to monitoring subsurface water clarity than surface water clarity, archival tag light sensors provide a lower barrier to entry than specialized equipment because they use photodiodes that are produced for many commercial applications, yet still provide a useful characterization of light (Mobley, 1994).

Chapters 3 and 4 show different consequences of climate change via changes in light environment:the potential to affect gear efficiency of fisheries, stock assessment survey catchability of walleye pollock, and visual foraging by walleye pollock on copepods and juvenile conspecifics. These consequences are complex, varying in time and space, owing to interactive effects of latitudinal variation in light regime, shallow bathymetry in the Bering Strait region, and spatial variation in optically active physical and biological constituents that affect water clarity (i.e., subsurface nepheloid layer). Thus, these chapters illustrate that a holistic evaluation of all dimensions of the light environment are necessary to draw inferences about the consequences of pole-ward distributional shifts.

Changes in fisheries gear efficiency and stock assessment survey catchability will depend on where stocks are moving to and from, along with where and when interactions between fish and fishing gears occur. Although the regional fishing fleets in United States and Russian comprises vessels that are capable of adapting to ongoing changes in stock distribution, the extent of shifts in fishing effort and changes in interactions between fish and fishing gears will depend on the details of regional spatial fisheries management. For example, the current ban on commercial bottom trawling in the northern Bering Sea and eastern Chukchi Sea constrains

poleward reallocation of commercial fishing effort within the United States Exclusive Economic Zone, whereas a total allowable catch was set for walleye pollock in the western Chukchi Sea in 2020.

Although Chapter 3 shows how variation in light may influence catchability over space and time in the Bering Sea and Chukchi Sea, there are key knowledge gaps in light-dependent catchability relationships for individual stocks. Among Bering Sea groundfishes, walleye pollock is the only species for which light-dependent catchability variation has been evaluated across a gradient of light levels (Kotwicki et al., 2018, 2015, 2013, 2009; Olla et al., 2000; Ryer and Olla, 2000; Williams et al., 2011). For the remainder of groundfish stocks (e.g. yellowfin sole, northern rock sole, flathead sole, arrowtooth flounder, Alaska plaice), only patterns of diel variation in catch rates have been reported (Ryer et al., 2010). Additional research is needed to clarify light-dependent catchability relationships for specific stocks and gear types of interest, which may be obtained by conducting experiments to characterize light-dependent variation in catchability across gradients of light.

In Chapter 4, the visual reaction distance model (Chapter 1) and an extension of methods for characterizing water clarity data (Chapter 2) provide insight into how spatial variation in light regime, bathymetry, and water clarity contribute to variation in reaction distances of walleye pollock to copepods and 15-cm juvenile walleye pollock prey in the southeastern and northeastern Bering Sea. Due to the asymmetric effects of turbidity on reaction distance for prey of different sizes and inherent contrast, areas with elevated turbidity reduce reaction distances of walleye pollock to juvenile walleye pollock but have maximum reaction distances to copepods. This suggests that as fish distributions change, there may be changes in growth or mortality depending on how visual foraging conditions differ from historical ranges. Environmental features that

contributed to variation in reaction distance were not limited to surface layers, as shown by the influence of the bottom nepheloid layer on reaction distance. The role of subsurface layers in driving variation in reaction distance and areal variation in water clarity highlight how areal variation in water clarity at mesoscales (1–100 km) and subsurface layers may play an important role in structuring visual predator-prey interactions.

A potential next step to build on Chapter 4 would be to combine predicted visual reaction distance information with prey density, migration, and temperature data to estimate habitat-specific growth potential for walleye pollock. Doing so has the potential to contribute Level-3 habitat information (growth, reproduction, or survival rates) for specific age-classes of walleye pollock to meet NOAA's goals for characterizing Essential Fish Habitat (Sigler et al., 2017). Such work would be similar to previous studies in the southern Bering Sea and Gulf of Alaska, where individual-based models were used to estimate habitat-specific growth potential for age-0 walleye pollock as a function of prey densities, functional response models, temperature, vertical migration behavior, and bioenergetics models (Ciannelli et al., 2002; Siddon et al., 2013). However, achieving this goal will require closing knowledge gaps to better characterize ecological communities, predator and prey behavior, and environmental conditions across the entire eastern Bering Sea continental shelf. First, model predictions and prey densities should be validated based on realized outcomes of predator-prey interactions (i.e., stomach contents analysis), similar to the approach used by Aarflot et al. (2020) to characterize the role of topographic blockage on foraging success of capelin in the North Sea. Doing so will require information about prey densities and vertical migration, based on either in situ sampling or reliable model-based estimates of prey densities from a coupled model of physical processes, biogeochemical processes, primary production, and secondary production with accurate vertical migration dynamics. Second, better

information about light-dependent vertical migration behavior of walleye pollock is necessary to model migration behaviors across a latitudinal gradient. Although vertical migration patterns have been described in the Gulf of Alaska and southern Bering Sea (e.g., Adams et al., 2009; Bailey, 1989), vertical migration is an adaptive behavior that is likely to vary with latitude as occurs in other vertically migrating Arctic and subarctic species (e.g., Benoit et al., 2010; Gjelland et al., 2009; Hobbs et al., 2018). Recent efforts to collect movement data from upward-facing fix acoustic moorings that were equipped with archival tags may provide a basis to characterize light-dependent vertical migration patterns of walleye pollock (Alex De Robertis, personal communication).

Emerging knowledge gaps due to the rapid pace of ecosystem change and budgetary constraints on research highlight the tremendous value in leveraging extant data sets and platforms to achieve new insights into patterns and mechanisms of ecosystem change. In this dissertation, I achieve this goal by developing new methods to make use of existing information on visual predator-prey interactions and light to facilitate understanding of how light and water clarity are likely to affect visual foraging and gear efficiency across a large marine ecosystem. Resources for monitoring and experimentation are stressed by emerging knowledge gaps due to rapid changes that are occurring not only in Arctic and subarctic, but across the globe. Rapid rates of change are challenging resource monitoring and management systems that have been set up to manage fish stocks and ecosystems within static boundaries (Link et al., 2011) and major knowledge gaps about the effects of change are emerging rapidly. Thus, it will continue to be a priority for marine ecologists to find novel ways to make better use of existing information to characterize and understand ecological shifts in a rapidly changing world.

REFERENCES

Aarflot, J.M., Dalpadado, P., Fiksen, Y., 2020. Foraging success in planktivorous fish increases with topographic blockage of prey distributions. Mar. Ecol. Prog. Ser. 644, 129–142. https://doi.org/10.3354/meps13343

Adams, C.F., Foy, R.J., Kelley, J.J., Coyle, K.O., 2009. Seasonal changes in the diel vertical migration of walleye pollock (*Theragra chalcogramma*) in the northern Gulf of Alaska. Environ. Biol. Fishes 86, 297–305. https://doi.org/10.1007/s10641-009-9519-y

Aksnes, D.L., Dupont, N., Staby, A., Fiksen, Ø., Kaartvedt, S., Aure, J., 2009. Coastal water darkening and implications for mesopelagic regime shifts in Norwegian fjords. Mar. Ecol. Prog. Ser. 387, 39–49. https://doi.org/10.3354/meps08120

Aksnes, D.L., Ohman, M.D., 2009. Multi-decadal shoaling of the euphotic zone in the southern sector of the California Current System. Limnol. Oceanogr. 54, 1272–1281. https://doi.org/10.4319/lo.2009.54.4.1272

Bailey, K.M., 1989. Interaction between the vertical distribution of juvenile walleye pollock *Theragra chalcogramma* in the eastern Bering Sea, and cannibalism. Mar. Ecol. Prog. Ser. 53, 205–213.

Bayle, S., Monestiez, P., Guinet, C., Nerini, D., 2015. Moving toward finer scales in oceanography: Predictive linear functional model of Chlorophyll *a* profile from light data. Prog. Oceanogr. 134, 221–231. https://doi.org/10.1016/j.pocean.2015.02.001

Benoit, D., Simard, Y., Gagné, J., Geoffroy, M., Fortier, L., 2010. From polar night to midnight sun: Photoperiod, seal predation, and the diel vertical migrations of polar cod (Boreogadus saida) under landfast ice in the Arctic Ocean. Polar Biol. 33, 1505–1520. https://doi.org/10.1007/s00300-010-0840-x

Bouchet, P.J., Peterson, A.T., Zurell, D., Dormann, C.F., Schoeman, D., Ross, R.E., Snelgrove, P., Sequeira, A.M.M., Whittingham, M.J., Wang, L., Rapacciuolo, G., Oppel, S., Mellin, C., Lauria, V., Krishnakumar, P.K., Jones, A.R., Heinänen, S., Heikkinen, R.K., Gregr, E.J., Fielding, A.H., Caley, M.J., Barbosa, A.M., Bamford, A.J., Lozano-Montes, H., Parnell, S., Wenger, S., Yates, K.L., 2019. Better model transfers require knowledge of mechanisms. Trends Ecol. Evol. 34, 489–490. https://doi.org/10.1016/j.tree.2019.04.006

Boyce, D.G., Worm, B., 2015. Patterns and ecological implications of historical marine phytoplankton change. Mar. Ecol. Prog. Ser. 534, 251–272. https://doi.org/10.3354/meps11411

Brown, Z.W., Arrigo, K.R., 2012. Contrasting trends in sea ice and primary production in the Bering Sea and Arctic Ocean. ICES J. Mar. Sci. 69, 1180–1193.

Ciannelli, L., Brodeur, R.D., Swartzman, G.L., Salo, S., 2002. Physical and biological factors influencing the spatial distribution of age-0 walleye pollock (*Theragra chalcogramma*) around the Pribilof Islands, Bering Sea. Deep. Res. Part II Top. Stud. Oceanogr. 49, 6109–6126. https://doi.org/10.1016/S0967-0645(02)00336-3

Dupont, N., Aksnes, D.L., 2013. Centennial changes in water clarity of the Baltic Sea and the North Sea. Estuar. Coast. Shelf Sci. 131, 282–289. https://doi.org/10.1016/j.ecss.2013.08.010

Edmondson, W.T., 1994. Sixty Years of Lake Washington: A Curriculum Vitae. Lake Reserv. Manag. 10, 75–84. https://doi.org/10.1080/07438149409354178

Gjelland, K.Ø., Bøhn, T., Horne, J.K., Jensvoll, I., Knudsen, F.R., Amundsen, P.A., 2009. Planktivore vertical migration and shoaling under a subarctic light regime. Can. J. Fish. Aquat. Sci. 66, 525–539. https://doi.org/10.1139/F09-014

Grebmeier, J.M., Frey, K.E., Cooper, L.W., Kędra, M., 2018. Trends in benthic macrofaunal populations, seasonal sea ice persistence, and bottom water temperatures in the bering strait region. Oceanography 31, 136–151. https://doi.org/10.5670/oceanog.2018.224

Hobbs, L., Cottier, F.R., Last, K.S., Berge, J., 2018. Pan-Arctic diel vertical migration during the polar night. Mar. Ecol. Prog. Ser. 605, 61–72. https://doi.org/doi.org/10.3354/meps12753

Huntington, H.P., Danielson, S.L., Wiese, F.K., Baker, M., Boveng, P., Citta, J.J., De Robertis, A., Dickson, D.M.S.S., Farley, E., George, J.C., Iken, K., Kimmel, D.G., Kuletz, K., Ladd, C., Levine, R., Quakenbush, L., Stabeno, P., Stafford, K.M., Stockwell, D., Wilson, C., 2020. Evidence suggests potential transformation of the Pacific Arctic ecosystem is underway. Nat. Clim. Chang. 10, 342–348. https://doi.org/10.1038/s41558-020-0695-2

Kotwicki, S., De Robertis, A., Ianelli, J.N., Punt, A.E., Horne, J.K., 2013. Combining bottom trawl and acoustic data to model acoustic dead zone correction and bottom trawl efficiency parameters for semipelagic species. Can. J. Fish. Aquat. Sci. 70, 208–219. https://doi.org/10.1139/cjfas-2012-0321

Kotwicki, S., De Robertis, A., von Szalay, P., Towler, R., 2009. The effect of light intensity on the availability of walleye pollock (*Theragra chalcogramma*) to bottom trawl and acoustic surveys. Can. J. Fish. Aquat. Sci. 66, 983–994. https://doi.org/10.1139/f09-055

Kotwicki, S., Horne, J.K., Punt, A.E., Ianelli, J.N., 2015. Factors affecting the availability of walleye pollock to acoustic and bottom trawl survey gear. ICES J. Mar. Sci. 72, 1425–1439. https://doi.org/10.1093/icesjms/fsv011

Kotwicki, S., Ressler, P.H., Ianelli, J.N., Punt, A.E., Horne, J.K., 2018. Combining data from bottom trawl and acoustic surveys to estimate an index of abundance for semipelagic species. Can. J. Fish. Aquat. Sci. 75, 60–71.

Lewis, K.L., van Dijken, G.L., Arrigo, K.R., 2020. Changes in phytoplankton concentration, not sea ice, now drive increased Arctic Ocean primary production. Science (80-.). 369, 198–202.

Link, J.S., Nye, J.A., Hare, J.A., 2011. Guidelines for incorporating fish distribution shifts into a fisheries management context. Fish Fish. 12, 461–469. https://doi.org/10.1111/j.1467-2979.2010.00398.x

Mobley, C.D., 1994. Light and water: Radiative transfer in natural waters. Academic Press.

Newman, A.J., Monaghan, A.J., Clark, M.P., Ikeda, K., Xue, L., Gutmann, E.D., Arnold, J.R., 2021. Hydroclimatic changes in Alaska portrayed by a high-resolution regional climate simulation. Clim. Change 164, 1–21. https://doi.org/10.1007/s10584-021-02956-x

Olla, B.L., Davis, M.W., Rose, D.C., 2000. Differences in orientation and swimming of walleye pollock *Theragra chalcogramma* in a trawl net under light and dark conditions: concordance between rield and laboratory observations. Fish. Res. 44, 261–266.

Opdal, A.F., Lindemann, C., Aksnes, D.L., 2019. Centennial decline in North Sea water clarity causes strong delay in phytoplankton bloom timing 3946–3953. https://doi.org/10.1111/gcb.14810

Pitarch, J., 2020. A review of Secchi's contribution to marine optics and the foundation of Secchi disk science. Oceanography 33, 26–37. https://doi.org/10.5670/oceanog.2020.301

Ryer, C.H., Olla, B.L., 2000. Avoidance of an approaching net by juvenile walleye pollock *Theragra chalcogramma* in the laboratory: the influence of light intensity. Fish. Res. 45, 195–199.

Ryer, C.H., Rose, C.S., Iseri, P.J., 2010. Flatfish herding behavior in response to trawl sweeps: A comparison of diel responses to conventional sweeps and elevated sweeps. Fish. Bull. 108, 145–154.

Siddon, E.C., Kristiansen, T., Mueter, F.J., Holsman, K.K., Heintz, R.A., Farley, E. V, 2013. Spatial match-mismatch between juvenile fish and prey provides a mechanism for recruitment variability across contrasting climate conditions in the eastern Bering Sea. PLoS One 8, 13. https://doi.org/10.1371/journal.pone.0084526

Sigler, M.F., Eagleton, M.P., Helser, T.E., Olson, J.V., Pirtle, J.L., Rooper, C.N., Simpson, S.C., Stone, R.P., 2017. Alaska Essential Fish Habitat research plan: A research plan for the National Marine Fisheries Service's Alaska Fisheries Science Center and Regional Office. AFSC Processed Rep. 2015-05. Alaska Fish. Sci. Cent., NOAA, Nat. Mar. Fish. Serv., 7600 Sand Point Way NE, Seattle, WA 98115. https://doi.org/10.7289/V5/AFSC-PR-2017-05

Sørnes, T.A., Aksnes, D.L., 2006. Concurrent temporal patterns in light absorbance and fish abundance. Mar. Ecol. Prog. Ser. 325, 181–186. https://doi.org/10.3354/meps325181

Stevenson, D.E., Lauth, R.R., 2019. Bottom trawl surveys in the northern Bering Sea indicate recent shifts in the distribution of marine species. Polar Biol. 42, 407–421. https://doi.org/10.1007/s00300-018-2431-1

Wernand, M.R., van der Woerd, H.J., Gieskes, W.W.C., 2013. Trends in ocean colour and chlorophyll concentration from 1889 to 2000, worldwide. PLoS One 8, e63766. https://doi.org/10.1371/journal.pone.0063766

Williams, K., Punt, A.E., Wilson, C.D., Horne, J.K., 2011. Length-selective retention of walleye pollock, *Theragra chalcogramma*, by midwater trawls. ICES J. Mar. Sci. 68, 119–129. https://doi.org/10.1093/icesjms/fsq155

Yates, K.L., Bouchet, P.J., Caley, M.J., Mengersen, K., Randin, C.F., Parnell, S., Fielding, A.H., Bamford, A.J., Ban, S., Barbosa, A.M., Dormann, C.F., Elith, J., Embling, C.B., Ervin, G.N., Fisher, R., Gould, S., Graf, R.F., Gregr, E.J., Halpin, P.N., Heikkinen, R.K., Heinänen, S., Jones, A.R., Krishnakumar, P.K., Lauria, V., Lozano-Montes, H., Mannocci, L., Mellin, C., Mesgaran, M.B., Moreno-Amat, E., Mormede, S., Novaczek, E., Oppel, S., Ortuño Crespo, G., Peterson, A.T., Rapacciuolo, G., Roberts, J.J., Ross, R.E., Scales, K.L., Schoeman, D., Snelgrove, P., Sundblad, G., Thuiller, W., Torres, L.G., Verbruggen, H., Wang, L., Wenger, S., Whittingham, M.J., Zharikov, Y., Zurell, D., Sequeira, A.M.M., 2018. Outstanding challenges in the transferability of ecological models. Trends Ecol. Evol. 33, 790–802. https://doi.org/10.1016/j.tree.2018.08.001

APPENDIX A: CHAPTER 1—APPENDIX

Chapter 1 Appendix A: Theoretical Basis

Contrast propagation

The physical dynamics of mechanistic models are derived from classic visibility theory (Duntley, 1952, 1948; Lythgoe, 1972; Middleton, 1952). In classic visibility theory, a target is visible to an observer if $C_T(r)$, the apparent contrast of a target at distance r, exceeds the minimum detectable contrast, C_{min}, of an observer's vision system (i.e. $C_T(r) > C_{min}$). Contrast is defined as the proportional difference in radiance between a target and background:

$$C_T = \frac{L_T - L_B}{L_B}, \tag{A1}$$

where L_T is radiance of the target, and L_B is radiance of the background. In classic visibility theory, the contrast of a target decreases with viewing distance, r (m), according to the law of contrast reduction (i.e. Koschmieder's law) as:

$$C_T(r) = C_T(0)\exp(-cr), \tag{A2}$$

where $C_T(r)$ is the apparent contrast of the target at distance r, $C_T(0)$ is contrast of the target at distance zero (i.e. inherent contrast), and c is beam attenuation (m^{-1}). Beam attenuation is the rate of attenuation of a collimated beam of light along a path, which occurs due to scattering and absorption (Kirk, 2011). Therefore, Eqn. A2 assumes that the only light that contributes to contrast propagation is light that travels along a direct path between the object and an observer (Duntley, 1952; Lee et al., 2015; Middleton, 1952; Preisendorfer, 1986).

The assumption of Eqn. A2 is valid if background and target radiances originate from positions that subtend a small angle relative to the resolution of the observer's visual field (Lee et

al., 2015). In other words, Eqn. A2 is valid if the target can be treated as a point source (Duntley, 1952, 1948; Middleton, 1952). However, Eqn. A2 may not be valid in many underwater visibility applications because viewing distances are relatively short and forward-scattered light contributes to image propagation (Lee et al., 2015).

Following the radiative transfer equation, the radiance of a target at distance *r* is:

$$\frac{dL_T(r,\Theta,\lambda)}{dr} = -c(\lambda)L_T(r,\Theta,\lambda) + \int_{4\pi} L_T(r,\phi,\lambda)\beta(r,\phi,\lambda)d\Omega\,, \tag{A3}$$

and the radiance of a background reference location *r*', that is close to but does not overlap with the target, is:

$$\frac{dL_B(r',\Theta',\lambda)}{dr} = -c(\lambda)L_B(r',\Theta',\lambda) + \int_{4\pi} L_B(r',\phi,\lambda)\beta(r',\phi',\lambda)d\Omega\,. \tag{A4}$$

In Eqns. A3 and A4, Θ and Θ' are the three-dimensional directions between the observer and target, and observer and background, respectively, ϕ and ϕ' are directions towards the observer relative to Θ and Θ', Ω is an infinitesimal solid angle (steradians) oriented along ϕ or ϕ', and λ is wavelength. Conceptually, $-c(\lambda)L_T(r,\Theta,\lambda)$ and $-c(\lambda)L_B(r',\Theta',\lambda)$ represent losses of radiance along a path due to beam attenuation. The volume scattering functions, $\int_{4\pi} L_T(r,\phi,\lambda)\beta(r,\phi,\lambda)d\Omega$ and $\int_{4\pi} L_B(r',\phi,\lambda)\beta(r',\phi,\lambda)d\Omega$, represent radiance gained due to forward scattering. The key assumption to derive the law of contrast reduction from the radiative transfer equation, it is that:

$$\int_{4\pi} L_T(r,\phi,\lambda)\beta(r,\phi,\lambda)d\Omega = \int_{4\pi} L_B(r',\phi,\lambda)\beta(r',\phi',\lambda)d\Omega\,, \tag{A5}$$

which is asymptotically true for a point source. Based on the assumption of Eqn. A5, the radiance difference between a target and background is:

$$L_T(r) - L_B(r') = \big(L_T(0) - L_B(0)\big)\exp(-cr)\,, \tag{A6}$$

which is equivalent to Eqn. A2. However, when a target cannot be considered a point source,

$$L_T(r) - L_B(r') = \big(L_T(0) - L_B(0)\big)\exp\big(-\big(c - \varepsilon b_f\big)r\big), \quad \text{(A7)}$$

where b_f is the forward scattering coefficient (m^{-1}), and ε is a term that depends on L_T and L_B, and the distance between L_T and L_B (Lee et al., 2015). Expressed in terms of contrast:

$$C_a = C_0 \exp\big(-\big(c - \varepsilon b_f\big)r\big). \quad \text{(A8)}$$

Unfortunately, there is no generalizable value of ε; ε→1 when the target is large, while for a point source, ε→0 (Lee et al., 2015).

Contrast reduction following Eqn. A8 instead of Eqn. A2 has implications for visual reaction distance experiments and mechanistic encounter distance models. To satisfy Eqn. A2, some studies have emphasized the importance of deriving beam attenuation, *c*, from transmittance measurements that minimize or are adjusted to minimize contributions of forward scattered light, to avoid underestimating beam attenuation (e.g. Utne-Palm 1999; Meager et al. 2005). To fit their model to data from a visual foraging experiment, Aksnes and Utne (1997) adjusted spectrophotometer absorbance measurements to derive values of beam attenuation that were corrected to omit contributions of forward-scattered light to spectrophotometer measurements, following Zaneveld et al. (1979). However, based on Eqn. A8, omitting forward-scattering would underestimate contrast propagation.

Naka-Rushton function

Aksnes and Utne (1997) used a Michaelis-Menten function to represent the light intensity-response of a fish vision system, based on the suggestion by Cornsweet (1970) that such a functional form provides a generic representation of the retinal-neural intensity response of the vertebrate vision system to light, rather than being an explicit representation of a mechanism. However, a Michaelis-Menten function is equivalent to the Naka-Rushton function that

characterizes the light intensity-response of horizontal cells of vertebrate retina (Naka et al., 1988; Naka and Rushton, 1966b, 1966a). In the Naka-Rushton function,

$$V = \frac{V_{max} I^{\alpha}}{I_{50}^{\alpha} + I^{\alpha}} + V_0, \qquad (A9)$$

V is the membrane voltage potential (mV) that is stimulated by light intensity I, V_{max} is the maximum induced voltage potential (mV), V_0 is resting potential (mV), I_{50} is a half-saturation level, and α is a slope parameter (Naka et al., 1988; Naka and Rushton, 1966b). For vertebrates, retinal-neural intensity-response relationships can often be approximated using the Naka-Rushton function assuming $\alpha = 1$ and $V_0 = 0$.

The functional representation of the Naka-Rushton function for scaling the visual response is related to the contrast propagation assumption of the Aksnes and Utne model as follows. In the fish retinae, horizontal cells receive inputs from photoreceptors, interplexiform cells, and other horizontal cells (Djamgoz and Yamada, 1990; Kaneko, 1971). Coupled horizontal cells of the same type integrate across inputs and functionally 'measure' ambient illumination (Djamgoz and Yamada, 1990). This is important because the absolute intensity-response of the vision system to a response scales incrementally with the adapting level of ambient illumination (Naka et al., 1979; Sakai et al., 1995). The contrast propagation function of the Aksnes and Utne model assumes that contrast scales in constant proportion with background illumination (i.e. contrast remains constant regardless of light levels). Thus, in the Aksnes and Utne model, the Naka-Rushton function scales the incremental absolute sensitivity of the vision system to a stimulus of constant contrast across varying levels of light intensity. These mechanisms of adaptation and intensity-response are more proximal in the neural-retinal pathway than quantum integration by photoreceptors that can overestimate visual range in the absence of outside constraints on contrast sensitivity (e.g. Ruxton and Johnsen, 2016).

Chapter 1 Appendix B: Data sources, preparation, code, and model-fitting

Screening predator-prey reaction distance experiments

We reviewed every visual predator-prey experimental study we are aware of and evaluated whether they were suitable for model fitting and evaluation in our study based on eight criteria (Table B1). Criteria #1–5 were essential for model fitting in our study. Criteria #6–8 were desirable for evaluating model performance but not essential for specific cases if criteria #1–5 were met. Our review included every published visual predator-prey experiment we were aware of that reported reaction distances of fish to prey under varying conditions in the visual environment were manipulated for experimental treatments (Table B2). Aside from our screening criteria (Table B1), we aimed to include at least one case where there was evidence of a non-visual reaction at low light levels (based on the authors' description in the text, visual examination of figures, and the structure of empirical models fitted to the experimental data, at least one piscivore case, at least one planktivore case, and at least one case where reaction angles were recorded during experiments.

The 32 studies we reviewed included 59 predator-prey systems of which 96.7% (57/59) had data we could either directly access (10/59) or digitize from figures (47/59; Table B3). Of the systems where we could obtain data, 31.6% (18/57) manipulated light and turbidity or could be combined with other experiments to fill gaps from a single study (Criteria #1; Table B3). We note that in *Appendix G: Asymptotic equivalence between behavioral and theoretical models*, we examine the link between empirical models reported from light-treatment-only systems and mechanistic relationships that are used in the Aksnes and Utne model and generalized visual reaction distance model. Fourteen (14) out of 18 remaining systems included measurements of absorbance or beam attenuation, or manipulated turbidity using suspendoids and reported turbidity

units in a manner that would allow post hoc estimation of beam attenuation/effective attenuation coefficient using conversions reported in the literature (Criteria #2; Table B3). Among the 14 remaining predator-prey systems, Confer et al. (1978) did not manipulate or report light and turbidity simultaneously for a lean lake trout-cladoceran system (Criteria #1), Meager et al. (2005) did not have a sufficient sample size for Atlantic cod-mysid system (Criteria #3), and Utne (1997) did not have sufficient dynamic range of variation in light treatments for two-spotted goby reacting to individual *Calanus finmarchicus*/*Calanus helgolandicus* to fit models to data (Criteria #4), leaving eleven predator-prey systems that met our criteria for consideration in cases (Table B3). We now discuss the remaining predator-prey systems (seven piscivore, four planktivore).

The seven remaining studies that reported results of piscivore experiments were conducted using similar experimental protocols and considered a similar suite of empirical models to fit to experimental data (Hansen et al., 2013; Mazur and Beauchamp, 2003; Vogel and Beauchamp, 1999). However, only Hansen et al. (2013) reported a relationship between experimentally measured nephelometric turbidity units (NTU) and absorbance (as a proxy for beam attenuation; Criteria #2). Plots and models from Hansen et al. (2013) provided some indication that non-visual reaction may have occurred during experimental trials (Criteria #5), and we had access to original data to facilitate direct comparison with best-fit empirical models (Criteria #8). We therefore selected Hansen et al. (2013) as a piscivore case (subsection 2.4.1 Case #1—Piscivore reacting to fish prey) to minimize potential uncertainty associated with conversions from the literature.

Among the four zooplanktivore systems, three used the same predator and prey species and measurements were obtained using similar experimental protocols (Utne-Palm, 1999; Utne, 1997). One of the systems (two-spotted goby reacting to 10 *Calanus finmarchicus/helgolandicus*) was used as an example in Aksnes and Utne (1997) and parameters from the system have been used in

numerous visual foraging model applications (e.g. Langbehn and Varpe 2017) and, we used the system for *Case #2—Planktivore reacting to a group of ten zooplankton prey* (subsection 2.4.2). Utne-Palm (1999) reported results for three predator-prey systems, each of which used two-spotted goby as the predator, but only manipulated turbidity and not light levels (Criteria #1). We determined that it would be feasible to estimate parameters for the predator-prey systems from Utne-Palm (1999) if parameter estimates from Case #2 could be transferred. Thus, we used the three predator-prey systems from Utne-Palm (1999; predator: two-spotted goby, prey: transparent mobile, transparent immobile, and red mobile *C. finmarchicus/helgolandicus*) for *Case #3—Planktivore reacting to a single zooplankton prey* (subsection 2.4.3).

The final zooplanktivore system, stone moroko reacting to *Daphnia pulex*, was the only system where nadir viewing angle at the point of reaction was reported along with reaction distance (Asaeda et al., 2002; Criteria #6). The study did not report a relationship between turbidity measurements presented for the experiments (nephelometric turbidity units) generated using kaolinite and physically interpretable attenuation coefficients. However, relationships between NTU and beam attenuation/absorption have been reported in the literature. Therefore, we used the stone moroko-*Daphnia pulex* system for *Case #4—Planktivore reacting to single zooplankton, with angular dependence* (subsection 2.4.4).

Table B1. Criteria for selecting predator-prey cases for our study.

#	Criteria	Rationale
1	Did experiments manipulate both light and turbidity?	The generalized visual reaction distance model and Aksnes and Utne model is fitted to light and turbidity data.
2	Were beam attenuation or absorbance measured? If not, is a reasonable conversion available for experimental units (e.g. conversion from NTU to beam attenuation for bentonite)?	The generalized visual reaction distance model and Aksnes and Utne model characterize the transmission of light through water based on physically interpretable attenuation coefficients (beam attenuation, effective attenuation coefficient, and diffuse attenuation coefficient). Nephelometric turbidity units (NTU) must be converted to directly characterize light attenuation.
3	Were sample sizes large enough for model fitting?	Available sample sizes should be adequate for model-fitting given the number of parameters estimated in each model. Models and number of parameters (in parenthesis): AUM.1 (3); AUM.2 (6); GVRDM.1 (9); GVRDM.2 (8); GVRDM.3 (6); GVRDM.4 (5)
4	Was the dynamic range of treatment levels sufficient?	Experimental treatments need to span a sufficient absolute and dynamic range for model-fitting.
5	Was there evidence of a visual reaction?	Visual encounter distance models are not appropriate for cases where predators use senses other than vision are used for prey detection.
6	Were reaction angles measured?	We sought to include at least one case where reaction angles were reported in order to evaluate if information about reaction angle improved model fit.
7	Was there evidence of non-visual reaction at low light levels?	We sought to include at least one case where a non-visual reaction may have occurred at low light levels.
8	Direct access to the original data?	Fitting the model to original data allows direct comparison between the GVRDM, AUM, and and best-fit empirical models from visual foraging experiments.

Table B2. Visual encounter distance experiments reviewed. Columns show predator and prey treatments, measurements reported for reaction distance (*r*), light, and turbidity, the suspendoid used (Susp.), availability of a conversion to beam attenuation or absorption (Conv.; Y = Yes, reported or conversion measured by authors; N = No; Ext. = External, conversion available in the literature), nadir viewing angle reported (Y = Yes, N = No); sample size available as either the original data set or digitization of data from plots (n), source. Dashes (-) indicate no treatment or that data were not collected or reported by the authors.

		Measurement units							
Predator	Prey	*r*	Light	Turbidity	Susp.	Conv.	θ	n	Source
stone moroko, *Pseudorasbora parva*	**cladoceran *Daphnia pulex***	**body length**	**lx**	**NTU**	**kaolinite**	**Ext.**	**Y**	**209**	Asaeda et al. (2002)
rainbow trout, *Oncorhynchus mykiss*	mealworm	cm	-	NTU	Stream sediment	No	N	57	Barrett et al. (1992)
bluegill, *Lepomis macrochirus*	cladoceran *Daphnia galeata mendotae*	cm	PFD	-	-	-	N	3	Breck and Gitter (1983)
bluegill, *Lepomis macrochirus*	cladoceran *Daphnia magna*	cm	PFD	-	-	-	N	8	Breck and Gitter (1983)
bay anchovy *Anchoa mitchilli*	brine shrimp (nauplii) *Artemia* sp.	mm	lx	-	-	-	N	51	Chesney (2008)
bay anchovy *Anchoa mitchilli*	brine shrimp (nauplii) *Artemia* sp. L-rotifer	body length	lx	-	-	-	Y	42	Chesney (2008)
bay anchovy *Anchoa mitchilli*	L-rotifer	mm	lx	NTU	algae (*Isochyris galbana*)	N	N	145	Chesney (2008)
brook trout *Salvelinus fontinalis*	cladoceran *Daphnia pulex*	cm	lx	-	-	-	N	9	Confer et al. (1978)
lean lake trout *Salvelinus namaycush*	cladoceran *Daphnia magna*	cm	lx	-	-	-	N	29	Confer et al. (1978)
lean lake trout *Salvelinus namaycush*	cladoceran *Daphnia magna*	cm	lx	absorbance m^{-1}	Green clay	No	N	8	Confer et al. (1978)

		Measurement units							
Predator	Prey	*r*	Light	Turbidity	Susp.	Conv.	θ	n	Source
pumpkinseed *Lepomis gibbosus*	cladoceran *Daphnia pulex*	cm	lx	-	-	-	N	11	Confer et al. (1978)
largemouth bass *Micropterus salmoides*	crayfish (moving)	cm	lx	JTU	bentonite	Ext.	N	107	Crowl (1989)
largemouth bass *Micropterus salmoides*	crayfish (not moving)	cm	lx	JTU	bentonite	Ext.	N	410	Crowl (1989)
Chinook salmon *Oncorhynchus tshawytscha*	brine shrimp *Artemia salina*	cm	PFD	NTU	marsh sediment	N	N	14	Gregory and Northcote (1993)
Chinook salmon *Oncorhynchus tshawytscha*	coastal cutthroat trout *Oncorhynchus clarkia clarkii*	cm	lx	NTU	-	Y	N	73*	Hansen et al. (2013)
Chinook salmon *Oncorhynchus tshawytscha*	**rainbow trout *Oncorhynchus mykiss***	**cm**	**lx**	**NTU**	**kaolin**	**Y**	**N**	**629***	**Hansen et al. (2013)**
coastal cutthroat trout *Oncorhynchus clarkii clarkii*	rainbow trout *Oncorhynchus mykiss*	cm	lx	NTU	-	-	N	269*	Hansen et al. (2013)
coastal cutthroat trout *Oncorhynchus clarkii clarkii*	threespine stickleback *Gasterosteus aculeatus*	cm	lx	NTU	-	-	N	70*	Hansen et al. (2013)
Cape silverside *Atherina breviceps*	cladoceran *Daphnia* sp.	cm	-	NTU	Estuarine silt	N	N	4	Hecht and van der Lingen (1992)
coastal cutthroat trout *Oncorhynchus clarkii clarkii*	copepod *Diaptomus kenai*	cm	PFD	-	-	-	N	5	Henderson and Northcote (1985)

		Measurement units							
Predator	Prey	*r*	Light	Turbidity	Susp.	Conv.	θ	n	Source
coastal cutthroat trout *Oncorhynchus clarkii clarkii*	food pellets	cm	PFD	-	-	-	N	5	Henderson and Northcote (1985)
Dolly Varden trout *Salvelinus malma*	copepod *Diaptomus kenai*	cm	PFD	-	-	-	N	6	Henderson and Northcote (1985)
Dolly Varden trout *Salvelinus malma*	food pellets	cm	PFD	-	-	-	N	6	Henderson and Northcote (1985)
lean lake trout *Salvelinus namaycush*	amphipod (stationary) *Hyalella azteca*	cm	PFD	-	-	-	N	6	Holbrook et al. (2013)
lean lake trout *Salvelinus namaycush*	amphipod (moving) *Hyalella azteca*	cm	PFD	-	-	-	N	6	Holbrook et al. (2013)
lean lake trout *Salvelinus namaycush*	cladoceran *Daphnia magna*	cm	PFD	-	-	-	N	6	Holbrook et al. (2013)
lean lake trout *Salvelinus namaycush*	mysid (moving) *Mysis diluviana*	cm	PFD	-	-	-	N	6	Holbrook et al. (2013)
lean lake trout *Salvelinus namaycush*	mysid (stationary) *Mysis diluviana*	cm	PFD	-	-	-	N	6	Holbrook et al. (2013)
largemouth bass *Micropterus salmoides*	redside shiner *Richardsonius balteatus*	cm	lx	-	-	-	N	0	Howick and O'Brien (1983)
largemouth bass *Micropterus salmoides*	bluegill *Lepomis macrochirus*	cm	lx	-	-	-	N	0	Howick and O'Brien (1983)

		Measurement units							
Predator	Prey	*r*	Light	Turbidity	Susp.	Conv.	θ	n	Source
pike *Esox lucius*	cladoceran *Daphnia* sp.	cm	-	Other	algae, dissolved organic matter	N	-	3	Jönsson et al. (2012)
pike *Esox lucius*	roach *Rutilus rutilus*	cm	-	Other	algae, dissolved organic matter	N	-	3	Jönsson et al. (2012)
siscowet lake trout *Salvelinus namaycush siscowet*	golden shiner *Notemigonus crysoleucas*	cm	PFD	-	-	-	N	6	Keyler et al. (2015)
siscowet lake trout *Salvelinus namaycush siscowet*	golden shiner (large) *Notemigonus crysoleucas*	cm	PFD	-	-	-	N	6	Keyler et al. (2015)
siscowet lake trout *Salvelinus namaycush siscowet*	golden shiner (moving) *Notemigonus crysoleucas*	cm	PFD	-	-	-	N	6	Keyler et al. (2015)
siscowet lake trout *Salvelinus namaycush siscowet*	golden shiner (small) *Notemigonus crysoleucas*	cm	PFD	-	-	-	N	6	Keyler et al. (2015)
siscowet lake trout *Salvelinus namaycush siscowet*	golden shiner (stationary) *Notemigonus crysoleucas*	cm	PFD	-	-	-	N	4	Keyler et al. (2015)
siscowet lake trout *Salvelinus namaycush siscowet*	deepwater sculpin *Myoxocephalus thompsonii*	cm	PFD	-	-	-	N	15	Keyler et al. (2019)

		Measurement units							
Predator	Prey	*r*	Light	Turbidity	Susp.	Conv.	θ	n	Source
lake herring *Coregonus artedi*	copepod *Limnocalanus macrurus*	cm	lx	-	-	-	Y	8	Link and Edsall (1996)
cutthroat trout *O. clarkii clarkia*	cutthroat trout *O. clarkii clarkii*	cm	lx	NTU	bentonite	Ext.	N	174*	Mazur and Beauchamp (2003)
cutthroat trout *O. clarkii clarkii*	rainbow trout *Oncorhynchus mykiss*	cm	lx	NTU	bentonite	Ext.	N	369*	Mazur and Beauchamp (2003)
lake trout *Salvelinus namaycush*	cutthroat trout *O. clarkii clarkii*	cm	lx	NTU	bentonite	Ext.	N	263*	Mazur and Beauchamp (2003)
lake trout *Salvelinus namaycush*	rainbow trout *Oncorhynchus mykiss*	cm	lx	NTU	bentonite	Ext.	N	92*	Mazur and Beauchamp (2003)
rainbow trout *Oncorhynchus mykiss*	cutthroat trout *O. clarkii clarkii*	cm	lx	NTU	bentonite	Ext.	N	111*	Mazur and Beauchamp (2003)
rainbow trout *Oncorhynchus mykiss*	rainbow trout *Oncorhynchus mykiss*	cm	lx	NTU	bentonite	Ext.	N	155*	Mazur and Beauchamp (2003)
Atlantic cod *Gadus morhua*	mysid *Praunus neglectus*	cm	PFD	-	-	-	N	5	Meager et al. (2010)
Atlantic cod *Gadus morhua*	mysid *Praunus neglectus*	cm	PFD	absorbance m^{-1}	kaolin	Y	N	5	Meager et al. (2005)
emerald shiner *Notropis atherinoides*	cladoceran *Daphnia magna*	cm	-	NTU	emulsified spinach, lake mud	N	N	7	Nieman and Gray (2019)

		Measurement units							
			Ligh			Con			
Predator	Prey	*r*	t	Turbidity	Susp.	v.	θ	n	Source
walleye *Sander vitreus*	emerald shiner *Notropis atherinoides*	cm	-	NTU	emulsified spinach, lake mud	N	N	4	Nieman and Gray (2019)
walleye *Sander vitreus*	golden shiner *Notemigonus crysoleucas*	cm	-	NTU	emulsified spinach, lake mud	N	N	7	Nieman and Gray (2019)
threespine stickleback *Gasterosteus aculeatus*	brine shrimp *Artemia salina*	cm	-	NTU	bentonite	Ext.	N	4	Quesenberry et al. (2007)
pike *Esox lucius*	roach *Rutilus rutilus*	cm	-	Other	algae, humic substance, clay	N	N	3	Ranåker et al. (2012)
yellow perch *Perca flavescens*	cladoceran *Daphnia pulicaria*	cm	lx	-	-	-	N	13	Richmond et al. (2004)
Miry's demoiselle *Neopomacentrus miryae*	brine shrimp *Artemia salina*	cm	lx	-	-	-	N	14	Rickel and Genin (2005)
Arctic grayling *Thymallus arcticus*	cladoceran *Bosmina longirostris*	cm	lx	-	-	-	N	18	Schmidt and O'Brien (1982)
Arctic grayling *Thymallus arcticus*	copepod *Cyclops scutifer*	cm	lx	-	-	-	N	19	Schmidt and O'Brien (1982)
Arctic grayling *Thymallus arcticus*	cladoceran *Daphnia longiremis*	cm	lx	-	-	-	N	41	Schmidt and O'Brien (1982)
Arctic grayling *Thymallus arcticus*	cladoceran *Daphnia pulex*	cm	lx	-	-	-	N	26	Schmidt and O'Brien (1982)

		Measurement units							
Predator	Prey	*r*	Light	Turbidity	Susp.	Conv.	θ	n	Source
Arctic grayling *Thymallus arcticus*	copepod *Heterocope septentrionalis*	cm	lx	-	-	-	N	71	Schmidt and O'Brien (1982)
flavescent peacock *Aulonocara stuartgranti*	brine shrimp *Artemia* sp. (dead)	cm	PFD	-	-	-	N	5	Schwalbe and Webb (2015)
flavescent peacock *Aulonocara stuartgranti*	brine shrimp *Artemia* sp. (living)	cm	PFD	-	-	-	N	5	Schwalbe et al. (2015)
Tramitichromis sp.	brine shrimp *Artemia* sp. (dead)	cm	PFD	-	-	-	N	5	Schwalbe et al. (2015)
Tramitichromis sp.	brine shrimp *Artemia* sp. (living)	cm	PFD	-	-	-	N	5	Schwalbe et al. (2015)
brook trout *Salvelinus fontinalis*	housefly *Musca domestica*	cm	lx	NTU	riparian soil	-	N	39	Sweka and Hartman (2001)
smallmouth bass *Micropterus dolomieu*	housefly *Musca domestica*	cm	lx	NTU	riparian soil	-	N	54	Sweka and Hartman (2003)
two-spotted goby *Gobius flavescens*	**copepod (red mobile) *Calanus finmarchicus* *C. helgolandicus***	**cm**	**PFD**	**absorbance m^{-1}**	**Diatomaceous earth**	**Yes**	**N**	**8**	**Utne-Palm (1999)**
two-spotted goby *Gobius flavescens*	**copepod (transparent immobile) *Calanus finmarchicus* *C. helgolandicus***	**cm**	**PFD**	**absorbance m^{-1}**	**Diatomaceous earth**	**Yes**	**N**	**8**	**Utne-Palm (1999)**

		Measurement units							
Predator	Prey	*r*	Light	Turbidity	Susp.	Conv.	θ	n	Source
two-spotted goby *Gobius flavescens*	**copepod (transparent mobile) *Calanus finmarchicus* *C. helgolandicus***	**cm**	**PFD**	**absorbance m^{-1}**	**Diatomaceous earth**	**Yes**	**N**	**8**	**Utne-Palm (1999)**
two-spotted goby *Gobius flavescens*	copepod (10 prey) *Acartia clausi*	cm	PFD	absorbance m^{-1}	-	-	N	51	Utne (1997)
two-spotted goby *Gobius flavescens*	copepod (1 prey) *Calanus finmarchicus*	cm	PFD	absorbance m^{-1}	Diatomaceous earth	Yes	N	81	Utne (1997)
two-spotted goby *Gobius flavescens*	**copepod (10 prey) *Calanus finmarchicus***	**cm**	**PFD**	**absorbance m^{-1}**	**Diatomaceous earth**	**Yes**	**N**	**214**	**Utne (1997)**
bluegill *Lepomis macrochirus*	cladoceran *Daphnia pulex*	cm	lx	JTU	Pond sediment	No	N	57	Vinyard and O'Brien (1976)
lake trout *Salvelinus namaycush*	cutthroat trout *O. clarkii clarkii*	cm	lx	NTU	bentonite	Ext.	N	648*	Vogel and Beauchamp (1999)
lake trout *Salvelinus namaycush*	rainbow trout *Oncorhynchus mykiss*	cm	lx	NTU	bentonite	Ext.	N	1,321*	Vogel and Beauchamp (1999)

*—Original data from experiments were available. Sample size indicates number of individual reactions.

Table B3. Evaluation of cases based on screening criteria. Cases selected for our study are shown in bold.

Predator	Prey	Criteria								Source
		1	2	3	4	5	6	7	8	
stone moroko, *Pseudorasbora parva*	**cladoceran *Daphnia pulex***	**Y**	**Y**	**Y**	**Y**	**Y**	**Y**	**N**	**N**	**Asaeda et al. (2002)**
rainbow trout, *Oncorhynchus mykiss*	mealworm	N	N	Y	N	Y	N	N	N	Barrett et al. (1992)
bluegill, *Lepomis macrochirus*	cladoceran *Daphnia galeata mendotae*	N	N	Y	N	Y	N	N	N	Breck and Gitter (1983)
bluegill, *Lepomis macrochirus*	cladoceran *Daphnia magna*	N	N	Y	N	Y	N	N	N	Breck and Gitter (1983)
bay anchovy *Anchoa mitchilli*	brine shrimp (nauplii) *Artemia* sp.	N	N	Y	N	Y	N	N	N	Chesney (2008)
bay anchovy *Anchoa mitchilli*	brine shrimp (nauplii) *Artemia* sp. L-rotifer	N	N	Y	N	Y	Y	N	N	Chesney (2008)
bay anchovy *Anchoa mitchilli*	L-rotifer	Y	N	Y	N	Y	N	N	N	Chesney (2008)
brook trout *Salvelinus fontinalis*	cladoceran *Daphnia pulex*	N	N	Y	N	Y	N	N	N	Confer et al. (1978)
lean lake trout *Salvelinus namaycush*	cladoceran *Daphnia magna*	N	N	Y	N	Y	N	N	N	Confer et al. (1978)
lean lake trout *Salvelinus namaycush*	cladoceran *Daphnia magna*	Y	N	Y	N	Y	N	N	N	Confer et al. (1978)
pumpkinseed *Lepomis gibbosus*	cladoceran *Daphnia pulex*	N	N	Y	N	Y	N	N	N	Confer et al. (1978)
largemouth bass *Micropterus salmoides*	crayfish (moving)	N	Y	Y	N	Y	N	N	N	Crowl (1989)
largemouth bass *Micropterus salmoides*	crayfish (not moving)	N	Y	Y	N	Y	N	N	N	Crowl (1989)

Predator	Prey	Criteria 1	2	3	4	5	6	7	8	Source
Chinook salmon *Oncorhynchus tshawytscha*	brine shrimp *Artemia salina*	N	N	Y	N	Y	N	N	N	Gregory and Northcote (1993)
Chinook salmon *Oncorhynchus tshawytscha*	coastal cutthroat trout *Oncorhynchus clarkia clarkii*	N	Y	Y	N	Y	N	U	Y	Hansen et al. (2013)
Chinook salmon *Oncorhynchus tshawytscha*	**rainbow trout *Oncorhynchus mykiss***	**Y**	**Y**	**Y**	**Y**	**Y**	**N**	**U**	**Y**	**Hansen et al. (2013)**
coastal cutthroat trout *Oncorhynchus clarkii clarkii*	rainbow trout *Oncorhynchus mykiss*	N	Y	Y	N	Y	N	U	Y	Hansen et al. (2013)
coastal cutthroat trout *Oncorhynchus clarkii clarkii*	threespine stickleback *Gasterosteus aculeatus*	N	Y	Y	N	Y	N	U	Y	Hansen et al. (2013)
Cape silverside *Atherina breviceps*	cladoceran *Daphnia* sp.	N	N	N	N	Y	N	N	N	Hecht and van der Lingen (1992)
coastal cutthroat trout *Oncorhynchus clarkii clarkii*	copepod *Diaptomus kenai*	N	N	N	N	Y	N	N	N	Henderson and Northcote (1985)
coastal cutthroat trout *Oncorhynchus clarkii clarkii*	food pellets	N	N	N	N	Y	N	N	N	Henderson and Northcote (1985)
Dolly Varden trout *Salvelinus malma*	copepod *Diaptomus kenai*	N	N	N	N	Y	N	N	N	Henderson and Northcote (1985)
Dolly Varden trout *Salvelinus malma*	food pellets	N	N	N	N	Y	N	N	N	Henderson and Northcote (1985)
lean lake trout *Salvelinus namaycush*	amphipod (stationary) *Hyalella azteca*	N	N	N	N	N	N	Y	N	Holbrook et al. (2013)

Predator	Prey	Criteria								Source
		1	2	3	4	5	6	7	8	
lean lake trout *Salvelinus namaycush*	amphipod (moving) *Hyalella azteca*	N	N	N	N	N	N	Y	N	Holbrook et al. (2013)
lean lake trout *Salvelinus namaycush*	cladoceran *Daphnia magna*	N	N	N	N	Y	N	N	N	Holbrook et al. (2013)
lean lake trout *Salvelinus namaycush*	mysid (moving) *Mysis diluviana*	N	N	N	N	U	N	U	N	Holbrook et al. (2013)
lean lake trout *Salvelinus namaycush*	mysid (stationary) *Mysis diluviana*	N	N	N	N	U	N	U	N	Holbrook et al. (2013)
largemouth bass *Micropterus salmoides*	redside shiner *Richardsonius balteatus*	N	N	N	N	Y	N	N	N	Howick and O'Brien (1983)
largemouth bass *Micropterus salmoides*	bluegill *Lepomis macrochirus*	N	N	N	N	Y	N	N	N	Howick and O'Brien (1983)
pike *Esox lucius*	cladoceran *Daphnia* sp.	N	N	N	N	Y	N	N	N	Jönsson et al. (2012)
pike *Esox lucius*	roach *Rutilus rutilus*	N	N	N	N	Y	N	N	N	Jönsson et al. (2012)
siscowet lake trout *Salvelinus namaycush siscowet*	golden shiner *Notemigonus crysoleucas*	N	N	Y	N	Y	N	N	N	Keyler et al. (2015)
siscowet lake trout *Salvelinus namaycush siscowet*	golden shiner (large) *Notemigonus crysoleucas*	N	N	Y	N	Y	N	N	N	Keyler et al. (2015)
siscowet lake trout *Salvelinus namaycush siscowet*	golden shiner (moving) *Notemigonus crysoleucas*	N	N	Y	N	Y	N	N	N	Keyler et al. (2015)
siscowet lake trout *Salvelinus namaycush siscowet*	golden shiner (small) *Notemigonus crysoleucas*	N	N	Y	N	Y	N	N	N	Keyler et al. (2015)

Predator	Prey	Criteria 1	2	3	4	5	6	7	8	Source
siscowet lake trout *Salvelinus namaycush siscowet*	golden shiner (stationary) *Notemigonus crysoleucas*	N	N	Y	N	Y	N	N	N	Keyler et al. (2015)
siscowet lake trout *Salvelinus namaycush siscowet*	deepwater sculpin *Myoxocephalus thompsonii*	N	N	Y	N	Y	N	N	N	Keyler et al. (2019)
lake herring *Coregonus artedi*	copepod *Limnocalanus macrurus*	N	N	Y	N	Y	Y	N	N	Link and Edsall (1996)
cutthroat trout *O. clarkii clarkia*	cutthroat trout *O. clarkii clarkii*	Y	Y	Y	Y	Y	N	U	Y	Mazur and Beauchamp (2003)
cutthroat trout *O. clarkii clarkii*	rainbow trout *Oncorhynchus mykiss*	Y	Y	Y	Y	Y	N	U	Y	Mazur and Beauchamp (2003)
lake trout *Salvelinus namaycush*	cutthroat trout *O. clarkii clarkii*	Y	Y	Y	Y	Y	N	U	Y	Mazur and Beauchamp (2003)
lake trout *Salvelinus namaycush*	rainbow trout *Oncorhynchus mykiss*	Y	Y	Y	Y	Y	N	U	Y	Mazur and Beauchamp (2003)
rainbow trout *Oncorhynchus mykiss*	cutthroat trout *O. clarkii clarkii*	Y	Y	Y	Y	Y	N	U	Y	Mazur and Beauchamp (2003)
rainbow trout *Oncorhynchus mykiss*	rainbow trout *Oncorhynchus mykiss*	Y	Y	Y	Y	Y	N	U	Y	Mazur and Beauchamp (2003)
Atlantic cod *Gadus morhua*	mysid *Praunus neglectus*	N	N	N	N	Y	N	U	N	Meager et al (2010)

Predator	Prey	Criteria								Source
		1	2	3	4	5	6	7	8	
Atlantic cod *Gadus morhua*	mysid *Praunus neglectus*	N	Y	N	N	Y	N	U	N	Meager et al. (2005)
emerald shiner *Notropis atherinoides*	cladoceran *Daphnia magna*	N	N	Y	N	Y	N	N	N	Nieman and Gray (2018)
walleye *Sander vitreus*	emerald shiner *Notropis atherinoides*	N	N	N	N	Y	N	N	N	Nieman and Gray (2018)
walleye *Sander vitreus*	golden shiner *Notemigonus crysoleucas*	N	N	N	N	Y	N	N	N	Nieman and Gray (2018)
threespine stickleback *Gasterosteus aculeatus*	brine shrimp *Artemia salina*	N	Y	N	N	Y	N	N	N	Quesenberry et al. (2007)
pike *Esox lucius*	roach *Rutilus rutilus*	N	N	N	N	Y	N	N	N	Ranåker et al. (2012)
yellow perch *Perca flavescens*	cladoceran *Daphnia pulicaria*	N	N	Y	N	Y	N	Y	N	Richmond et al. (2004)
Miry's demoiselle *Neopomacentrus miryae*	brine shrimp *Artemia salina*	N	N	Y	N	Y	N	N	N	Rickel and Genin (2005)
Arctic grayling *Thymallus arcticus*	cladoceran *Bosmina longirostris*	N	N	N	N	Y	N	N	N	Schmidt and O'Brien (1982)
Arctic grayling *Thymallus arcticus*	copepod *Cyclops scutifer*	N	N	N	N	Y	N	N	N	Schmidt and O'Brien (1982)
Arctic grayling *Thymallus arcticus*	cladoceran *Daphnia longiremis*	N	N	N	N	Y	N	N	N	Schmidt and O'Brien (1982)
Arctic grayling *Thymallus arcticus*	cladoceran *Daphnia pulex*	N	N	N	N	Y	N	N	N	Schmidt and O'Brien (1982)
Arctic grayling *Thymallus arcticus*	copepod *Heterocope septentrionalis*	N	N	N	N	Y	N	N	N	Schmidt and O'Brien (1982)

Predator	Prey	Criteria 1	2	3	4	5	6	7	8	Source
flavescent peacock *Aulonocara stuartgranti*	brine shrimp *Artemia* sp. (dead)	N	N	Y	N	Y	N	N	N	Schwalbe et al. (2015)
flavescent peacock *Aulonocara stuartgranti*	brine shrimp *Artemia* sp. (living)	N	N	Y	N	Y	N	N	N	Schwalbe et al. (2015)
Tramitichromis sp.	brine shrimp *Artemia* sp. (dead)	N	N	Y	N	Y	N	N	N	Schwalbe et al. (2015)
Tramitichromis sp.	brine shrimp *Artemia* sp. (living)	N	N	Y	N	Y	N	N	N	Schwalbe et al. (2015)
brook trout *Salvelinus fontinalis*	housefly *Musca domestica*	N	N	Y	N	Y	N	N	N	Sweka and Hartman (2001)
smallmouth bass *Micropterus dolomieu*	housefly *Musca domestica*	N	N	Y	N	Y	N	N	N	Sweka and Hartman (2003)
two-spotted goby *Gobius flavescens*	**copepod (red mobile) *Calanus finmarchicus* *C. helgolandicus***	**N**	**Y**	**Y**	**C**	**Y**	**N**	**N**	**N**	**Utne-Palm (1999)**
two-spotted goby *Gobius flavescens*	**copepod (transparent immobile) *Calanus finmarchicus* *C. helgolandicus***	**N**	**Y**	**Y**	**C**	**Y**	**N**	**N**	**N**	**Utne-Palm (1999)**
two-spotted goby *Gobius flavescens*	**copepod (transparent mobile) *Calanus finmarchicus* *C. helgolandicus***	**N**	**Y**	**Y**	**C**	**Y**	**N**	**N**	**N**	**Utne-Palm (1999)**
two-spotted goby *Gobius flavescens*	copepod (10 prey) *Acartia clausi*	N	Y	Y	N	Y	N	N	N	Utne (1997)

Predator	Prey	Criteria								Source
		1	2	3	4	5	6	7	8	
two-spotted goby *Gobius flavescens*	copepod (1 prey) *Calanus finmarchicus*	Y	Y	Y	N	Y	N	N	N	Utne (1997)
two-spotted goby *Gobius flavescens*	**copepod (10 prey) *Calanus finmarchicus***	**Y**	**Y**	**Y**	**Y**	**Y**	N	**N**	**N**	**Utne (1997)**
bluegill *Lepomis macrochirus*	cladoceran *Daphnia pulex*	Y	N	Y	Y	Y	N	N	N	Vinyard and O'Brien (1976)
lake trout *Salvelinus namaycush*	cutthroat trout *Oncorhynchus clarkii clarkii*	Y	Y	Y	Y	Y	N	U	N	Vogel and Beauchamp (1999)
lake trout *Salvelinus namaycush*	rainbow trout *Oncorhynchus mykiss*	Y	Y	Y	Y	Y	N	U	N	Vogel and Beauchamp (1999)

Case #1: Chinook salmon reacting to rainbow trout

Hansen et al. (2013) conducted experiments where piscivorous yearling Chinook salmon *Oncorhynchus tshawytscha* reacted to live juvenile rainbow trout *O. mykiss* under varying levels of light and turbidity. One or two predators were used for each experimental trial. Prey fish were tethered inside clear acrylic tubes during experiments to minimize the potential for non-visual stimuli. However, as light levels decreased, the distance where Chinook salmon reacted to prey approached an asymptote at approximately 50 cm, potentially owing to a response to a non-visual stimulus that may have been an artifact of experimental design.

Lighting for the experiments was generated by lamps with a spectral output of 380–760 nm, placed 2.4 m above the water surface within the experimental arena. Light intensity was manipulated using dimmer switches and fiberglass window screens placed between the lamp and a diffuser plate. Light was measured in lux using an LI-COR LI-210 cosine corrected photometric sensor with a spectral sensitivity from 380–770 nm and in quantum flux using an LI-190 cosine corrected terrestrial quantum sensor with a spectral sensitivity from 400–700 nm. Turbidity was generated by mixing pulverized kaolin into the experimental arena using a pump. For experimental trials, the authors measured turbidity in nephelometric turbidity units (NTU) using a LaMotte Model 2020e nephelometer. The authors reported a conversion between NTU and beam attenuation coefficient, c (c = 0.40×NTU), at a wavelength of 660 nm based on transmittance measurements obtained using a Milton Roy Spectronic 21 DV spectrophotometer with a 10 mm path length cuvette. Because measurements were not corrected for forward scattering, conversion between NTU and c reported by Hansen et al. (2013) was more likely to approximate the effective attenuation coefficient, κ. We fit models to the original data from Hansen et al. (2013).

Case #2: Two-spotted goby reacting to ten copepods

Utne (1997) conducted microcosm experiments where two-spotted goby *Gobius flavescens* reacted to *Calanus finmarchicus*, a transparent calanoid copepod, under varying levels of light and turbidity. Prey were added to the experimental tanks in clear glass vials, each containing 10 copepods. Lighting for the experiments was provided using three halogen lamps, directed at the white walls of the experimental room. Diffuse light conditions were maintained in the experimental tanks by placing tanks in a white linen tent. Light intensity was manipulated by shielding the halogen lamps with perforated metal sheets. Light was measured using a Biospherical Instruments QSP-170B with a QSR-240 quantum scalar reference sensor which, per the manufacturer, has a spectral response within ±10% of 400-700 nm. Turbidity was generated by mixing diatomaceous earth into experimental arenas, and maintained using a perforated bubbling tube. To characterize turbidity, Utne (1997) measured absorbance at 800 nm using a Shimadzu UV-VIS Recording Spectrophotometer UV-160 with a 100 mm path length cuvette.

For Case #2, we digitized reaction distances from individual reactions from Utne (1997). Utne (1997) measured absorbance in units of cm^{-1}, but axis titles in the paper were erroneously labeled in units of m^{-1} (A.C. Utne-Palm, personal communication, May 21, 2019). Thus, we multiplied absorbances by 100, and treated absorbance values as the effective attenuation coefficient, κ, for model fitting.

Case #3: Two-spotted goby reacting to single copepods

Utne-Palm (1999) measured the reaction of two-spotted goby to single *Calanus finmarchicus/Calanus helgolandicus* prey under varying levels of turbidity and a light intensity of 20 μE m^{-2} s^{-1}. Copepod treatments included mobile transparent, immobile transparent (glued to a glass coverslip), and mobile red-colored prey. As in Case #2, prey were inside glass vials for experiments. Light and turbidity were manipulated and measured using the same methods as Case #2. For Case #3, we digitized mean reaction distance data from Utne-Palm (1999).

Case #4: Stone moroko reacting to Daphnia pulex

Asaeda et al. (2002) measured the reaction distance and nadir viewing angle of stone moroko *Pseudorasbora parva* predators reacting to 0.8-1.0 mm *Daphnia pulex* prey under varying levels of light and turbidity. Free-swimming live prey were introduced to the experimental tanks containing a single predator, and data were collected until 20 reactions were recorded. Lighting was generated using fluorescent lamps that were partly covered by black paper and positioned 70 cm above the tanks. Turbidity was generated using kaolin. The authors did not report what equipment was used to obtain measurements of light and turbidity.

For Case #4, we digitized reaction distances from individual reactions from Asaeda et al. (2002). Measurement units reported in the study were incompatible with our models, so we transformed the data. The authors reported reaction distance in terms of predator body lengths. Predators used in the experiments were 50-60 mm, so we converted reaction distances to meters assuming a predator body length of 55 mm. Sagittal viewing angles were reported relative to a horizontal plane, where “upward” angles were positive and “downward” angles were negative, so we converted sagittal viewing angles to nadir viewing angles. Turbidity was reported as NTU, but no conversion to beam attenuation was provided and, for clear-water treatments, turbidity

measurements were reported as NTU < 1. No measurements of the vertical attenuation coefficient were reported. For clear-water treatments, we assumed turbidity was the same as clear-water treatments in Case #1 (0.352 NTU), and converted NTU to the effective attenuation coefficient, κ, using the NTU to absorbance conversion for kaolin from Hansen et al. (2013). There is no direct relationship between the beam attenuation coefficient, c, and the diffuse attenuation coefficient, k_d, or between the effective attenuation coefficient, κ, and k_d. The true relationship between the beam attenuation coefficient and diffuse attenuation coefficient varies depending on factors such as the scattering phase function and radiance structure of the light field (Baker and Smith, 1979; Gordon, 1989). In natural marine waters, the beam attenuation coefficient, c, in the visible spectrum is often 2–4 times the vertical attenuation coefficient (Duntley, 1967). We conducted a preliminary sensitivity analysis and determined that model performance was relatively insensitive to conversions ranging from $k_d = c$ through $k_d = c/5$, so we assumed $k_d = c/3$, the middle of Duntley's range. Although Asaeda et al. (2002) reported light intensity in lux, we did not transform light intensity data to quantum units prior to model fitting because the authors did not report a conversion. However, we note that post-hoc transformation could be applied to scale T and convert K_e to units of $\mu mol \cdot photons \cdot m^{-2} s^{-1}$.

Model fitting

Variance increased as reaction distance increased in each case, so we assumed reaction distances had log-normally distributed error. We estimated separate variances for visual, σ_V, and non-visual, σ_{NV}, components of models because they involve different predator sensory processes that would presumably have different residual error structures.

We fit models to data using constrained maximum likelihood estimation with the quasi-Newton L-BFGS-B algorithm. We imposed parameter constraints to ensure the parameter space was restricted to physically and biologically plausible values. We fit models and estimated 95% confidence intervals for parameters using R package 'bbmle' (Bolker, 2017).

For computational efficiency, we used the Lambert W function (i.e. product logarithm function), $W(\cdot)$, to numerically approximate r_V in the Aksnes and Utne model and generalized visual reaction distance model. As an example, for the generalized visual reaction distance model:

$$r_V = W\left(0.5 \times (\kappa - k_d \cos\theta) \times \left(\omega(\kappa)|C_0|A_p E' \frac{E_b}{K_e + E_b}\right)^{0.5}\right) \times \left(\frac{2}{\kappa - k_d \cos\theta}\right). \qquad (B1)$$

Data and R code

Data and R code for cases are available via an online GitHub repository (Sean-Rohan-NOAA/GVRDM). A gold-standard back-up of the data and code are maintained by NOAA's Alaska Fisheries Science Center.

Chapter 1 Appendix C: Empirical visual encounter distance model

For Case #1, we sought to compare the fit of an empirical visual encounter distance model to the Aksnes and Utne model and generalized visual reaction distance model. To do so, we used a continuous version of Hansen et al.'s (2013) broken-stick model (BSM). We chose the broken stick model because it was the most parsimonious empirical model out of four considered by Hansen et al. (2013). Hansen et al. (2013) parameterized the broken stick model by fitting separate models between turbidity and reaction distance (at a light intensity of ~50 lx), and light and reaction distance (at turbidity of 0.352 NTU):

$$r = \begin{cases} v + w\mathrm{E}_b & if\ E_b \le q_E \\ r_{maxE} & if\ E_b > q_E \end{cases}, \quad (C1)$$

$$r = \begin{cases} r_{maxc} & if\ c \le q_c \\ ue^{yc} & if\ c > q_c \end{cases}, \quad (C2)$$

where Eqn. B1 is the equation for light and Eqn. B2 is the equation for turbidity (see Table 3 for description of terms). Model parameters from Eqn. B1 and Eqn. B2 were subsequently used in a continuous model by Hansen et al. (2013) and Hansen and Beauchamp (2015), obtained by setting $u = e^{-\mathrm{yq}_c}$:

$$r = \begin{cases} (v + wE_b)p & if \quad E_b > q_E \\ pr_{max}p & if \quad E_b > q_E \end{cases}, \quad (C3)$$

$$p = \begin{cases} 1 & if \quad c \le q_c \\ ue^{yc} & if \quad c > q_c \end{cases}. \quad (C4)$$

For this study, we rearranged Eqn. B3 and B4 to create an equivalent form of the broken stick model, as:

$$r = \begin{cases} (v + wE_b)p & if\ E_b > q_E \\ r_{max}p & if\ E_b \le q_E \end{cases} \quad (C5)$$

$$p = \begin{cases} 1 & if\ c \le q_c \\ e^{y(c-q_c)} & if\ c > q_c \end{cases}. \quad (C6)$$

Chapter 1 Appendix D: Residual plots

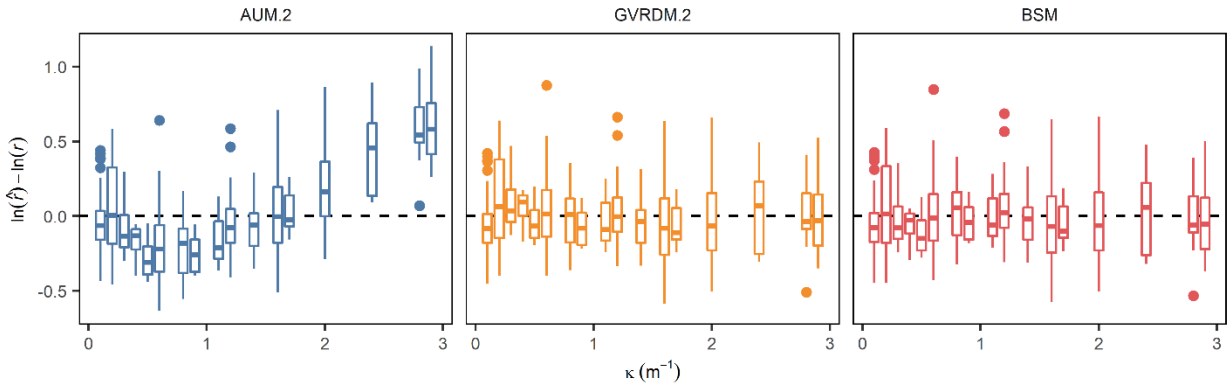

Figure D1. Case #1—Boxplot of residuals of the Aksnes and Utne model with a non-visual reaction (AUM.2), the generalized visual reaction distance model with a non-visual reaction, without β (GVRDM.2), and the empirical broken-stick model (BSM) along a gradient of effective attenuation coefficient, κ, grouped by treatment level.

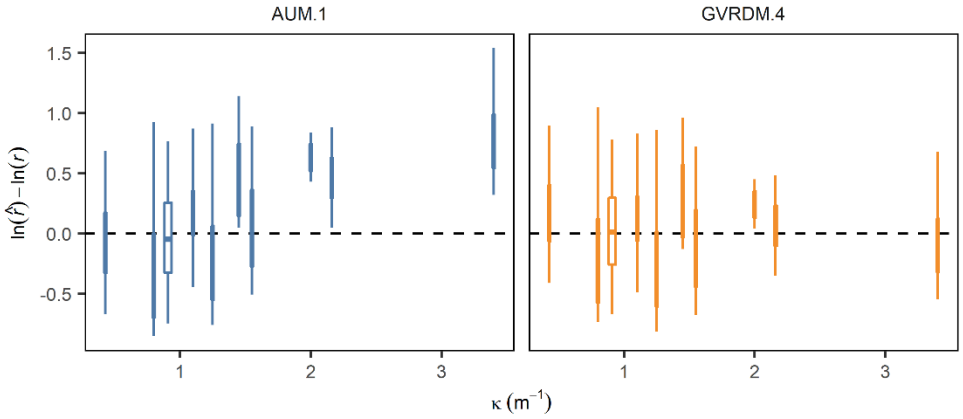

Figure D2. Case #2— Boxplot of residuals of the Aksnes and Utne model (AUM.1) and generalized visual reaction distance model without a non-visual reaction or β (GVRDM.4) along a gradient of effective attenuation coefficient, κ, grouped by treatment level.

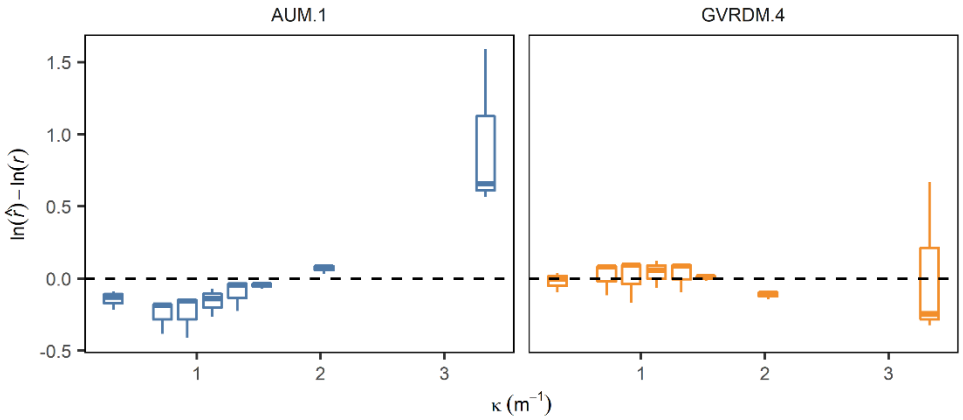

Figure D3. Case #3—Boxplot of residuals of the Aksnes and Utne model (AUM.1) and generalized visual reaction distance model without a non-visual reaction or β (GVRDM.4) along a gradient of effective attenuation coefficient, κ, grouped by κ treatment level.

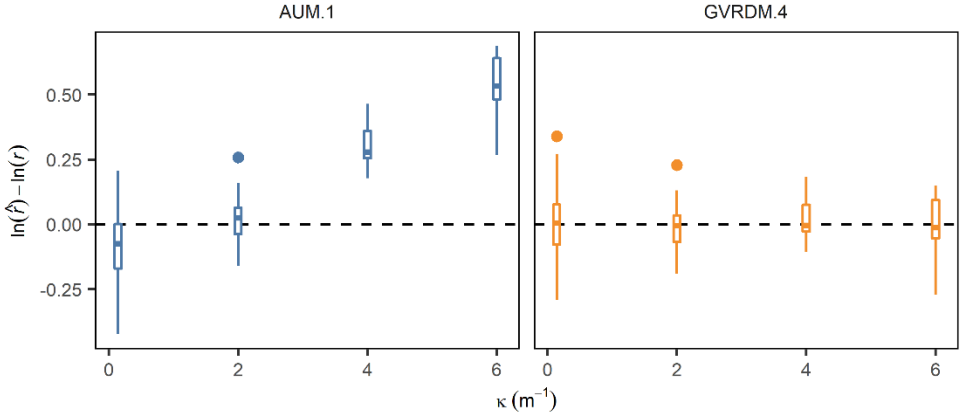

Figure D4. Case #4—Boxplot of residuals of the Aksnes and Utne model (AUM.1) and generalized visual reaction distance model without a non-visual reaction or β (GVRDM.4) along a gradient of effective attenuation coefficient, κ, grouped by κ treatment level.

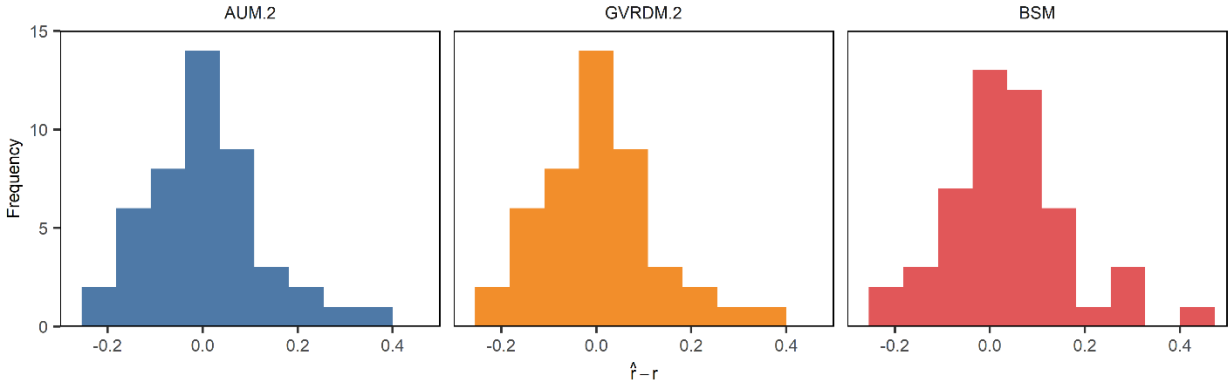

Figure D5. Case #1—Distributions of residuals for the Aksnes and Utne model with a non-visual reaction (AUM.2), the generalized visual reaction distance model with-non visual reaction,

without β (GVRDM.2), and the empirical broken-stick model (BSM), for the subset of reactions that were assigned to non-visual reaction distances in AUM.2 and GVRDM.2.

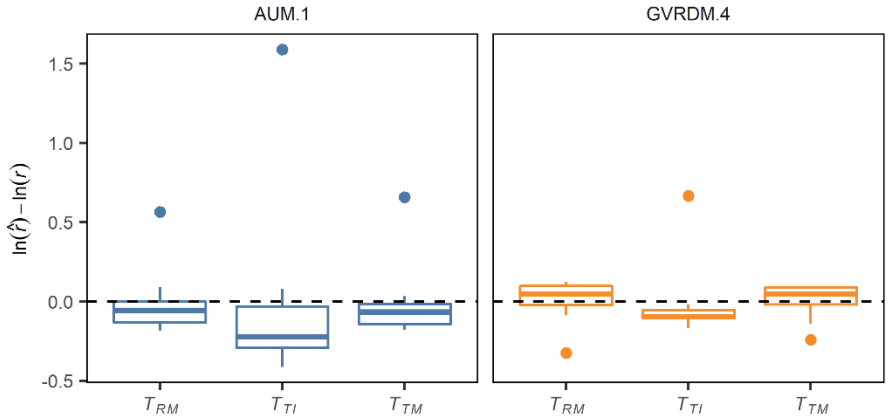

Figure D6. Case #3—Boxplots of error residuals of the Aksnes and Utne model (AUM.1) and the generalized visual reaction distance model without a non-visual reaction or β (GVRDM.4) for different copepod prey types. On the horizontal axis, *Calanus finmarchicus/helgolandicus* prey are denoted as: RM—red mobile, TI—transparent immobile, and TM—transparent mobile.

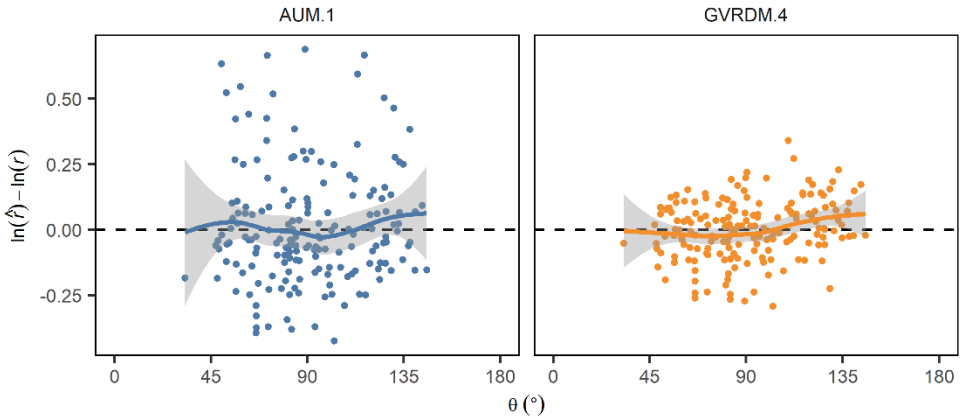

Figure D7. Case #4—Residuals of the Aksnes and Utne model (AUM.1) and the generalized visual reaction distance model without a non-visual reaction or β (GVRDM.4) along a gradient of sagittal viewing angle, θ. Lines and shaded areas denote the fit (mean ±2 standard errors) of loess models to residuals.

Chapter 1 Appendix E: Parameter estimates

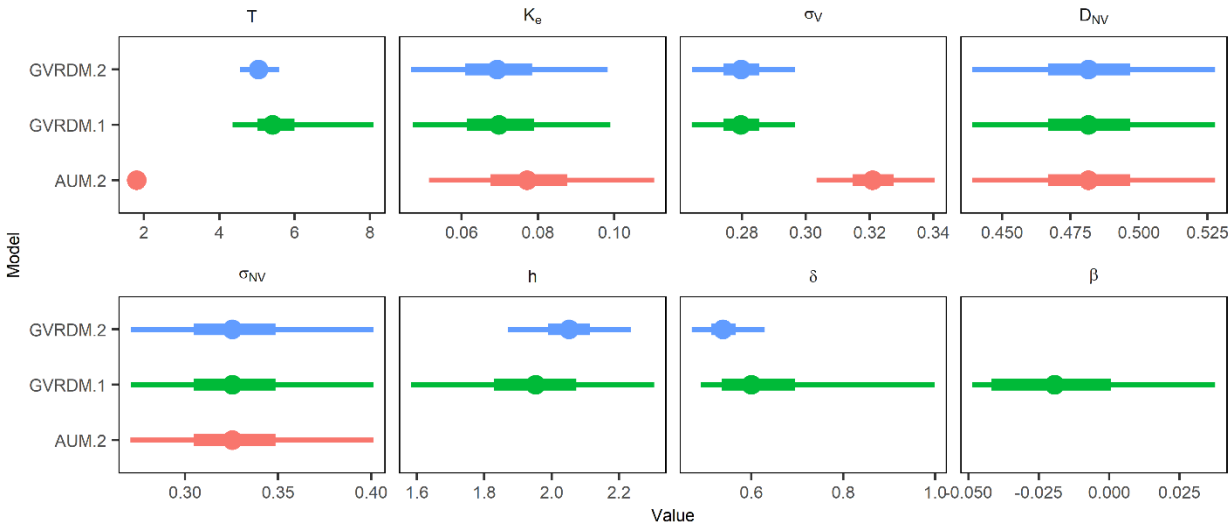

Figure E1. Case #1—Parameter estimates and confidence intervals for the Aksnes and Utne model with a non-visual reaction (AUM.2), the generalized visual reaction distance model with non-visual reaction and β (GVRDM.1), and the generalized visual reaction distance model without a non-visual reaction or β (GVRDM.2). Circles denote the means, thick lines denote 50% confidence intervals, and thin lines denote 95% confidence intervals.

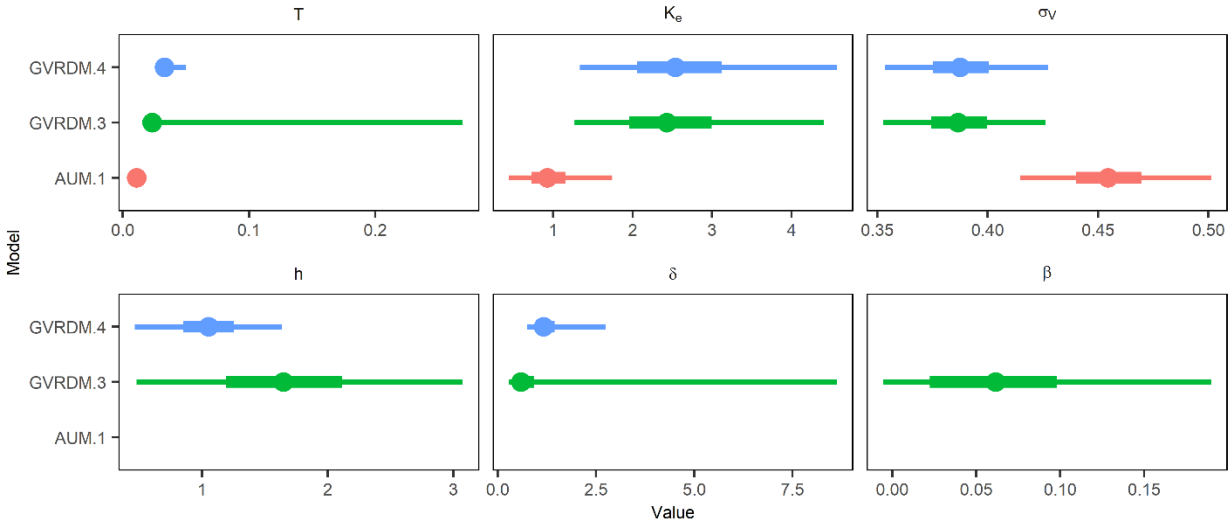

Figure E2. Case #2–Parameter estimates and confidence intervals for the Aksnes and Utne model (AUM.1); generalized visual reaction distance model without non-visual reaction, with β (GVRDM.3); generalized visual reaction distance model without a non-visual reaction or β (GVRDM.4). Circles denote the means, thick lines denote 50% confidence intervals, thin lines denote 95% confidence intervals.

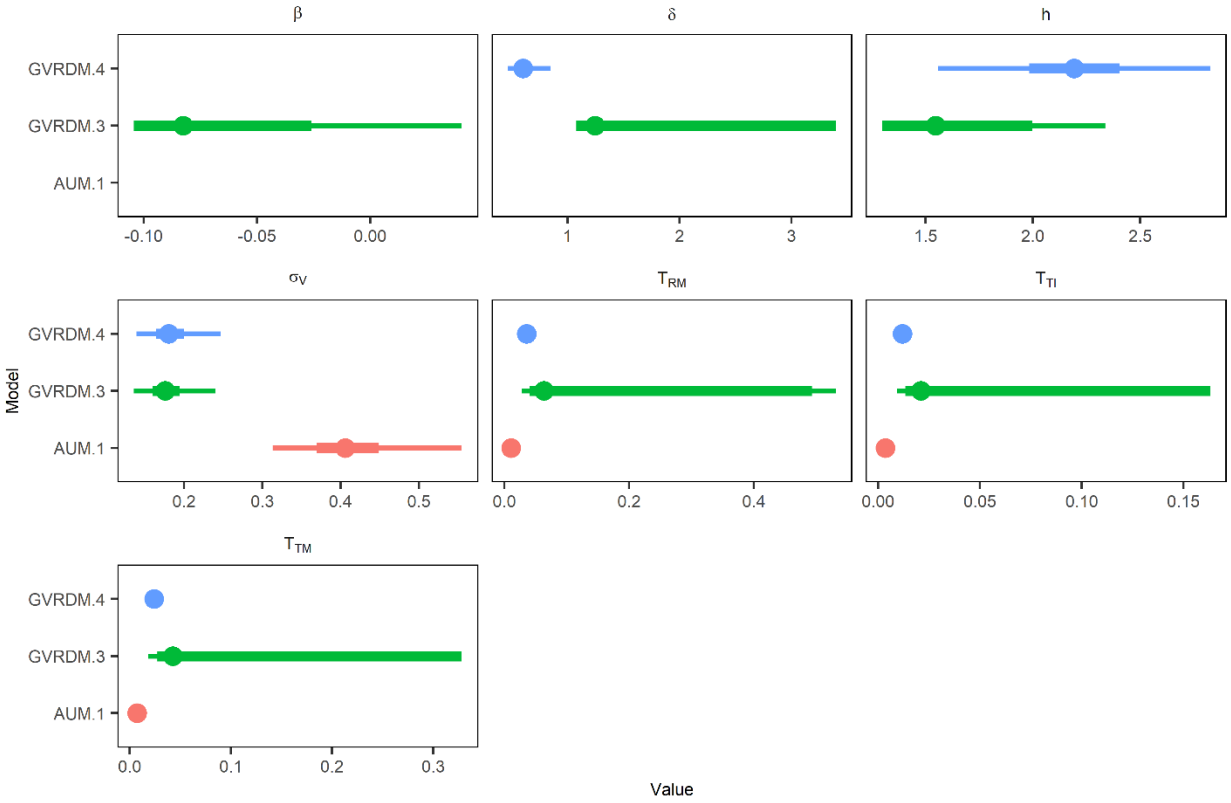

Figure E3. Case #3–Parameter estimates and confidence intervals for the Aksnes and Utne model (AUM.1), the generalized visual reaction distance model without non-visual reaction, with β (GVRDM.3), and the generalized visual reaction distance model without a non-visual reaction or β (GVRDM.4). Circles denote the means, thick lines denote 50% confidence intervals, thin lines denote 95% confidence intervals. Parameters for *Calanus finmarchicus/helgolandicus* prey are: T_{RM}—red mobile, T_{TI}—transparent immobile, and T_{TM}—transparent mobile.

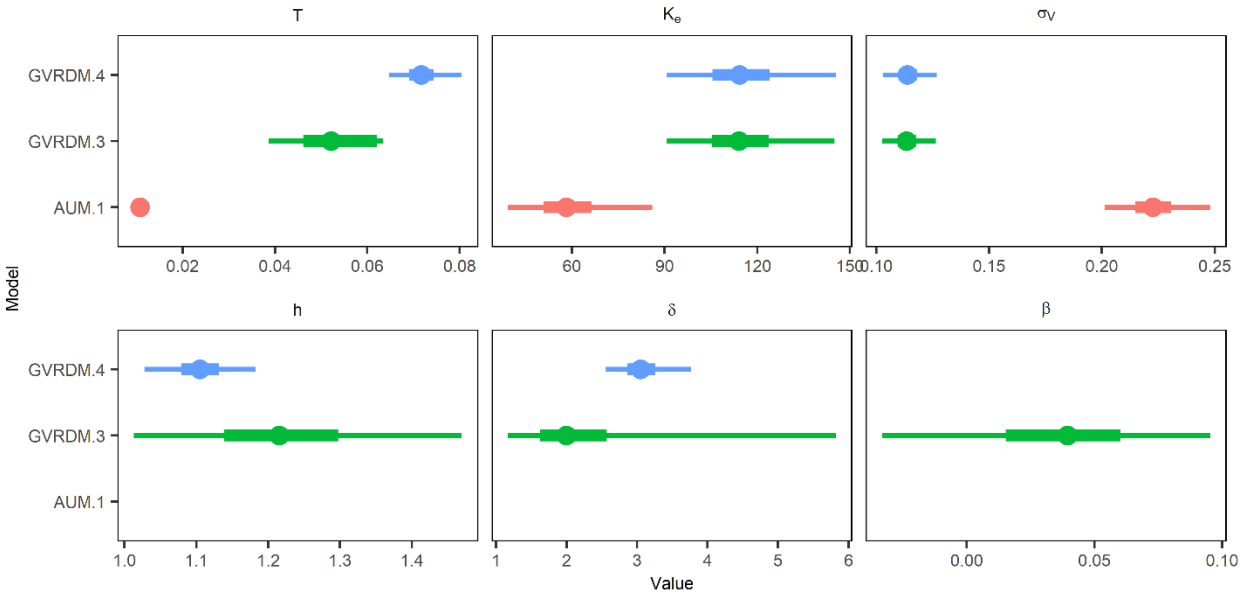

Figure E4. Case #4–Parameter estimates and confidence intervals for the Aksnes and Utne model (AUM.1), the generalized visual reaction distance model without non-visual reaction, with β (GVRDM.3), and the generalized visual reaction distance model without a non-visual reaction or β (GVRDM.4). Circles denote the means, thick lines denote 50% confidence intervals, thin lines denote 95% confidence intervals.

Chapter 1 Appendix F: Pseudoreplication, attenuation coefficients, and angular dependence

Pseudoreplication

Aside from Case #3, we fit models to multiple reaction distances from single experimental trials, without accounting for pseudoreplication. To evaluate whether pseudoreplication affected the outcomes of model comparisons, we fit models to mean reaction distances for individual trials from Case #1. Aggregating reaction distance data by treatment level did not affect model ranking (Table F1).

Table F1. Model fits to mean reaction distances for Case #1, accounting for pseudoreplication.

Model	Par. (#)	n	ΔAIC_c
AUM.2	6	83	73.0
GVRDM.1	9	83	1.7
GVRDM.2	**8**	**83**	**0.0**
BSM	7	83	10.2

Attenuation coefficients

Absorbances derived from spectrophotometer or beam transmissometer measurements do not necessarily approximate the beam attenuation coefficient, *c*. Forward scattered light can cause light that has been scattered out of a collimated beam to reach the detector of a spectrophotometer or beam transmissometer, causing a positive bias in measured transmittance, leading to an underestimation of the beam attenuation coefficient (Zaneveld et al., 1979). Measurement biases are typically higher when path lengths are short, detector acceptance angles are wide (>1°), media are highly scattering, and transmitted wavelengths are prone to forward scattering (Kirk, 2011).

Because the Aksnes and Utne model is based on the law of contrast reduction, Aksnes and Utne (1997) corrected for forward scattering and spectrophotometer acceptance angle based on Jackson Turbidity Units, spectrophotometer absorbance, spectrophotometer path length, and the half-angle acceptance of the detector of the spectrophotometer, prior to model fitting.

Although we assumed the law of contrast reduction is violated in aquatic predator-prey interactions for our primary analyses, we sought to determine whether adjusting the absorbances to estimate the beam attenuation coefficient, rather than using raw absorbances, would affect our conclusions. Therefore, using data from Case #2, we followed the approach of Aksnes and Utne (1997), to calculate beam attenuation coefficients. We then fit models using the beam attenuation coefficient, c, instead of the effective attenuation coefficient, κ. Using beam attenuation, the generalized visual reaction distance model had a better fit to Case #2 data than the Aksnes and Utne model, based on lower AIC_c values (Table F2).

Table F2. Summary of model fits to Case #2 data with corrected beam attenuation coefficient, *c*.

Model	Par. (#)	n	ΔAICc
Case #2			
AUM.1	3	214	13.94
GVRDM.3	6	214	0.21
GVRDM.4	**5**	**214**	**0.0**

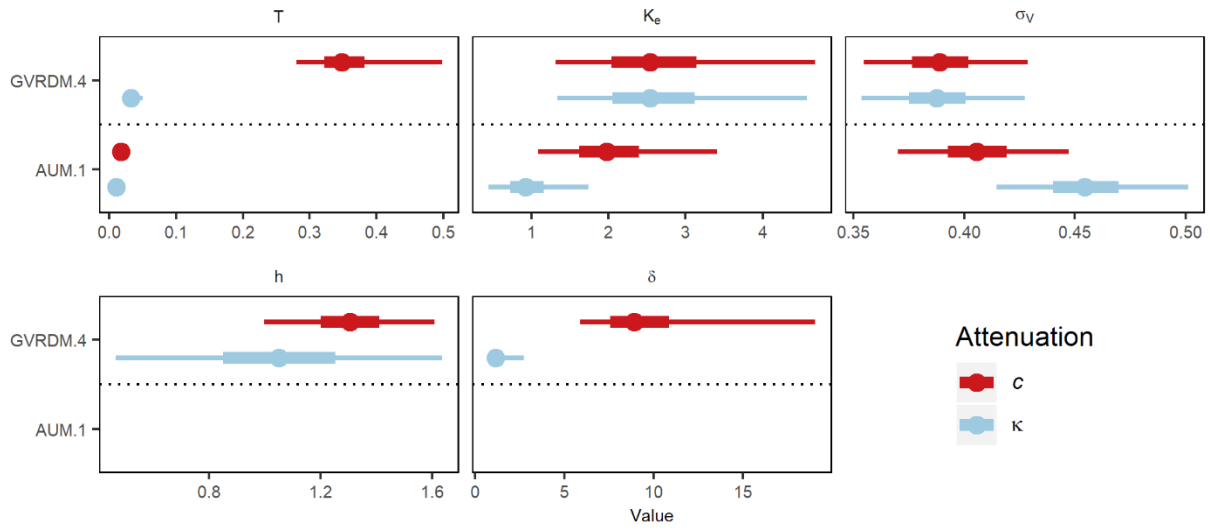

Figure F2. Parameter estimates for Case #2 data where spectrophotometer absorbance measurements were used as a proxy for the effective attenuation coefficient, κ, and where the beam attenuation coefficient, c, was estimated by adjusting absorbance measurements. Parameter estimates are shown for the generalized visual reaction distance model without a non-visual reaction or β (GVRDM.4) and the Aksnes and Utne model (AUM.1). Circles denote the means, thick lines denote 50% confidence intervals, thin lines denote 95% confidence intervals.

Angular dependence

Using data from Case #4, we evaluated whether accounting for nadir viewing angle, θ, in visual predator-prey interactions improved the fit of the generalized visual reaction distance model to data. To do so, we compared versions of the model where viewing angle data were included in the model to versions where viewing angle equaled 90°. The latter approach has typically been used to fit visual encounter distance models to experimental data. We found that including nadir viewing angle improved model fit, based on AIC_c (Table F3).

Table F3. Fits of the generalized visual reaction distance model to mean reaction distances from Case #4 assuming θ = 90° versus using observed values of θ.

Model	Par. (#)	n	AIC_c	ΔAIC_c
Assume θ = 90°				
GVRDM.3	6	177	-254.0	2.8
GVRDM.4	5	177	-254.9	1.9
Observed θ				
GVRDM.3	6	177	-255.8	1.0
GVRDM.4	5	177	-256.8	0.0

Chapter 1 Appendix G: Asymptotic equivalence between behavioral and theoretical models

Several studies have used Michaelis-Menten (e.g. Holling type-II) functions to model the relationship between light intensity and visual reaction distance under constant, clear-water conditions (i.e. low beam attenuation, low effective attenuation coefficient). Michaelis-Menten functions are structurally equivalent to a Naka-Rushton function with α=1. Here, we demonstrate that at low levels of turbidity and over short reaction distances, Michaelis-Menten models are an asymptotic approximation of the Aksnes and Utne model and generalized visual reaction distance model. Equations below are show using the symbols used by study authors and units of measure are shown using bracket notation (e.g. [m]).

Examples of Michaelis-Menten models are Richmond et al.'s (2004) model of age-0 yellow perch *Perca flavescens* reacting to *Daphnia pulicaria*, Holbrook et al.'s (2013) model of age-0 lake trout *Salvelinus namaycush* reacting to *Daphnia magna*, Keyler et al.'s (2015) model of siscowet lake trout *Salvelinus namaycush siscowet* reacting to golden shiner *Notemigonus crysoleucas*, and Keyler et al.'s (2019) model of siscowet lake trout *Salvelinus namaycush siscowet* reacting to deepwater sculpin *Myoxocephalus thompsonii*. In their models:

$$R_d[\mathrm{cm}] = \frac{R_{\max}[\mathrm{cm}] \cdot L_i[\mathrm{lux}]}{\alpha[\mathrm{lux}] + L_i[\mathrm{lux}]}, \tag{G1a}$$

or

$$R_d[\mathrm{cm}] = \frac{R_{\max}[\mathrm{cm}] \cdot L_i[\mathrm{photons} \cdot \mathrm{m}^{-2} \cdot \mathrm{s}^{-1}]}{\alpha[\mathrm{photons} \cdot \mathrm{m}^{-2} \cdot \mathrm{s}^{-1}] + L_i[\mathrm{photons} \cdot \mathrm{m}^{-2} \cdot \mathrm{s}^{-1}]}, \tag{G1b}$$

where R_d is reaction distance, R_{max} is maximum reaction distance, L_i is light intensity, and α is a half-saturation constant. Similarly, Hansen et al. (2013) considered a Holling type-II function with

an intercept as a candidate for modeling the reaction distance of yearling Chinook salmon to juvenile rainbow trout (i.e. Case #1):

$$RD[\mathrm{cm}] = C[\mathrm{cm}] + \frac{A[\mathrm{cm}]I[\mathrm{lux}]}{B[\mathrm{lux}] + I[\mathrm{lux}]} \tag{G2}$$

where *RD* is reaction distance, *C* is the reaction distance asymptote at low light, *A* is a parameter which represents the maximum visual reaction distance that is added to *C*, *B* is a half-saturation constant, and *I* is light intensity.

In the Aksnes and Utne model, as beam attenuation, *c*, and viewing distance, r_V, approach 0, e^{cr_V} approaches 1. Setting $e^{cr_V} = 1$ results in:

$$r_V^2[\mathrm{m}^2] = \frac{T[\mathrm{m}^2] \cdot E_b[\mu\mathrm{E} \cdot \mathrm{m}^2 \cdot \mathrm{s}^{-1}]}{K_e[\mu\mathrm{E} \cdot \mathrm{m}^2 \cdot \mathrm{s}^{-1}] + E_b[\mu\mathrm{E} \cdot \mathrm{m}^2 \cdot \mathrm{s}^{-1}]}. \tag{G3}$$

Similarly, in the generalized visual reaction distance model, as the effective attenuation coefficient, κ, and r_V approach 0, $e^{\kappa r_V}$ approaches 1. For the generalized visual reaction distance model, setting $e^{\kappa r_V} = 1$ results in:

$$r_V^2[\mathrm{m}^2] = \omega(\kappa)\frac{T[\mathrm{m}^2] \cdot E_b[\mu\mathrm{E} \cdot \mathrm{m}^2 \cdot \mathrm{s}^{-1}]}{K_e[\mu\mathrm{E} \cdot \mathrm{m}^2 \cdot \mathrm{s}^{-1}] + E_b[\mu\mathrm{E} \cdot \mathrm{m}^2 \cdot \mathrm{s}^{-1}]}, \tag{G4}$$

where $\omega(\kappa)$ is a constant.

Most visual encounter distance experiments measure light using the same general approach, regardless of differences in measurement units. Therefore, light quantities in equations G1–G4 are interchangeable if: $E_b \propto L_i \propto I$. Quantities R_{max} and T can be converted using $R_{max}/100[m] = \sqrt{T}[m]$, while r_V^2 and R_d can be converted using $R_d/100[m] = \sqrt{r_V^2}[m]$. Thus, through unit conversion:

$$\frac{E_b\sqrt{T}}{K_e + E_b} = \frac{L_i\left(\frac{R_{max}}{100}\right)}{\alpha + L_i} = \frac{I\left(\frac{A}{100}\right)}{B + I} + 0. \tag{G5}$$

This shows the models are effectively equal under clear-water conditions and over short distances.

References

Aksnes, D.L., Utne, A.C.W., 1997. A revised model of visual range in fish. Sarsia 82, 137–147. https://doi.org/10.1080/00364827.1997.10413647

Asaeda, T., Park, B.K., Manatunge, J., 2002. Characteristics of reaction field and the reactive distance of a planktivore, *Pseudorasbora parva* (Cyprinidae), in various environmental conditions. Hydrobiologia 489, 29–43. https://doi.org/10.1023/A:1023298823106

Baker, K.S., Smith, R.C., 1979. Quasi-inherent characteristics of the diffuse attenuation coefficient for irradiance. Ocean Opt. IV 208, 60–63.

Barrett, J.C., Grossman, G.D., Rosenfeld, J., 1992. Turbidity-induced changes in reactive distance of rainbow trout. Trans. Am. Fish. Soc. 121, 437–443. https://doi.org/10.1577/1548-8659(1992)121<0437:TICIRD>2.3.CO;2

Bolker, B.M., 2017. bbmle: Tools for General Maximum Likelihood Estimation.

Breck, J.E., Gitter, M.J., 1983. Effect of fish size on the reactive distance of bluegill (Lepomis macrochirus) sunfish. Can. J. Fish. Aquat. Sci. 40, 162–167. https://doi.org/10.1139/f83-026

Chesney, E.J., 2008. Foraging behavior of bay anchovy larvae, *Anchoa mitchilli*. J. Exp. Mar. Bio. Ecol. 362, 117–124. https://doi.org/10.1016/j.jembe.2008.06.011

Confer, J.L., Howick, G.L., Corzette, M.H., Kramer, S.L., Fitzgibbon, S., Landesberg, R., 1978. Visual predation by planktivores. Oikos 31, 27–37.

Crowl, T.A., 1989. Effects of crayfish size, orientation, and movement on the reactive distance of largemouth bass foraging in clear and turbid water. Hydrobiologia 183, 133–140.

Djamgoz, M.B.A., Yamada, M., 1990. Electrophysiological characteristics of retinal neurones: synaptic interactions and functional outputs, in: Douglas, R., Djamgoz, M. (Eds.), The Visual System of Fish. Chapman and Hall, New York, NY, pp. 159–210.

Duntley, S.Q., 1967. Visibility in the oceans. Opt. Spectra Fourth Qua, 64–69. https://doi.org/10.1166/jnn.20

Duntley, S.Q., 1952. The visibility of submerged objects. Cambridge, Massachusetts.

Duntley, S.Q., 1948. The reduction of apparent contrast by the atmosphere. J. Opt. Soc. Am. 38, 179–191.

Gordon, H.R., 1989. Can the Lambert-Beer law be applied to the diffuse attenuation coefficient of ocean water? Limnol. Oceanogr. 34, 1389–1409. https://doi.org/10.1097/00003246-200206000-00018

Gregory, R.S., Northcote, T.G., 1993. Surface, planktonic, and benthic foraging by juvenile Chinook salmon (*Oncorhynchus tshawytscha*) in turbid laboratory conditions. Can. J. Fish. Aquat. Sci. 50, 233–240.

Hansen, A.G., Beauchamp, D.A., Schoen, E.R., 2013. Visual prey detection responses of piscivorous trout and salmon: Effects of light, turbidity, and prey size. Trans. Am. Fish. Soc. 142, 854–867. https://doi.org/10.1080/00028487.2013.785978

Hecht, T., van der Lingen, C.D., 1992. Turbidity-induced changes in feeding strategies of fish in estuaries. South African J. Zool. 27, 95–107. https://doi.org/10.1080/02541858.1992.11448269

Henderson, M.A., Northcote, T.G., 1985. Visual prey detection and foraging in sympatric cutthroat trout (*Salmo clarki clarki*) and Dolly Varden (*Salvelinus malma*). Can. J. Fish. Aquat. Sci. 42, 785–790.

Holbrook, B. V., Hrabik, T.R., Branstrator, D.K., Mensinger, A.F., 2013. Foraging mechanisms of age-0 lake trout (*Salvelinus namaycush*). J. Great Lakes Res. 39, 128–137. https://doi.org/10.1016/j.jglr.2012.12.008

Howick, G.L., O'Brien, W.J., 1983. Piscivorous feeding behavior of largemouth bass: an experimental analysis. Trans. Am. Fish. Soc. 112, 508–516. https://doi.org/10.1577/1548-8659(1983)112<508

Jönsson, M., Ranåker, L., Anders Nilsson, P., Brönmark, C., 2012. Prey-type-dependent foraging of young-of-the-year fish in turbid and humic environments. Ecol. Freshw. Fish 21, 461–468. https://doi.org/10.1111/j.1600-0633.2012.00565.x

Kaneko, A., 1971. Electrical connexions between horizontal cells in the dogfish retina. J. Physiol. 213, 95–105. https://doi.org/10.1113/jphysiol.1971.sp009370

Keyler, T.D., Hrabik, T.R., Austin, C.L., Gorman, O.T., Mensinger, A.F., 2015. Foraging mechanisms of siscowet lake trout (*Salvelinus namaycush siscowet*) on pelagic prey. J. Great Lakes Res. 41, 1162–1171. https://doi.org/10.1016/j.jglr.2015.09.016

Keyler, T.D., Hrabik, T.R., Mensinger, A.F., Rogers, L.S., Gorman, O.T., 2019. Effect of light intensity and substrate type on siscowet lake trout (*Salvelinus namaycush siscowet*) predation on deepwater sculpin (*Myoxocephalus thompsonii*). Hydrobiologia 840, 77–88. https://doi.org/10.1007/s10750-019-3944-5

Kirk, J.T.O., 2011. Light and photosynthesis in aquatic ecosystems, 3rd ed. Cambridge University Press, New York.

Langbehn, T.J., Varpe, Ø., 2017. Sea-ice loss boosts visual search: Fish foraging and changing pelagic interactions in polar oceans. Glob. Chang. Biol. 23, 5318–5330. https://doi.org/10.1111/gcb.13797

Lee, Z., Shang, S., Hu, C., Du, K., Weidemann, A., Hou, W., Lin, J., Lin, G., 2015. Secchi disk depth: A new theory and mechanistic model for underwater visibility. Remote Sens. Environ. 169, 139–149. https://doi.org/10.1016/j.rse.2015.08.002

Link, J., Edsall, T.A., 1996. The effect of light on lake herring (*Coregonus artedi*) reactive volume. Hydrobiologia 332, 131–140. https://doi.org/10.1007/BF00016692

Lythgoe, J.., 1972. The adaptation of visual pigments to the photic environment, in: Dartnell, H.J.A. (Ed.), The Handbook of Sensory Physiology VII/1. Springer, pp. 566–603.

Mazur, M.M., Beauchamp, D.A., 2003. A comparison of visual prey detection among species of piscivorous salmonids: Effects of light and low turbidities. Environ. Biol. Fishes 67, 397–405. https://doi.org/10.1023/A:1025807711512

Meager, J.J., Moberg, O., Strand, E., Utne-Palm, A., 2010. Effects of light intensity on visual prey detection by juvenile Atlantic cod (*Gadus morhua* L.). Mar. Freshw. Behav. Physiol. 43, 99–108. https://doi.org/http://dx.doi.org/10.1080/10236241003798910

Meager, J.J., Solbakken, T., Utne-Palm, A., Oen, T., 2005. Effects of turbidity on the reaction distance, search time, and foraging success of juvenile Atlantic cod (*Gadus morhua*). Can. J. Fish. Aquat. Sci. 62, 1978–1984. https://doi.org/10.1139/F05-104

Middleton, W.E.K., 1952. Vision through the atmosphere. University of Toronto Press.

Naka, K.I., Chan, R.Y., Yasui, S., 1979. Adaptation in catfish retina. J. Neurophysiol. 42, 441–454. https://doi.org/10.1152/jn.1979.42.2.441

Naka, K.I., Chappell, R.L., Sakuranaga, M., Ripps, H., 1988. Dynamics of skate horizontal cells. J. Gen. Physiol. 92, 811–831. https://doi.org/10.1085/jgp.92.6.811

Naka, K.I., Rushton, W.A.H., 1966a. S-potentials from luminosity units in the retina of fish (Cyprinidae). J. Physiol. 185, 587–599.

Naka, K.I., Rushton, W.A.H., 1966b. S-potentials from colour units in the retina of fish (Cyprinidae). J. Physiol. 185, 536–555.

Nieman, C.L., Gray, S.M., 2019. Visual performance impaired by elevated sedimentary and algal turbidity in walleye *Sander vitreus* and emerald shiner *Notropis atherinoides*. J. Fish Biol. 95, 186–199. https://doi.org/10.1111/jfb.13878

Preisendorfer, R.W., 1986. Secchi disk science: Visual optics of natural waters. Limnol. Oceanogr. 31, 909–926.

Quesenberry, N.J., Allen, P.J., Cech, J.J., 2007. The influence of turbidity on three-spined stickleback foraging. J. Fish Biol. 70, 965–972. https://doi.org/10.1111/j.1095-8649.2007.01350.x

Ranåker, L., Jönsson, M., Nilsson, P.A., Brönmark, C., 2012. Effects of brown and turbid water on piscivore-prey fish interactions along a visibility gradient. Freshw. Biol. 57, 1761–1768. https://doi.org/10.1111/j.1365-2427.2012.02836.x

Richmond, H.E., Hrabik, T.R., Mensinger, A.F., 2004. Light intensity, prey detection and foraging mechanisms of age 0 year yellow perch. J. Fish Biol. 65, 195–205. https://doi.org/10.1111/j.0022-1112.2004.00444.x

Rickel, S., Genin, A., 2005. Twilight transitions in coral reef fish: the input of light-induced changes in foraging behaviour. Anim. Behav. 70, 133–144. https://doi.org/10.1016/j.anbehav.2004.10.014

Ruxton, G.D., Johnsen, S., 2016. The effect of aggregation on visibility in open water. Proc. R. Soc. B Biol. Sci. 283.

Sakai, H.M., Wang, J.L., Naka, K.I., 1995. Contrast gain control in the lower vertebrate retinas. J. Gen. Physiol. 105, 815–835.

Schmidt, D., O'Brien, W.J., 1982. Planktivorous feeding ecology of Arctic grayling (*Thymallus arcticus*). Can. J. Fish. Aquat. Sci. 39, 475–482. https://doi.org/10.1155/2011/352451

Schwalbe, M.A.B., Webb, J.F., 2015. The effect of light intensity on prey detection behavior in two Lake Malawi cichlids, *Aulonocara stuartgranti* and *Tramitichromis* sp. J. Comp. Physiol. A Neuroethol. Sensory, Neural, Behav. Physiol. 201, 341–356. https://doi.org/10.1007/s00359-015-0982-y

Sweka, J.A., Hartman, K.J., 2003. Reduction of reactive distance and foraging success in smallmouth bass, *Micropterus dolomieu*, exposed to elevated turbidity levels. Environ. Biol. Fishes 67, 341–347. https://doi.org/10.1023/A:1025835031366

Sweka, J.A., Hartman, K.J., 2001. Influence of turbidity on brook trout reactive distance and foraging success. Trans. Am. Fish. Soc. 130, 138–146. https://doi.org/10.1577/1548-8659(2001)130<0138:iotobt>2.0.co;2

Utne-Palm, A., 1999. The effect of prey mobility, prey contrast, turbidity and spectral composition on the reaction distance of *Gobiusculus flavescens* to its planktonic prey. J. Fish Biol. 54, 1244–1258. https://doi.org/10.1111/j.1095-8649.1999.tb02052.x

Utne, A., 1997. The effect of turbidity and illumination on the reaction distance and search time of the marine planktivore *Gobiusculus flavescens*. J. Fish Biol. 50, 926–938. https://doi.org/10.1111/j.1095-8649.1997.tb01619.x

Vinyard, G.L., O'Brien, W.J., 1976. Effects of light and turbidity on the reactive distance of bluegill (*Lepomis macrochirus*). J. Fish. Res. Board Canada 33, 2845–2849.

Vogel, J.L., Beauchamp, D.A., 1999. Effects of light, prey size, and turbidity on reaction distances of lake trout (*Salvelinus namaycush*) to salmonid prey. Can. J. Fish. Aquat. Sci. 56, 1293–1297. https://doi.org/10.1139/cjfas-56-7-1293

Zaneveld, J.R., Spinrad, R.W., Bartz, R., 1979. Optical properties of turbidity standards. Ocean Opt. IV 208, 159–168.

APPENDIX B: CHAPTER 2—SUPPLEMENTARY MATERIAL

Detecting archival tag orientation errors

The archival tag photodiode should be facing upward in order to calculate AOPs that approximate those based on diffuse downwelling irradiance. Improper orientation of trawl-mounted archival tags causes unreliable measurements of the underwater light field. However, archival tag assemblies were mistakenly attached to the trawl gear upside down during some casts and were likely deployed in an unstable orientation during other casts.

The algorithm has two methods for detecting and excluding anomalously dark casts to indirectly assess orientation. The choice of method depends on whether surface light measurements were obtained using a deck-mounted archival tag at the same time as a cast. For casts with surface light measurements, linear regressions are fit between surface light and near-surface light measurements, as:

$$\log_{10}\left(E_d\left(z,\lambda_{tag}\right)\right) \sim Vessel * Year + \log_{10}\left(E_d\left(0^+,\lambda_{tag}\right)\right) + \varepsilon, \qquad \varepsilon \sim N(0,\sigma^2)$$

where $E_d(z,\lambda_{tag})$ is near-surface light (1-m, 3-m, or 5-m), $Vessel * Year$ is a discrete interaction term intended to account for differences in absolute sensitivity among tags, $E_d(0^+,\lambda_{tag})$ is mean surface light from the deck-mounted archival tag for the 60 second interval around cast start (downcast) or end (upcast) time, and ε is the normally distributed error with mean zero and standard deviation, σ. Separate models are fitted to each depth bin. The residual distribution of the models are bimodal in the eastern Bering Sea and we assumed that large negative (dark) residuals were caused by improper archival tag orientation (Rohan et al., 2020). The algorithm calculates the kernel density distribution of archival tag residuals to assign a threshold for rejecting casts. Indirect cross-validation is used to automatically select the bandwidth of the kernel density

distribution because it yields stable bandwidth estimates that have low bias for samples sizes ≥ 100 (Heidenreich et al., 2013; Savchuk et al., 2010). The first derivative of the kernel density function is then calculated in order to find an inflection point in the bimodal kernel density distribution that is used as a threshold for determining the orientation of a cast. We define the threshold as the largest residual value less than zero where the first derivative of the kernel density distribution is negative.

A different outlier detection method is used to detect orientation errors when no shipboard light measurements are available. For such cases, a generalized additive model (GAM) is fit to data from all casts:

$$log_{10}\left(E_d\left(z,\lambda_{tag}\right)\right) \sim \beta_0 + s(log_{10}(E_d(0^+, PAR))) + \varepsilon, \qquad \varepsilon \sim N(0,\sigma^2)$$

where $E_d(z,\lambda_{tag})$ is near-surface light (1-m, 3-m, and 5-m depth bins), β_0 is an intercept parameter, s($E_d(0^+, PAR)$) is surface-incident irradiance estimated by a clear-sky global irradiance model (Frouin et al., 1989), and s(·) is a cubic regression spline. A separate model is fit to data from each near-surface depth bin. A kernel density distribution is fitted to the residuals using indirect cross-validation. For each depth bin, the first derivative of the kernel density distribution of model residuals is then used as a basis to assign a threshold for orientation error, as the largest residual value less than zero where the first derivative of the kernel density distribution is negative. Orientation errors based on shipboard measurements are accepted ahead of orientation based on the global irradiance model and errors based on shallower measurements are accepted ahead of deeper measurements (Rohan et al., 2020). Casts assigned to have improper orientation were excluded from subsequent processing and analyses.

Because casts can have up to six threshold assignments (two methods, three depth bins), the algorithm assigns a final orientation error to each cast based on a set of priority rules.

Orientation based on shipboard measurements are accepted ahead of orientation based on the global irradiance model because the global irradiance model does not account for variation in atmospheric conditions. Results based on shallower measurements are accepted ahead of deeper measurements because high attenuation near the surface can cause rapid light attenuation. The two methods of orientation error detection yield the same result for 94.0% of casts, and different depths from the same cast yield the same result for >96.7% of casts (Rohan et al., 2020). Casts assigned to have improper orientation were excluded from subsequent processing and analyses.

Numerical approximation of $K_d(z,\lambda_{tag})$

Three common methods of numerically approximating $K_d(z,\lambda)$ are to (1) estimate the first derivative of the slope of a smoothing spline between z and $\ln(E_d(z,\lambda))$ that uses a predetermined bandwidth, (2) estimate the slope of a moving-window linear regression between z and $\ln(E_d(z,\lambda))$, or (3) to calculate the slope between consecutive depth bins, as:

$$K_d(z_1 \leftrightarrow z_2, \lambda) = \frac{1}{z_2 - z_1} \ln\left(\frac{E_d(z_1, \lambda)}{E_d(z_2, \lambda)}\right), \quad (5)$$

where z_1 and z_2 are consecutive depth bins. However, these methods were unsuitable for deriving $K_d(z,\lambda_{tag})$ due to variation in cast depth, the small width of some light attenuating layers in the water column, and the absolute sensitivity of the archival tags. Fixed bandwidth non-parametric regression methods tended to over-or-under-fit the data depending on the chosen bandwidth, water column depth, and vertical structure of light-attenuating layers. Moving-window regression and slope calculation between consecutive points performed poorly because integer measurements of the tag changed more slowly deeper in the water column, at low light levels, and in parts of the water column with low $K_d(z,\lambda_{tag})$. This resulted in casts where consecutive depth bins had the same

$E_d(z,\lambda_{tag})$. For such casts, moving-window linear regression and simple slope calculation with small windows produced artifacts in profiles where $K_d(z,\lambda_{tag})$ was equal to zero at some depths and interspersed by spikes in $K_d(z,\lambda_{tag})$. Larger windows tended to over-smooth narrow light-attenuating layers that are important for characterizing bio-optical variability.

To circumvent these issues, our algorithm calculates $K_d(z,\lambda_{tag})$ using a numerical approximation of the first derivative of a first-order polynomial loess model fit between z and $\ln(E_d(z,\lambda_{tag}))$. The bandwidth for each cast is selected based on a bias-variance trade-off using bias-corrected Akaike's Information Criterion (Hurvich et al., 1998; Rohan et al., 2020). The first-order polynomial models were used instead of a higher-order polynomial base because they provide a better fit at the upper and lower limits of the predictor (Keele, 2008), an important consideration because meaningful variation in $K_d(z,\lambda_{tag})$ often occurs near the surface and bottom of the water column.

Spatial interpolation to generate rasters

We selected interpolation methods to generate annual rasters of environmental variables ($\zeta(z_{max}, \lambda_{tag})$, $Z_{10\%}$, $Z_{1\%}$, NLI, MLD, and $\Delta\sigma_t$) based on a comparison of out-of-sample predictive performance among multiple candidate interpolation methods. The spatial interpolation methods we evaluated were inverse-distance weighting, nearest-neighbor interpolation, Gaussian thin-plate splines, and ordinary kriging. For ordinary kriging, we evaluated seven semivariance structures: Gaussian, exponential, spherical, Bessel, power, logarithmic, pentaspherical, Matérn, and Stein's Matérn. We assessed out-of-sample predictive performance by calculating the root mean square error based on leave-one-out-cross validation for each year and variable. The spatial interpolation

used to generate rasters varied among years and variables due to differences in RMSE (Figs. S1–S6).

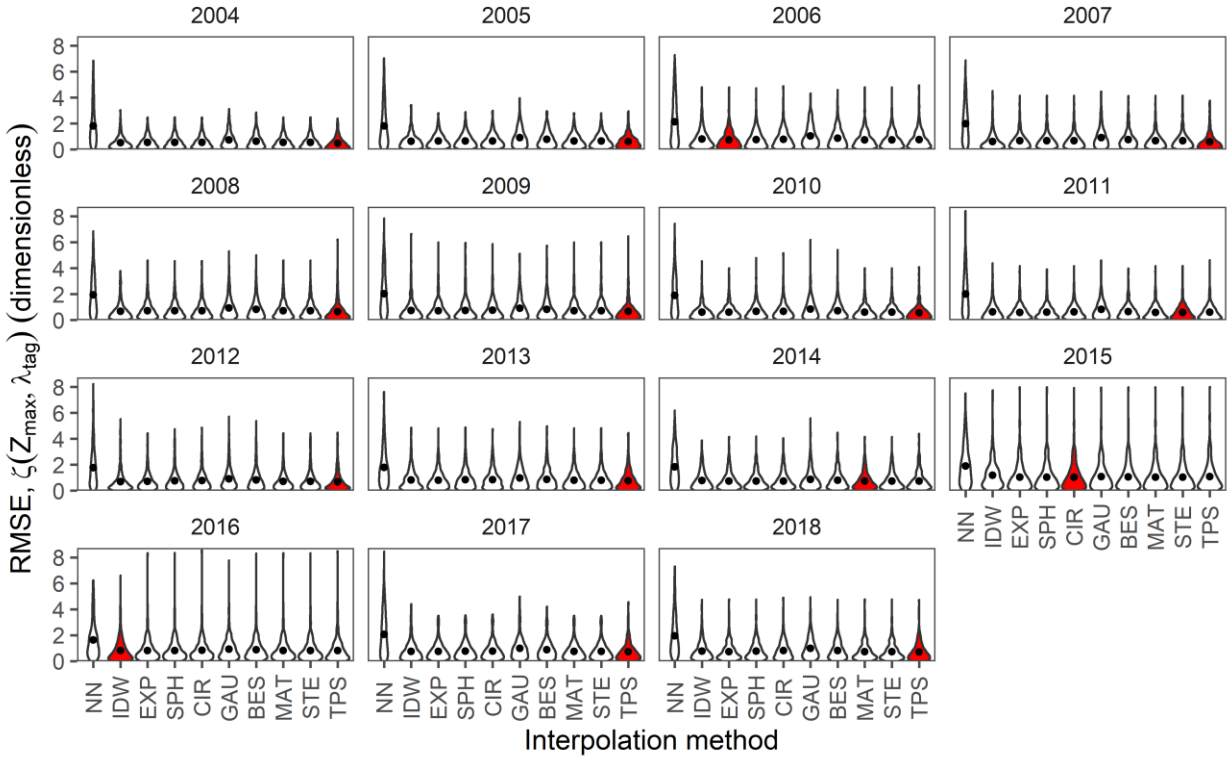

Figure S1. Root mean square error (RMSE) of candidate spatial interpolation methods for near-bottom optical depth, $\zeta(z_{max}, \lambda_{tag})$, by year, based on leave-one-out cross-validation. Points denote RMSE for the method and violin plots denote density distribution of errors for samples. Red fill denotes the best performing method for a year, based on RMSE.

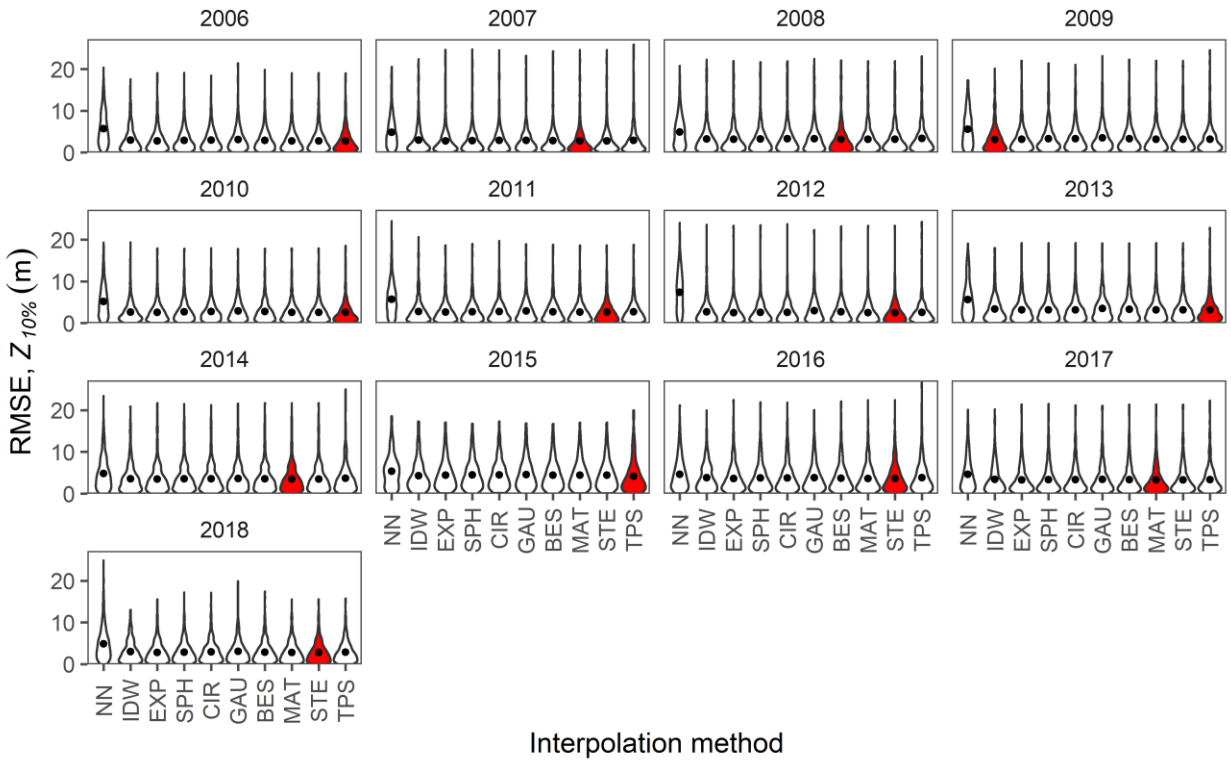

Figure S2. Root mean square error (RMSE) of candidate spatial interpolation methods for the depth of the 10% light level, $Z_{10\%}$ (m), by year, based on leave-one-out cross-validation. Points denote RMSE for the method and violin plots denote density distribution of errors for samples. Red fill denotes the best performing method for a year, based on RMSE.

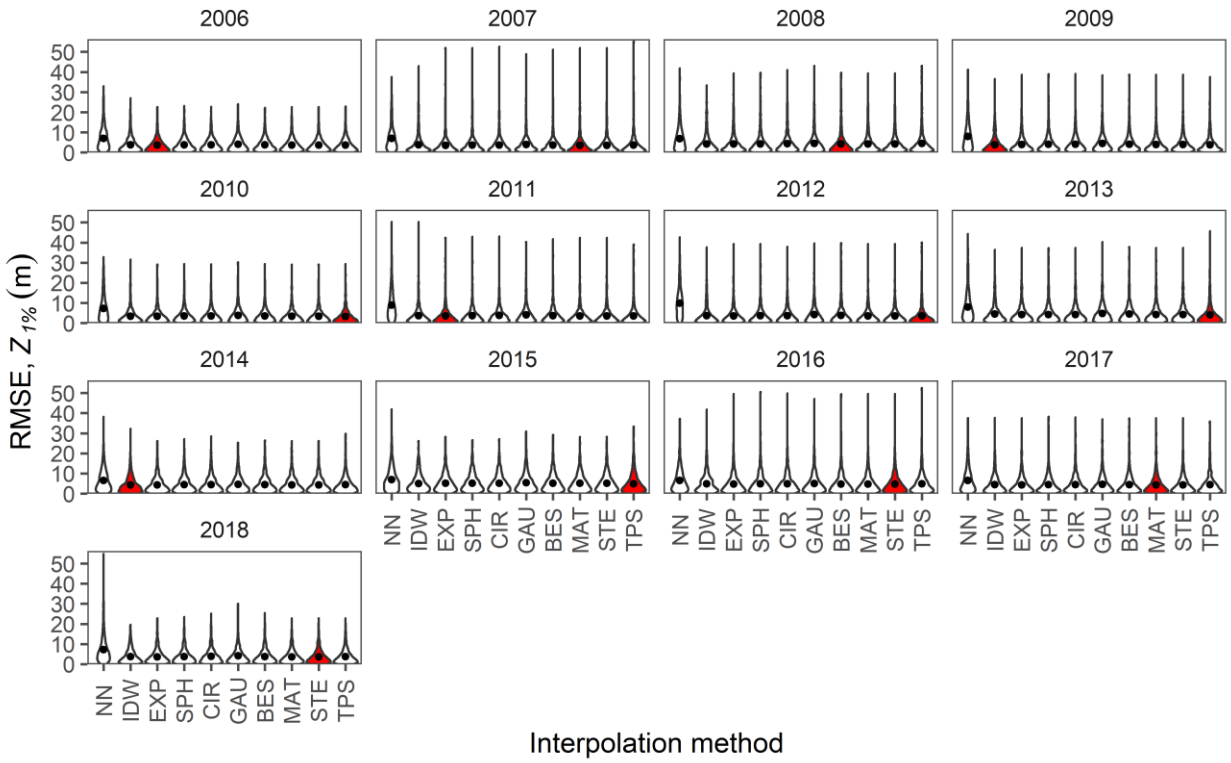

Figure S3. Root mean square error (RMSE) of candidate spatial interpolation methods for the depth of the 1% light level, $Z_{1\%}$ (m), by year, based on leave-one-out cross-validation. Points denote RMSE for the method and violin plots denote density distribution of errors for samples. Red fill denotes the best performing method for a given year, based on RMSE.

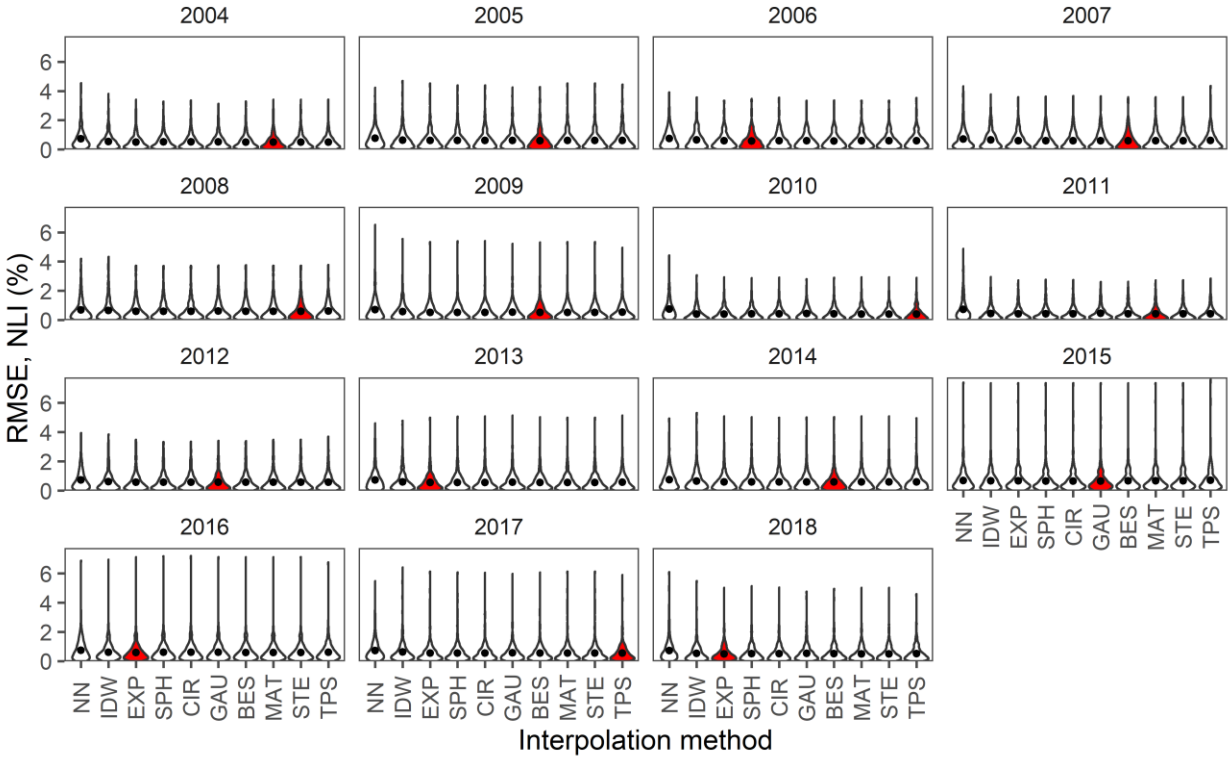

Figure S4. Root mean square error (RMSE) of candidate spatial interpolation methods for the nepheloid layer index, NLI (%), by year, based on leave-one-out cross-validation. Points denote RMSE for the method and violin plots denote density distribution of errors for samples. Red fill denotes the best performing method for a given year, based on RMSE.

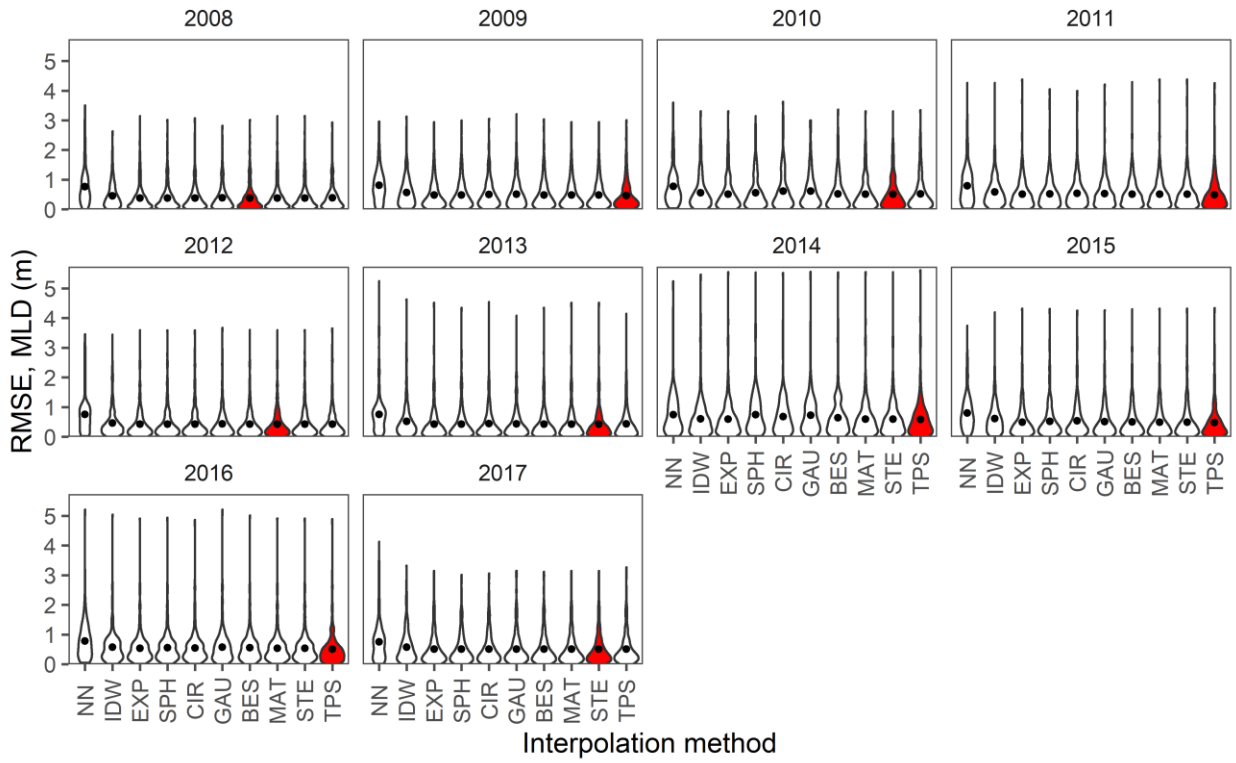

Figure S5. Root mean square error (RMSE) of candidate spatial interpolation methods for mixed layer depth, MLD (m), by year, based on leave-one-out cross-validation. Points denote RMSE for the method and violin plots denote density distribution of errors for samples. Red fill denotes the best performing method for a year, based on RMSE.

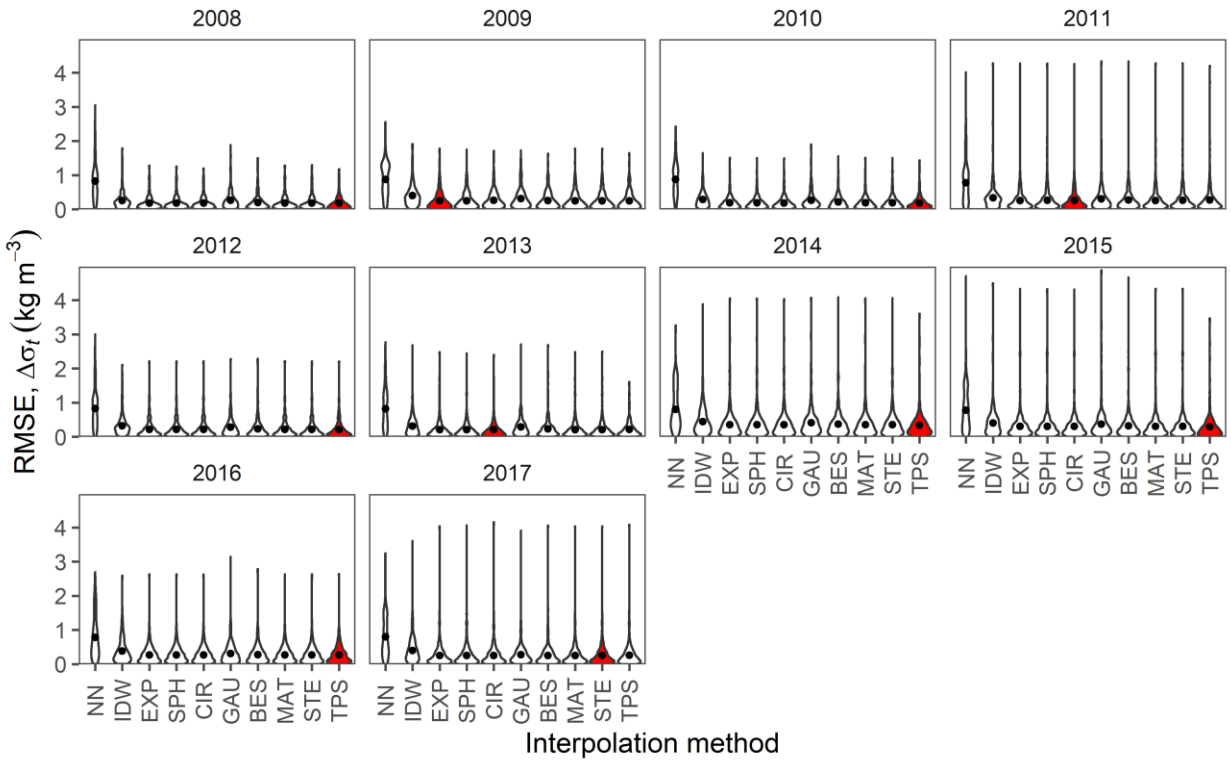

Figure S6. Root mean square error (RMSE) of candidate spatial interpolation methods for density anomaly, $\Delta\sigma_t$ (kg m^{-3}), by year, based on leave-one-out cross-validation. Points denote RMSE for the method and violin plots denote density distribution of errors for samples. Red fill denotes the best performing method for a year, based on RMSE.

Solar zenith angle

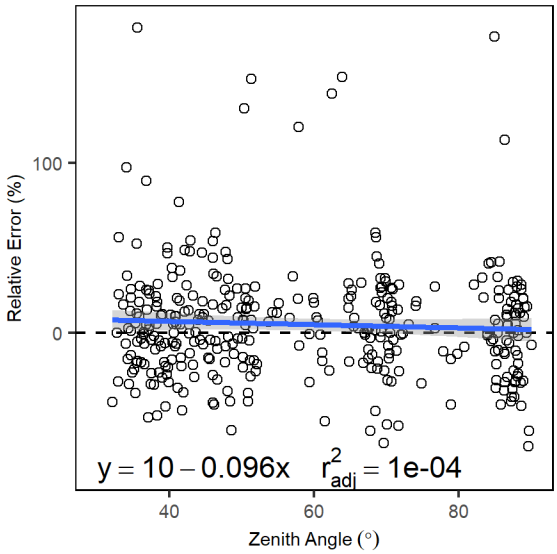

Figure S7. Ordinary least squares (OLS) regression between solar zenith angle (°) during archival tag casts and the relative error in predictions of $K_d(z_s, 490)$ from the OLS regression between archival tag $K_d(z_s, \lambda_{tag})$ and OC-CCI $K_d(z_s, 490)$. Regression equation and adjusted r^2 are shown on the plot.

References

Frouin, R., Lingner, D.W., Gautier, C., Baker, K.S., Smith, R.C., 1989. A simple analytical formula to compute clear sky total and photosynthetically available solar irradiance at the ocean surface. J. Geophys. Res. 94, 9731. https://doi.org/10.1029/JC094iC07p09731

Heidenreich, N.B., Schindler, A., Sperlich, S., 2013. Bandwidth selection for kernel density estimation: A review of fully automatic selectors. AStA Adv. Stat. Anal. 97, 403–433. https://doi.org/10.1007/s10182-013-0216-y

Hurvich, C.M., Simonoff, J.S., Tsai, C.-L., 1998. Smoothing parameter selection in nonparametric regression using an improved Akaike information criterion. J. R. Stat. Soc. B 60, 271–293.

Keele, L.J., 2008. Semiparametric Regression for the Social Sciences. John Wiley & Sons Ltd, Chichester.

Rohan, S.K., Kotwicki, S., Laman, E.A., Britt, L.L., Aydin, K., 2020. Deriving apparent optical properties from light measurements obtained using bottom-trawl-mounted archival tags. United States Department of Commerce, NOAA Technical Memorandum NMFS-AFSC-403, 91 p. https://doi.org/10.25923/42yn-1q79

Savchuk, O.Y., Hart, J.D., Sheather, S.J., 2010. Indirect cross-validation for density estimation. J. Am. Stat. Assoc. 105, 415–423. https://doi.org/10.1198/jasa.2010.tm08532

APPENDIX C: CHAPTER 3—SUPPLEMENTARY MATERIAL

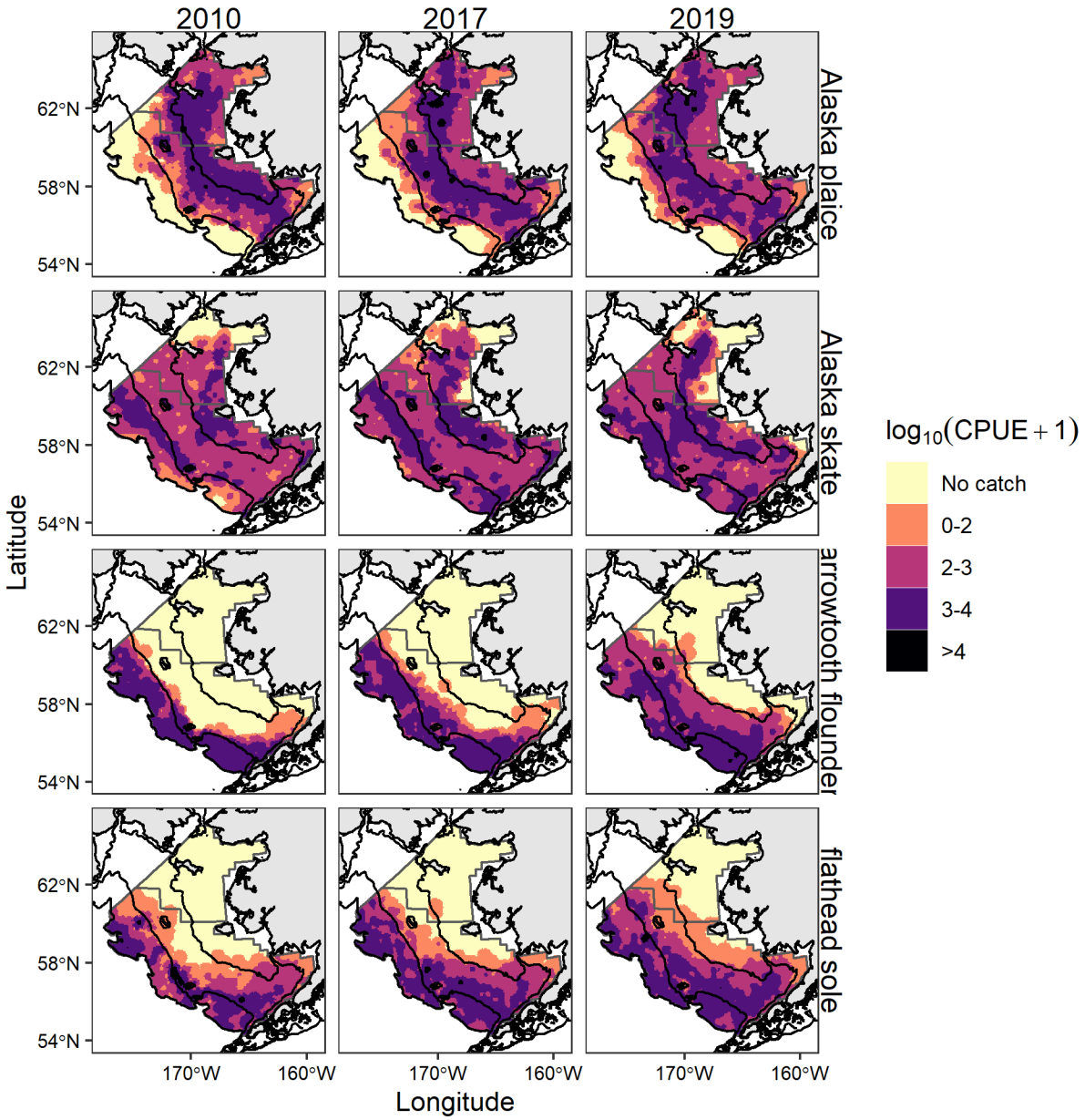

Figure S1. Inverse distance weighted maps of $\log_{10}$-transformed bottom trawl survey catch per unit effort, CPUE (kg ha^{-1}), for the eight most abundant groundfish species from NOAA eastern Bering Sea bottom trawl surveys conducted during summers (June–August) of 2010, 2017, and 2019 (most recent years with full summer bottom trawl surveys of the southeastern Bering Sea and northeastern Bering Sea).

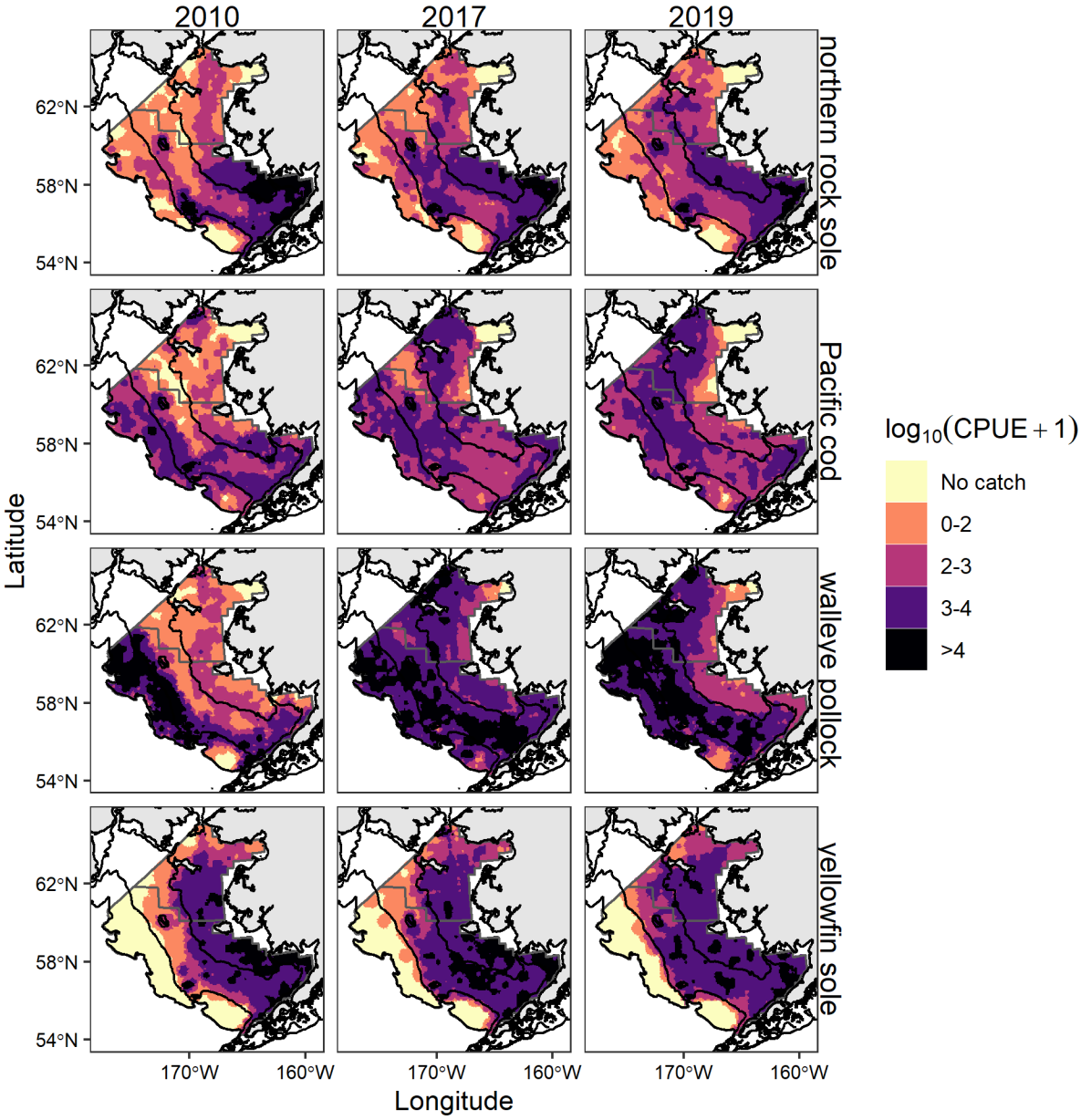

Figure S1 (continued).

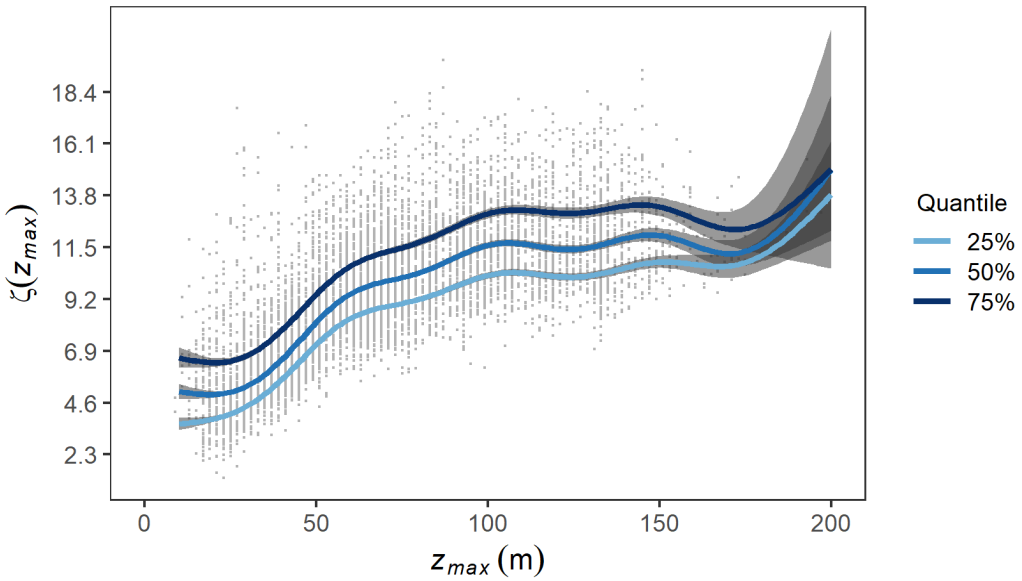

Figure S2. Quantile generalized additive model (QGAM) fits between the predictor maximum cast depth, z_{max} (m), and cast maximum optical depth, $\zeta(z_{max})$ (dimensionless), from the eastern Bering Sea during summers (May–August) of 2004–2019. Solid line and shaded area denote the fitted mean ± 2 standard errors.

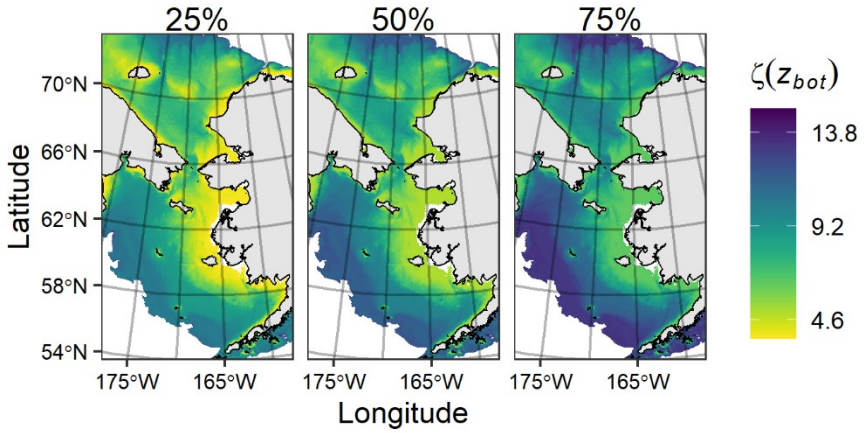

Figure S3. Quantiles (25%, 50%, 75%) of bottom optical depth, $\zeta(z_{bot})$ (dimensionless), on the continental shelf (10–200 m). Higher $\zeta(z_{bot})$ indicates darker conditions.

Walleye pollock availability data and model fitting

We modeled the vertical availability of walleye pollock to bottom-trawl and acoustic sampling using a beta regression model following the approach of Kotwicki et al. (2015). In that study, vertical availability of walleye pollock to bottom-trawl and acoustic sampling during daytime was modeled as a function of numerous covariates (details below) using a logit-link beta regression model (Cribari-Neto and Zeileis, 2010; Ferrari and Cribari-Neto, 2004),

$$logit(q_{v,s}) = \boldsymbol{\beta}\mathbf{X},$$

where $q_{v,s}$ is vertical availability for sampling method s (bottom-trawl or acoustic), $\boldsymbol{\beta}$ is a vector of regression parameters, and $\mathbf{X}$ is a design matrix of predictor variables. In the beta regression models, the variance of $q_{v,s}$ was modeled as

$$var(q_{v,s}) = \frac{\mu(1-\mu)}{1+\phi},$$

where μ is the expected mean response, and ϕ is a precision term. The precision term is a log-linked function of linear predictors,

$$\log(\phi) \sim \boldsymbol{\gamma}\mathbf{W},$$

where $\boldsymbol{\gamma}$ is a vector of regression parameters and $\mathbf{W}$ is a matrix of predictor variables.

Kotwicki et al.'s (2015) best-fit beta regression models included numerous predictors: bottom light, bottom depth, surface temperature, sediment grain size, tidal current speed, mean walleye pollock fork length in the bottom-trawl catch, walleye pollock biomass density along the trawl path, and year (as a discrete variable). We did not have the full suite of predictors from Kotwicki et al.'s (2015) best-fit models for our simulations. Therefore, we fit new beta regression models to Kotwicki et al.'s (2013, 2015) bottom-trawl ($q_{v,BT}$) and acoustic ($q_{v,A}$) vertical availability data using only bottom light and bottom depth as predictors. Bottom trawl catch and acoustic data were collected during annual NOAA bottom-trawl surveys of the southeastern Bering

Sea during 2007–2011. Surveys were conducted from June–July. Each year, the survey sampled 376 stations arranged on a regularly-spaced 20×20 nmi grid with corner stations located in areas historically associated with high densities of commercially important crab stocks. Hauls were conducted for a target duration of 30 minutes at a vessel speed of 2.8–3.2 knots.

The areal density of walleye pollock biomass was calculated for each bottom-trawl survey haul using the area-swept method (Alverson and Pereyra, 1969). Fork length measurements were obtained from 150–200 walleye pollock per haul. Areal density and fork lengths were used to estimate catch per unit effort by length (# fish nmi^{-2} $length^{-1}$) for each haul. Fork lengths were used to calculate target strength for each fork length as

$$TS = 20\log(L) - 66,$$

where *TS* is acoustic target strength (dB) for an individual fish and *L* is fork length (cm) (Traynor, 1996). Catch per unit effort by length and target strengths were then used calculate bottom trawl equivalent nautical area scattering coefficient, $s_{A,BT}$ (m^2 nmi^{-2}), for each haul. Nautical area scattering coefficient is a measure of backscatter per unit area (Simmonds and MacLennan, 2005).

Acoustic data at 38 kHz were collected during the bottom trawl survey hauls using Simrad ES60 splitbeam echosounders and ES-38B transducers (7° between half-power points; 1 ms pulse length; 0.5 m backstep above detected bottom). The echosounders were calibrated twice per survey using the standard sphere method (Foote et al., 1987). A correction was applied to omit acoustic data that were a result of a periodic and systematic 1 dB error in ES60 measurements (Kotwicki et al., 2013). The acoustic data were used to calculate acoustic s_A, for bottom-trawl survey hauls. Values of $s_{A,A}$ were integrated by depth bins that were 0.25 m thick between the acoustically detected bottom and 5 m off-bottom and 1 m thick above 5 m off-bottom.

Bottom trawl and acoustic availability were estimated from $s_{A,BT}$ and $s_{A,A}$ using data from hauls where walleye pollock comprised at least 75% bottom-trawl catch of pelagic fish and at least 50 kg walleye pollock were caught. Bottom trawl availability, $q_{v,BT}$ was calculated as

$$q_{v,BT} = \frac{s_{A,BT}}{s_{A,t}}$$

where $s_{A,BT}$ is s_A integrated from 0.5 m above the bottom (i.e., above the seafloor acoustic dead zone [ADZ]) to the effective fishing height (EFH) of the bottom trawl gear plus a correction to account for biomass in the ADZ, and $s_{A,t}$ is total s_A in the water column from the bottom to 20 m below the sea surface, including the correction for the ADZ (Kotwicki et al., 2013). The effective fishing height of the bottom trawl gear is greater than the height of the bottom trawl gear while in fishing configuration because walleye pollock dive in response to vessels approaching and passing overhead. Acoustic availability, $q_{v,A}$ was calculated as

$$q_{v,A} = \frac{s_{A,AC}}{s_{A,t}}$$

where $s_{A,t}$ is s_A integrated from 0.5 m above bottom to 20 m below the sea surface. Kotwicki et al. (2013) estimated $s_{A,BT}$ and $s_{A,t}$ using direct observations and a model combining bottom trawl and acoustic data,

$$s_{A,BT} = \left(\frac{1}{r_q\left(s_{A,BTZ}\right)} + \frac{1}{a}\right)^{-1} e^{\varepsilon}$$

$$s_{A,BTZ} = \sum_{0.5}^{EFH} s_{A,A} + e^{\boldsymbol{bX}} \sum_{0.5}^{h} s_{A,A} + e^{\boldsymbol{cX}},$$

where r_q is a catchability ratio, a is a density-dependence parameter, EFH is the effective fishing height of the trawl, e^{ε} is log-normally distributed error, h is the height of the near-bottom acoustic layer, $\boldsymbol{X}$ is a matrix of predictors, and $\boldsymbol{b}$ and $\boldsymbol{c}$ are vectors of parameters. Kotwicki et al. (2015)

conducted Markov chain Monte Carlo (MCMC) sampling using the Metropolis-Hastings algorithm and uniform priors on parameters to generate 1,000 samples of $q_{v,BT}$ and $q_{v,A}$ and from the posterior distribution for each sample. Additional details of chain-thinning and diagnostics are provided in Kotwicki et al. (2015).

Kotwicki et al. (2015) modeled the vertical availability of walleye pollock to bottom trawl and acoustic gear using numerous varieties of regression models where the response was the highest posterior density estimates of $q_{v,BT}$ and $q_{v,A}$ from MCMC samples and numerous candidate predictors that were screened based on variance inflation factors. Predictors in Kotwicki et al.'s (2015) best-fit models for $q_{v,BT}$ and $q_{v,A}$ included bottom light (archival tag integer units), bottom depth (m), surface temperature (°C), bottom temperature (°C), sediment size (Wentworth scale), mean fork length of walleye pollock in the bottom trawl catch (cm), log-transformed areal biomass density (kg ha^{-1}) of walleye pollock in the bottom trawl catch, total current speed (cm s^{-1}), and year (discrete variable).

We were unable to use all of the predictor data from Kotwicki et al. (2015) for modeling availability given the scope of our simulation. Therefore, we fit new beta regression models to $q_{v,BT}$ and $q_{v,A}$ using only bottom light and bottom depth as predictors (Table S1). In Kotwicki et al's (2015) models, bottom light was the mean from trawl-mounted archival tags equipped with blue-filtered photodiodes (Wildlife Computers TDR-MK9) with the archival tags facing upward. The archival tags recorded light measurements in integer values based on an onboard log-transformation. Following Kotwicki et al. (2015), we fit the beta regression models to $q_{av,BT}$ and $q_{av,A}$ using the integer light levels from the archival tags. To predict $q_{v,BT}$ and $q_{v,A}$ in simulations, we converted bottom light from quantum units to archival tag integer values based on a conversion reported by Kotwicki et al. (2009).

Because our beta regression models had fewer predictors, they had a worse fit to $q_{v,BT}$ and $q_{v,A}$ data than the best-fit models of Kotwicki et al. (2015) based on bias-corrected Akaike's Information Criterion (AICc) and root mean squared error (RMSE; Table S1). This was expected because we used the same data and model structure but with fewer useful predictors. Compared to the best-fit models of Kotwicki et al. (2015), the light-and-depth only models we used in our simulations had a 13.6% and 19.8% increase in RMSE for bottom trawl and acoustic availability, respectively. However, based on visual inspection of diagnostic plots, there was no systematic lack-of-fit in our models compared to the best-fit models of Kotwicki et al. (2015) (Figs. S4–S5). Model fits for $q_{v,BT}$ and $q_{v,A}$ are shown in Figure S6.

Table S1. Summary of beta regression model fits for acoustic, $q_{v,A}$, and bottom trawl, $q_{v,BT}$, availability of walleye pollock showing the best fit models from Kotwicki et al. (2015) with the full suite of parameters versus the light-and-depth only models for this study. Table shows the number of observations (n), number of model parameters (k), root mean square error (RMSE), and bias-corrected Akaike's Information Criterion (AIC_c).The models used for this study are bolded.

Model	n	k	RMSE	AIC_c	
Acoustic availability, $q_{v,A}$					
$q_{v,A} \sim BL+z_{bot}+ST+PP+FL\times log(CPUE)+Year$ $\phi_{v,A} \sim BL+ z_{bot} +PP+TC +Year$	355	24	0.126	-404.4	Kotwicki et al. (2015)
$q_{v,A} \sim BL\times z_{bot}$ $\phi_{v,A} \sim BL+ z_{bot}$	355	7	0.151	-259.5	This study
$\boldsymbol{q_{v,A} \sim BL+ z_{bot}}$ $\boldsymbol{\phi_{v,A} \sim BL+ z_{bot}}$	**355**	**6**	**0.151**	**-261.6**	This study
Bottom trawl availability, $q_{v,BT}$					
$q_{v,BT} \sim BL\times z_{bot} +PP+FL\times log(CPUE)+Year$ $\phi_{v,A} \sim BL+ z_{bot} +PP+FL\times log(CPUE)+Year$	355	23	0.070	-1314.3	Kotwicki et al. (2015)
$\boldsymbol{q_{v,BT} \sim BL\times z_{bot}}$ $\boldsymbol{\phi_{v,A} \sim BL+ z_{bot}}$	**355**	**7**	**0.079**	**-1256.1**	This study
$q_{v,BT} \sim BL+ z_{bot}$ $\phi_{v,A} \sim BL+ z_{bot}$	355	6	0.079	-1252.4	This study

Note: *BL*–bottom light (archival tag units), z_{bot}–bottom depth (m); *ST*–surface temperature (°C); BT–bottom temperature (°C); FL–mean walleye pollock for length in bottom trawl catch (cm); PP–sediment size (Wentworth scale); CPUE–catch per unit effort (kg ha^{-1}); Year–Year as a discrete variable.

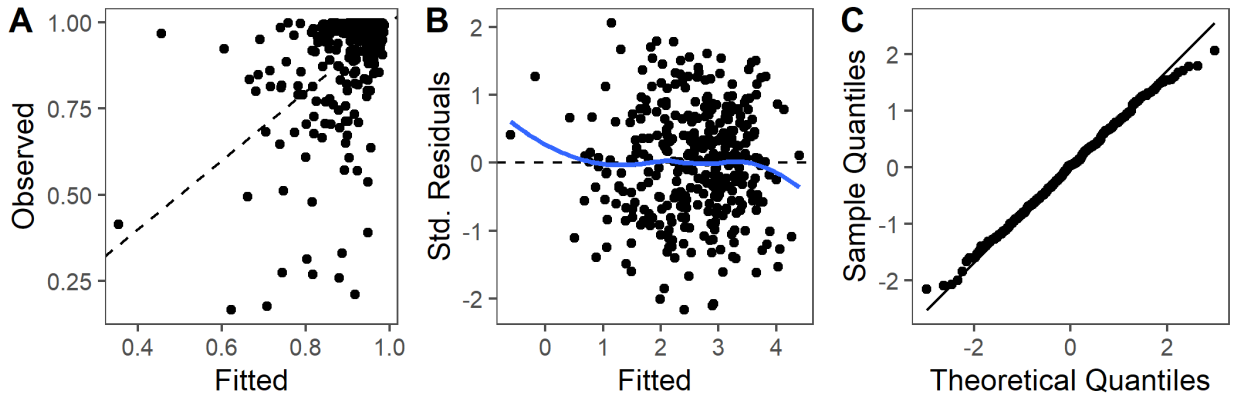

Figure S4. Diagnostic plots for bottom trawl availability, $q_{v,BT}$, beta regression model with only light and bottom depth as predictors. Panels show: (A) fitted versus observed; (B) Fitted versus standardized residuals; (C) Q-Q plot of standardized residuals.

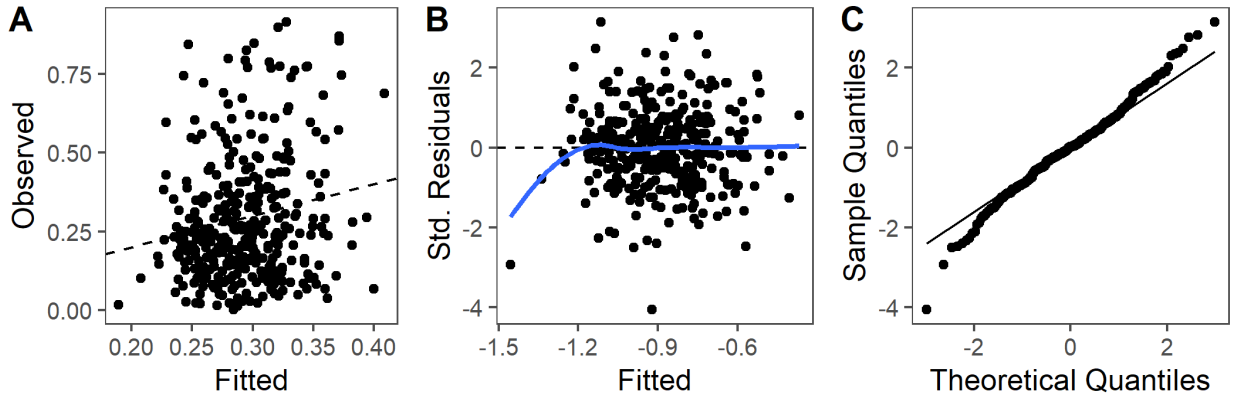

Figure S5. Diagnostic plots for acoustic availability, $q_{v,A}$, beta regression model with only light and bottom depth as predictors. Panels show: (A) fitted versus observed; (B) Fitted versus standardized residuals; (C) Q-Q plot of standardized residuals.

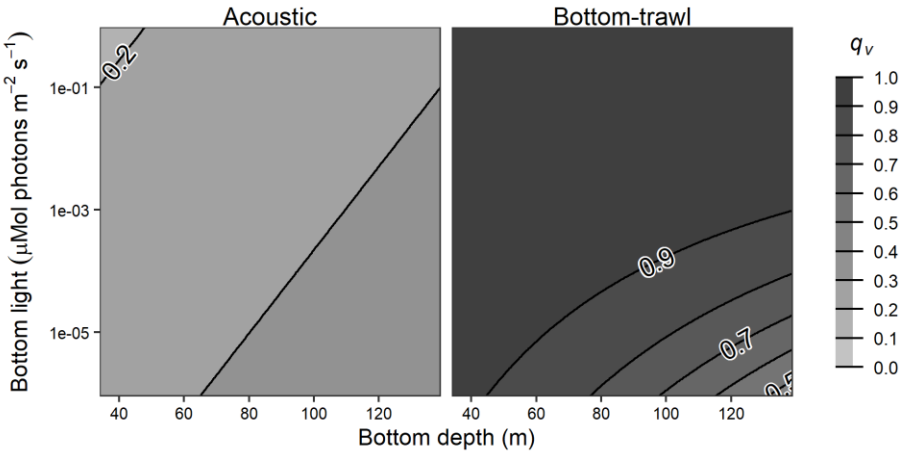

Figure S6. Estimated vertical availability of walleye pollock to acoustic ($q_{v,A}$) and bottom-trawl ($q_{v,BT}$) survey sampling as functions of bottom depth (m) and bottom light (μMol Photons m^{-2} s^{-1}) based on fitted means of beta regression models.

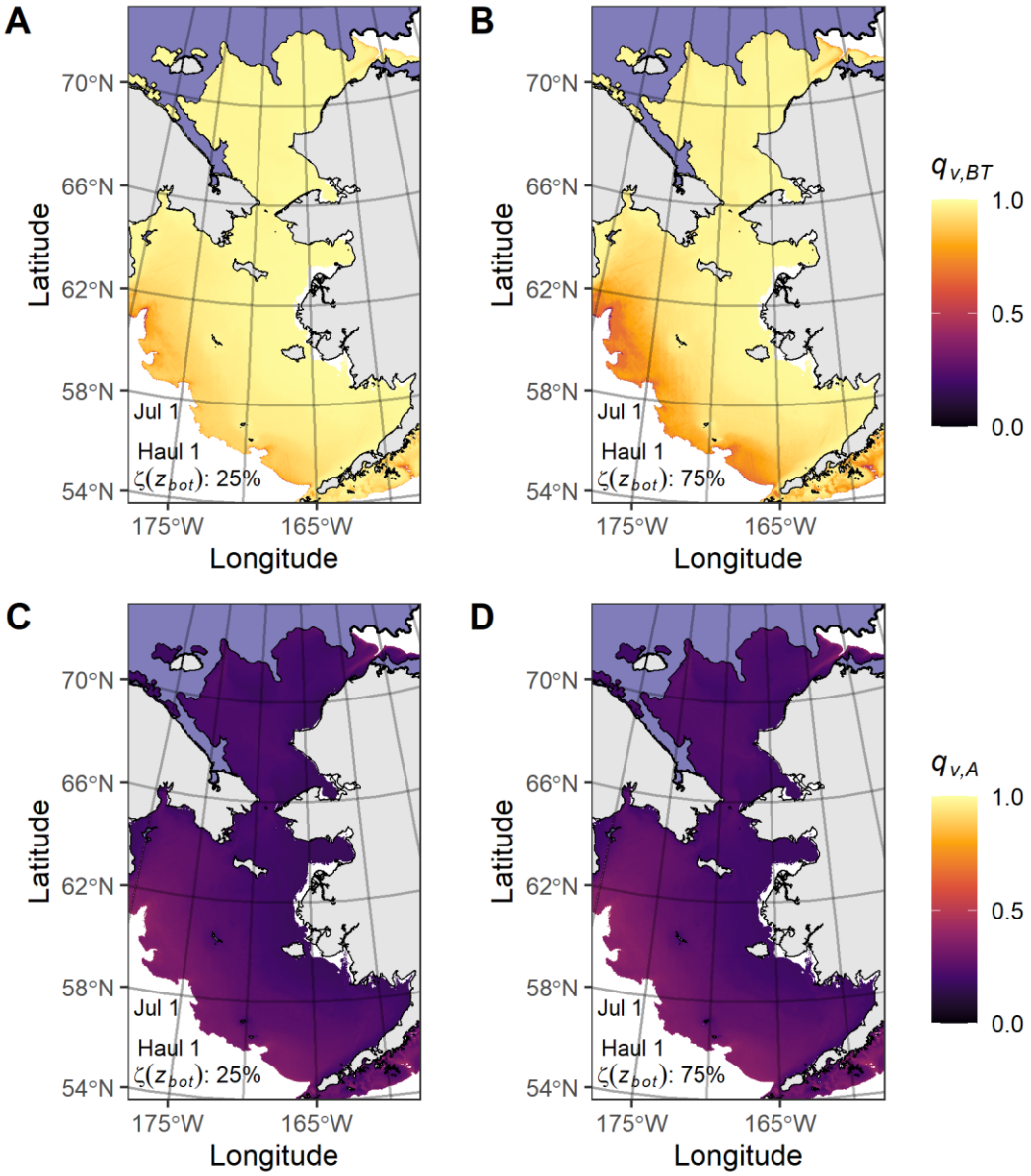

Figure S7. Vertical availability of walleye pollock to fishery-independent survey bottom trawl ($q_{v,BT}$) and acoustic ($q_{v,A}$) sampling for the first haul of the day on July 1. Panels: (A) $q_{v,BT}$ at the 25% optical depth quantile; (B) $q_{v,BT}$ at the 75% optical depth quantile; (C) $q_{v,A}$ at the 25% optical depth quantile; (D) $q_{v,A}$ at the 75% optical depth quantile. Gradient fill shows gear efficiency, light purple shading denotes sea ice extent on July 1, 2019.

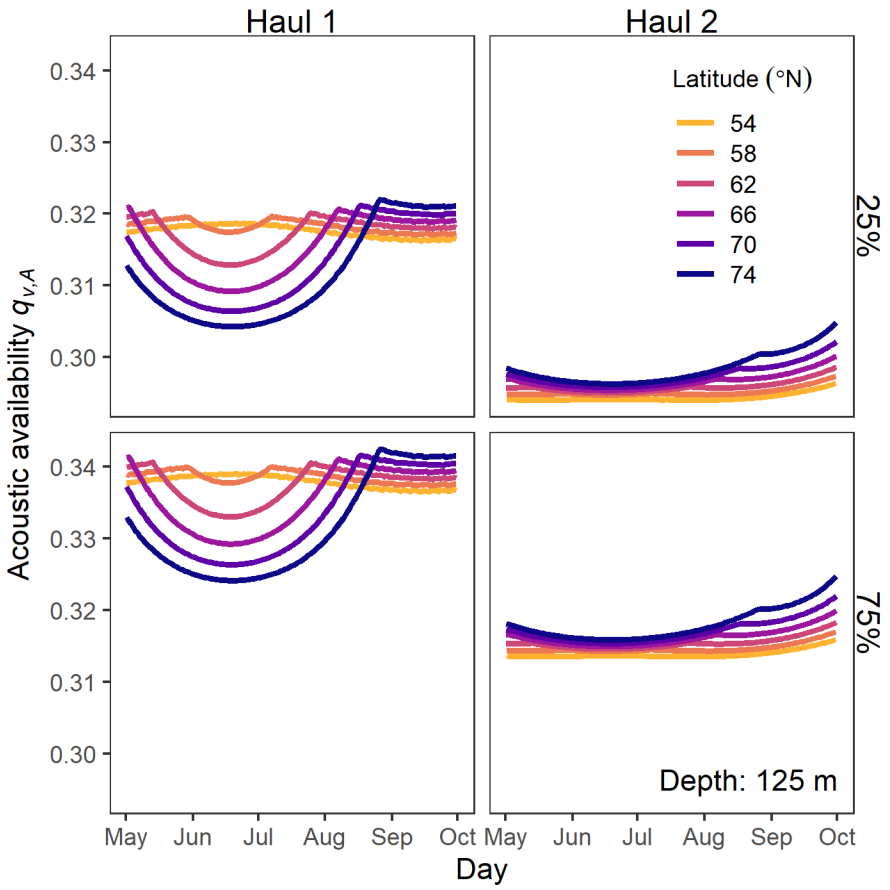

Figure S8. Availability of walleye pollock to acoustic sampling ($q_{v,A}$) at 125 m depth. Axes show day of year (horizontal) and q_e (vertical). Panels show the first and second hauls of the day (columns) and the 25% and 75% quantiles of optical depth (rows). Line colors denote latitude.

Modeled light versus Pacific cod archival tag light

To evaluate whether model predictions of bottom light were reasonable we compared model bottom light predictions to light measurements from satellite-tagged Pacific cod in the eastern Bering Sea. Tag data were from Pacific cod (n = 38) that were tagged with Wildlife Computers MiniPAT archival tags during August–September 2019 near St. Lawrence Island (63°21′N 170°16′W). Tags recorded time, depth, temperature, light, and three-axis acceleration at three-or-five-second intervals, depending on the programmed deployment duration for the tag. Pacific cod for the tagging study were captured using hook-and-line and released at bottom depths ranging from 25–48 m. Satellite tags were attached to fish with a padded harness secured by two wires through the dorsal musculature and a monofilament tether that connected the tag to the harness. Six tagged fish were recaptured in commercial fisheries after 3–222 days at liberty. Fish with known tagging and fisheries recapture locations provide an accurate estimate of the location for each fish. We extracted a subset of the tag data for a 24-hour period within three days of tagging or recapture to compare with model predictions.

Table S2. Release and capture information for Pacific cod (n = 6) with physically recovered MiniPAT archival tags. PSAT ID, fork length (cm), release date, release latitude/longitude, recovery date, and recovery latitude/longitude.

		Release			Recovery		
Tag ID	FL (cm)	Date	Lat. (°N)	Lon. (°E)	Date	Lat. (°N)	Lon. (°E)
183947	77	8/14/2019	63.35059	-168.67671	2/20/2020	57.20167	-171.06500
183949	73	8/14/2019	63.34951	-168.67768	10/23/2019	64.66683	-167.93417
183962	78	8/11/2019	64.03327	-171.39852	10/26/2019	64.83667	-167.66833
183968	68	8/10/2019	63.84805	-170.96346	9/3/2019	64.03528	-170.37778
183971	71	8/11/2019	64.03324	-171.39876	3/22/2020	59.98800	-175.74900
184064	73	9/8/2019	63.75170	-170.31874	9/12/2019	63.98733	-169.77167

The archival tags use an on-board log-transformation to record light relative integer units. The absolute response range of tags varies among tags but the dynamic range and relative response

of the tag to changes in light is relatively consistent among tags (Rohan et al., 2020; L. Britt, unpublished data). To account for the differences among tags, we calculated adjusted archival tag light measurements by shifting measurements based on the difference between the archival tag and the average minimum for archival tag light sensors that is reported by the manufacturer, 25 units. For example, if an archival tag had a minimum light level of seven, we added 18 to each archival tag light measurement for the tag. We then converted light measurements to quantum irradiance ($\mu Mol \cdot photons \cdot m^{-2} \cdot s^{-1}$) based on Kotwicki et al.'s (2009) conversion.

We used our model framework to predict archival tag light based on depth measurements and tagging or recapture locations, assuming a 50% quantile of optical depth. We used performance metrics to evaluate whether model predictions were consistent with Pacific cod tag data by comparing tag quantum unit values to model predictions. The performance measures we used were mean absolute error, root mean square log error, mean relative error, mean bias (Table S3), and Pearson correlation coefficient. We limited comparison to observations where archival tag light measurements was at least two integer units greater than the archival tag minimum (i.e., tag light measurement ≥ 27) because the model can predict light values that are lower than the lowest possible archival tag response and because archival tags show some measurement variability in the dark (Fig. S9). If model assumptions were valid, we expected model predictions would be higher than archival tag measurements because the model predicts downwelling irradiance whereas the light sensor on the archival tag points horizontally when the fish is not swimming and there is no current.

Table S3. Performance measure for model versus archival tag comparison.

Performance measure	Formula
Mean absolute error (MAE)	$MAE = 10^{\left(\frac{\sum_{i=1}^{n}\lvert\log_{10}(M_i)-\log_{10}(O_i)\rvert}{n}\right)}$
Root mean square log error (RMSLE)	$RMSLE = \frac{\sum_{i=1}^{n}\sqrt{(\log_{10}(M_i)-\log_{10}(O_i))^2}}{n}$
Mean relative error (MRE)	$MRE = n^{-1}\sum_{i=1}^{n}\left(\frac{M_i - O_i}{O_i}\right)$
Mean bias	$bias = 10^{\left(\frac{\sum_{i=1}^{n}\log_{10}(M_i)-\log_{10}(O_i)}{n}\right)}$

Formula terms: *M*-model prediction, *O*-observation, *n*-sample size for the capture or recapture subset, *i*-index for the prediction or observation.

Model predictions closely tracked diel cycles of variation in light, as shown by the high Pearson's correlation coefficients for all tagging and recapture subsets (Fig. S10A). Model predictions were within an order of magnitude of measured light levels for five tag and recapture subsets and two orders of magnitude for the other five subsets, as shown by the mean absolute error, root mean square log error, and mean relative error (Fig. S10B-D). The magnitude of the bias for individual tags appears to suggest the model provides a reasonable approximation of in-situ conditions based on the in-situ range of variability in optical depth during summer (Fig. S2). For a given depth, the model predicted mean difference between the 75% and 25% quantiles of optical depth is ~2.3, which corresponds with an order of magnitude difference in light, although the total range of variation in optical depth can span multiple orders of magnitude (Fig. S2). Nine out ten subsets had a mean bias > 1, indicating that predicted light levels were higher than measured light levels, which is what we expected if assumptions of the model were met (Fig. S10E).

Subsets where the model poorly predicted tag light were likely due to variation in water clarity rather than overall model misspecification or tag measurement error, which is shown by spatial-temporal patterns of bias (Fig. S10E, Fig. S11). Tags 183947 had a bias of 72.5 at the tagging location on August 17, 2019, which decreased to 8.1 for the recapture location on February

19, 2020. Tag 183949 was released at approximately the same time (August 15, 2019) and location as 183947 and showed a bias of 75.4, similar to tag 183947, but that decreased to 21.2 for the recapture on October 22, 2019 (Fig. S10E, Fig. S11). The bias for the tag 183947 recapture was similar to the bias for the recapture of tag 183962 (bias = 10.0) in the same area three days later (October 25, 2019). However, the bias of tag 183962 was only 1.4 at the tagging location in August 12, 2019, which was similar to biases for other tags deployed at around the same date and location (tags 183971, 183968).

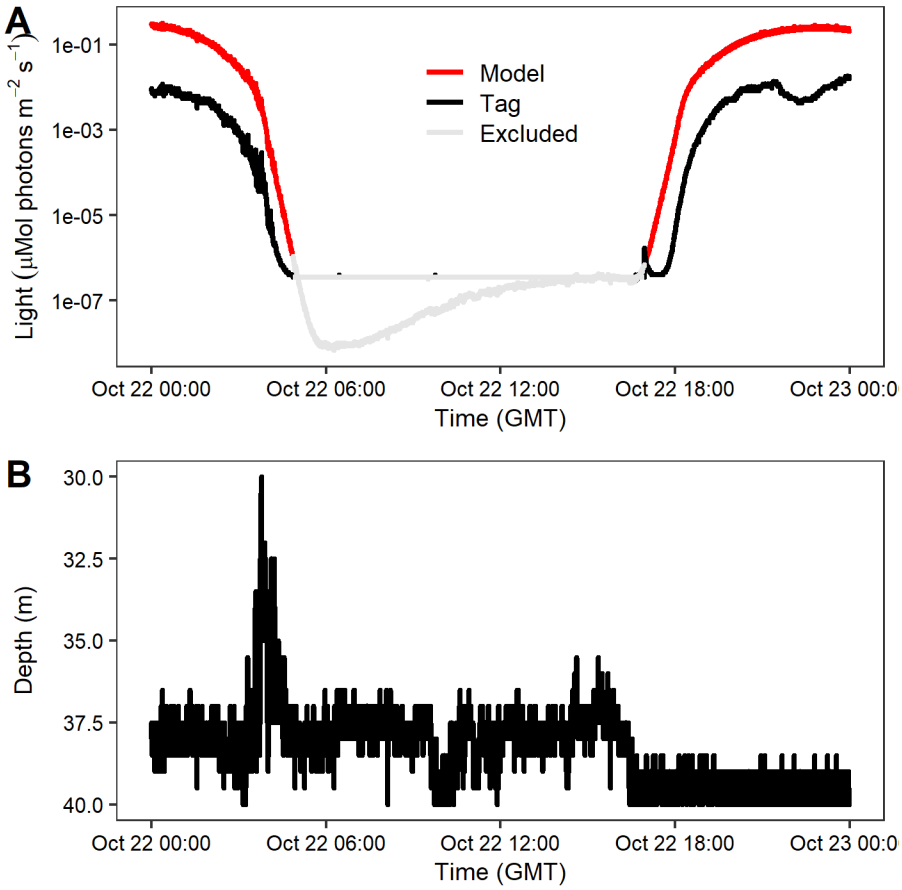

Figure S9. Modeled light and Pacific cod archival tag light and depth data for the recapture of tag 183949 on October 22, 2019 at 64°40'N, 167°56'W. Panels show: (A) Model predictions (red line), archival tag measurements (black line), and model predictions and tag data excluded from performance measures (grey line); (B) archival tag depth.

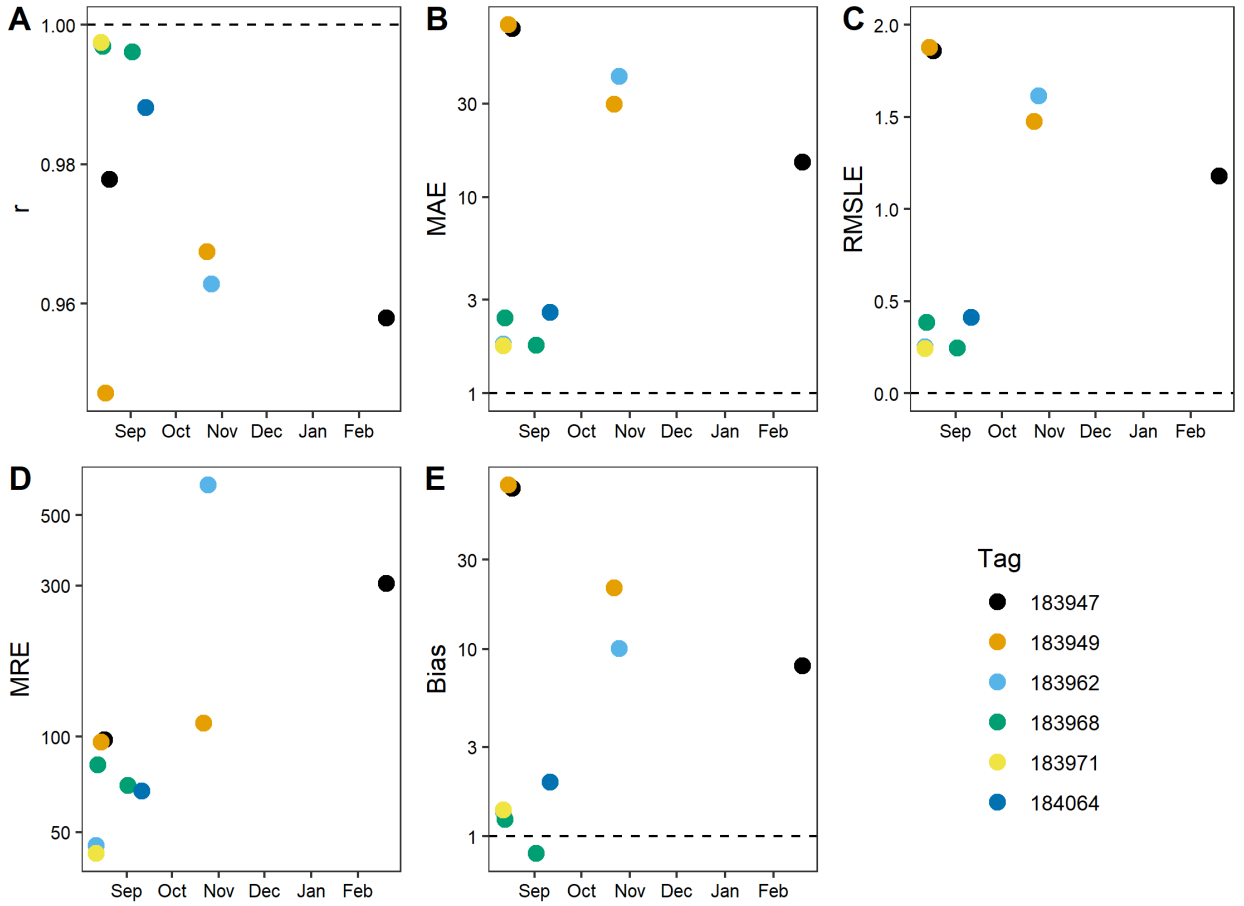

Figure S10. Performance measures for comparing model predictions to Pacific cod archival tag light measurements. Panels show: (A) Pearson's correlation coefficient; (B) mean absolute error; (C) root mean square log error; (D) mean relative error, (E) mean bias. Point colors denote unique tags/fish, dashed lines denote expectation if the model perfectly predicted observations.

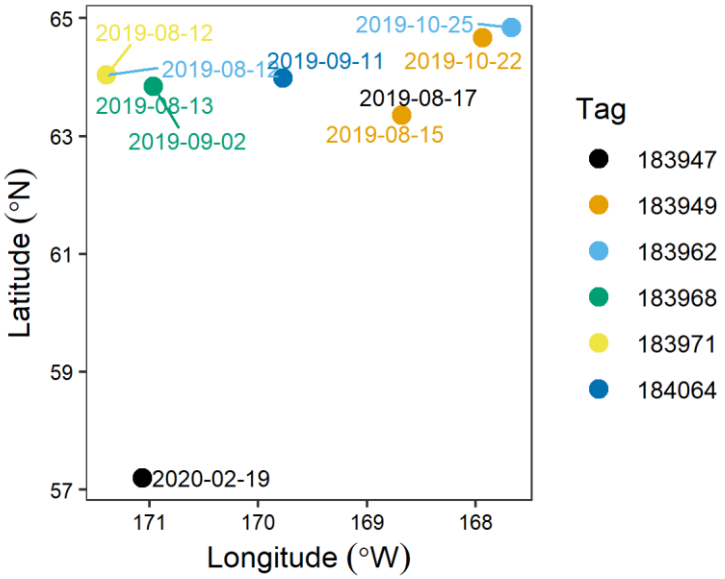

Figure S11. Deployment and recapture locations and dates for Pacific cod. Point colors denote unique tags/fish.

References

Alverson, D. L., & Pereyra, W. T. (1969). Demersal Fish Explorations in the Northeastern Pacific Ocean — An Evaluation of Exploratory Fishing Methods and Analytical Approaches to Stock Size and Yield Forecasts. Journal of the Fisheries Research Board of Canada, 26(8), 1985–2001. https://doi.org/10.1139/f69-188

Cribari-Neto, F., & Zeileis, A. (2010). Beta regression in R. Journal of Statistical Software, 34(2), 1–24. https://doi.org/10.18637/jss.v069.i12

Ferrari, S. L. P., & Cribari-Neto, F. (2004). Beta regression for modelling rates and proportions. Journal of Applied Statistics, 31(7), 799–815. https://doi.org/10.1080/0266476042000214501

Foote, K. G., Knudsen, H. P., Vestnes, G., MacLennan, D. N., & Simmonds, E. J. (1987). Calibration of acoustic instruments for fish density estimation: a practical guide. ICES Cooperative Research Report, 144, 1–69. https://doi.org/10.1121/1.396131

Kotwicki, S., De Robertis, A., Ianelli, J. N., Punt, A. E., & Horne, J. K. (2013). Combining bottom trawl and acoustic data to model acoustic dead zone correction and bottom trawl efficiency parameters for semipelagic species. Canadian Journal of Fisheries and Aquatic Sciences, 70(2), 208–219. https://doi.org/10.1139/cjfas-2012-0321

Kotwicki, S., De Robertis, A., von Szalay, P., & Towler, R. (2009). The effect of light intensity on the availability of walleye pollock (*Theragra chalcogramma*) to bottom trawl and acoustic surveys. Canadian Journal of Fisheries and Aquatic Sciences, 66(6), 983–994. https://doi.org/10.1139/f09-055

Kotwicki, S., Horne, J. K., Punt, A. E., & Ianelli, J. N. (2015). Factors affecting the availability of walleye pollock to acoustic and bottom trawl survey gear. ICES Journal of Marine Science, 72(5), 1425–1439. https://doi.org/10.1093/icesjms/fsv011

Rohan, S. K., Kotwicki, S., Laman, E. A., Britt, L. L., & Aydin, K. (2020). Deriving apparent optical properties from light measurements obtained using bottom-trawl-mounted archival tags [United States Department of Commerce, NOAA Technical Memorandum NMFS-AFSC-403, 91 p]. https://doi.org/10.25923/42yn-1q79

Simmonds, E. J., & MacLennan, D. (2005). Fisheries Acoustics: Theory and Practice (2nd ed.).

Traynor, J. (1996). Target-strength measurements of walleye pollock (*Theragra chalcogramma*) and Pacific whiting (*Merluccius productus*). ICES Journal of Marine Science, 53(2), 253–258. https://doi.org/10.1006/jmsc.1996.0031

APPENDIX D: CHAPTER 4 (SUPPLEMENTARY MATERIAL)

Table S1. Ratio between downwelling diffuse attenuation coefficient, K_d, and beam attenuation, c, from casts at locations with bottom depths ≤ 200 m. Data from the Worldwide Ocean Optics Database (WOOD; NCEI Accession 0092528).

	c/K_d			
λ (nm)	Mean	Median	s.d.	n
412	2.55	2.31	1.12	3487
440	3.02	2.62	2.02	4099
488	3.57	3.20	1.51	5401
489	3.18	2.83	0.91	420
490	2.23	2.12	0.88	6886
510	3.32	3.14	1.01	5626
532	3.49	3.36	1.49	2706
555	3.20	3.03	1.02	4550
630	3.38	3.20	1.69	433
715	8.10	8.77	3.71	382

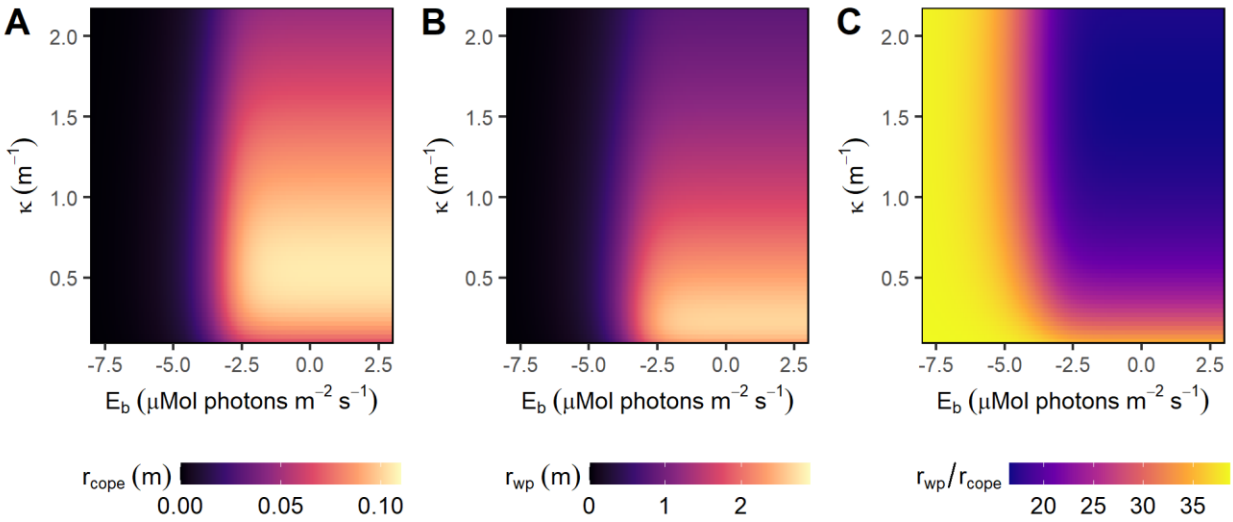

Figure S1. Predicted reaction distances of the generalized visual reaction distance model along gradients of background irradiance, E_b (μMol photons m^{-2} s^{-1}), and effective attenuation coefficient, κ (m^{-1}). Panels show (A) reaction distance to a *Calanus* copepod, r_{cope}, (B) reaction distance to a 15-cm juvenile walleye pollock, r_{wp}, and (C) ratio between reaction distances showing asymmetric effects of E_b and κ on reaction distances to different prey.

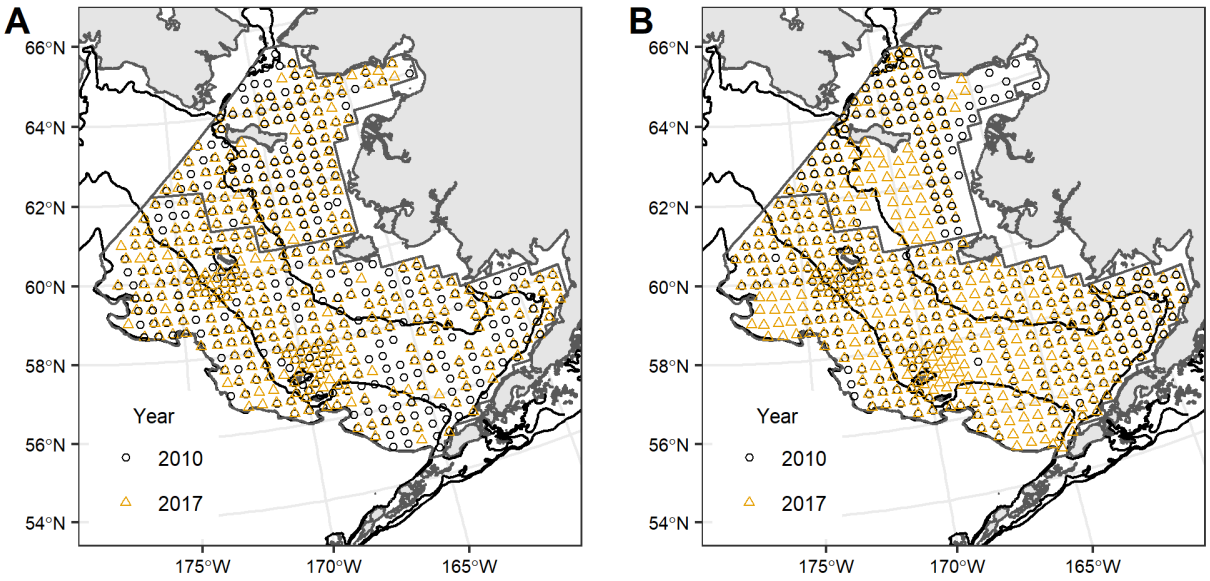

Figure S2. Locations of profiles of (A) diffuse attenuation coefficient, $K_d(z,\lambda_{tag})$, and (B) temperature and salinity from CTD casts from in June–August 2010 and 2017. Symbol shape and color denote year.

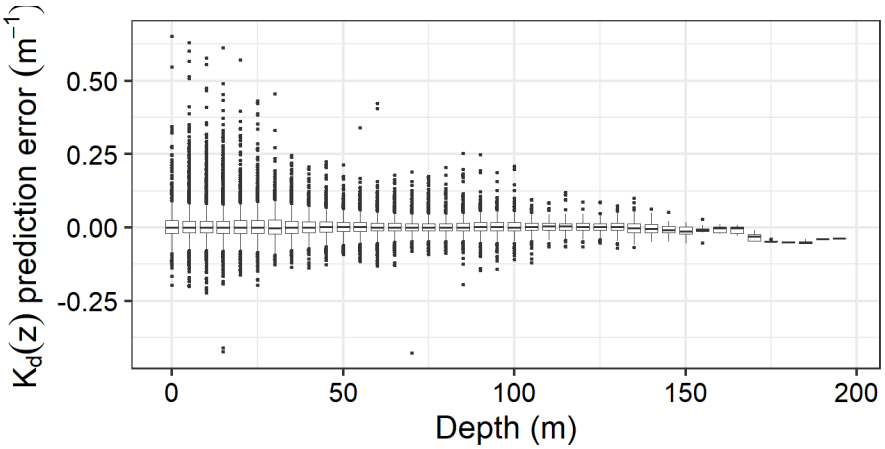

Figure S3. Prediction error in interpolation of downwelling diffuse attenuation coefficient, $K_d(z)$ from five-fold cross validation, by depth. Prediction errors are displayed in 5-m depth bins to aid interpretation.

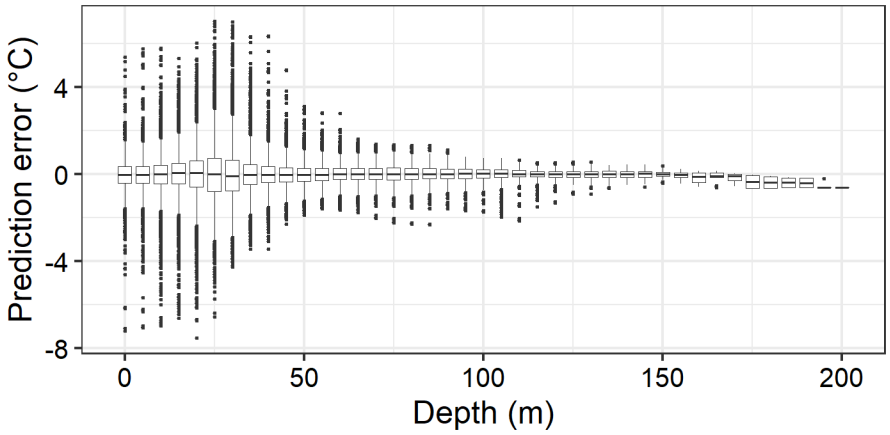

Figure S4. Prediction error in interpolation of temperature (°C) from five-fold cross validation, by depth. Prediction errors are displayed in 5-m depth bins to aid interpretation.

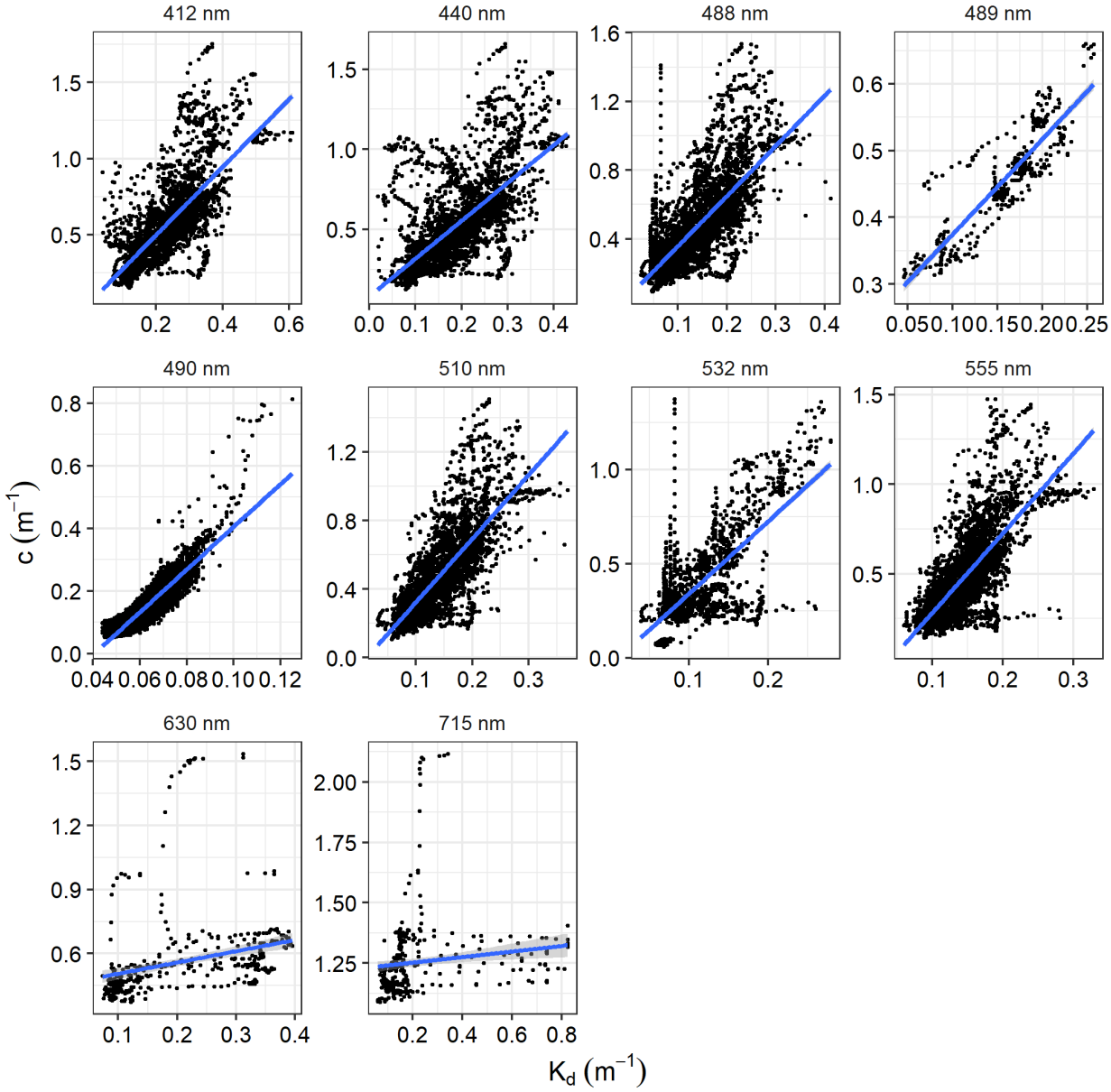

Figure S5. Downwelling diffuse attenuation coefficient, K_d, versus beam attenuation, c, from casts at locations with bottom depths ≤ 200 m. Data from the Worldwide Ocean Optics Database (WOOD; NCEI Accession 0092528).

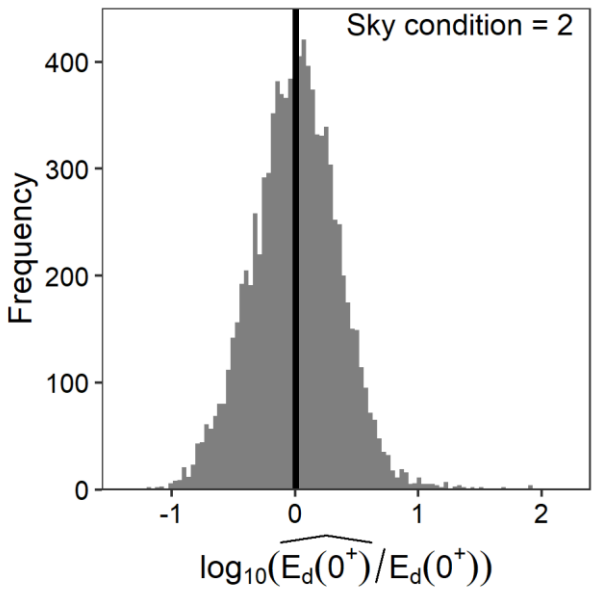

Figure S6. Log ratio between modeled downwelling irradiance $\widehat{E_d(0^+)}$ and downwelling irradiance from ship-board measurements, $E_d(0^+)$, in the eastern Bering Sea.

VITA

Sean Khosuke Rohan was born in Seattle, Washington. He developed an interest in marine science after taking a marine biology class at James A. Garfield High School in Seattle. Sean earned a Bachelors of Science in Aquatic and Fishery Sciences and minor in Quantitative Science from the University of Washington in 2010. He spent six years working as a University of Washington contractor for the NOAA Alaska Fisheries Science Center's Groundfish Trophic Interactions Program (Food Habits Lab). In 2016, Sean returned to the University of Washington School of Aquatic and Fishery Sciences to pursue a Doctoral degree. He is a Research Fishery Biologist at NOAA's Alaska Fishery Science Center. Sean's dissertation research focuses on understanding how variatiation in light and water clarity influence visual foraging and interactions between fish and fishing gear.